INFORMATION TO USERS

This manuscript has been reproduced from the microfilm master. UMI films the text directly from the original or copy submitted. Thus, some thesis and dissertation copies are in typewriter face, while others may be from any type of computer printer.

The quality of this reproduction is dependent upon the quality of the copy submitted. Broken or indistinct print, colored or poor quality illustrations and photographs, print bleedthrough, substandard margins, and improper alignment can adversely affect reproduction.

In the unlikely event that the author did not send UMI a complete manuscript and there are missing pages, these will be noted. Also, if unauthorized copyright material had to be removed, a note will indicate the deletion.

Oversize materials (e.g., maps, drawings, charts) are reproduced by sectioning the original, beginning at the upper left-hand corner and continuing from left to right in equal sections with small overlaps. Each original is also photographed in one exposure and is included in reduced form at the back of the book.

Photographs included in the original manuscript have been reproduced xerographically in this copy. Higher quality 6" x 9" black and white photographic prints are available for any photographs or illustrations appearing in this copy for an additional charge. Contact UMI directly to order.

UMI

A Bell & Howell Information Company
300 North Zeeb Road, Ann Arbor MI 48106-1346 USA
313/761-4700 800/521-0600

MIXED CONVECTION FROM AN ELLIPTIC TUBE PLACED IN A FLUCTUATING FREE STREAM

BY

EBALL HIFTHY ABDUL-RAHIM AHMAD

A Dissertation Presented to the

FACULTY OF THE COLLEGE OF GRADUATE STUDIES

KING FAHD UNIVERSITY OF PETROLEUM & MINERALS

DHAHRAN, SAUDI ARABIA

In Partial Fulfillment of the
Requirements for the Degree of

DOCTOR OF PHILOSOPHY

In

MECHANICAL ENGINEERING

DECEMBER 1996

KING FAHD UNIVERSITY OF PETROLEUM AND MINERALS
DHAHRAN 31261, SAUDI ARABIA

COLLEGE OF GRADUATE STUDIES

This dissertation, written by **Eball Hifthy Abdul-Rahim Ahmad** under the direction of his dissertation advisor and approved by his Dissertation Committee, has been presented to and accepted by the Dean of the College of Graduate Studies, in partial fulfillment of the requirements for the degree of **DOCTOR OF PHILOSOPHY.**

Dissertation Committee:

Dr. Hassan M. Badr (Chairman)

Dr. Syed M. Zubair (Member)

Dr. Syed A. Said (Member)

Dr. Mohamed A. El-Gebeily (Member)

Department Chairman

Dean, College of Graduate Studies

24-2-97
Date

كلية الدراسات العليا
COLLEGE OF GRADUATE STUDIES

Acknowledgment

First and foremost, all praise to the Almighty Allah who gave me the courage and patience to carry out this work. I am happy to have had a chance to glorify His name in the sincerest way through this small accomplishment and ask Him to accept my efforts.

Acknowledgement is due to King Fahd University of Petroleum and Minerals for providing support to this work.

My deep appreciation goes to my major thesis advisor Dr. Hassan Badr for his constant help, guidance and the countless hours of attention he devoted throughout the course of this work . His priceless suggestions made this work interesting and learning for me. He was always kind, understanding and encouraging. Working with him was indeed a wonderful and learning experience which I thoroughly enjoyed.

Thanks are also due to my thesis committee members Dr. Syed Zubair, Dr. Syed Said and Dr. Mohamed El-Gebeily for their interest, cooperation, advice and constructive criticism.

I am also indebted to the department chairman, Dr. Mohhammad O. Budair and other faculty members for their support.

Contents

List of Tables

List of Figures

Abstract

Name: Eball Hifthy A. Ahmad

Title: Mixed Convection from an Elliptic Tube Placed in a Fluctuating Free Stream.

Major Field: Mechanical Engineering

Date of Degree: December 1996

Heat transfer from an inclined elliptic tube in a convective environment with fluctuations in the free stream velocity is investigated numerically including the effect of buoyancy forces. The free stream direction is horizontal and normal to the tube axis and the flow field is essentially two dimensional. The investigation is based on a numerical solution of the conservation equations of mass, momentum and energy. The study focuses on the effect of the amplitude and frequency of fluctuations on the heat transfer process. The time-average of the Nusselt number is found to increase with increasing the amplitude of the fluctuations and with decreasing the frequency. Details of the velocity and thermal fields are presented in the form of isotherms and streamline patterns in addition to the surface vorticity and local Nusselt number distributions.

DOCTOR OF PHILOSOPHY DEGREE
KING FAHD UNIVERSITY OF PETROLEUM AND MINERALS
Dhahran, Saudi Arabia
December 1996

خلاصة الرسالة

الاسم : عبال حفظي عبد الرحيم أحمد

عنوان الرسالة : الانتقال الحراري بالحمل من أنبوب اهليلجي موضوع في تيار متذبذب

التخصص هندسة ميكانيكية

تاريخ الشهادة : ديسمبر ١٩٩٦

تم في هذا البحث دراسة رقمية للانتقال الحراري بالحمل من أنبوب اهليلجي مائل في وسط مائع متذبذب السرعة بافتراض أن السريان أفقي وعمودي على المحور الرئيسي للأنبوب وأن المجال كله ثنائي الابعاد . وقد تمت الدراسة بواسطة حل معادلات حفظ الكتلة والحركة والطاقة رقميا مع التركيز على تأثير تغير سعة وتردد الذبذبات على الانتقال الحراري .

وقد أفادت نتائج البحث أن معدل رقم نسلت يزداد بازدياد سعة الذبذبة وبنقصان ترددها . تم في هذا البحث أيضا استنباط تفاصيل المجال الحركي والحراري حول الأنبوب وعرضها في صورة خطوط الانسياب وخطوط ثبوت درجة الحرارة ، بالاضافة الى دراسة التغير المحلي في رقم نسلت والدوامات السطحية حول الأنبوب .

درجة الدكتوراه في الفلسفة

جامعة الملك فهد للبترول والمعادن

الظهران – المملكة العربية السعودية

ديسمبر ١٩٩٦

Chapter 1

Introduction

Heat transfer from cylinders of various shapes has been the subject of many theoretical and experimental studies because of its direct relevance to engineering practice. Heat convection from tubes of circular, rectangular or triangular cross-section represent few examples. Of special interest is the case of an elliptic cylinder. Tubes of elliptic cross-section have been used in compact heat exchangers not only to increase heat transfer rates but also to reduce the pressure drop across the heat exchanger. Moreover, the elliptic tube geometry is flexible enough to represent a circular tube or a very thin two-dimensional fin depending on the axis ratio. The rate of heat transfer from an elliptic tube depends on its geometry (i.e. axis ratio, surface roughness, and angle of inclination), the fluid properties, the approaching flow conditions and the tube surface temperature distribution. In general, various heat transfer modes may take place ranging from forced convection dominated regime to free convection dominated one. Combined (free and forced) heat transfer may also take place when

the inertial and buoyancy forces are comparable. The local heat transfer features for an elliptic tube set normal to an approaching stream differs considerably from that of a circular tube. The heat transfer characteristics are strongly influenced by the axis ratio, the angle of inclination and by Reynolds and Grashof numbers.

This study deals with heat transfer from a stationary tube of elliptic cross-section placed in a fluctuating free stream. These flow regimes occur in many engineering applications where it is required to enhance the heat transfer rates. Convective heat transfer rates from fluctuating turbulent flows are found to be higher than those of steady flows at the same mean Reynolds numbers, Dec et al. [1]. Such effect can lead to the design of low-cost compact heat exchangers. Pulse combustor tail pipe heat transfer, and the heat exchanger of sterling engines are examples of devices in which the increased heat transfer rates from fluctuating flow is used advantageously. Accordingly, it is important to understand the effect of fluctuating flows on heat transfer enhancement, and how this enhancement is related to various flow parameters. Studying the temperature fields during the flow fluctuations can provide valuable information for fluctuating flow modeling and an insight into the fundamental mechanism responsible for heat transfer enhancement. Also, understanding the behavior of the velocity fields can provide valuable information about the skin frictional drag which is related to the pressure drop in heat exchangers.

This work is the first in studying the heat transfer from a stationary tube of

elliptic cross-section placed in a fluctuating free stream. The investigation is based on the solution of two-dimensional momentum and energy equations.

In this study, we focus on the effect of different flow parameters including Reynolds number, Grashof number, angle of inclination and free stream fluctuations on the pressure, surface vorticity and local Nusselt number distributions . The effect of all of the above parameters, on the skin friction, pressure variation and Nusselt number are also investigated.

Chapter 2

Literature Survey

Published research focusing on heat transfer from cylinders and wires of various shapes is extensive. A brief review of the previous theoretical and experimental work is presented in this chapter. The work reviewed is that related to laminar forced and free convection heat transfer from horizontal cylinders of circular or elliptic cross-section placed in Boussinesq fluids of infinite extent. The effect of flow oscillations forced and mixed convection from cylinders is also reviewed.

2.1 Unsteady Flow Over Circular Cylinders

In 1970, Dennis and Chang [2] presented a numerical solution for steady flow past a circular cylinder for a range of Reynolds numbers from Re = 5 to Re = 100. The wake length was found to increase approximately linearly with Re over the considered range of Re. They calculated the values of drag coefficient, the angle of separation and the pressure and vorticity distribution over the cylinder surface.

The mathematical approach was based on approximating the stream function and vorticity using a finite Fourier series. In 1977, Coutanceau and Bouard [3] presented their experimental results showing the main features of the hydrodynamic field for flow past a circular cylinder moving at a constant speed in a direction perpendicular to its axis in a tank filled with a viscous liquid. The investigation covered the wake region and the velocity distribution near the cylinder surface. They compared their results with the solution by Nieuwstadt and Keller [4] and found a good agreement. Lecointe and Piquet [5] studied the unsteady incompressible flow around a circular cylinder using several compact methods. The fourth order method of Mehrstellen type was used to study the problem for several Reynolds numbers. The numerical technique was proven to be successful when they compared their results with others. Badr and Dennis [6] presented a numerical study for the development of the two-dimensional flow of a viscous incompressible fluid around a circular cylinder which suddenly starts rotating about its axis with a constant angular speed and translating at right angles to the axis with a constant speed. In the solution, they reduced the governing partial differential equations in two space variables and time to a set of time dependent equations in one space variable by means of Fourier analysis. In this analysis, a truncated Fourier series was used to approximate the stream function and vorticity. The analysis resulted in a finite set of differential equations in one space coordinate and time. They compared their results with experimental results

and found an excellent agreement. Dalton and Wang [7] presented a numerical study of the unsteady two-dimensional flow past a circular cylinder using vorticity and stream functions as dependent variables. They considered the two cases of impulsively started and decelerated flows. They used a predictor-corrector method for the vorticity transport equation along with a fast Poisson solver for the stream function equation. They tested their results with previous work and found a very good agreement. In 1992, Zverkhovskiy [8] carried out an experimental study on the flow around a vertical cylinder rotating in a Newtonian or non-linear viscoplastic suspension. He presented the behavior of the unsteady flow developing around cylinders 35 and 60 mm in diameter. Experimental results were also presented for the shear stress acting on the cylinder. In 1994, Hakizumwami [9] solved numerically the early stages of unsteady viscous flow past a circular cylinder at Re = 3000 and Re = 9500. He solved the vorticity transport equation by second order finite-difference method in both directions of the flow domain. His computed results were compared qualitatively with experimental data and found a satisfactory agreement.

2.2 Heat Convection from Circular Cylinders in Unsteady Flows

This section focuses on the literature related to forced, natural or combined convection heat transfer from circular cylinders. In 1966 Acrivos [10] investigated the

combined effect of forced and free convection heat transfer in laminar boundary-layer flows. In this problem the momentum and energy equation, coupled with the gravitational term, were solved theoretically. It was shown that for large values of the Prandtl number, the relative importance of forced and free convection is controlled by the parameter Gr/Re^3 whereas for Pr less than one the controlling parameter is Gr/Re^2. In 1972, Vest and Lawson [11] studied the problem of the onset of convection near a suddenly heated horizontal wire. Their work deals with the early transient process occurring in a fluid surrounding a thin wire which was suddenly heated by an electric current. They found that the heat transfer at the beginning was dominated by conduction only. After a period of time (delay time) convection was observed. The problem of mixed convection about a horizontal circular cylinder was also studied by Sparrow and Lee [12]. The general case of mixed convection about a heated cylinder placed in a cross flow was not readily amenable to solution. However, they solved a less general problem of an isothermal heated cylinder in a vertical up flow provided that a boundary layer exists. They presented local and average Nusselt number values. A comparison with experimental work showed deviations ranging from 10 % at the stagnation point up to 30 % at an angle of 70° measured from the stagnation point.

In 1983, Badr [13] investigated the problem of laminar mixed convection from a horizontal circular cylinder placed in a cross stream. The study was based on the

solution of the full Navier-Stokes and energy equation for two dimensional flow of a Boussinesq fluid. The investigation covered the ranges of Reynolds number from 1 to 40, and Grashof number up to $Gr = 5Re^2$ at a constant Prandtl number. In solving the governing equations, he obtained the steady solution through integrating the governing equations in time until the fully developed temperature and velocity fields were reached.

2.3 Unsteady Flow Over Elliptic Cylinders

Research interest on flow over elliptic cylinder started as early as 1924, when Harrison [14] studied the motion of elliptic cylinder through viscous liquid. However, the focus in this review is on the work done in the last two decades.

In 1974, Lugt and Haussling [15] presented a numerical solution for laminar incompressible fluid flow past an abruptly started elliptic cylinder at 45 degrees incidence. They used a finite-difference scheme for the stream function and vorticity formulation. Steady state solution was reached for Re = 15 and 30, whereas for Re = 200 a Karaman vortex street developed. They also investigated the transient period from the start until reaching the steady or quasi-steady state value. The streamlines, equi-vorticity lines, drag, lift, and moment coefficients were presented. The problem was solved using stream function-vorticity formulation and the pressure distribution was presented for several cases. The results showed some discontinuity in the surface pressure distribution.

The next research in this area was done in 1980 by Patel [16] where the flow around an impulsively started elliptic cylinder at various angles of incidence was investigated. The flow was viscous, incompressible and the motion was governed by the Navier-Stokes equations. Semi-analytical solutions were obtained by solving numerically the system of coupled partial differential equations which resulted from

approximating the stream function and vorticity using a finite Fourier series. Symmetrical solutions were presented for Reynolds number 200 and eccentricities 0.809 and 0.943 in terms of patterns of streamlines, lines of constant vorticity, surface pressure and vorticity distributions. A comparison of the calculations had been made for Reynolds number 100 and eccentricity 0.648 with different number of terms in the series. He found that a Karman vortex street develops for Reynolds number 60 and 200 at 30° and 45° incidence respectively. He also found that the vanishing of wall-shear does not denote separation in any meaningful sense in various cases.

Loc et al. [17] studied the early stages of viscous flow development over an elliptic cylinder at an angle of attack both experimentally and numerically. Experimental study was basically a flow visualization involving some quantitative measurements of velocity distributions. The numerical method was based on the use of a high order compact finite-difference scheme. They presented qualitative and quantitative comparisons between the results by both methods which were found to be quite satisfactory. These comparisons enabled them to give an accurate description of the separation phenomenon which occurred at the early stages of the flow development.

In 1985, Lee and Leal [18] proposed a numerical implementation of the method of matched asymptotic expansions to analyze the two-dimensional uniform streaming flow at low Reynolds number past a straight cylinder of arbitrary cross-sectional shape. General solutions for both the Stokes and Oseen equations in two dimen-

sions were expressed in terms of a boundary distribution of fundamental single- and double-layer singularities. These general solutions were then converted to integral equations for the unknown distributions of singularity strengths by application of boundary conditions at the cylinder surface, and matching conditions between the Stokes and Oseen solutions. By solving these integral equations using collocation methods, they generated a uniformly valid approximation to the solution for the whole domain. They demonstrated the method by considering, numerical examples such as, uniform flow past an elliptic cylinder, uniform flow past a cylinder of rectangular cross-section, and uniform flow past two parallel cylinders which may be either equal in radius, or of different sizes. The approach is limited to low Reynolds number flows.

More recently a mathematical model was proposed for investigating two dimensional flow of a viscous fluid past a cylinder by Dalessio and Dennis [19]. The model was consistent both with boundary-layer theory for sufficiently large Reynolds number and with the asymptotic solution at large distances from the cylinder. The governing Navier-Stokes equations were transformed to a set of equations which were referred to as the modified Navier-Stokes equations and are then solved numerically. Solutions have been obtained for the cases of flow past a stationary and a rotating circular cylinder and flow past an inclined elliptic cylinder. They found a good agreement with existing results.

2.4 Heat Convection from Elliptic Cylinders

Heat convection from elliptic cylinder was a subject of a number of investigations not only because of its fundamental nature but also because of the related engineering applications. In 1974, Lin and Chao [20] replaced the buoyancy term in the boundary-layer equations by a hypothetical outer stream velocity function. After suitable transformation, series solutions were generated for two dimensional or axisymmetric isothermal smooth objects with circular and elliptic cylinders as special cases. The solution had the drawback of its inapplicability in the buoyant plume region. Raithby and Hollands [21] presented a study for the free convection from elliptic cylinders with a vertical plates and circular cylinders as special cases. Their method of solution was based on presenting thin layer analysis at the beginning. This was applicable when the boundary layer was everywhere much thinner than the local radius of curvature. Later, the thin layer analysis was modified to take into account the effect of curvature. Local and average Nusselt numbers were reported. Finally correlations of average Nusselt number for elliptic cylinder, with major axis vertical were also presented. These correlations compare reasonably well with experimental data. In 1976, Merkin solved the boundary layer equations for elliptical cylinders with major-axis either vertical or horizontal. Local and average heat transfer rates for isothermal cylinder and also for constant heat flux cylinders

were calculated. Badr and Shamsher [22] solved the problem of free convection from an elliptic cylinder with major axis vertical. The investigation was based on the solution of the conservation equations of mass, momentum, and energy. Rayleigh numbers considered in the study ranges from 10 to 1000 and for a constant value of Prandtl number (Pr = 0.7). The cylinder axis ratio (minor to major) was varied from 0.1 to 0.964 approaching a flat plate at one end and a circular cylinder at the other. Results were presented for the local and average Nusselt numbers along with details of the thermal and velocity fields given in the form of isotherm and streamline patterns. The method of solution was validated by comparing results with the available theoretical and experimental data for the circular cylinder and the flat plate as limiting cases.

In 1994, Badr [23] solved the problem of laminar mixed (natural and forced) convective heat transfer from a straight isothermal tube of elliptic cross-section placed in a uniform stream. The free stream direction was horizontal and normal to the tube axis and the flow field was essentially two dimensional. The investigation was based on a numerical solution of the conservation equations and the resulting velocity and thermal fields were found to be either steady or quasi-steady depending on vortex shedding. The study focused on the effects of Reynolds number, Grashof number, and on the heat transfer process in the Re range from 20 to 500, Gr range from 0 to 1.25×10^6 and for angles of inclination varying from 0° to 180° . The

average Nusselt number was found to increase considerably with the increase of the ratio Gr/Re^2 . The response of the total rate of heat transfer to changes in the inclination angle was found to depend on the Reynolds number. Results also showed that the increase of Gr for a given value of Re tends to suppress vortex shedding. The details of the velocity and thermal fields were presented in the form of isotherm and streamline patterns in addition to the surface vorticity and local Nusselt number distributions. In 1995, Kaminski et al. [24] analysed numerically and experimentally the combined convective and radiative heat transfer in laminar flow over elliptic cylinder. They simulated the two-dimensional conditions by taking the length to major axis ratio of the cylinder to be 10. They used finite element methods to solve the problem for low Reynolds number flow. They solved the coupled equation of momentum, energy, and continuity in a radiative medium. The medium was assumed to be non-gray non-scattering. They calculated the average and local Nu at Re = 500.

2.5 Oscillating Flow Over Cylinders of Circular or Elliptic Cross-sections

The first extensive study on oscillating flow was that by Watson [25] who solved the Navier-Stokes equations for two dimensional incompressible flow past an infinite porous wall. He obtained relations for the velocity distribution as a function of the given free stream velocity. Among the particular cases he studied was the case of flow in which the free stream velocity consists of mean flow with a super-imposed decaying part. In this case, he found that the fluctuating skin friction had a phase advance on the fluctuating free stream velocity. For large frequencies, the amplitude of the skin friction fluctuation was found to be proportional to the square root of the frequency and also proportional to the amplitude of the free stream velocity fluctuation. In 1967, Wang [26] investigated the equations governing high frequency oscillatory viscous flows, through the separation of the steady and unsteady terms. All Reynolds number ranges were studied and the order of magnitude of the steady streaming produced by the Reynolds stresses were established. He studied the oscillating circular cylinder at low Reynolds numbers through the method of inner and outer expansions. He found steady recirculating cells to exist near the cylinder. The obtained results compared very well with experiments. He also obtained analytical expressions for the stream function and the drag coefficient . The oscillating flow towards an infinite plate was also investigated. The pressure gradient was found to

cause reverse flow near the solid boundary. Takallu and Wlliams [27] conducted a theoretical investigation to determine the time variation of lift on a slender elliptic cylinder moving at uniform speed but oscillating in pitch. His analysis couple a potential flow calculation for the flow past the cylinder with a calculation of the unsteady, two dimensional, laminar boundary layer on the surfaces of the pitching ellipse. The coupling was achieved by matching the rate at which vorticity was shed into the wake with the time rate of circulation about the ellipse. The unsteady lift was determined from an integration of the unsteady pressure distribution on the body. The effects of mean angle of attack and oscillation frequency on the lift hysteresis showed that the hysteresis loops change direction as the mean angle of attack is increased. In 1984, Kurzweg [28] examined enhanced conduction heat transfer via sinusoidal oscillatory flow through circular tubes connecting two fluid reservoirs that are maintained at different temperatures. He used a multiscale expansion technique for the solution of the governing partial differential equation. The spatial and temporal temperature variations within the tubes were determined for low values of α^2 Pr, where α is the Womersley number. The effective thermal diffusivity was calculated and used to determine the enhanced conduction heat transfer from the high- to low-temperature reservoir. The enhanced heat transfer produced by the oscillations was shown to be proportional to the square of the oscillation amplitude and a function of the Prandtl number, the frequency, and the tube radius.

In 1985, Bearman et al. [29] presented a paper on the comparison between theory and experiment for the in-line forces on cylinders of general cross-section in planer oscillatory flows of small amplitude. Their theoretical analysis evaluated corrections to the standard inviscid inertial force at low Keulegan-Carpenter numbers which arise from the presence of viscous laminar boundary-layers and from the development of vortex shedding. The boundary-layer contribution due to both skin friction and displacement effects was calculated to first order in the Stokes parameter . The contribution to the in-line force from separation and vortex shedding was taken from previous work on vortex shedding from isolated edges using the discrete vortex modeling technique. The theoretical results were compared to measurements taken in a U-tube water channel on a number of cylinders of different cross-sections including circular cylinders and sharp-edged sections. The comparisons suggest that the theory was valid for Keulegan-Carpenter numbers below about 3 and for moderately high values of the Stokes parameter. Sarpkaya, [30] calculated the in-line force coefficients for a circular cylinder in planer oscillatory flows of small amplitudes. He compared his results with the theoretical predictions of Wang [26] for two dimensional, attached- and laminar-flow conditions. The data were in good agreement with Wang's analysis. The oscillatory viscous flow became unstable to axially periodic vortices above a critical Keulegan-Carpenter number, K ($K = U_m T/D$, U_m is the maximum velocity in a cycle, T is the time period of flow, and D is the diameter

of the cylinder) of the ratio $B = Re/K$, as shown experimentally by Honji [31] and theoretically by Hall [32]. His investigation showed that the Keulegan-Carpenter number at which the drag coefficient (C_D) deviates rather from the Wang's prediction nearly corresponds to the critical K at which the vortical instability occurs. In 1986, Baba and Miyata [33] presented a higher order difference solution of vortex generation from a circular cylinder in an oscillatory flow. The Navier-Stokes equation in a rotational form, which conserves both momentum and kinetic energy, was approximated into a difference form by a fourth-order compact differencing in a general boundary-fitted curvilinear coordinate system. A time-marching procedure was derived and the high resolution property was demonstrated with the computations of some simple problems. They simulated viscous flow around a circular cylinder sinusoidally oscillating at low Keulegan-Carpenter number.

In 1987, Lam [34] described a method for predicting the response of the two-dimensional, incompressible, laminar boundary layer on a semi-infinite flat plate under small harmonic progressive oscillations of the free stream velocity for arbitrary frequency and wave speed. The free stream considered consists of a constant mean on which an oscillating amplitude varying with downstream distance was superimposed. The governing equations were solved numerically by a finite-difference technique in conjunction with a series solution for small reduced frequencies. His results were compared with those obtained by other methods. The results were ac-

curate for a full range of frequency, and the response was very sensitive to changes in the wave convection speed. Recently, Justesen [35] solved numerically the stream function-vorticity formulation of the Navier-Stokes equations for flow around a circular cylinder in planer oscillating flow at small Keulegan-Carpenter numbers (KC) in the subcritical Reynolds number range. The equations were solved by finite-difference methods. For very small KC, his numerical results coincided with the obtained analytical solutions. As KC increased, the incipient separation and instability leading to asymmetrical flow with vortex shedding were predicted. Computed flow fields at small KC values were compared with flow visualizations, and a good agreement was found for moderate values of KC. The well-documented flow regimes with the transverse vortex street single-, double-, and three-pair shedding were predicted by his model. He compared the calculated drag and inertia coefficients with experimental data for three different values of the frequency parameter and for KC less than 26 and showed a good agreement. Wang and Dalton [36] solved numerically the problem of sinusoidally oscillating flow past a fixed circular cylinder. Calculations were performed for conditions which lead to both symmetric and asymmetric wakes. Solutions were obtained for Reynolds number ranges from 100 to 3000 and Keulegan-Carpenter number range from 1 to 12. A hybrid differencing scheme was introduced to provide a stable solution for large values of the parameters.

More recently, Badr [37] solved the problem of oscillating inviscid flow over a

stationary cylinder of elliptic cross-section analytically. The free stream direction was horizontal and was always normal to the cylinder axis and oscillations were only allowed in the magnitude of the free stream velocity. The flow was incompressible, and two-dimensional and the free stream oscillations were harmonic. The study focused on the hydrodynamic forces acting on the cylinder as well as the pressure distribution and their time variation. The parameters involved were the cylinder axis ratio, angle of incidence and Strouhal number. The solution for the problems of oscillating flow over flat plates and circular cylinders can be obtained as special cases. Analytical expressions were obtained for the drag coefficient, the lift coefficient and the surface pressure distribution and their variations with time.

In another work, Badr [38] solved the problem of oscillating viscous flow over a stationary cylinder of elliptic cross-section. The free stream direction was horizontal and was always normal to the cylinder axis. The flow was incompressible, and two-dimensional and the free stream oscillations were harmonic. The considered elliptic cylinder has a major to minor axis ratio of 0.6 and was inclined to the free stream direction at angles of incidence of either 30^{o} or 60^{o}. His investigation was based on the solution of the time-dependent Navier-Stokes equations together with the energy conservation equation. He studied the flow for Reynolds number range between 100 and 1000 and the Strouhal number range between $\pi/4$ and $\pi/2$. The time variation of the flow field was presented in the form of streamline patterns as well as surface

vorticity distribution. The surface pressure distribution and the time variation of the in-line and transverse force coefficients were also presented and compared with the inviscid flow solution for the same problem. The comparison between viscous and inviscid flow solutions showed a better agreement for higher values of Reynolds and Strouhal numbers.

In 1995, Nguyen et al. [39] investigated heat transfer from a rotating circular cylinder in a convective environment with small fluctuations in the free-stream including the effects due to buoyancy forces. The flow equations, based on the vorticity and stream function, were recast in the form a biharmonic equation which together with the energy equation were solved by a hybrid spectral method that combines Fourier spectral and Chebyshev collocation in the angular and radial directions, respectively. They simulated several cases for Grashof numbers up to 104, Reynolds numbers up to 200, and a range of dimensionless rotational speed from -0.5 to 0.5. Detailed results were presented for cross flow, aiding flow, and opposing flow together with a parametric study to show the effects of the Reynolds number, Grashof number, rotational speed, and the gravity direction on the resulting Nusselt number. Their results provided a significant physical insight into the convective phenomena under simultaneous rotation and flow pulsation. However, no comparison with the steady free stream cases was provided to show the effect of fluctuations on heat transfer rates.

Chakrabarti et al. [40] studied the resulting forces due to a sinusoidal progressive waves on a small circular tube arbitrarily oriented with respect to the wave direction. In their experiment, they measured two-component normal forces in a wave tank. Their results show that the resultant force could be as much as twice the in-line force depending on the period of oscillations. In 1981, Sarpkaya et al. [41] presented the results of two investigations on the vortex-induced oscillations of circular cylinders. The first was on the dynamic response of spring-mounted, smooth and rough, rigid cylinders in a sinusoidally-oscillating two-dimensional flow. The second was on the in-line and transverse oscillations of cantilevered piles at or near resonance conditions in regular laboratory waves at intermediate- and deep-water conditions. The results of both studies had shown that the test bodies undergo hydroelastic oscillations in a relatively well defined region of the reduced velocity and that the local as well as the average of the lift force was considerably amplified due to the nonlinear interactions between the body and the separated fluid motion.

Another work related to oscillating free stream flow over a body was done by Brendel and Mueller [42]. They investigated experimentally the influence of a periodic non-reversing wind-tunnel flow on an airfoil operating at low Reynolds numbers. The focus of his work was on the temporal behavior of the transitional separation bubbles that occur at low speeds. Unsteady pressure distributions and flow visualization were used to determine whether periodic bubble bursting would result from

large-amplitude periodic fluctuations in the Reynolds number. It was found that the transitional bubble remains intact even when the instantaneous Reynolds number was below the steady-flow bubble-bursting free stream speed (critical Reynolds number). The cause of this was connected with a flow hysteresis that was a function of changes in Reynolds number. In more detailed experiments, mean unsteady and phase-locked velocity profiles were obtained using hot-wire anemometry for an unsteady flow having an oscillation period of 0.5 s, an amplitude of 7 percent of the mean flow, and a mean Reynolds number of 100,000.

Chapter 3

Problem Statement and Governing Equations

3.1 Problem Statement

The problem considered in this work is that of mixed convection heat transfer from a straight tube of elliptic cross section subjected to a fluctuating flow field. The tube which has an isothermal outer surface temperature, T_s, is placed with its axis horizontal in a uni-directional horizontal free stream of temperature, T_∞, approaching perpendicular to the tube axis as shown in Figure 3.1. The fluctuations in the free stream are only in the magnitude of the velocity which is expressed as

$$U_\infty = \overline{u} + A\cos(\omega t) \tag{3.1}$$

Although the work done is limited to the above form of fluctuations, the numerical scheme is flexible enough to handle the more general case in which the velocity

fluctuations is expressed in the form

$$U_\infty = \overline{u} + \sum_{n=1}^{N} [A_n \cos(\omega_n t) + B_n \sin(\omega_n t)] \tag{3.2}$$

The tube cross-section has major and minor axes 2a and 2b respectively and the The major axis of the cylinder may be horizontal or inclined at an angle λ as shown in Figure 3.1. The following assumptions are also utilized in the analysis of the problem:

1. The cylinder is of infinite length i.e., the end effects of the cylinder on the velocity and temperature fields are neglected, hence the flow is two dimensional.

2. The cylinder is immersed in viscous fluid of infinite extend.

3. The effect of temperature variation on fluid properties are considered negligible except for the body forces in the momentum equation. This is commonly referred to as the Boussinesq approximation.

4. Effect of viscous dissipation is neglected.

5. Radiation heat transfer effects are neglected.

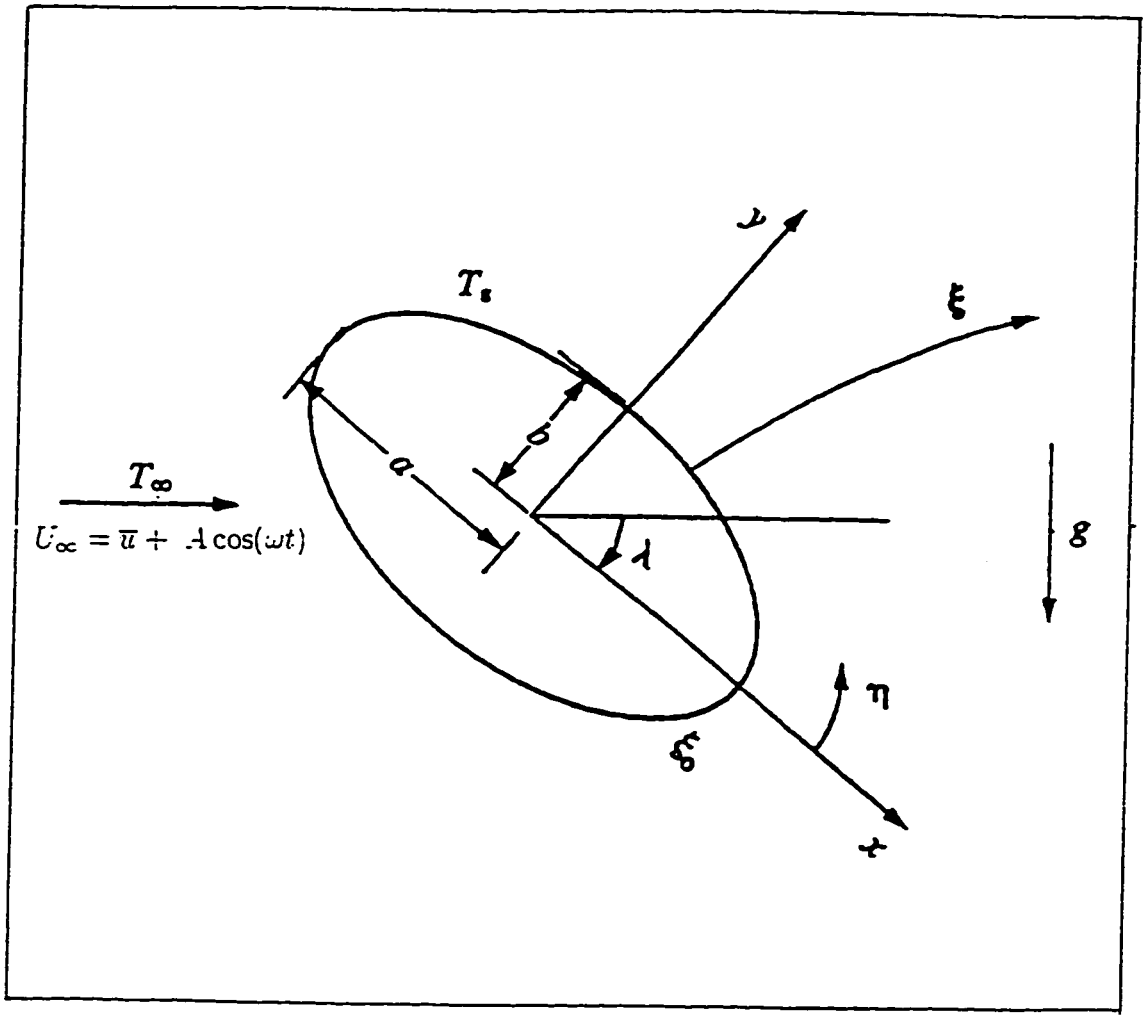

Figure 3.1: The elliptic section geometry and the coordinate systems.

3.2 The Governing Equations

Based on the assumptions stated in section (3.1) The mass, momentum and energy conservation equations in cartesian coordinates take the following forms:

$$\frac{\partial u}{\partial x} + \frac{\partial v}{\partial y} = 0 \tag{3.3}$$

$$\frac{\partial u}{\partial t} + u\ \frac{\partial u}{\partial x} + v\ \frac{\partial u}{\partial y} = -\frac{1}{\rho}\ \frac{\partial p}{\partial x} + \frac{\mu}{\rho}\ [\frac{\partial^2 u}{\partial x^2} + \frac{\partial^2 u}{\partial y^2}] + \frac{1}{\rho}\ F_x \tag{3.4}$$

$$\frac{\partial v}{\partial t} + u\ \frac{\partial v}{\partial x} + v\ \frac{\partial v}{\partial y} = -\frac{1}{\rho}\ \frac{\partial p}{\partial y} + \frac{\mu}{\rho}\ [\frac{\partial^2 v}{\partial x^2} + \frac{\partial^2 v}{\partial y^2}] + \frac{1}{\rho}\ F_y \tag{3.5}$$

Where the body force components F_x and F_y appearing in equations (3.4) and (3.5) are due to the effect of buoyancy. The buoyancy force is acting vertically upward and can be expressed in the form

$$F = g\ (\rho_\infty - \rho) \tag{3.6}$$

We now introduce the volumetric thermal expansion coefficient defined as

$$\beta = -\frac{1}{\rho}\ (\frac{\partial \rho}{\partial T})_p \tag{3.7}$$

For small temperature changes, β can be expressed in the approximate form by

$$\beta = -\frac{1}{\rho}\,(\frac{\rho_\infty - \rho}{T_\infty - T}) \tag{3.8}$$

and the buoyancy force per unit volume becomes

$$F = \rho\,\beta\,g\,(T - T_\infty) \tag{3.9}$$

The x- and y- components (see Figure 3.1) of this force become

$$F_x = \rho\,\beta\,g\,(T - T_\infty)\sin\lambda, \tag{3.10}$$

$$F_y = \rho\,\beta\,g\,(T - T_\infty)\cos\lambda, \tag{3.11}$$

Now, by introducing the stream function ψ and vorticity ζ defined as

$$u = \frac{\partial\psi}{\partial y} \quad , \quad v = -\frac{\partial\psi}{\partial x} \tag{3.12}$$

$$\zeta = (\frac{\partial v}{\partial x} - \frac{\partial u}{\partial y}), \tag{3.13}$$

the continuity equation [Equation (3.3)], becomes automatically satisfied. Differentiating both sides of the x-momentum equation [Equation 3.4] with respect to y and the y-momentum equation [Equation (3.5)] with respect to x, subtracting and using the definition of vorticity [Equation (3.13)], the following expression for the rate of change of vorticity is obtained:

$$\frac{\partial\zeta}{\partial t} = \nu(\frac{\partial^2\zeta}{\partial x^2} + \frac{\partial^2\zeta}{\partial y^2}) - \frac{\partial\zeta}{\partial x}\frac{\partial\psi}{\partial y} + \frac{\partial\zeta}{\partial y}\frac{\partial\psi}{\partial x} + \frac{1}{\rho}\,[\frac{\partial F_y}{\partial x} + \frac{\partial F_x}{\partial y}] \tag{3.14}$$

where

$$\zeta = -\left(\frac{\partial^2 \psi}{\partial x^2} + \frac{\partial^2 \psi}{\partial y^2}\right) \tag{3.15}$$

The energy equation will, also, take the following form :

$$\frac{\partial T}{\partial t} + u \frac{\partial T}{\partial x} + v \frac{\partial T}{\partial y} = + \frac{k}{\rho c} \left[\frac{\partial^2 T}{\partial x^2} + \frac{\partial^2 T}{\partial y^2}\right] \tag{3.16}$$

and by the definition given in [equation (3.12)], it can be written in the form

$$\frac{\partial T}{\partial t} = \frac{k}{\rho c} \left(\frac{\partial^2 T}{\partial x^2} + \frac{\partial^2 T}{\partial y^2}\right) - \frac{\partial T}{\partial x} \frac{\partial \psi}{\partial y} + \frac{\partial T}{\partial y} \frac{\partial \psi}{\partial x} \tag{3.17}$$

3.3 Normalizing the Governing Equations

Since it is convenient to work with dimensionless quantities, the governing equations are made dimensionless by redefining the dependent and independent variables as follows :

$$\grave{x} = \frac{x}{c} \qquad \grave{y} = \frac{y}{c} \qquad \grave{u} = \frac{u}{\overline{u}} \qquad \grave{v} = \frac{v}{\overline{u}}$$

$$\grave{t} = \frac{t\,\overline{u}}{c} \qquad \grave{\psi} = \frac{\psi}{\overline{u}\,c} \qquad \grave{\zeta} = -\frac{\zeta\,c}{\overline{u}} \qquad \phi = \frac{T - T_\infty}{T_s - T_\infty} \tag{3.18}$$

where $c = (a^2 - b^2)^{\frac{1}{2}}$ is the focal distance of the elliptic section and all variables with prime are dimensionless in addition to the dimensionless temperature ϕ. The Reynolds, Prandtle and Grashof numbers are defined as :

$$Re = \frac{2\,\overline{u}\,c}{\nu} \tag{3.19}$$

$$Pr = \frac{\nu}{\alpha} \tag{3.20}$$

$$Gr = \frac{g\,\beta\,(2c)^3\,(T_s - T_\infty)}{\nu^3} \tag{3.21}$$

By introducing the above variables in equations (3.14) to (3.17) and omitting the primes from all the variables we obtain the following dimensionless form of the governing equations

$$\frac{\partial \zeta}{\partial t} + u\,\frac{\partial \zeta}{\partial x} + v\,\frac{\partial \zeta}{\partial y} = \frac{2}{Re}\,\nabla^2\,\zeta - \frac{Gr}{2\,Re^2}[\cos\lambda\,\frac{\partial \phi}{\partial x} + \sin\lambda\,\frac{\partial \phi}{\partial y}] \tag{3.22}$$

$$\zeta = \nabla^2 \psi \tag{3.23}$$

$$\frac{\partial \phi}{\partial t} + u \frac{\partial \phi}{\partial x} + v \frac{\partial \phi}{\partial y} = \frac{2}{Re\ Pr} \nabla^2 \phi \tag{3.24}$$

The dimensionless free stream velocity fluctuations are now expressed as

$$U_\infty = 1 + \beta \cos St \tag{3.25}$$

where $S = c\omega/\overline{u}$ is the Strouhal number and β is the amplitude of the free stream fluctuations.

3.4 Coordinate Transformation

In order to have a highly accurate numerical solution, the coordinate system must match the flow field geometry. For this reason, all the governing equations are transformed to elliptic coordinates using the following transformations:

$$x = c \cosh\xi \ \cos\eta, \tag{3.26}$$

$$y = c \sinh\xi \ \sin\eta, \tag{3.27}$$

where

$$\xi \in [\xi_o , \infty), \quad \eta \in [0 , 2\pi]$$

and $\xi_o = \tan^{-1}\frac{b}{a}$ representing the outer surface of the elliptic tube After transformation into elliptic coordinates equations (3.22) to (3.24) take the following forms :

$$\begin{aligned} H\frac{\partial\zeta}{\partial t} + \frac{\partial\psi}{\partial\eta}\frac{\partial\zeta}{\partial\xi} - \frac{\partial\psi}{\partial\xi}\frac{\partial\zeta}{\partial\eta} &= \frac{2}{Re}\left(\frac{\partial^2\zeta}{\partial\xi^2} + \frac{\partial^2\zeta}{\partial\eta^2}\right) \\ -\frac{Gr}{2\,Re^2}\Big[\frac{\partial\phi}{\partial\xi}&(\cosh\xi\sin\eta\sin\lambda + \sinh\xi\cos\eta\cos\lambda) \\ -\frac{\partial\phi}{\partial\eta}&(\cosh\xi\sin\eta\cos\lambda) - (\sinh\xi\cos\eta\sin\lambda)\Big] \end{aligned} \tag{3.28}$$

$$H\,\zeta = \frac{\partial^2\psi}{\partial\xi^2} + \frac{\partial^2\psi}{\partial\eta^2} \tag{3.29}$$

$$H\frac{\partial \phi}{\partial t} + \frac{\partial \psi}{\partial \eta}\frac{\partial \phi}{\partial \xi} - \frac{\partial \psi}{\partial \xi}\frac{\partial \phi}{\partial \eta} = \frac{2}{Pe}\left(\frac{\partial^2 \phi}{\partial \xi^2} + \frac{\partial^2 \phi}{\partial \eta^2}\right) \tag{3.30}$$

where

$$H = \frac{1}{2}(\cosh 2\xi - \cos 2\eta) \tag{3.31}$$

The velocity components in the ξ and η directions are now defined as

$$u_\xi = \frac{1}{H^{\frac{1}{2}}}\frac{\partial \psi}{\partial \eta} \tag{3.32}$$

$$u_\eta = \frac{-1}{H^{\frac{1}{2}}}\frac{\partial \psi}{\partial \xi} \tag{3.33}$$

The elliptical coordinate system used in this transformation is logarithmic in nature. This has the advantage of reaching very large distances away from the tube surface while keeping ξ limited to a small value.

3.5 Boundary Conditions

The boundary conditions are based on the no-slip, impermeability and isothermal conditions on the tube surface and the free stream conditions far away from it. These boundary conditions are defined as:

$$\psi = \frac{\partial \psi}{\partial \xi} = \frac{\partial \psi}{\partial \eta} = 0 \quad at \quad \xi = \xi_o \tag{3.34}$$

$$\left.\begin{aligned} \zeta &\rightarrow 0 \\ \frac{\partial \psi}{\partial \xi} &= -\tfrac{1}{2} U_\infty \, e^{\xi} \sin(\lambda - \eta) \\ \frac{\partial \psi}{\partial \eta} &= \tfrac{1}{2} U_\infty \, e^{\xi} \cos(\lambda - \eta) \end{aligned}\right\} \; as \; \xi \rightarrow \infty \tag{3.35}$$

The thermal-field boundary conditions are simply the constant temperature on the tube surface and the free stream temperature far away. These can be written as:

$$\begin{aligned} \phi &= 1 \quad at \quad \xi = \xi_o \\ \phi &\rightarrow 0 \quad as \quad \xi \rightarrow \infty \end{aligned} \tag{3.36}$$

Chapter 4

The Method of Solution

4.1 Solution Procedure

The method of solution is based on integrating the time-dependent governing equations of motion and energy till reaching almost fully periodic velocity and thermal fields. The procedure adopted for the solution involves the use of certain initial conditions and then with the use of the boundary conditions we advance the solution in time. In the present study, the velocity and the thermal field are unsteady due to the unsteadiness of the free stream and also due to the formation of vortices near the tube surface and its shedding downstream. The time development of the flow and thermal fields is carried out in two stages. In the first stage, the free stream velocity U_∞ described in equation (3.25) is assumed to start suddenly from rest with no temperature difference between the surface and the approaching stream. At the beginning of this stage, the boundary-layer region starts in the immediate neighborhood of the tube surface and then grows with time. As the boundary layer

becomes thick enough, the tube temperature is suddenly and uniformly increased to T_s allowing the thermal and velocity fields to develop simultaneously with time. This approach is similar to the one adopted successfully for studying the laminar mixed convection from horizontal cylinders [13], [23].

4.2 The Series Truncation Method

In order to reduce the number of independent variables, the dependent variables (stream function ψ, vorticity ζ and temperature ϕ) are approximated in the form of Fourier series following the work of Badr [23] . Accordingly ψ , ζ and ϕ are written in the form,

$$\psi = \frac{1}{2} F_o(\xi,t) + \sum_{n=1}^{\infty} [f_n(\xi,t) \sin n\eta + F_n(\xi,t) \cos n\eta] \qquad (4.1)$$

$$\zeta = \frac{1}{2} G_o(\xi,t) + \sum_{n=1}^{\infty} [g_n(\xi,t) \sin n\eta + G_n(\xi,t) \cos n\eta] \qquad (4.2)$$

$$\phi = \frac{1}{2} H_o(\xi,t) + \sum_{n=1}^{\infty} [h_n(\xi,t) \sin n\eta + H_n(\xi,t) \cos n\eta] \qquad (4.3)$$

The series truncation method consists of two main steps. The first step is to substitute the Fourier series in the governing equations [3.28 to 3.30] and boundary

conditions. The second step aims to use mathematical manipulation to obtain differential equations for every one of the Fourier coefficients. This is achieved by first multiplying each equation by 1, sin $n\eta$ and cos $n\eta$ respectively and integrating with respect to η from 0 to 2π. These two steps will result in a set of nine differential equations governing the Fourier coefficients (F_0, f_n, F_n, G_0, g_n, G_n, H_0, h_n, H_n).

The number of independent variables in the resulting set of equations was reduced from three (ξ, η, t) independent variables to two (ξ, t). This means that the main governing equations was approximated analytically along one of the independent variables (which is taken as η) and will be solved numerically along the other variable (ξ).

In applying the above procedure to the vorticity equation [Equation (3.28)], we obtain the following set of partial differential equations :

$$\frac{1}{2}\cosh 2\xi\frac{\partial G_0}{\partial t} - \frac{1}{2}\frac{\partial G_2}{\partial t} = \frac{2}{Re}\frac{\partial^2 G_0}{\partial \xi^2} + S_{n0}(\xi, t) \tag{4.4}$$

$$\begin{aligned}\cosh 2\xi\ \frac{\partial g_n}{\partial t} - \frac{1}{2}\,sgn(n-2)\,\frac{\partial g_{|n+2|}}{\partial t} - \frac{1}{2}\frac{\partial g_{n+2}}{\partial t} \\ = \frac{4}{Re}[\frac{\partial^2 g_n}{\partial \xi^2} - n^2 g_n] + S_{n1}[\xi, t, \lambda, \frac{Gr}{2Re^2}]\end{aligned} \tag{4.5}$$

$$\begin{aligned}\cosh 2\xi\ \frac{\partial G_n}{\partial t} - \frac{1}{2}\,[\delta_{n2}\,\frac{\partial G_0}{\partial t} + \frac{\partial G_{|n-2|}}{\partial t} + \frac{\partial G_{n+2}}{\partial t}] \\ = \frac{4}{Re}\,[\frac{\partial^2 G_n}{\partial \xi^2} - n^2\,G_n] + S_{n2}[\xi, t, \lambda, \frac{Gr}{2Re^2}]\end{aligned} \tag{4.6}$$

with the functions S_{n0} , S_{n1} and S_{n2} defined in Appendix A. Equations (4.4)

to (4.6) define a set of (2N + 1) differential equations to be solved where N is the order of truncation in the Fourier series.

Similar to the above, we substitute equations (4.1 - 4.3) into equation (3.29) and integrate both sides of the resulting equations with respect to η between the limits 0 to 2π after multiplying each side at a time by 1, sin $n\eta$ and cos $n\eta$, we obtain the following set of partial differential equations :

$$\frac{\partial^2 F_0}{\partial \xi^2} = \frac{1}{2} G_0 \cosh 2\xi - \frac{1}{2} G_2 \tag{4.7}$$

$$\frac{\partial^2 f_n}{\partial \xi^2} - n^2 f_n = \frac{1}{2} g_n \cosh 2\xi - \frac{1}{4}[sgn(n-2) g_{|n-1|} + g_{n+2}] \tag{4.8}$$

$$\frac{\partial^2 F_n}{\partial \xi^2} - n^2 F_n = \frac{1}{2} G_n \cosh 2\xi - \frac{1}{4}[\delta_{n2} G_0 + G_{|n-2|} + G_{n+2}] \tag{4.9}$$

Equations (4.7) to (4.9) define another set of (2N+1) differential equations relating the Fourier components of the stream function to the corresponding components of the vorticity.

A third set of differential equations can be obtained by using (4.1 - 4.3) with the energy equation (3.30) and following the same steps to obtain

$$\frac{1}{2} \cosh 2\xi \frac{\partial H_0}{\partial t} - \frac{1}{2}\frac{\partial H_2}{\partial t} = \frac{2}{Pe}\frac{\partial^2 H_0}{\partial \xi^2} + Z_{n0}(\xi, t) \tag{4.10}$$

$$\cosh 2\xi \frac{\partial h_n}{\partial t} - \frac{1}{2} sgn(n-2)\frac{\partial h_{|n-2|}}{\partial t} - \frac{1}{2}\frac{\partial h_{n+2}}{\partial t} = \frac{4}{Pe}[\frac{\partial^2 h_n}{\partial \xi^2} - n^2 h_n] + Z_{n1}(\xi, t) \tag{4.11}$$

$$\cosh 2\xi \frac{\partial H_n}{\partial t} - \frac{1}{2}[\delta_{n2}\frac{\partial H_0}{\partial t} + \frac{\partial H_{|n-2|}}{\partial t} + \frac{\partial H_{n+2}}{\partial t}] = \frac{4}{Re}[\frac{\partial^2 H_n}{\partial \xi^2} - n^2 H_n] + Z_{n2}(\xi, t) \tag{4.12}$$

with the functions Z_0 , Z_{n1} and Z_{n2} are defined in Appendix A.

All the functions with subscripts less than unity or more than N should be equated to zero and

$$g_{|n-2|} = 0, \;\; G_{|n-2|} = 0 \, , H_{|n-2|} = H_0 \quad \text{for} \quad n = 2$$

where, δ is the kronecker delta defined as. .

$$\delta_{mn} = \begin{cases} 1 & when \;\; n = m \\ 0 & when \;\; n \neq m \end{cases}$$

4.2.1 The Boundary Conditions

The boundary conditions given in equations (3.34 - 3.36) can be used to obtain the boundary conditions for all the Fourier components using equations (4.1 - 4.3). This gives the following set of boundary conditions:

$$H_0 = 2, \;\; h_n = H_n = F_0 = F_n = f_n = \frac{\partial}{\partial \xi}(F_0, f_n, F_n) = 0 \text{ at } \xi = \xi_0 \qquad (4.13)$$

and

$$H_0, \; h_n, \; H_n, \; G_0, \; g_n, \; G_n, \; F_0 \, , \; \frac{\partial F_0}{\partial \xi} \rightarrow 0 \text{ as } \xi \rightarrow \infty \qquad (4.14)$$

$$\left.\begin{array}{rl} f_n & \rightarrow \; \frac{1}{2} \, \delta_{n1} \, e^{\xi} \, U_{\infty} \;\; \cos\lambda \\ F_n & \rightarrow \; -\frac{1}{2} \, \delta n_1 \, e^{\xi} \, U_{\infty} \;\; \sin\lambda \end{array}\right\} \text{ as } \xi \rightarrow \infty \qquad (4.15)$$

By the above Fourier series approximations, the governing partial differential equations in two space variables (ξ and η) and time (t) are reduced to two sets of partial differential equations in one space variable and time in addition to one set of equations in one space variable only.

4.2.2 Integral Conditions

The boundary conditions for the vorticity functions G_0, g_n and G_n at the surface are not easy to specify since it requires information about the velocity gradients which are not known a priori. To calculate the vorticity at the surface, integral equations are used. These integral equations are obtained by integrating equations (4.7 - 4.9) with respect to ξ from ξ_0 to ∞ and using the boundary conditions given in Equations (4.13 - 4.15) to obtain the following set of integral equations:

$$\int_{\xi_0}^{\infty} (G_0 \cosh 2\xi - G_2)\, d\xi = 0 \tag{4.16}$$

$$\int_{\xi_0}^{\infty} \{\frac{1}{2} g_n \cosh 2\xi - \frac{1}{4}[sgn(n-2) g_{|n-2|} + g_{(n+2)}]\} e^{-n\xi}\, d\xi = \delta_{n1} U_\infty \cos\lambda \tag{4.17}$$

$$\int_{\xi_0}^{\infty} \{\frac{1}{2} G_n \cosh 2\xi - \frac{1}{4}[\delta_{n2} G_o + G_{|n-2|} + G_{n+2}]\} e^{-n\xi}\, d\xi = -\delta_{n1} U_\infty \sin\lambda \tag{4.18}$$

The above integral conditions represent an essential part of the method of solution, they are used to predict $G_0(\xi, t)$, $g_n(\xi_0, t)$, $G_n(\xi_0, t)$ at every time step on the tube surface.

4.2.3 Initial Solution

In order to start integration scheme an initial solution for the governing equations at $t = 0$ must be known. Staniforth [43] obtained a time series solution for the governing equations for the case when an elliptic cylinder starts its motion impulsively in a quiescent fluid of infinite extent. Such a solution is only valid for short time following the start of cylinder motion and for the case of constant velocity only. The first step is to transfer the governing equations to a new coordinate system which are the boundary-layer coordinates. These coordinates are appropriate to the flow field structure at small times. This flow is characterized by very thin boundary-layer region close to the cylinder surface bounded by a potential flow. The solution used by Stanforth [43] and Badr [37] is applicable to the present problem since the stream velocity at the start of the fluid motion (t=0) is exactly the same as that in the case of a cylinder impulsively started from rest. Let us now introduce the boundary-layer coordinates (z, τ) defined as:

$$\xi = \xi_0 + kZ$$

where

$$k = 2\sqrt{\frac{2\tau}{Re}} \quad , \quad \tau = t$$

We also introduce ψ^* and ζ^* defined as

$$\psi^* = \frac{\psi}{k}$$

and

$$\zeta^* = k\,\zeta$$

The use of ζ^* and ψ^* is appropriate to the flow field structure at small times where the layer of viscous flow over the cylinder is very thin. In this layer the stream function ψ is very small and the surface vorticity ζ is very large. The Fourier functions corresponding to the given boundary coordinate system are as follows:

$$G_0^* = k\,G_0, \quad g_n^* = k g_n, \quad G_n^* = k G_n$$

$$F_0^* = \frac{F_0}{k}, \quad f_n^* = \frac{f_n}{k}, \quad F_n^* = \frac{F_n}{k} \tag{4.19}$$

The second step is to transfer all the governing equations (4.4 - 4.12) and (4.13 - 4.15) to the new coordinate system and then solve using Cranck- Nicolson scheme for equations (4.4 - 4.6) and (4.10 - 4.12) and special integration scheme for equations (4.7 - 4.9) similar to that done by Badr and Dennis [5]. The important characteristics of this boundary layer coordinates is that the x-coordinates will continuously stretch with time when viewed in the physical coordinates. This characteristic matches the phenomenon under investigation since the viscous region starts with zero thickness at t=0 and grows as time increases. The initial solution obtained by Staniforth [43] at t=0, as shown in Badr [38], is expressed as

$$\psi^* = e^{\xi_0}\sin(\eta-\lambda)[z\ \ erf(H_{\xi_0}^{\frac{1}{2}}\ \ z)\ \ + \frac{1}{\pi^{\frac{1}{2}}H_{\xi_0}^{\frac{1}{2}}}(e^{-H_{\xi_0}z^2}-1)] \tag{4.20}$$

$$\zeta^{*} = \frac{2e^{\xi_0}}{\pi^{\frac{1}{2}} H_{\xi_0}^{\frac{1}{2}}} \sin(\eta - \lambda) e^{-H_{\xi_0} z^2} \tag{4.21}$$

where $H_{\xi_0} = \frac{1}{2}(\cosh 2\xi_0 - \cos 2\eta)$

4.3 The Finite-Difference Formulation

The set of partial differential equations obtained are integrated numerically, using the Crank-Nicolson finite difference scheme to advance the solution of ψ, ξ and ϕ in time. At any time $t + \Delta t$, where Δt is the time increment, it is required to obtain G_0, g_n, G_n at $(t + \Delta t)$ to determine the distribution of vorticity $\zeta(t + \Delta t)$, the functions F_0, f_n, F_n at $(t + \Delta t)$ to determine the stream function $\psi(t + \Delta t)$ and the functions H_o, h_n, H_n at $(t + \Delta t)$ to determine the dimensionless temperature $\phi(t + \Delta t)$, provided that all these functions are known at time level t. The finite difference equations are first obtained and then an iterative method of solution is utilized since the resulting equations are non-linear and coupled and the integral conditions [equations (4.16 - 4.18)] are to be satisfied at every time step. Consider the following equation as an example to show the complete method of solution.

$$\frac{1}{2}\cosh 2\xi \frac{\partial G_0}{\partial t} - \frac{1}{2}\frac{\partial G_2}{\partial t} = \frac{2}{R_e}\frac{\partial^2 G_0}{\partial \xi^2} + S_{n0}$$

This equation is solved numerically using Cranck-Nicolson finite difference scheme. By applying the above equation at the middle of the time step Δt using central

difference of time and space derivatives, we obtain

$$(\frac{1}{2}\frac{\cosh 2\xi}{\Delta t})[G_0(\xi,t+\Delta t)-G_0(\xi,t)]-\frac{1}{2\Delta t}[G_2(\xi,t+\Delta t)-G_2(\xi,t)]=$$
$$\frac{1}{Re(\Delta\xi)^2}[[G_0(\xi+\Delta\xi,\ t+\Delta t)-2G_0(\xi,t+\Delta t)+G_0(\xi-\Delta\xi,t+\Delta t)]$$
$$+[G_0(\xi+\Delta\xi,t)-2G_0(\xi,t)+G_0(\xi-\Delta\xi,t)]+\frac{1}{2}[S_{n0}(\xi,t+\Delta t)+S_{n0}(\xi,t)]]$$

By putting all unknown values of G_0 at $(t+\Delta t)$ on the left side and all other terms on the right side, we obtain

$$A\ G_0(\xi-\delta\xi,t+\Delta t)+B\ G_0(\xi,t+\Delta t)+C\ G_0(\xi-\Delta\xi,t+\Delta t)=$$
$$E(\xi,t+\Delta t)+D\ G_0(\xi,t)+F(\xi,t)$$

where

$$A=C=-\frac{2.0}{Re\ \cosh 2\xi}$$

$$B=[\frac{(\Delta\xi)^2}{\Delta t}+\frac{4}{Re\ \cosh(2\xi)}]$$

$$D=[\frac{(\Delta\xi)^2}{\Delta t}-\frac{4}{Re\ \cosh(2\xi)}]$$

$$E=\frac{(\Delta\xi)^2}{\cosh 2\xi}[\frac{1}{\Delta t}G_2(\xi,t+\Delta t)+S_{n0}(\xi,t+\Delta t)]$$

$$F=-A[G_0(\xi-\Delta\xi,t)+G_0(\xi+\Delta\xi,t)]+$$
$$\frac{(\Delta\xi)^2}{\cosh 2\xi}S_{n0}(\xi,t)-\frac{(\Delta)^2}{\cosh 2\xi}\frac{1}{\Delta t}\ G_2(\xi,t)$$

It is clear that the above equation when applied at every space step will give rise to a tri-diagonal matrix problem to be solved. The matrix of coefficients is fully defined while the right hand side depends on the solution at $(t + \Delta t)$. To overcome this problem, an iterative type procedure is utilized. In this procedure we first assume the unknown function at $(t + \Delta t)$ on the right side to be approximated by their values at time t. Better approximations are obtained and used through this iterative procedure. The iteration process is stopped when the difference in the solution of $G_0(\xi, t + \Delta t)$ between two successive iterations is within a certain allowable limit, i.e.,

$$\left|G_0^{m+1}(\xi, t + \Delta t) - G_0^m(\xi, t + \Delta t)\right| < 10^{-5}$$

where the superscript m denotes the iteration number. This same procedure will be applied to all the partial differential equations that includes time and space derivatives

4.4 Integration Procedure

The procedure used for integrating equations (4.4 - 4.6 and 4.10 - 4.12) in time is based on a modified Cranck-Nicolson scheme. In theory, these equations should be integrated in the region $\xi = 0$ to $\xi = \infty$. However, since the problem is solved numerically, the conditions at ∞ are applied at $\xi = \xi_{max}$ where ξ_{max} defines the distance away from the tube surface at which ζ and ϕ and have negligible small

values ($\approx 10^{-10}$). For example, for Ar=0.5, $\xi_{max} = 10$ represents a distance approximately 5000 times the major axis of the cylinder. The numerical solution is started at $t = 0$, when the temperature everywhere is T_∞, except at the tube surface where $T = T_s$. In terms of the Fourier series functions, it means that all the functions are zero except $H_0(\xi_0, t) = 2.0$. The solution is then advanced in time to predict the development of the thermal and velocity fields until reaching final time required. Difference equations similar to equation (4.22) are written for the cooefficient g_n, G_n, H_0, H_n, and h_n, based on differential equations (4.5,4.6,4.10 - 4.12) and applied at every mesh point in the range $\xi = \xi_0 + \Delta\xi$ to $\xi = \xi_{max}$. At the mesh point $\xi = \xi_0$, all Fourier series functions have known values for $t > 0$ except for the vorticity components g_n, G_n, G_0. The boundary conditions for those variables will be solved using the integral conditions given in equations (4.16 - 4.18).

After obtaining the new values of G_0, G_n, g_n at time $(t+\Delta t)$ the heat equations (4.10 - 4.12) are converted to finite-difference forms and then solved using similar procedure to that mentioned previously for equations (4.4 - 4.6). However, a direct finite-difference approximation for equations (4.7 - 4.9) is unstable for large values of n as proven by Dennis and Chang [2]. Accordingly they proposed that these equations should be solved using step-by-step integration procedure. In the following, the procedure is presented for equation (4.8) as an example. Equation (4.8) can be

written in the form:

$$\ddot{f} - n^2 f = r(\xi) \tag{4.22}$$

The step-by-step method starts by splitting the above equation into two first order equations

$$\dot{p} - np = r(\xi) \tag{4.23}$$

and

$$\dot{q} + nq = r(\xi) \tag{4.24}$$

Where $p(\xi)$ and $q(\xi)$ are two new function that satisfy the previous first order equations and from which the value of f and $\dot{f}$ can be obtained from the equations

$$f = \frac{(p-q)}{2n} \tag{4.25}$$

$$\dot{f} = \frac{(p+q)}{2} \tag{4.26}$$

If we express the first derivatives by simple forward differences, an approximation to equations (4.23) and (4.24) gives

$$p_{m+1} = (1 + n\ \Delta\xi)p_m + (\Delta\xi)r_m \tag{4.27}$$

and to equation 4.24

$$q_{m+1} = (1 - n\ \Delta\xi)q_m + (\Delta\xi)r_m \tag{4.28}$$

The boundary conditions for p and q are

$$p(0) = q(0) = 0 \text{ and } p(\xi_{max}) = q(\xi_{max}) = 0 \tag{4.29}$$

Equation (4.24) is integrated in the increasing ξ-direction while equation (4.23) is integrated backwards starting from ξ_{max} in the direction of ξ An equivalent way of looking at the latter integration is to put $\xi = \xi_{max} - z$ in equation (4.23) so it becomes:

$$\frac{\partial p}{\partial z} + np = -r(\xi_{max} - z) \tag{4.30}$$

A detailed error analysis conducted by Dennis and Chang [2] shows that this procedure will give accurate results only when $n\Delta\xi < 1$. Since $(\Delta\xi)$ is fixed and n may be large, this condition will not be satisfied. So we need a method that will be accurate for large values of n. In this method we denote the value of $\xi = m(\Delta\xi)$ by ξ_m and the corresponding value of $q(\xi_m)$ by q_m. Equation (4.24). may be written as

$$\frac{\partial}{\partial\xi}[e^{n\xi}q(\xi)] = e^{n\xi}r(\xi)$$

where

$$q(\xi) = e^{-n(\xi-\xi_m)}q_m + e^{-n\xi}\int_{\xi_m}^{\xi} e^{n\xi}r(\xi)d\xi \tag{4.31}$$

and

$$\xi = \xi_m + s\Delta\xi.$$

This formula is a multi-step formula for the step-by-step integration of equation (4.24).

The computer program is written in a way such that computations can be performed to advance the solution through one time interval. The intermediate steps

(iterations) are examined for convergence and then computations are further advanced in time. In case of divergence, the programme reduces the time step to one half of its value and later on it increases again. Computations are stopped after reaching the required time. This procedure allows to choose suitable values of (Δt) to obtain accurate solutions in a reasonable computational time. At the start of computations, the number of terms, N, in the Fourier series is chosen to be small (N taken as 7). This number is allowed to increase with time whenever any of the last terms in the series exceeds a certain small value. In a similar manner, the size of computational domain ξ_{max} is varied with time by increasing the number of points in the ξ direction whenever the values of any of the non-zero terms at the last spatial point exceeds a certain small value. By this way the far field boundary conditions are satisfied and also the domain of computation is kept small at the start of motion. As time increases the increase in the number of terms as well as spatial points is stopped automatically by the preset conditions.

Using the present approach, the size of the solution domain is small at small times and grows with the increase of time until reaching a maximum distance of more than 5000 times the major axis length from the surface when reaching final time. This large distance is very essential to ensure the free stream conditions far away from the surface. The growth of the solution domain matches the natural growth of the flow and thermal fields following the sudden temperature rise. This is not only important

for minimizing the time of computation but also essential in achieving an accurate solution. The logarithmic nature of the ξ coordinate enables to have equal space steps in the discretization process while the physical space steps are very small near the solid boundary and large far away. This matches also the physical problem since the temperature and velocity gradients are large near the surface and become very small far away. A sensitivity test was performed for spatial increment for an axis ratio Ar=0.5. It is found that by reducing $\Delta\xi$ by 50%, keeping Δt the same, the change in average Nusselt number is only 1.2%. However, the increase in computer time was 76% higher than that for larger $\Delta\xi$.

4.5 Local and Average Nusselt Numbers

The local and average Nusselt numbers are defined, respectively as:

$$Nu = \frac{h\,2a}{k} \tag{4.32}$$

and

$$\overline{Nu} = \frac{\overline{h}\,2a}{k} \tag{4.33}$$

The coefficient of heat transfer (h) can be defined as

$$h = \frac{\grave{q}}{T_s - T_\infty} \tag{4.34}$$

The Fourier Law of heat conduction is given by:

$$\grave{q} = -k\,\frac{\partial T}{\partial n}|_{\xi=\xi_0} \tag{4.35}$$

where $\grave{q}$ is the rate of heat transfer per unit area and n is a coordinate normal to the tube surface. Substituting Equation (4.35) in Equation (4.34) gives

$$h = \frac{-k}{T_s - T_\infty}[\frac{\partial T}{\partial n}]_{\xi_0} \tag{4.36}$$

converting this expression to elliptic coordinates, we get

$$h = -\frac{\frac{k}{c}}{H_{\xi_0}^{\frac{1}{2}}}[\frac{\partial \phi}{\partial \xi}]_{\xi_0}$$

where

$$H = \frac{1}{2}(\cosh 2\xi - \cos 2\eta)$$

We now define the local Nusselt number

$$Nu = \frac{2ah}{k} = -\frac{2\cosh \xi_0}{H_{\xi_0}^{\frac{1}{2}}}[\frac{\partial \phi}{\partial \xi}]_{\xi_0} \tag{4.37}$$

and the average Nusselt number $\overline{Nu}$ can be obtained from

$$\overline{Nu} = \frac{1}{L}\int_0^L Nu \ ds \tag{4.38}$$

where L is the elliptic section perimeter and ds is the elementary length along that perimeter. Finally by integrating equation (4.37), we get the following results for $\overline{Nu}$

$$\overline{Nu} = -\frac{2\pi}{(\frac{L}{a})}[\frac{\partial H_0}{\partial \xi}]_{\xi_0} \tag{4.39}$$

The time average Nusselt number, $\overline{\overline{Nu}}$, is obtained from

$$\overline{\overline{Nu}} = \frac{1}{T}\int_t^{t+T} \overline{Nu} \ dt \tag{4.40}$$

where L is the elliptic section perimeter and T is the time period for the last complete oscillation.

4.6 Pressure Variation on the Tube Surface

In order to obtain an expression for the pressure distribution let us first introduce the dimensionless pressure.

$$p^* = \frac{p - p_\pi}{\frac{1}{2}\rho \overline{u^2}}$$

By applying the Navier-Stocks equations at the tube surface and making use of the boundary conditions, we obtain after some simplifications

$$[\frac{\partial p^*}{\partial \eta}]_{\xi_0} = -\frac{4}{Re}[\frac{\partial \zeta}{\partial \xi}]_{\xi_0}. \tag{4.41}$$

We then integrate the above expression with respect to η on the surface $\xi = \xi_0$, to obtain

$$p^* = -\frac{4}{Re}[\frac{1}{2}\frac{\partial G_0}{\partial \xi}(\eta - \pi) + \sum_{n=1}^{N} \frac{1}{n}\{\frac{\partial G_n}{\partial \xi}\sin n\eta - \frac{\partial g_n}{\partial \xi}(\cos n\eta - \cos n\pi)\}] \tag{4.42}$$

The periodicity of p^* requires that $[\frac{\partial G_0}{\partial \xi}]_{\xi_0}$ must be zero at all times. This is implicitly satisfied by the integral conditions given in equation (4.16)

4.7 The Lift and Drag Coefficients

The fluid forces acting on the tube are mainly the inline and transverse forces (C_D, C_L). These forces arise from the fluid pressure and shearing forcing acting

on the tube surface. An expression for the pressure variation has been obtained in the previous section. The in-line and transverse forces can be calculated by the usual process of considering an elementary surface area and then writing the components of pressure and shearing forces in the x and y directions. The elementary forces are then integrated around the tube surface to obtain expressions for the x and y components of the fluid forces in terms of the Fourier functions. These can be written as :

$$F_{xf} = \pi\mu\overline{u}\ \ g_1(\xi_0, t) \tag{4.43}$$

$$F_{yf} = -\pi\mu\overline{u}\ \tanh\xi_0\ \ G_1(\xi_0, t) \tag{4.44}$$

$$F_{xp} = -\pi\mu\overline{u}\ \tanh\xi_0\ [\frac{\partial g_1(\xi, t)}{\partial\xi}]_{\xi_0} \tag{4.45}$$

$$F_{yp} = \pi\mu\overline{u}\ [\frac{\partial G_1(\xi, t)}{\partial\xi}]_{\xi_0} \tag{4.46}$$

where equations (4.43) - (4.44) represent the x and y components of the friction forces and equations (4.45) - (4.46) are the corresponding components of the pressure forces. An expression for the in-line and transverse forces (D and L) can be obtained from the contribution of the pressure and friction forces as:

$$D = (F_{xf} + F_{xp})\cos\lambda + (F_{yf} + F_{yp})\sin\lambda \tag{4.47}$$

$$L = (F_{yf} + F_{yp})\cos\lambda - (F_{xf} + F_{xp})sin\lambda \tag{4.48}$$

The in-line and transverse force coefficients C_D and C_L are defined as:

$$C_D = \frac{D}{\frac{1}{2}\rho\overline{u^2}(2c)} \tag{4.49}$$

$$C_L = \frac{L}{\frac{1}{2}\rho\overline{u^2}(2c)} \tag{4.50}$$

One can split each one of the above coefficients into two parts, one due to frictional forces and the other due to pressure forces. The resulting coefficients can be expressed in terms of the Fourier functions as:

$$C_{DF} = \frac{2\pi}{Re}[g_1 \cos\lambda - G_1 \tanh\xi_0 \sin\lambda]_{\xi_0} \tag{4.51}$$

$$C_{DP} = \frac{2\pi}{Re}[\frac{\partial G_1}{\partial \xi}\sin\lambda - \frac{\partial g_1}{\partial \xi}]_{\xi_0} \tanh\xi_0 \cos\lambda \tag{4.52}$$

$$C_{LF} = -\frac{2\pi}{Re}[g_1 \sin\lambda - G_1 \tanh\xi_0 \cos\lambda]_{\xi_0} \tag{4.53}$$

$$C_{LP} = \frac{2\pi}{Re}[\frac{\partial G_1}{\partial \xi}\cos\lambda + \frac{\partial g_1}{\partial \xi}]_{\xi_0} \tan\xi_0 \sin\lambda \tag{4.54}$$

Where C_{DF} and C_{DP} are the friction and pressure components of C_D and C_{LF} and C_{LP} are the friction and pressure components of C_L.

Chapter 5

Discussion of Results

5.1 Introduction

Based on the governing equations of motion and energy and the fluctuating free stream, it is clear that the velocity and thermal fields are dependent on Reynolds number, Grashof number, Prandtl number, axis ratio, angle of inclination and the fluctuation parameters (amplitude and frequency). In the present study the Prandtl number is fixed at 0.73. The full conservation equations are solved in the manner described in chapter (4). Because of the large number of parameters involved, the effect of one parameter is investigated at a time. In this chapter, results are presented in the form of spatial variation of the surface vorticity, pressure and local Nusselt number around the tube surface. Because of the flow fluctuations, the time variation of the average Nusselt number and lift and drag coefficients are presented for a number of cases. The time-average Nusselt numbers are tabulated for all the cases considered. In order to show the details of the velocity and thermal fields in the

vicinity of the tube, the streamlines and isotherm patterns are plotted for a number of cases over a period of one complete cycle of oscillations. The accuracy of the mathematical model and the numerical technique are verified by considering special cases which were previously studied by other researchers.

5.2 Verification of the Method of Solution

The mathematical model and the numerical scheme used in this study are validated by studying the two limiting cases of the elliptic tube. namely the circular tube and the flat plate. In the first case, two heat transfer regimes are considered. The first is a forced convection regime while the second is a mixed convection one. In the case of forced convection regime the average Nusselt number for the case of forced convection from an elliptic cylinder of axis ratio close to unity (Ar=0.965) is compared with the available data for the case of circular cylinder. Table 5.1 shows a comparison between the present results and those obtained by Hatton et al. [44], Collis and Williams [45] and Dinnes et al. [46] and Nguyen [39]. The table shows a maximum difference of 7.2 % with reference [44] , 8.7 % with reference [45] and 2.3 % with reference [46] . Part of the differences are attributed to the difference in the cylinder geometry. In the case of mixed convection regime, Table 5.2 shows a comparison between the present results for the case of Ar=0.965 and those obtained by H. Nguyen et al. [39] and Gebhart et al. [48] for a circular

cylinder. The table shows a maximum difference of 7 % with reference [39] and 8% with reference [48]. The next case to be considered for the mixed convection regime is a comparison with the problem considered by Nguyen et al. [39] for a fluctuating flow over circular cylinder in the presence of buoyancy forces. Figure 5.1 shows the local Nusselt number distributions for the case of Re=100, Gr=20000, S=2π and $\beta = 0.2$ from the present study and that provided by Nguyen et al. [39] at a maximum free stream velocity. The figure shows small differences between the two cases execpt at $\eta = 40^o$ where the difference in geometry causes some difference in the results.

The case of forced convection from an elliptic tube with Ar=0.05 were tested against the forced convection case from a horizontal flat plate. Figure 5.2 shows a comparison between the local Nusselt number distribution for the case of Re=100, Ar=0.05 and the forced convection from a horizontal flat plate by Dennis and Smith [49] and Pohlhausen's solution. The figure shows a very close agreement over most of the plate surface except for the leading and trailing edges where the difference in geometry between a flat plate ($\xi_0 = 0$) and a thin elliptic tube ($\xi = 0.05$) causes the differences shown in the figure.

Table 5.1: Comparison between the obtained average Nusselt numbers for Ar=0.965 and the results reported by Hatton et al. [44], Collis and Williams [45] and Dennis et al. [46] and Nguyen et al.[39] for the case of forced convection from a circular cylinder

Re	$\overline{Nu}$ Present study for Ar=0.965	Hatton et al.	Collis and Williams	Dennis et al.	Nguyen et al.
5	1.456	1.561	1.395	1.423	—
20	2.550	2.548	2.396	2.557	—
40	3.490	3.318	3.185	3.840	—
100	5.30	—	—	—	5.23
200	7.27	—	—	—	7.10

Table 5.2: Comparison between the obtained average Nusselt numbers for Ar=0.965 and the results reported by Nguyen et al. [39], and Gebhart et al.[48] for the case of mixed convection from a circular cylinder

Re	Gr	$\overline{Nu}$ Present study for Ar=0.965	Nguyen et al.	Gebhart et al.
5	100	1.83	1.89	1.99
20	1000	2.92	3.13	3.13
40	6400	4.35	4.59	4.46
100	20000	6.39	6.42	—

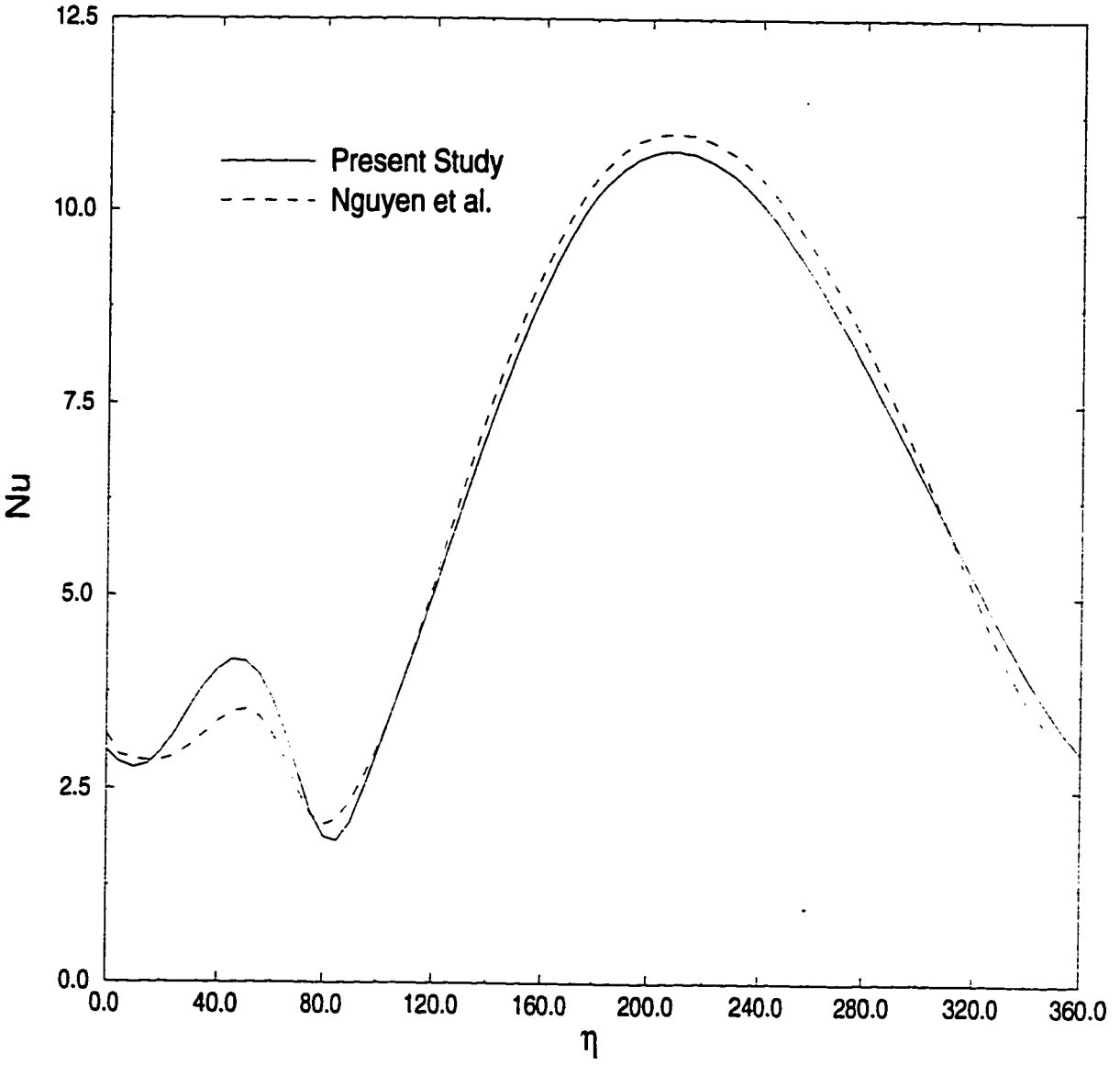

Figure 5.1: Comparison between the obtained local Nusselt number distribution and that given by Nguyen et al. [39] for the case of Re=100, Gr=20000, Ar=0.965, S=2π and $\beta = 0.2$

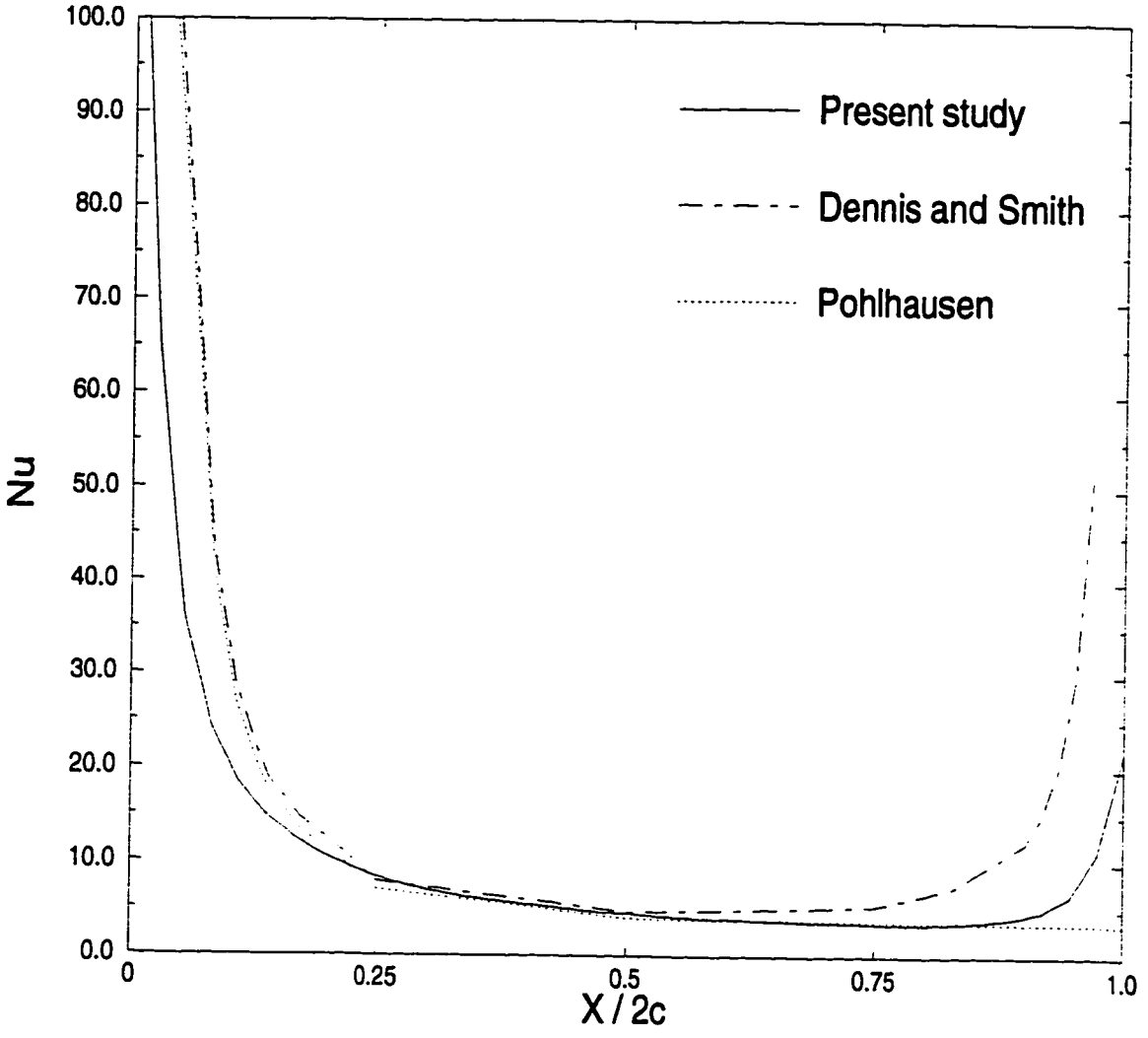

Figure 5.2: Comparison between the obtained local Nusselt number distribution for the case of Re=100. Ar=0.05 and the flat plate results given by Dennis and Smith [49] and Pohlhausen's solution.

5.3 The Effect of Amplitude of Fluctuations

In this section, the effect of amplitude on the velocity and thermal fields, average and local Nusselt numbers, pressure and surface vorticity distributions is presented. The approaching stream fluctuations cover the range of amplitudes from $\beta = 0.25$, to 1.0, Strouhal numbers S = $\pi/4$ and $\pi/2$, while keeping all other parameters unchanged (Re=100, Gr=20000, Ar=0.5, $\lambda = 30^o$) .

5.3.1 The Effect of Amplitude on the Average Nusselt Number

The effect of amplitude of fluctuations on the average and time-average Nusselt numbers are presented for all the cases mentioned in Table 5.3. The table also contains a code number for each case for easy referencing. The table shows that a small increase in $\overline{\overline{Nu}}$ occurs in the low Reynolds number case of Re=50 when increasing the amplitude from $\beta = 0.25$ to 1.0. The maximum increase did not exceed 6.46 % . For the moderate Reynolds number case of Re=100, the combination of low frequency (S=$\pi/4$) and large amplitude (β =1.0) resulted in a significant increase in $\overline{\overline{Nu}}$. The maximum increase reached is 11.4 % . On the other hand, higher frequency (cases A-9 to A-12) resulted in less increase in heat transfer rates. The response in the case of Re=500 is similar to the case of Re=100 (i.e. low S and high β lead to higher $\overline{\overline{Nu}}$).

Figure 5.3 shows the time variation of the average Nusselt number following the sudden temperature rise of the tube surface for different amplitudes at Strouhal number, S = $\pi/4$. The figure shows that $\overline{Nu}$ has its maximum value at t=0, the value decreases with time until reaching periodic variation at large time. This is due to the fact that immediately following the step temperature rise, the thermal boundary layer is very small and is confined to the immediate neighborhood of the tube surface. The temperature gradient near the tube surface is very high which leads to conduction dominated heat transfer regime. With the increase of time the thermal boundary layer thickness increases and $\overline{Nu}$ decreases accordingly. In a response similar to that of the free stream, the amplitude of $\overline{Nu}$ gets higher with the increase of β. The quasi-steady state is reached for low β faster than that for high β values. Figures 5.4 to 5.7 show the time variation of the average Nusselt number $\overline{Nu}$, the time-average Nusselt number, $\overline{\overline{Nu}}$, and the value of $\overline{Nu}$ for the case of steady free stream. The time variation of the free stream velocity is also plotted in each figure for easy comparison.

Figure 5.4 shows that at Strouhal number S = $\pi/4$ and β = 0.25, there is an increase in the heat transfer rate at all times. The enhancement of heat transfer due to fluctuations is higher for higher values of amplitude as shown in Figures 5.5 to 5.7. The free stream velocity is drawn on the same figures. It is clear that the $\overline{Nu}$ fluctuations have a phase lag behind the free stream velocity fluctuations.

The phase lag increases from 10° for $\beta = 0.25$ to 45° for $\beta = 0.5$ and reaching a maximum value of 75° for $\beta = 1.0$. Figure 5.8 shows the average Nusselt number variations with time for the higher Strouhal number case of S = $\pi/2$ and for the same four different amplitudes (cases (A-5) to (A-8)). The average Nusselt number is fluctuating with the same frequency as that of the free stream. When a comparison of $\overline{Nu}$ is made with the steady stream values (shown in Figures 5.9 to 5.12), the heat transfer enhancement is found to be less than that for low Strouhal number case of S = $\pi/4$ for same β. This means that the heat transfer enhancement decreases with the increase of frequency of free stream fluctuations. It is also found that the phase lag between fluctuations in $\overline{Nu}$ and the free stream velocity depends only on the amplitude of fluctuations.

Table 5.3: The effect of the amplitude of fluctuations on the time-average Nusselt number.

Code #	Re	Gr	λ	Ar	S	β	$\overline{\overline{Nu}}$	$\overline{Nu}$ ($\beta = 0$)	% Increase
A-1	50	20000	30°	0.5	$\frac{\pi}{4}$	0.25	4.84	4.79	1.06 %
A-2	50	20000	30°	0.5	$\frac{\pi}{4}$	0.50	4.91	4.79	2.55 %
A-3	50	20000	30°	0.5	$\frac{\pi}{4}$	0.75	4.98	4.79	3.97 %
A-4	50	20000	30°	0.5	$\frac{\pi}{4}$	1.00	5.10	4.79	6.46 %
A-5	100	20000	30°	0.5	$\frac{\pi}{4}$	0.25	6.41	6.23	2.83 %
A-6	100	20000	30°	0.5	$\frac{\pi}{4}$	0.50	6.57	6.23	5.58 %
A-7	100	20000	30°	0.5	$\frac{\pi}{4}$	0.75	6.70	6.23	7.58 %
A-8	100	20000	30°	0.5	$\frac{\pi}{4}$	1.00	6.94	6.23	11.4 %
A-9	100	20000	30°	0.5	$\frac{\pi}{2}$	0.25	6.35	6.23	2.01 %
A-10	100	20000	30°	0.5	$\frac{\pi}{2}$	0.50	6.43	6.23	3.10 %
A-11	100	20000	30°	0.5	$\frac{\pi}{2}$	0.75	6.54	6.23	5.09 %
A-12	100	20000	30°	0.5	$\frac{\pi}{2}$	1.0	6.63	6.23	6.51 %
A-13	500	20000	30°	0.5	$\frac{\pi}{4}$	0.25	13.95	13.1	6.48 %
A-14	500	20000	30°	0.5	$\frac{\pi}{4}$	0.50	14.89	13.1	13.7 %

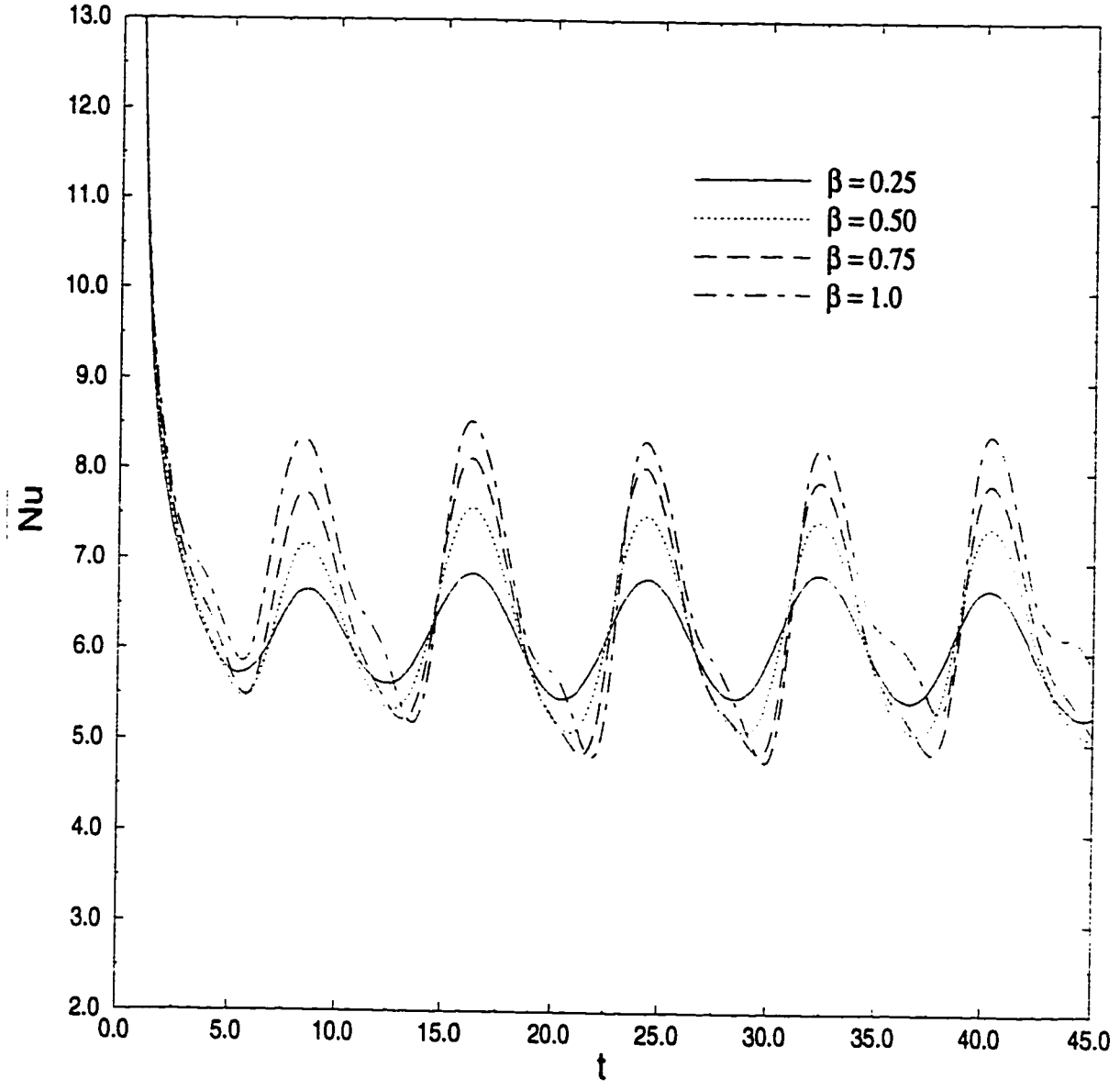

Figure 5.3: The time variation of $\overline{Nu}$ following the sudden temperature rise for various amplitudes in the case of Re=100, Gr=20000 , Ar=0.5, $\lambda = 30.0^o$ and $S = \pi/4$, .

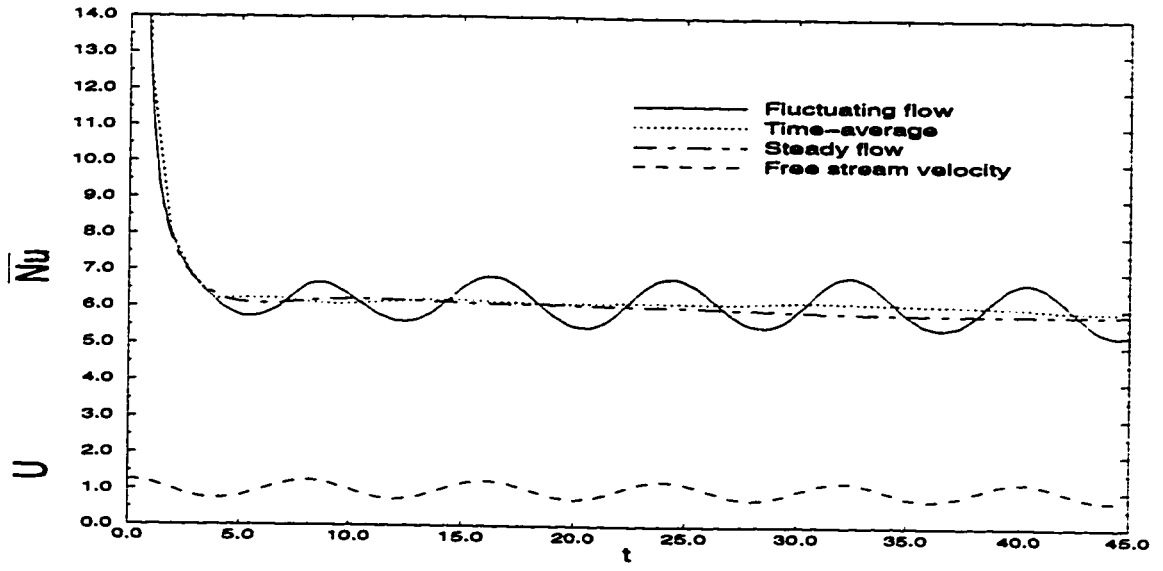

Figure 5.4: The variation of $\overline{Nu}$ for case A-5 and comparison with the case of steady free stream.

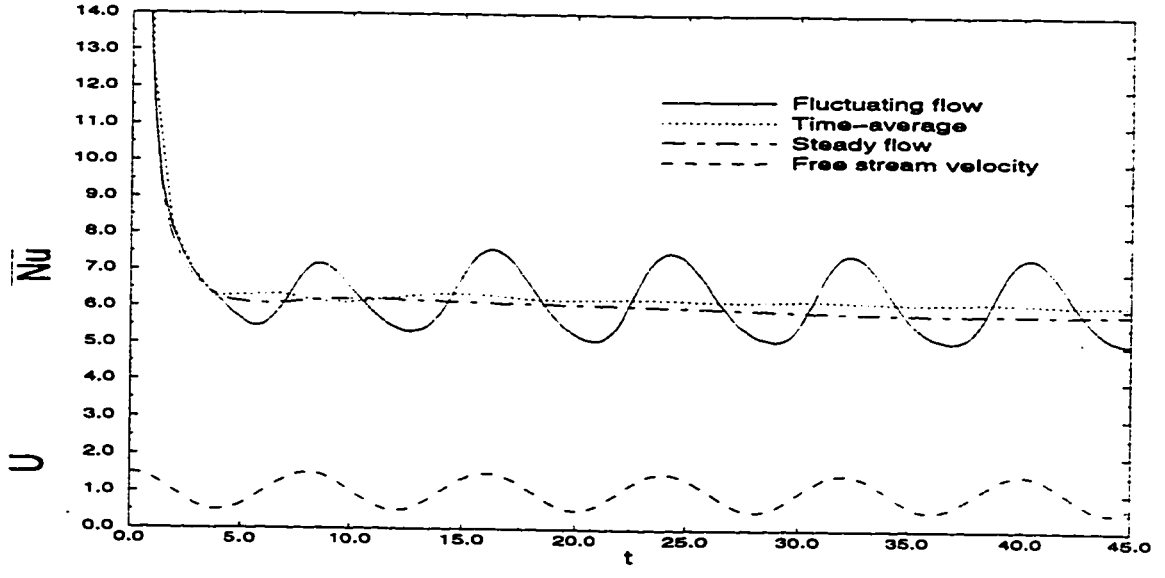

Figure 5.5: The variation of $\overline{Nu}$ for case A-6 and comparison with the case of steady free stream.

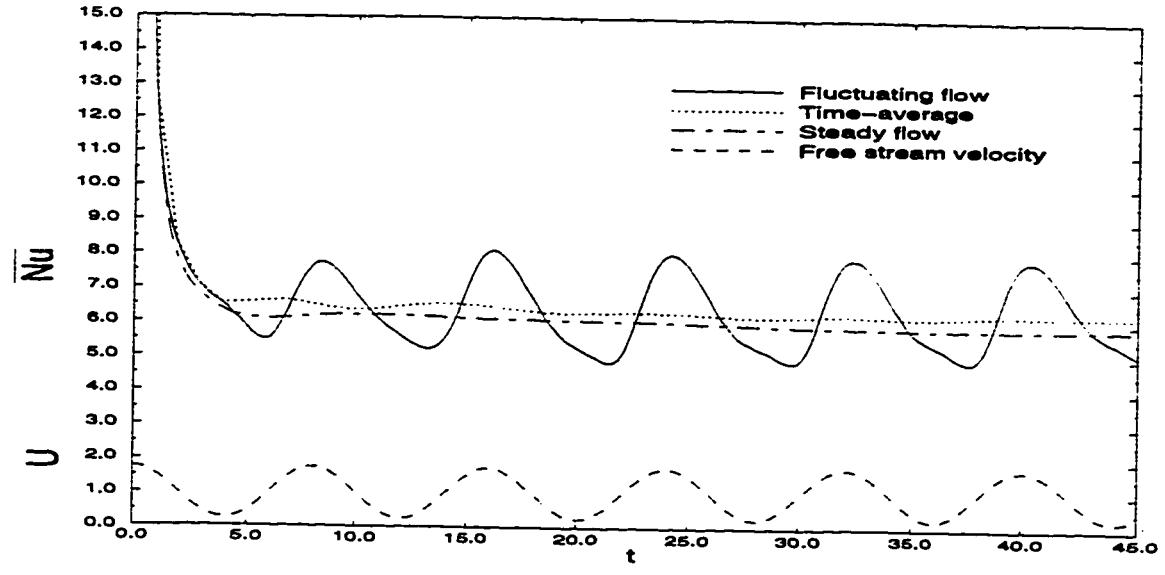

Figure 5.6: The variation of $\overline{Nu}$ for case A-7 and comparison with the case of steady free stream.

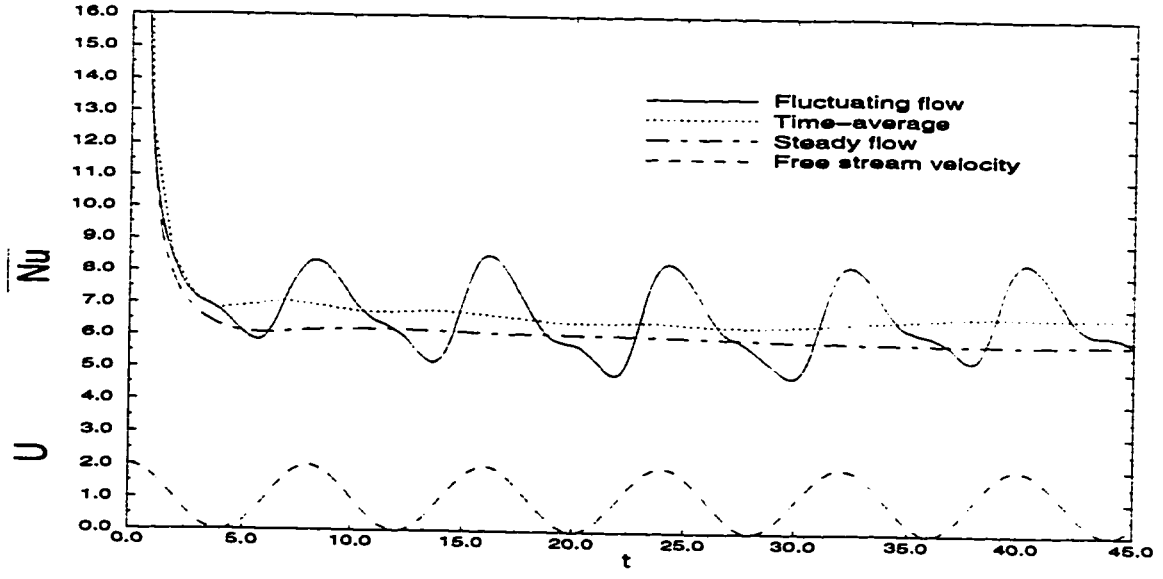

Figure 5.7: The variation of $\overline{Nu}$ for case A-8 and comparison with the case of steady free stream.

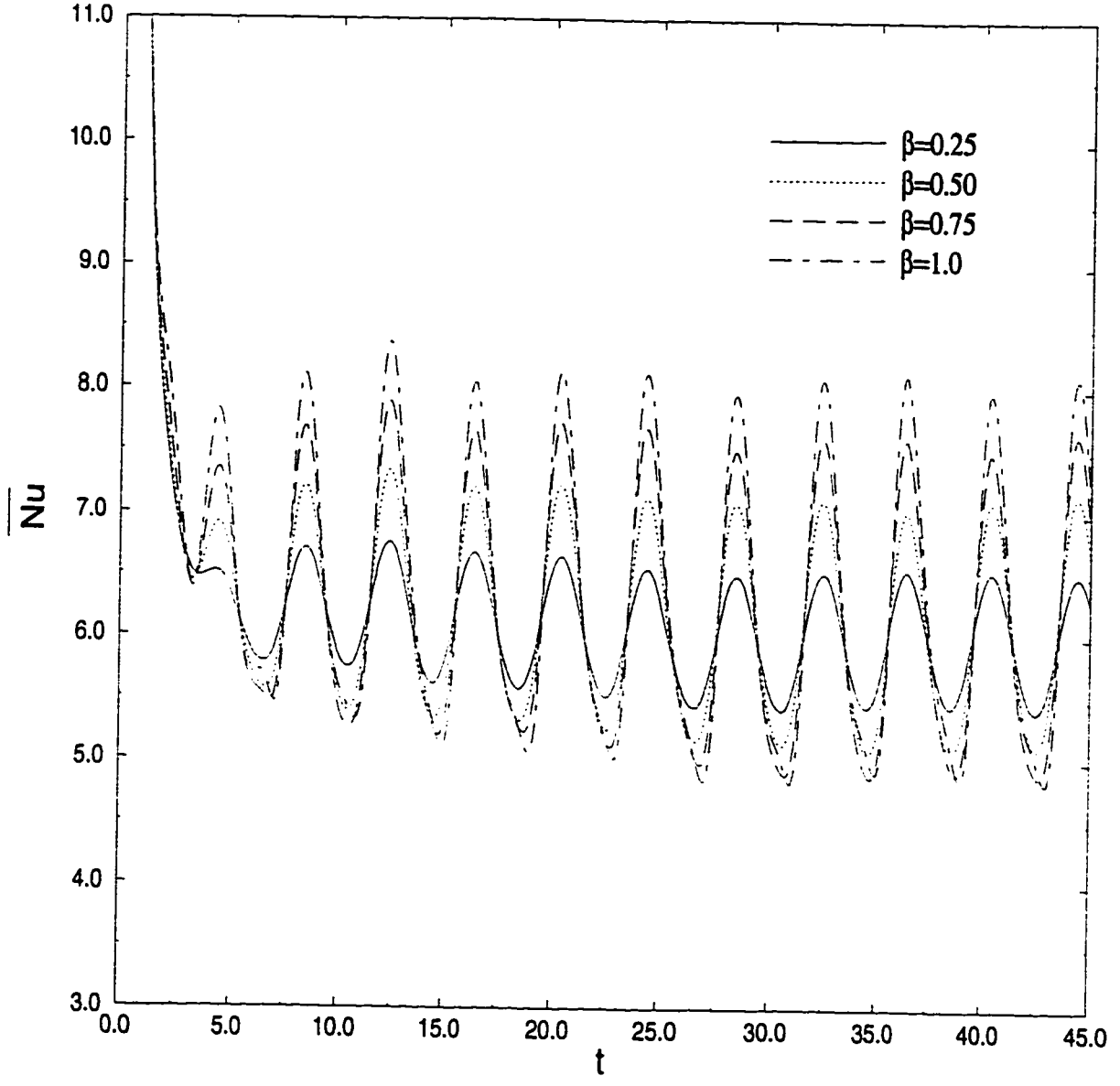

Figure 5.8: The time variation of $\overline{Nu}$ following the sudden temperature rise for amplitudes in the case of Re=100, Gr=20000, Ar=0.5 and $\lambda = 30.0^o$, and , $S = \pi/2$

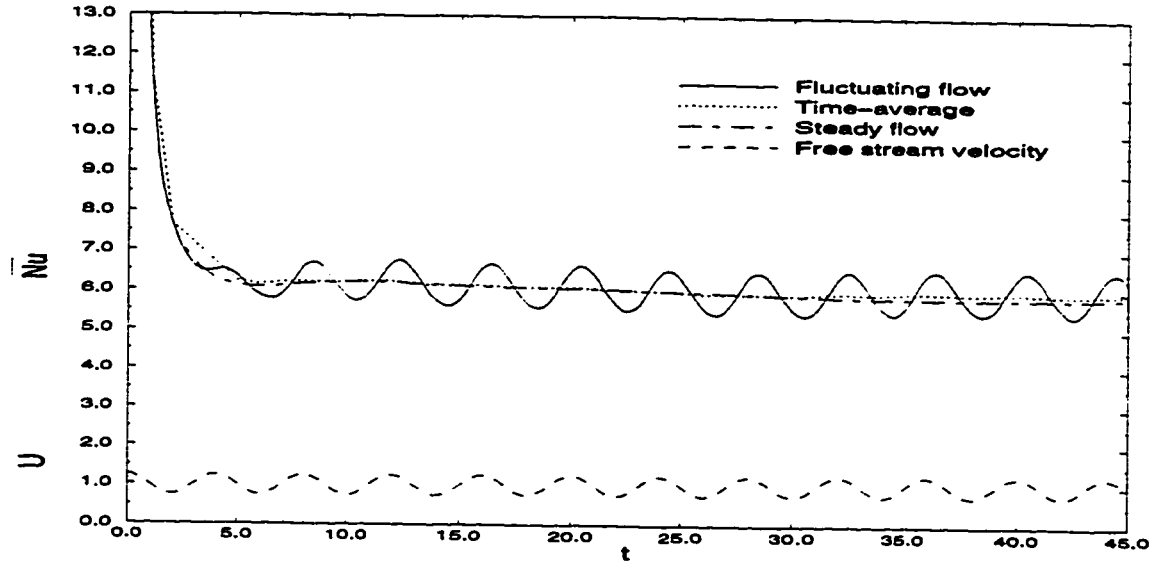

Figure 5.9: Time variation of $\overline{Nu}$ for case A-9 and comparison with the case of steady free stream.

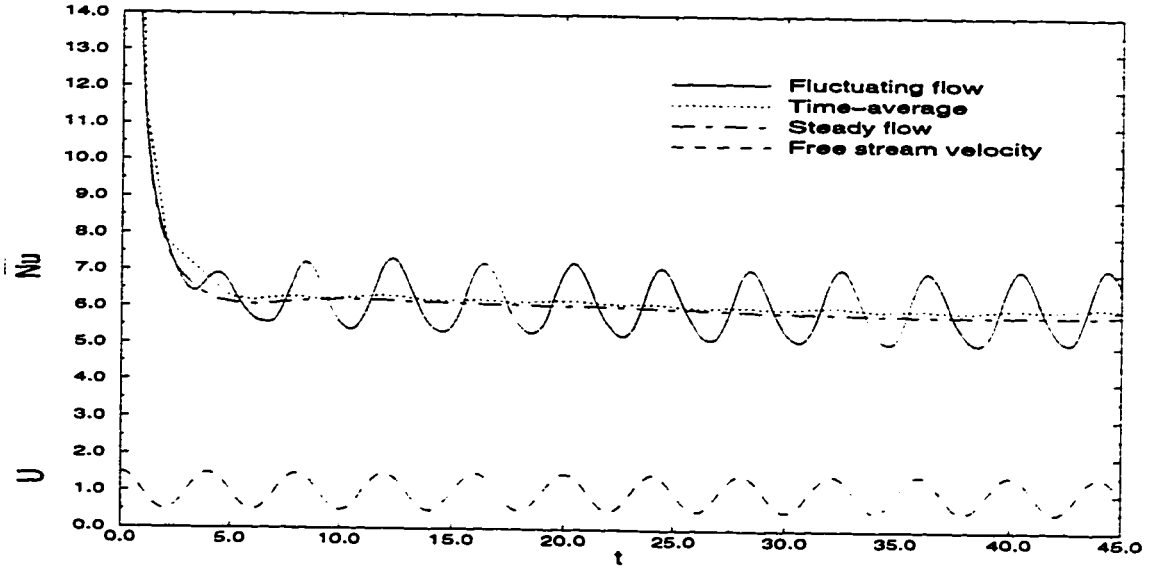

Figure 5.10: Time variation of $\overline{Nu}$ for case A-10 and comparison with the case of steady free stream.

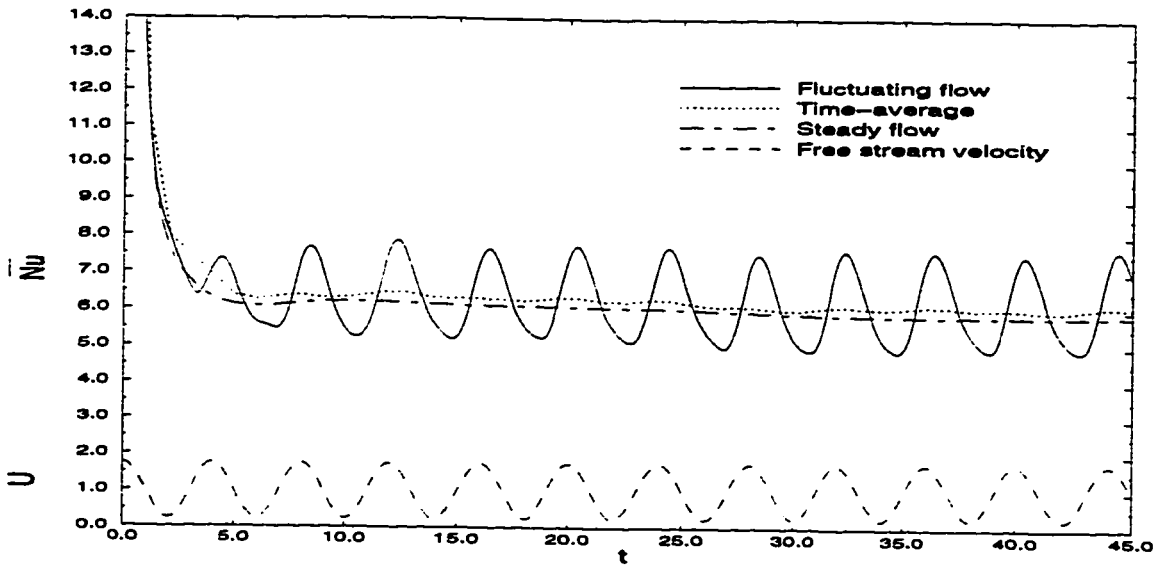

Figure 5.11: Time variation of $\overline{Nu}$ for case A-11 and comparison with the case of steady free stream.

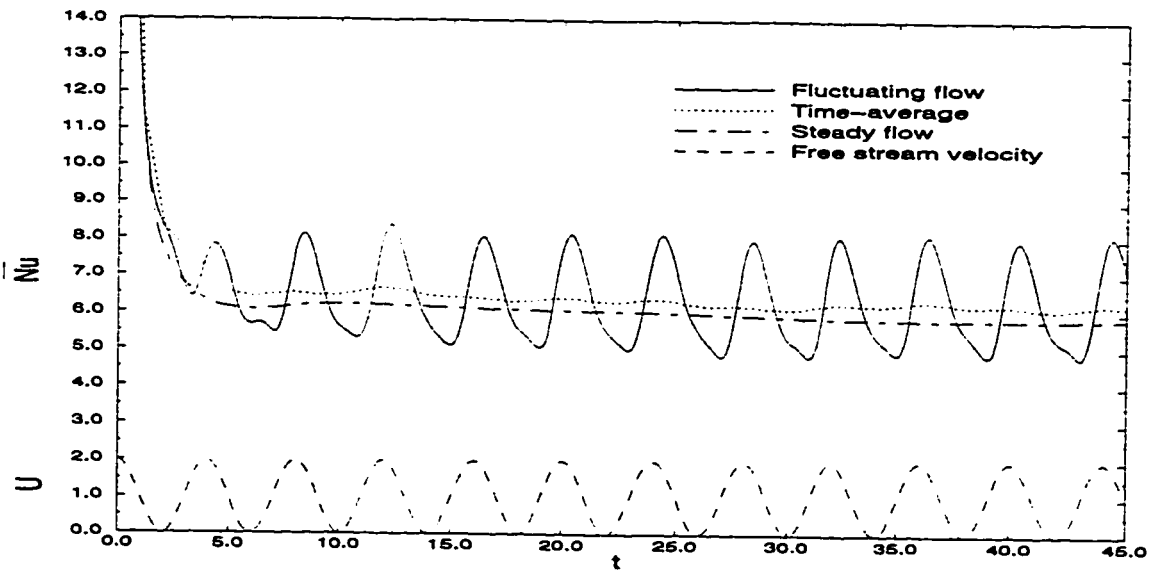

Figure 5.12: Time variation of $\overline{Nu}$ for case A-12 and comparison with the case of steady free stream.

5.3.2 The Effect of Amplitude on the Local Nusselt Number, Pressure and Surface Vorticity Distributions

Figures 5.13 and 5.14 show the effect of amplitude of fluctuations on the local Nusselt number distribution around the tube surface for cases (A-5) to (A-8) given in Table 5.3. Figure 5.13 corresponds to maximum free stream velocity , U_{max}, at the start of the fifth cycle, while Figure 5.14 corresponds to minimum free stream velocity , U_{min}, in the middle of the fifth cycle. Figure 5.13 shows that for all forms of fluctuations, Nu is higher than its steady value on almost all the tube surface except for small region near the rear point. This is expected, since higher stream velocity leads to higher velocity and temperature gradients near the surface. The figure also shows that the increase of the amplitude, results in further increase of Nu over most of the tube surface. The higher Nusselt number value for the steady stream case at the rear point may be explained due to the change of the location of the point of separation and also the size of the vortical flow region behind the tube ($\eta = 0^o - 80^o$). A full explination of this phenomena will be discussed in detail in section (5.3.4). On the other hand when the free stream velocity is minimum, Nu decreases below its steady stream value all over the tube surface except for the rear part ($\eta = 0^o - 80^o$) where Nu becomes higher than the steady flow case as shown in Figure 5.14. In order to explain this phenomenon the surface vorticity distributions are plotted for the same two cases in Figures 5.15 and 5.16. Figure 5.15 shows a small value of the

absolute vorticity at the surface $|\zeta_s|$ in the wake region (η = 0° - 80°) indicating a small velocity gradient and accordingly a weak vortical motion when U = U_{max}. However when U = U_{min} , the size and strength of the vortex driven flow in the wake region becomes more prominent as shown in Figure 5.16. For example, in the case of β = 0.50, the wake behind the tube occupies the region between $\eta = -90°$ and $\eta = 90°$ with a higher value of $|\zeta_s|$ in comparison with the steady stream case. Stronger vortical motion in the wake leads to higher velocity and temperature gradients and accordingly higher rates of heat transfer.

Figures 5.17-5.20 shows the local Nusselt number distribution for cases (A-5) to (A-8) at different times for one complete cycle of oscillation. At time t = 16 when the free stream velocity is maximum, Nu has higher value on almost all the tube surface except at the rear of the tube. In the next two time steps (t=18, 20) Nu decreases on most of the surface due to the decrease of the free stream velocity. The figures also show that for all values of β, Nu values at the rear of the tube are highest when the free stream velocity is minimum (t=20). One can also see that the distribution of Nu at the start and end of the cycle have minor differences. These differences are expected since a large number of cycles is needed before reaching a perfect quasi-steady state. The vorticity distribution for the same cases are shown in Figures 5.21 to 5.24. These figures show that the values of $|\zeta_s|$ at the rear part of the tube for all β values were found to be higher when U=U_{min} (t=20). The same behavior for the

Nusselt number and vorticity distributions was found for higher Strouhal numbers as shown in Figures 5.25 to 5.32. The number of cycles completed for this case was eight cycles compared to five for S = $\pi/4$, and still more number of cycles is needed to reach a fully quasi-steady behavior.

Figures 5.33 and 5.34 show the pressure variation around the tube surface for different β values when S = $\pi/4$. Figure 5.33 shows the pressure variation at the maximum free stream velocity for different β values. It is clear that increasing the amplitude results in a considerable decrease in the minimum pressure values. For instance, the value of minimum pressure decreases from -2.2 to -6.4 as β increases from 0.25 to 1.0. It was found that increasing β shifts the location of the point of minimum pressure from $\eta = 140^o$ to 150^o . The maximum pressure also increases as β increases with a small shift in its location around the tube surface. For $\beta =$ 0.25, the maximum dimensionless pressure is 0.6 occurring at $\eta = 200^o$ while for $\beta = 1.0$, the maximum dimensionless pressure is 4.5 occurring at $\eta = 210^o$. It is found from the figures that the absolute value of the surface pressure for fluctuating free stream is higher allover the tube surface when compared with the steady free stream case. Figure 5.34 shows the pressure distribution for different β values when the free stream velocity is minimum.

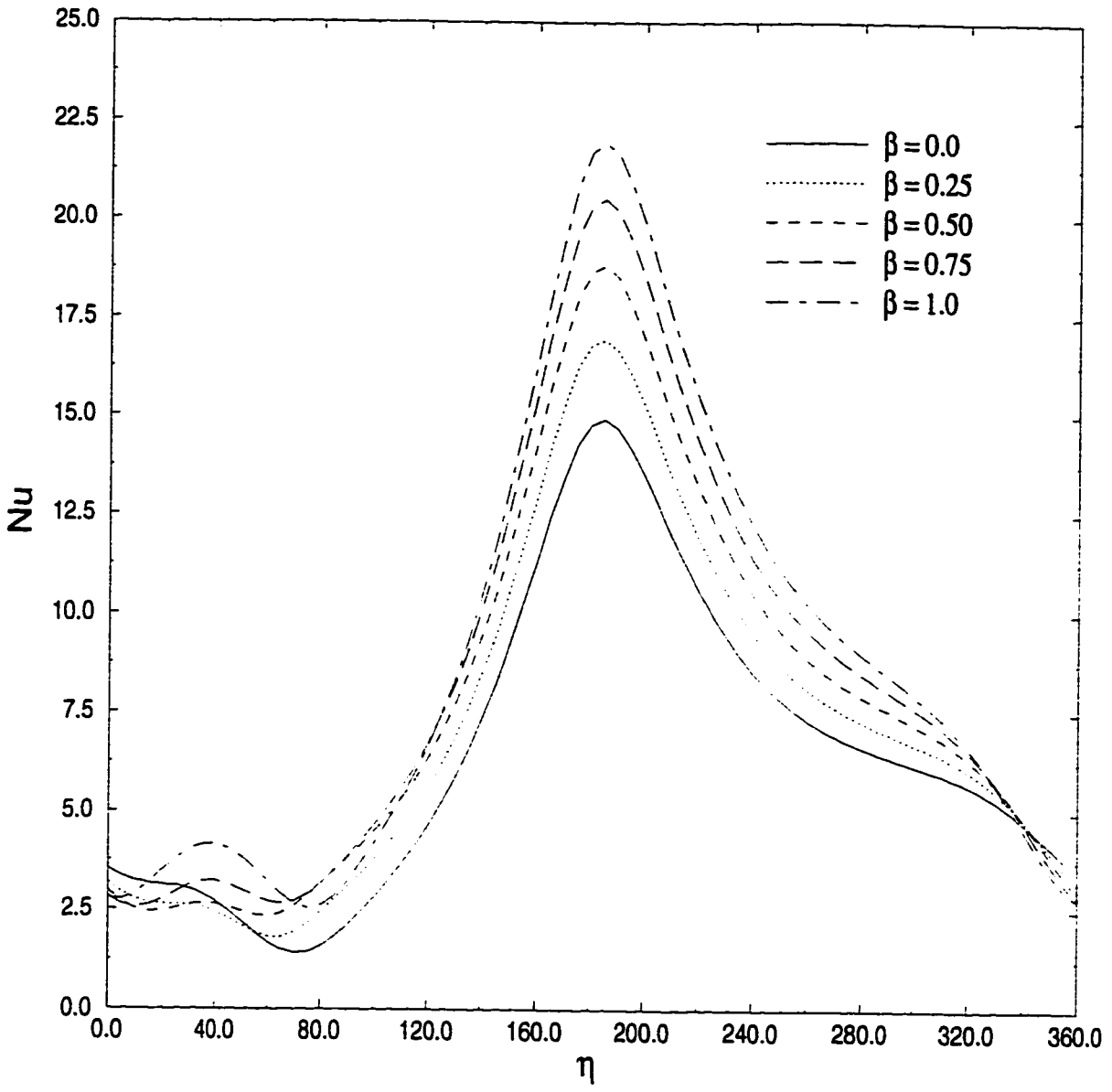

Figure 5.13: The effect of amplitude of fluctuations on the local Nusselt number distribution at maximum free stream velocity for the case of Re=100, Gr=20000, Ar=0.5, $\lambda = 30^o$ and $S = \pi/4$..

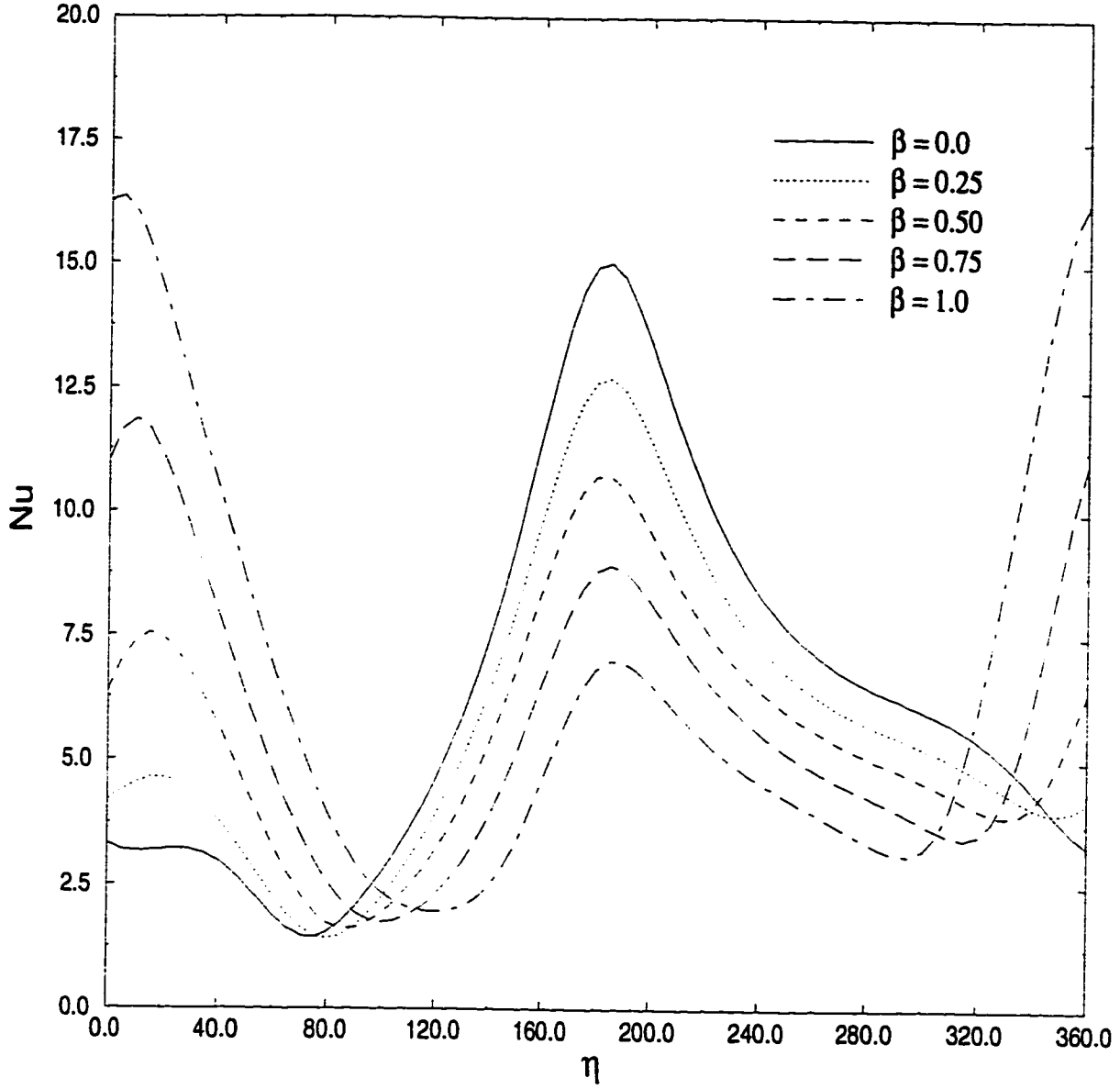

Figure 5.14: The effect of amplitude of fluctuations on the local Nusselt number distribution at minimum free stream velocity for the case of Re=100, Gr=20000, Ar=0.5, $\lambda = 30^o$ and $S = \pi/4$.

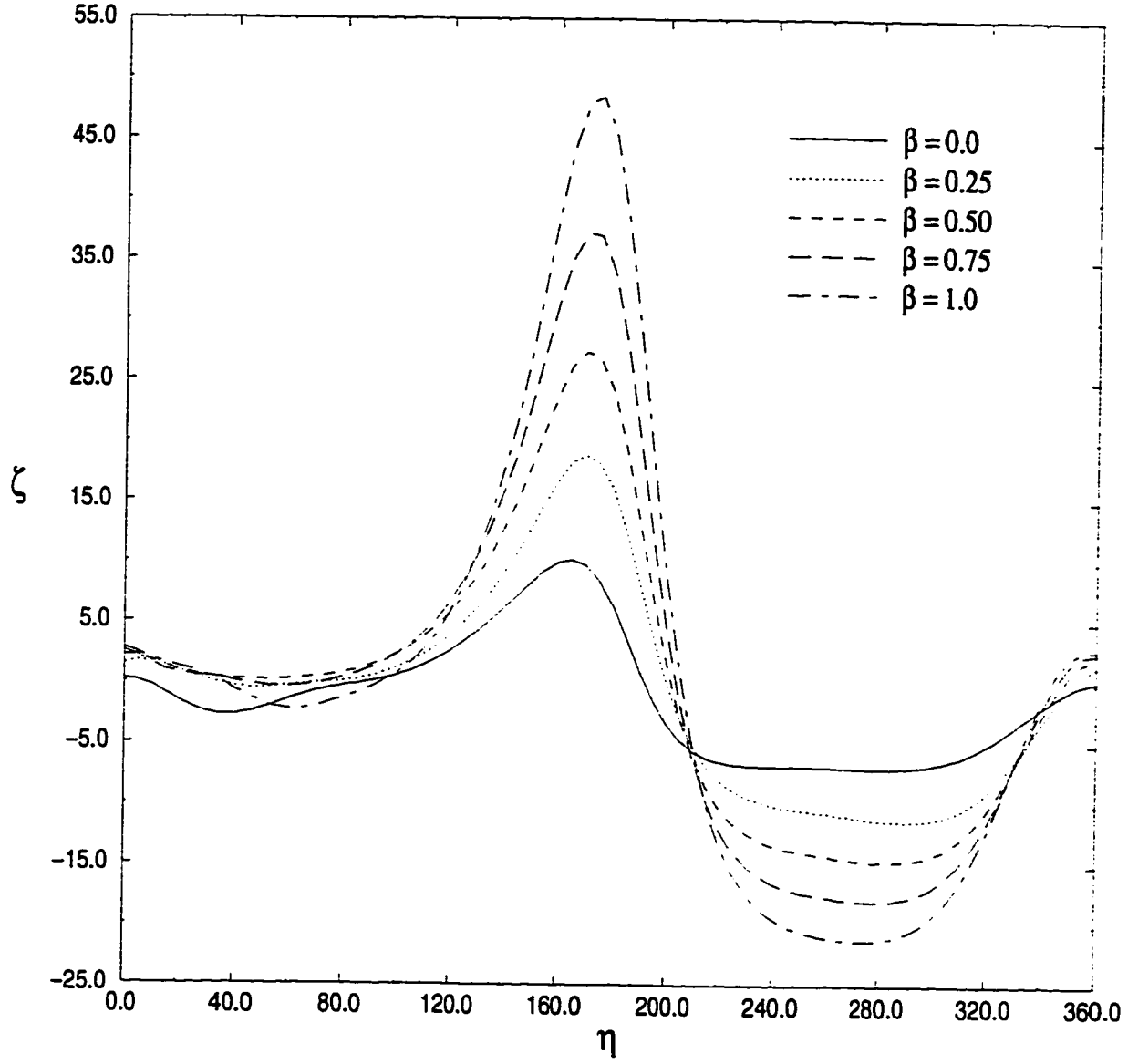

Figure 5.15: The effect of amplitude of fluctuations on the surface vorticity distribution at maximum free stream velocity for the case of Re=100, Gr=20000, Ar=0.5, $\lambda = 30^{o}$ and $S = \pi/4$.

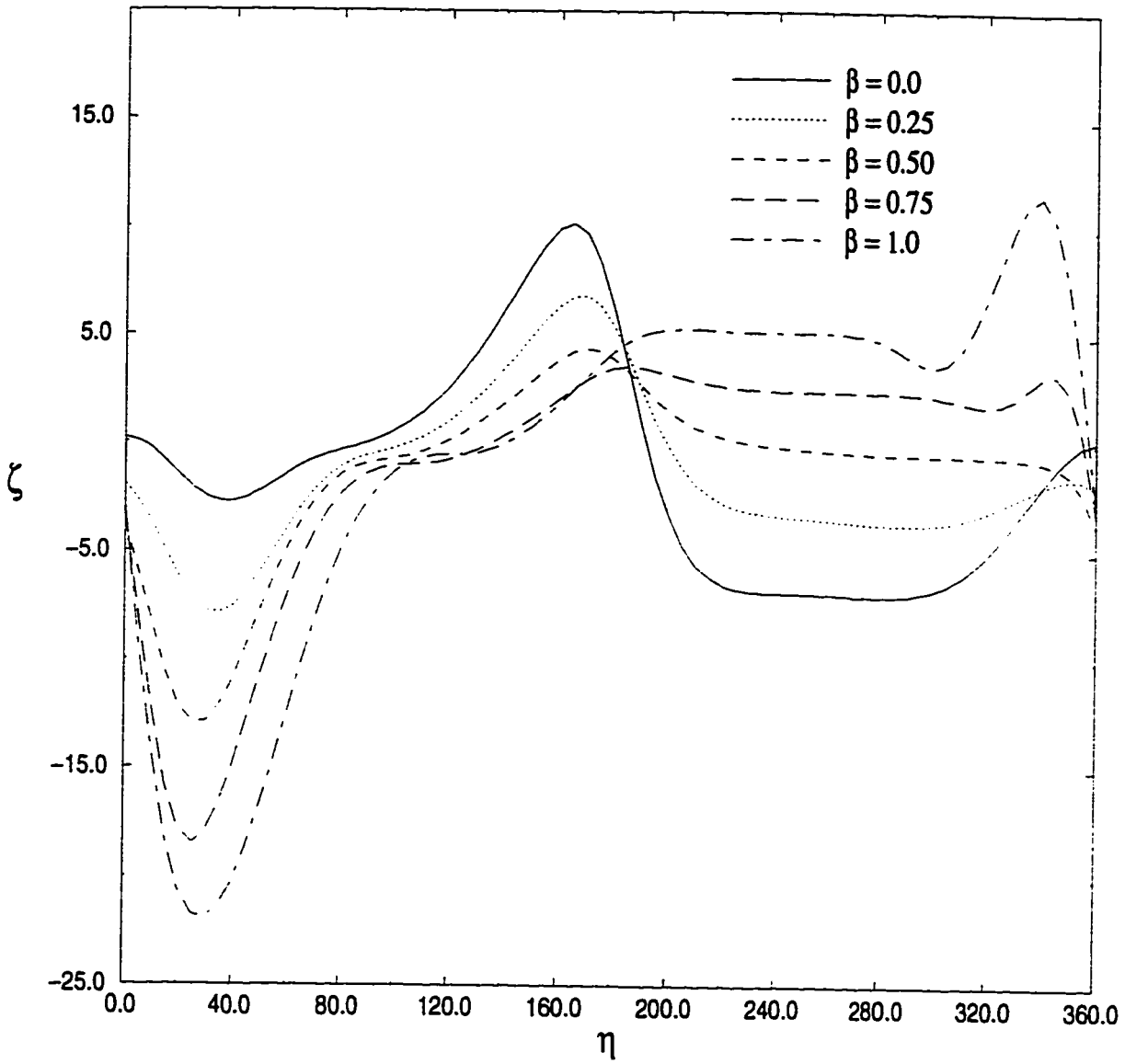

Figure 5.16: The effect of amplitude of fluctuations on the surface vorticity distribution at minimum free stream velocity for the case of Re=100, Gr=20000, Ar=0.5, $\lambda = 30^o$ and $S = \pi/4$.

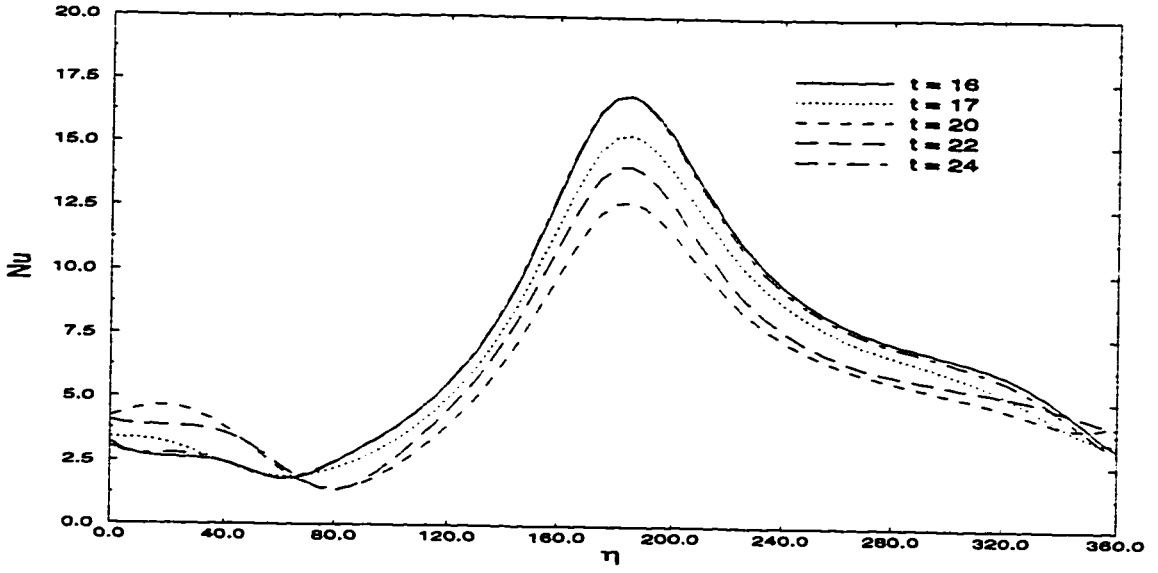

Figure 5.17: The local Nusselt number distribution at various times during one complete cycle in case A-5.

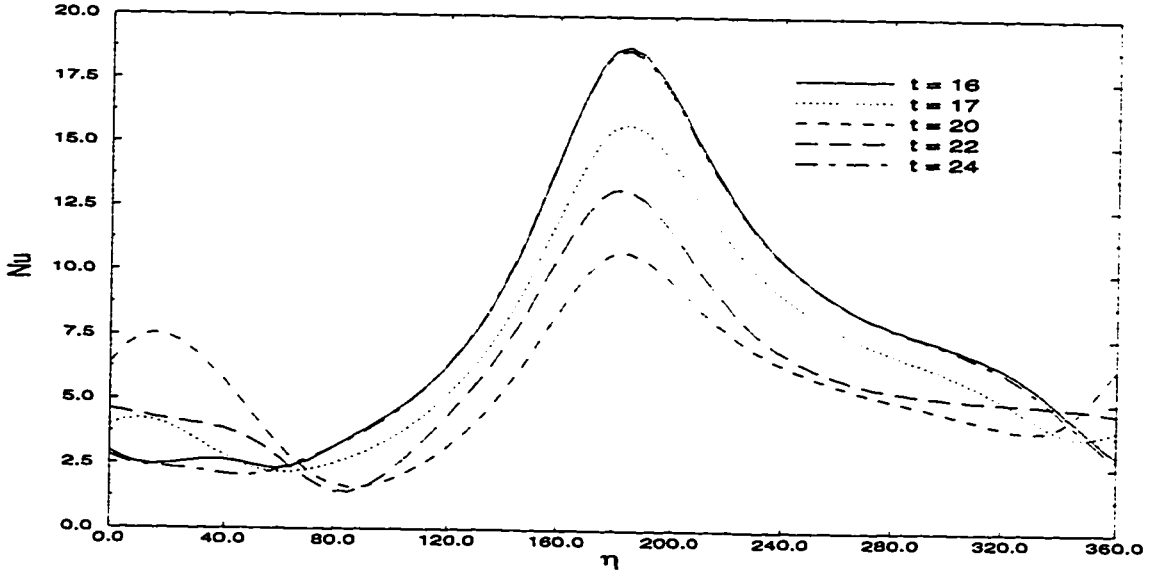

Figure 5.18: The local Nusselt number distribution at various times during one complete cycle in case A-6.

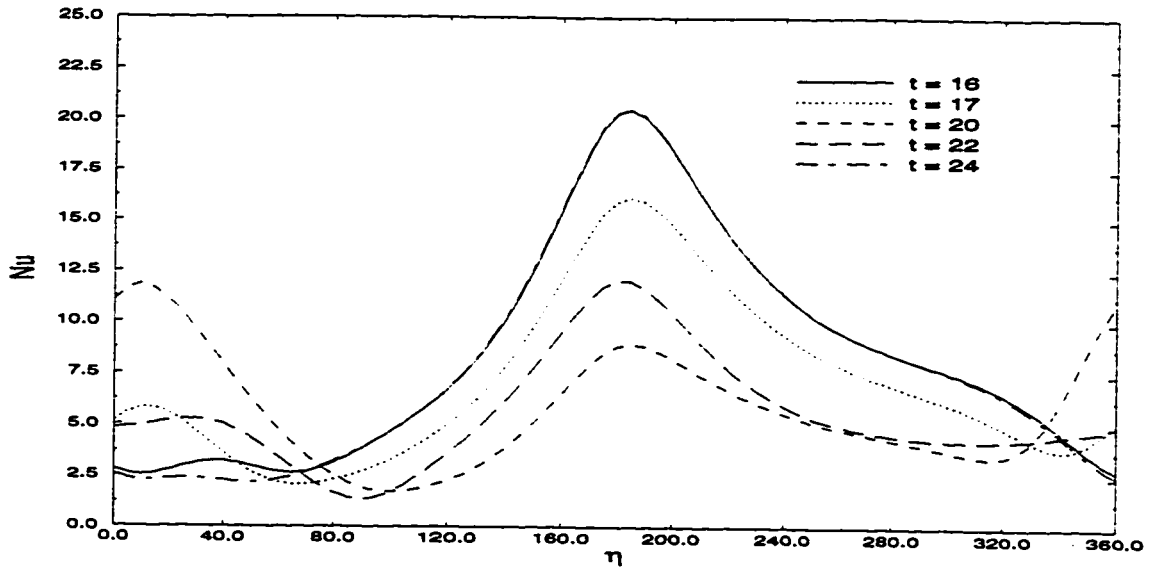

Figure 5.19: The local Nusselt number distribution at various times during one complete cycle in case A-7.

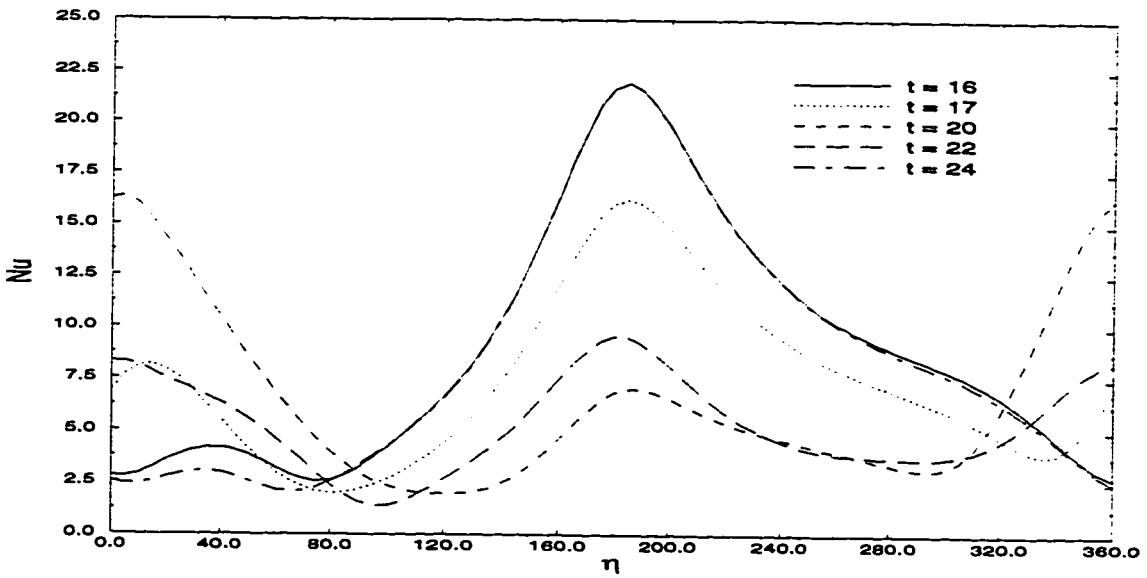

Figure 5.20: The local Nusselt number distribution at various times during one complete cycle in case A-8.

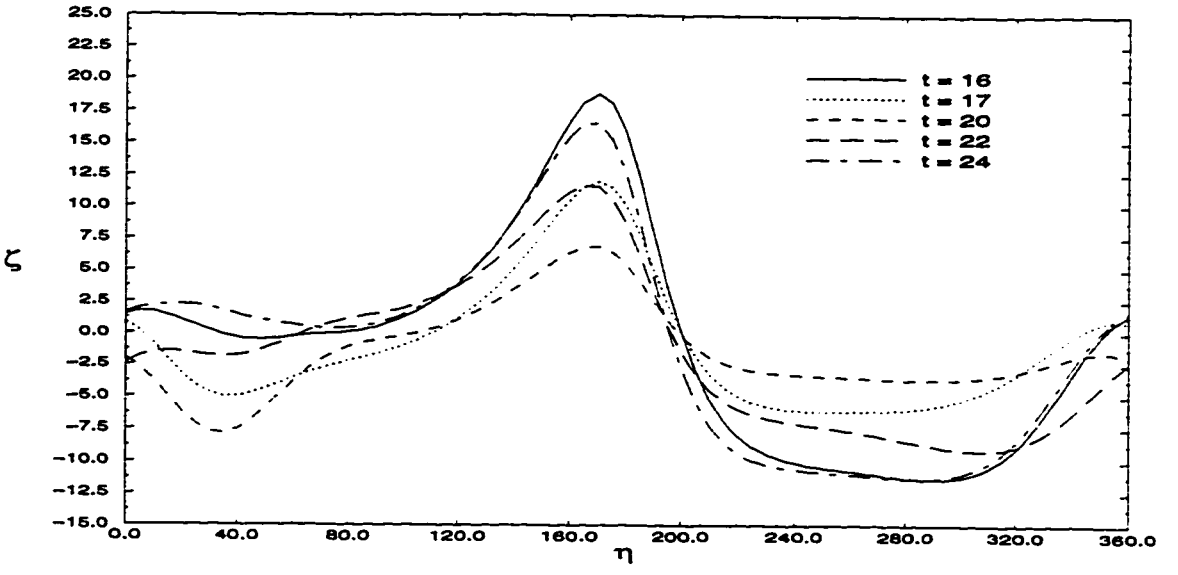

Figure 5.21: The surface vorticity distribution at various times during one complete cycle in case A-5.

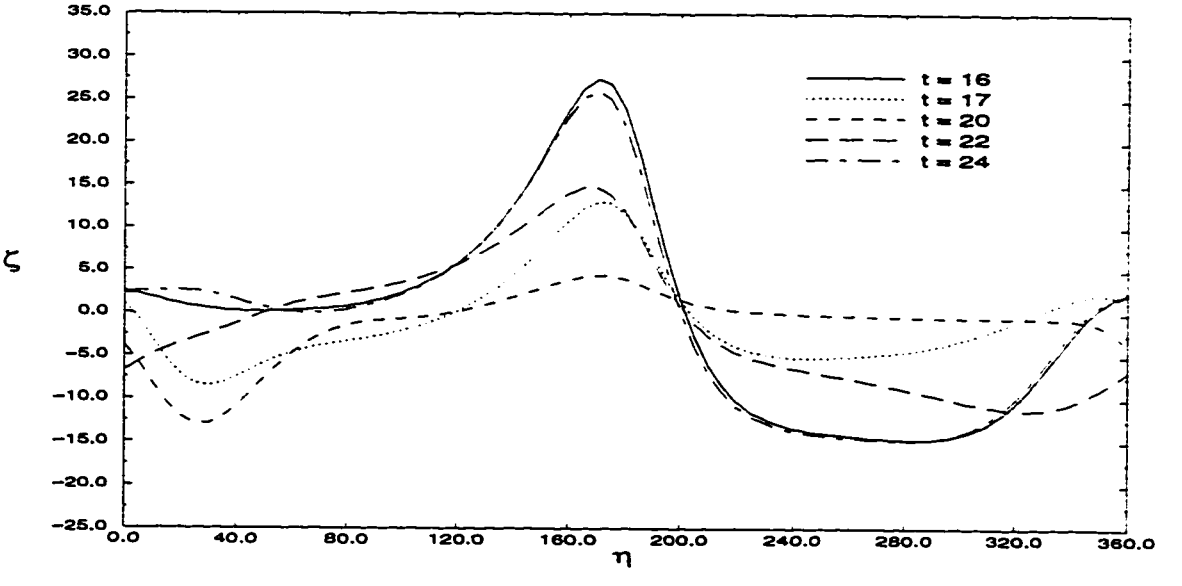

Figure 5.22: The surface vorticity distribution at various times during one complete cycle in case A-6.

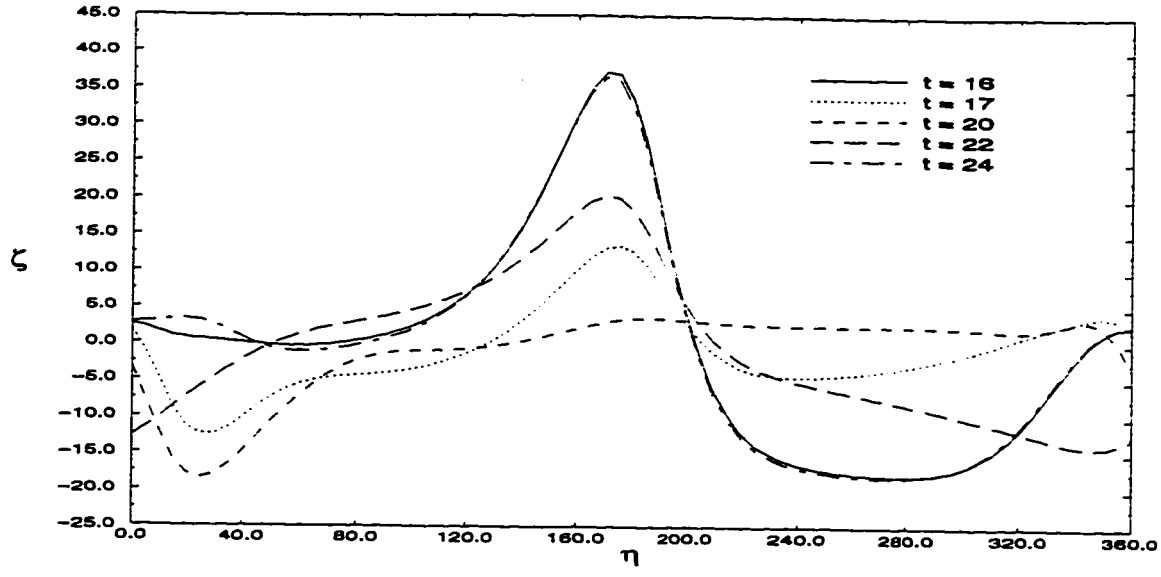

Figure 5.23: The surface vorticity distribution at various times during one complete cycle in case A-7.

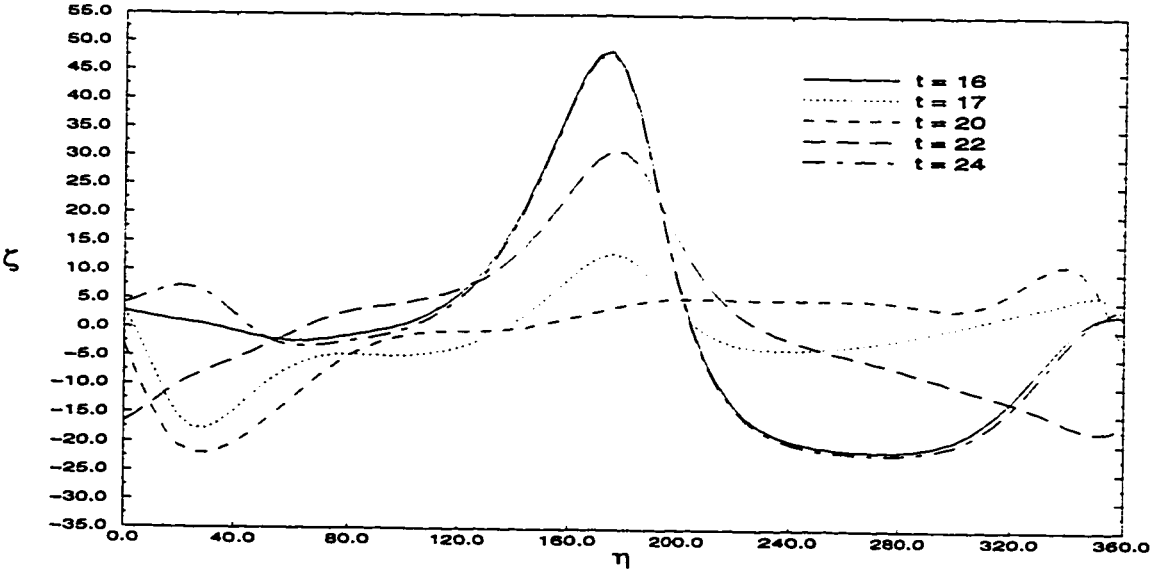

Figure 5.24: The surface vorticity distribution at various times during one complete cycle in case A-8.

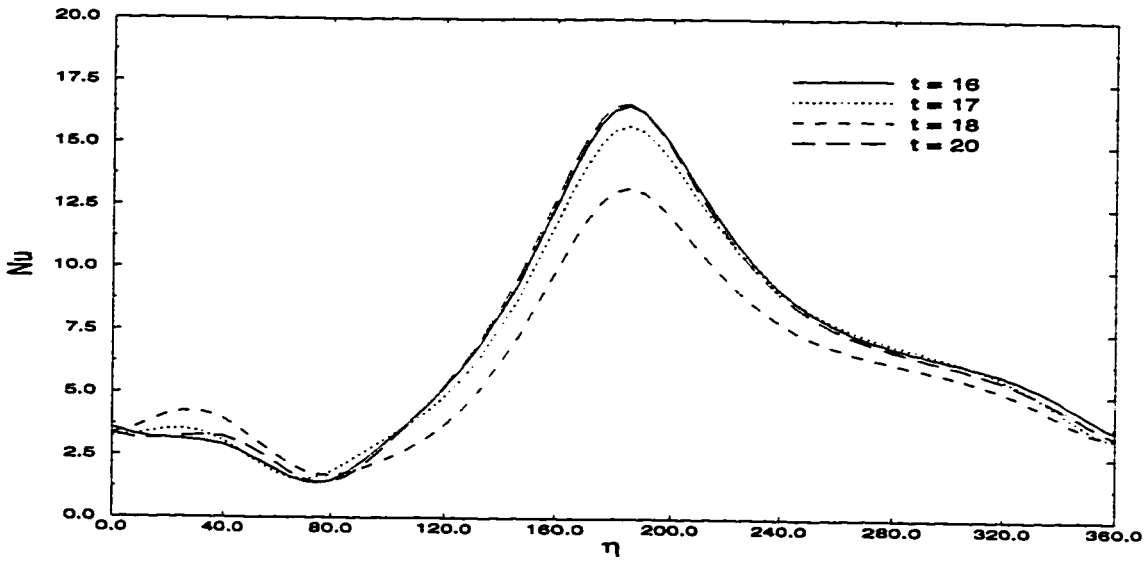

Figure 5.25: The local Nusselt number distribution at various times during one complete cycle in case A-9.

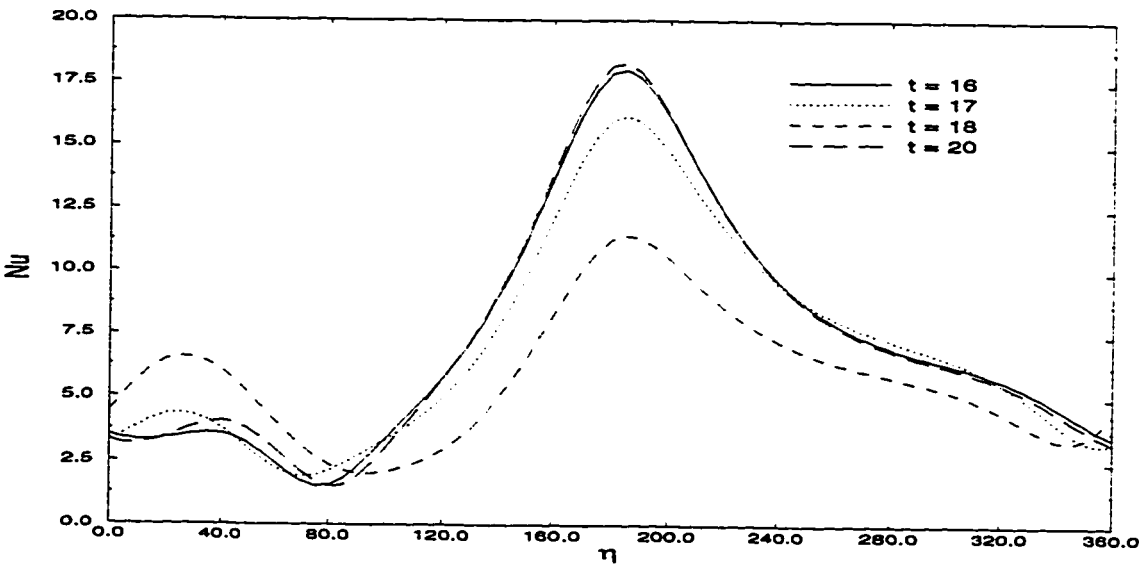

Figure 5.26: The local Nusselt number distribution at various times during one complete cycle in case A-10.

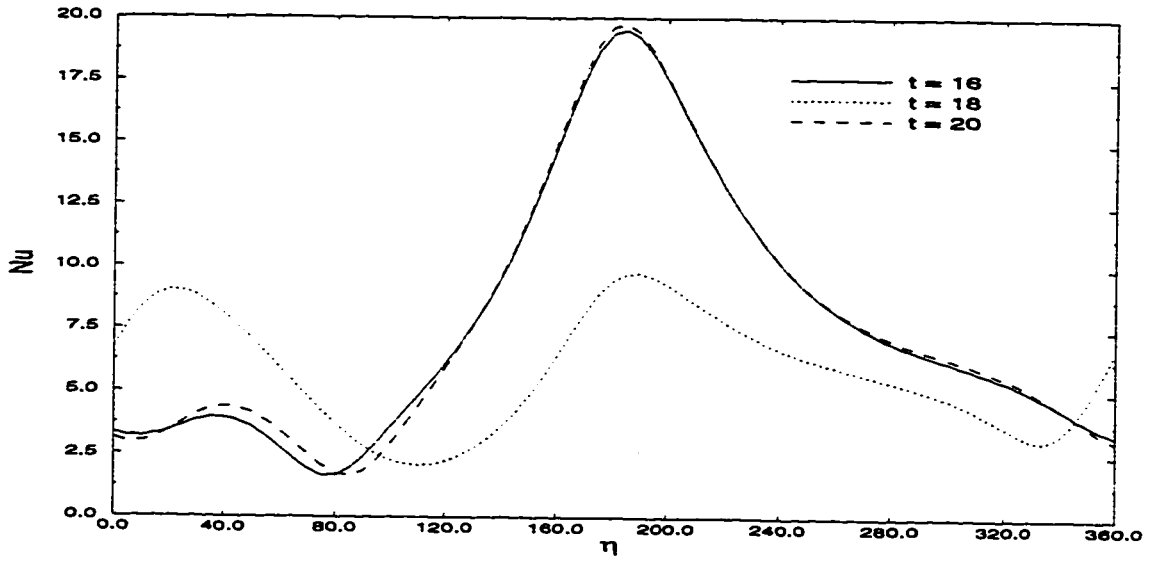

Figure 5.27: The local Nusselt number distribution at various times during one complete cycle in case A-11.

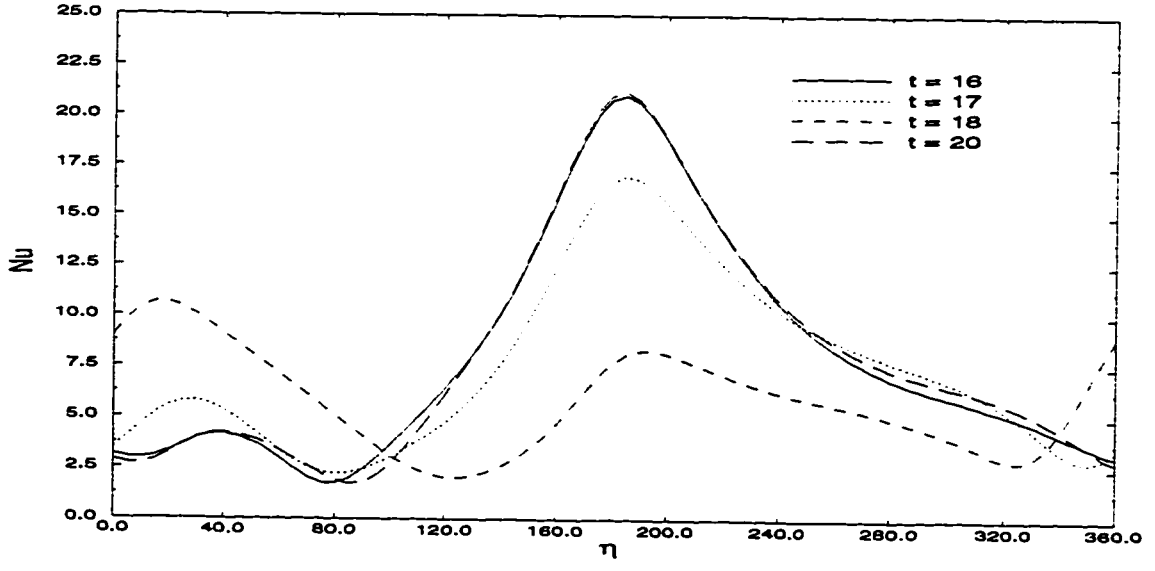

Figure 5.28: The local Nusselt number distribution at various times during one complete cycle in case A-12.

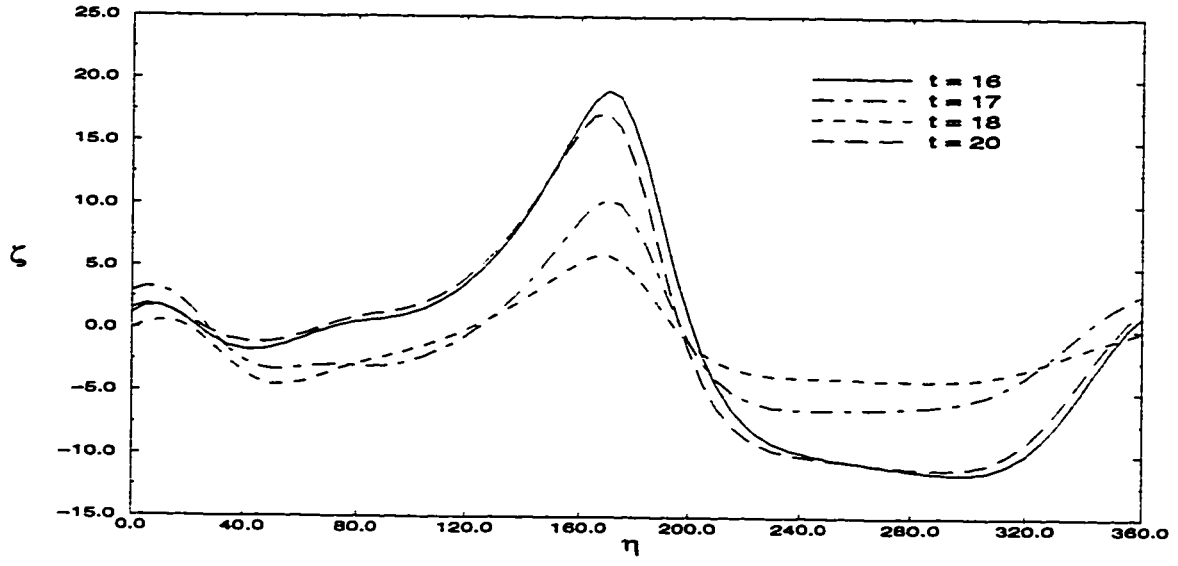

Figure 5.29: The surface vorticity distribution at various times during one complete cycle in case A-9.

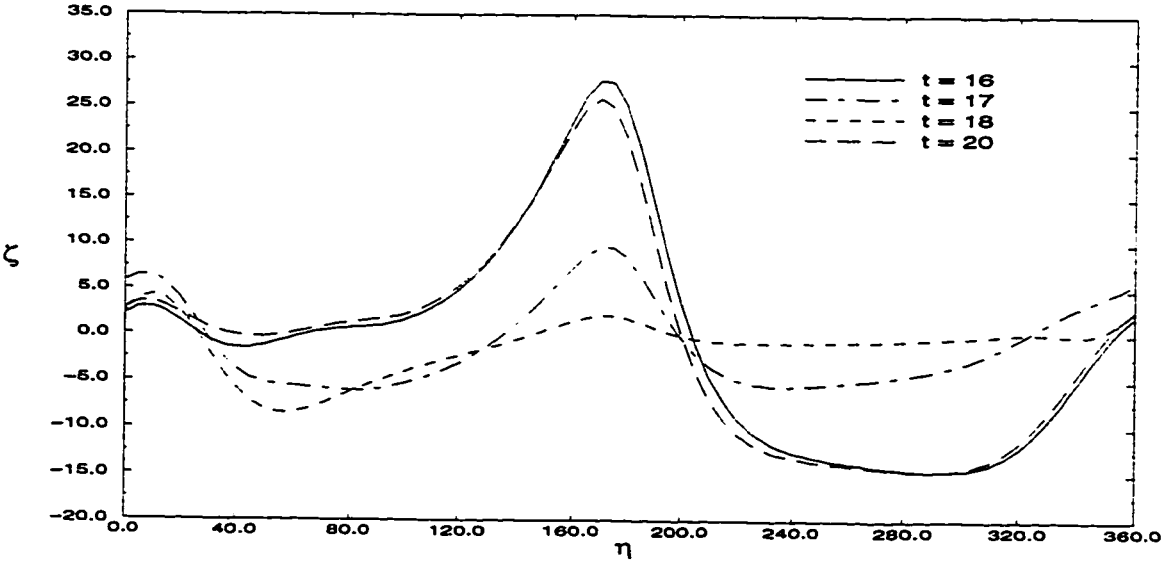

Figure 5.30: The surface vorticity distribution at various times during one complete cycle in case A-10.

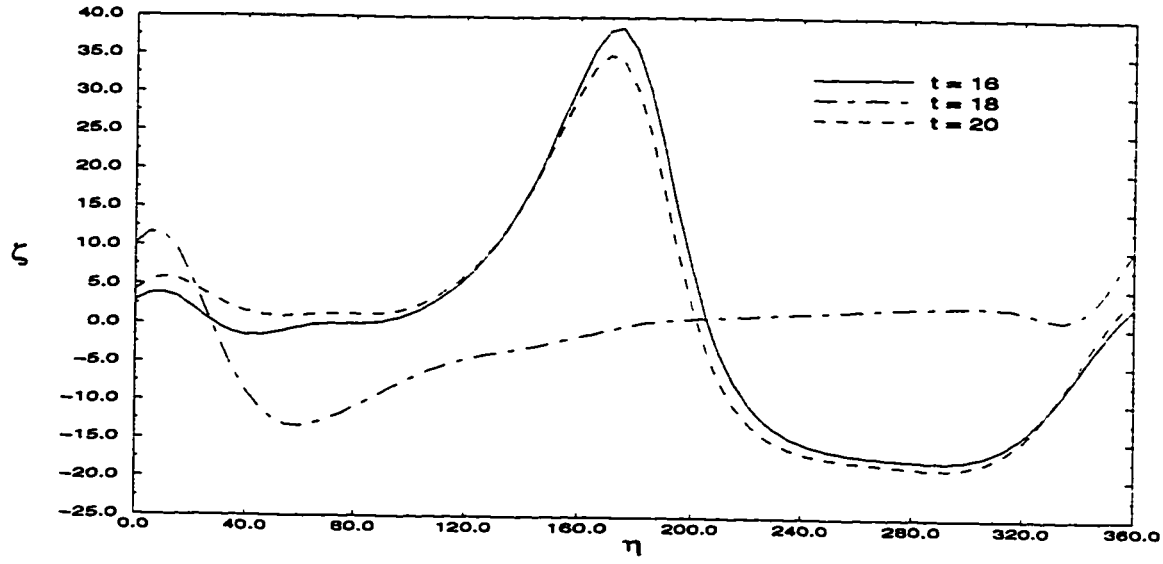

Figure 5.31: The surface vorticity distribution at various times during one complete cycle in case A-11.

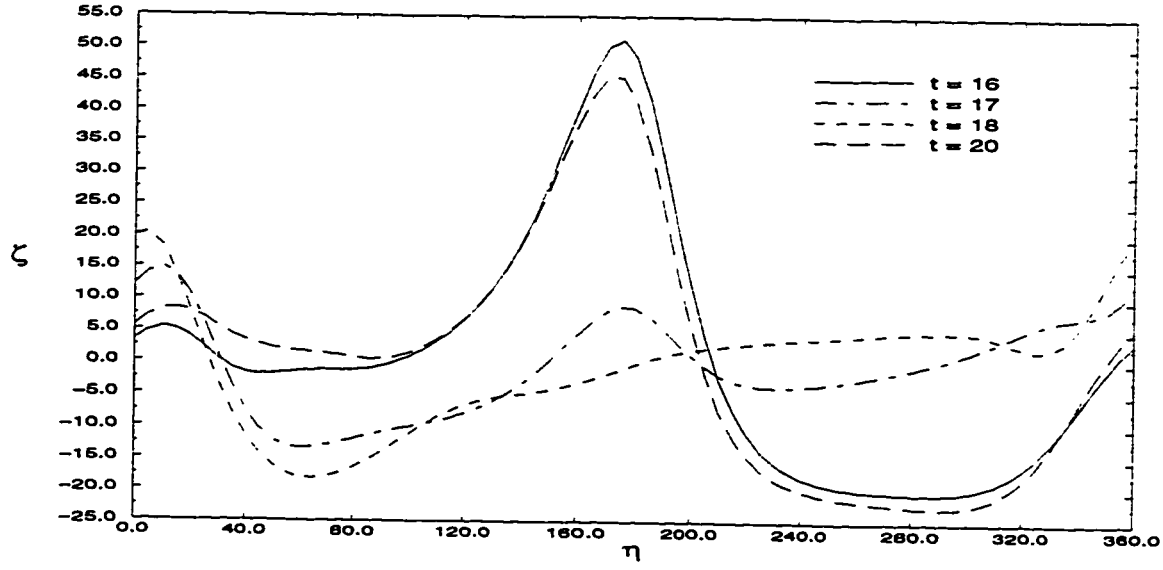

Figure 5.32: The surface vorticity distribution at various times during one complete cycle in case A-12.

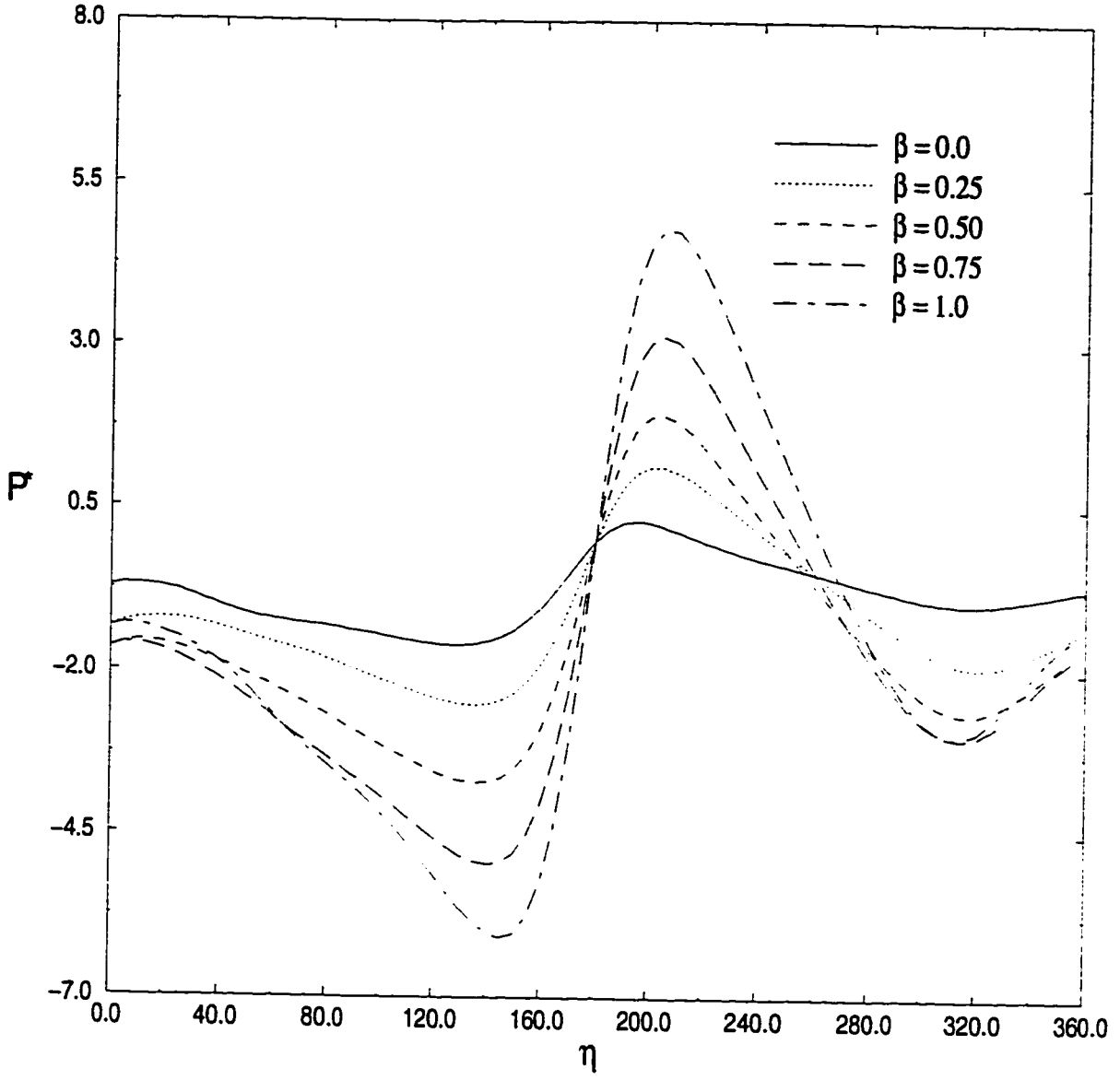

Figure 5.33: The effect of amplitude of fluctuations on the pressure distribution at maximum free stream velocity in case of Re=100, Gr=20000, Ar=0.5, $\lambda = 30^{o}$ and $S = \pi/4$.

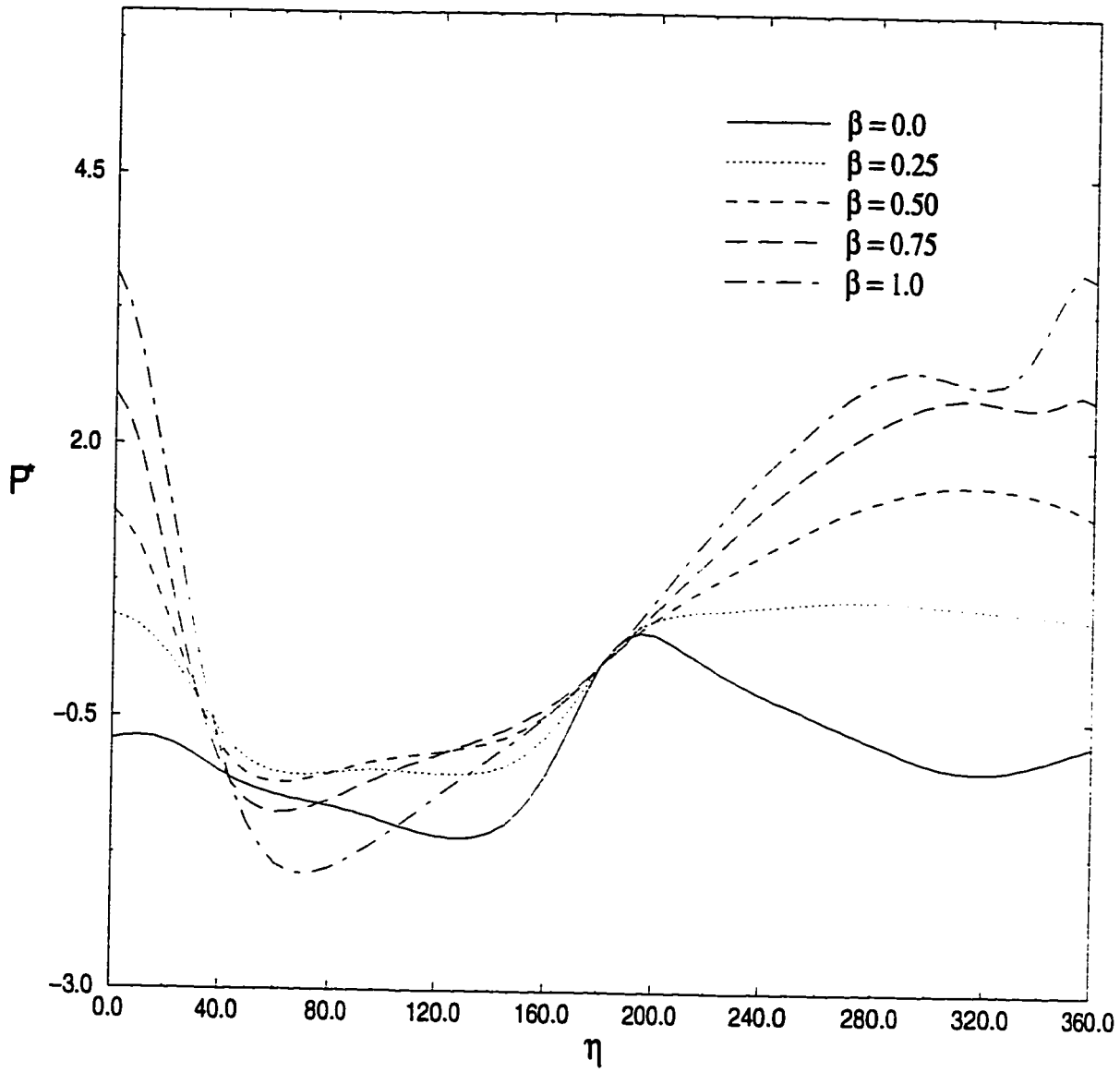

Figure 5.34: The effect of amplitude of fluctuations on the pressure distribution at minimum free stream velocity in case of Re=100, Gr=20000, Ar=0.5, $\lambda = 30^o$ and $S = \pi/4$.

5.3.3 The Effect of Amplitude on the Drag and Lift Forces

The in-line and transverse force coefficients C_D and C_L are plotted for different amplitudes at S = $\pi/2$ together with the steady free stream velocity coefficients. Figure 5.35 shows the drag coefficient variation with time for cases (A-10) to (A-12). It is clear that the drag force is fluctuating with a frequency equal to that of the free stream velocity. There is a clear indication that increasing the amplitude of fluctuations has no effect on the average drag force. Figure 5.36 shows the variation of the coefficient of the transverse forces acting on the tube surface. Similar to C_D, the frequency of fluctuations of C_L is the same as that of the steady stream case. The effect of vortex shedding and interaction is causing the peaks of C_L to vary with time. When compared with the steady free stream the cyclic variation of C_L shows an average value higher than that of the free stream case.

The variation of C_D, C_{DF} and C_{DP} with time for cases (A-9) to (A-12) are plotted in Figures 5.37 to 5.40, while the variations of C_L, C_{LF} and C_{LP} with time for the same cases are shown in Figures 5.41 to 5.42. All of these figures show that there is a negligible contribution of the frictional force to the total resistance and the pressure forces are the dominating force for lift and drag.

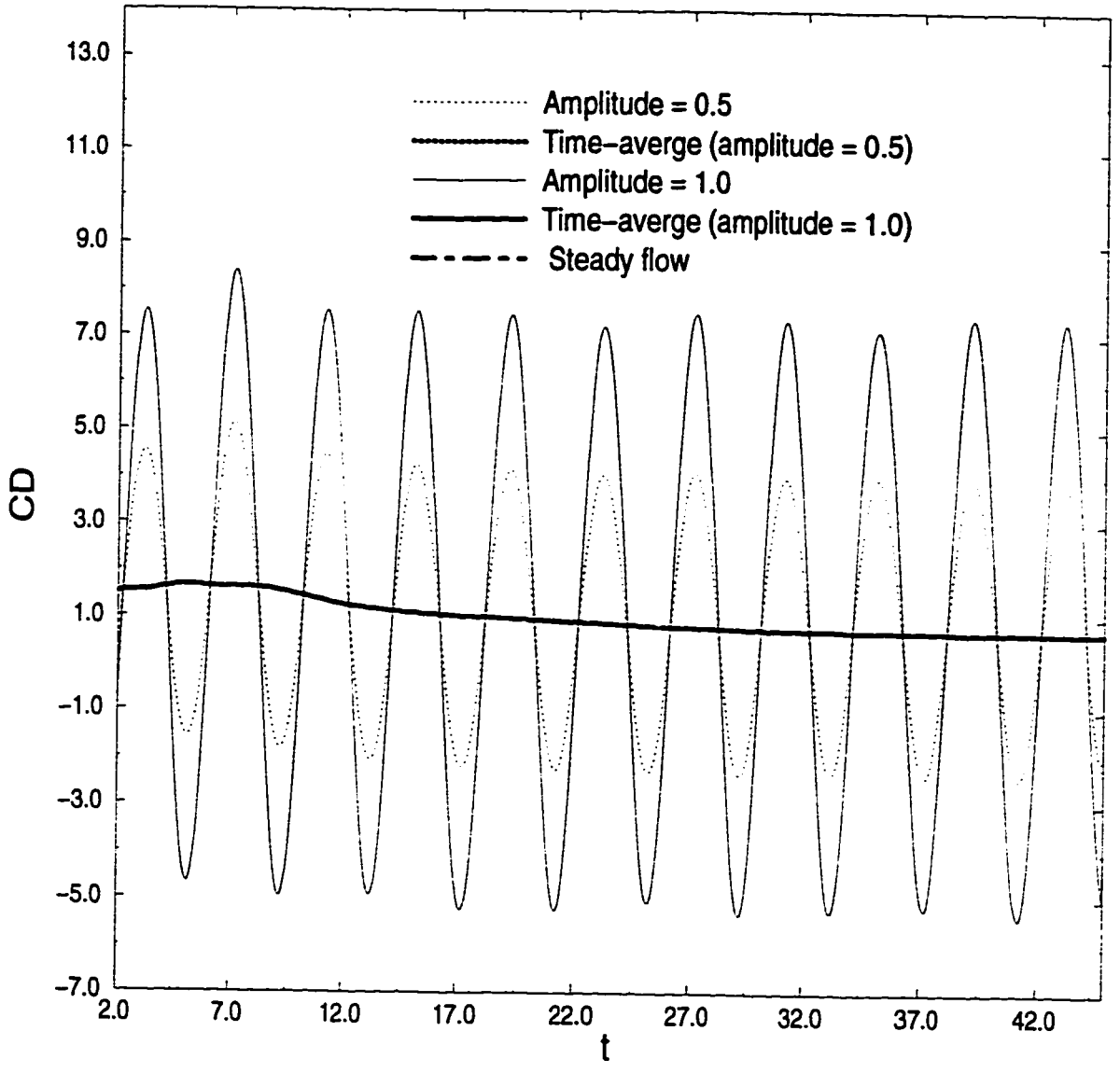

Figure 5.35: The time variation of the in-line force coefficient for various amplitudes in case of Re=100, Gr=20000, Ar=0.5, $\lambda = 30.0^o$ and $S = \pi/2$.

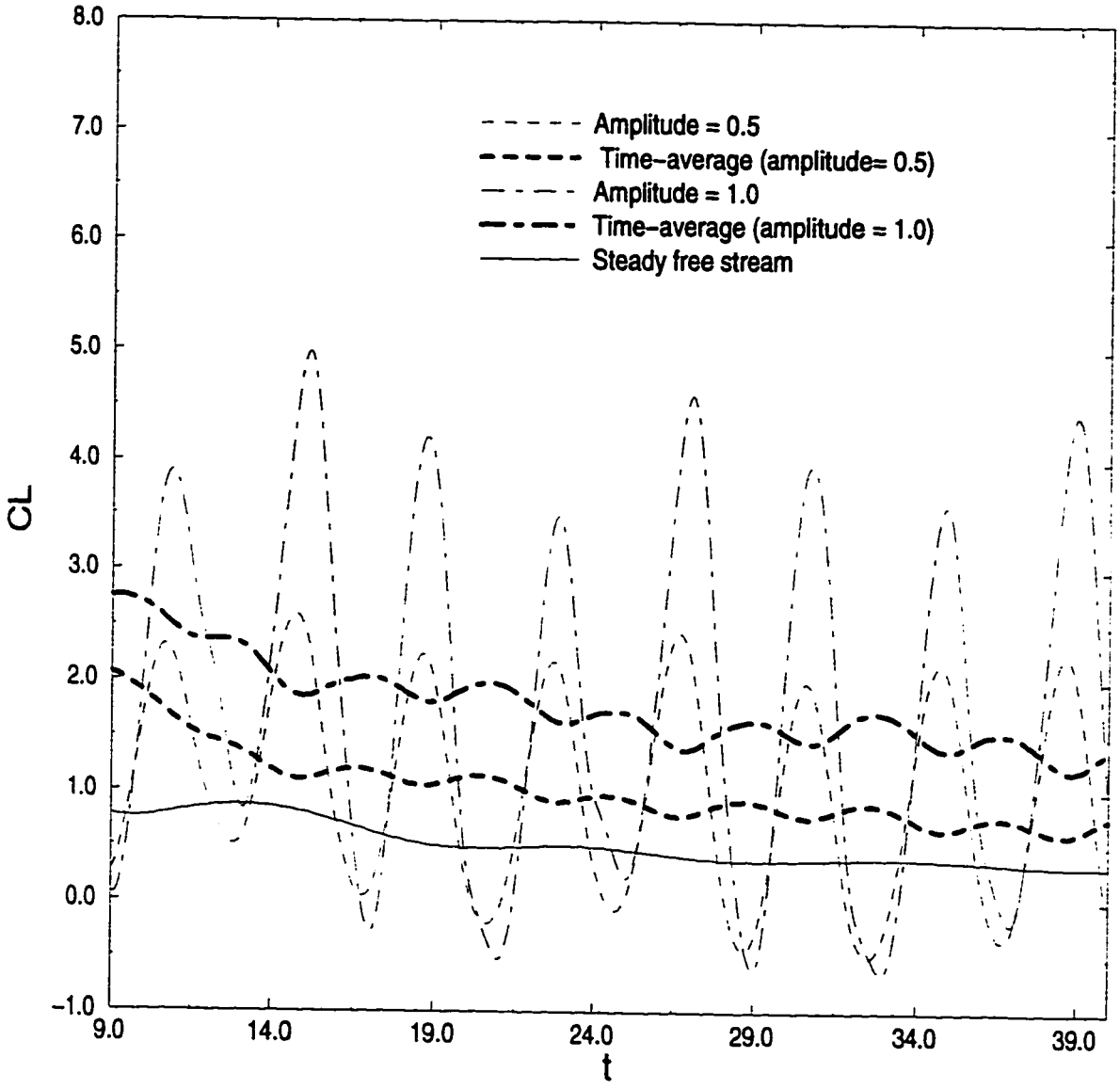

Figure 5.36: The time variation of the transverse force coefficient for various amplitudes in the case of Re=100, Gr=20000, Ar=0.5, $\lambda = 30.0°$ and $S = \pi/2$.

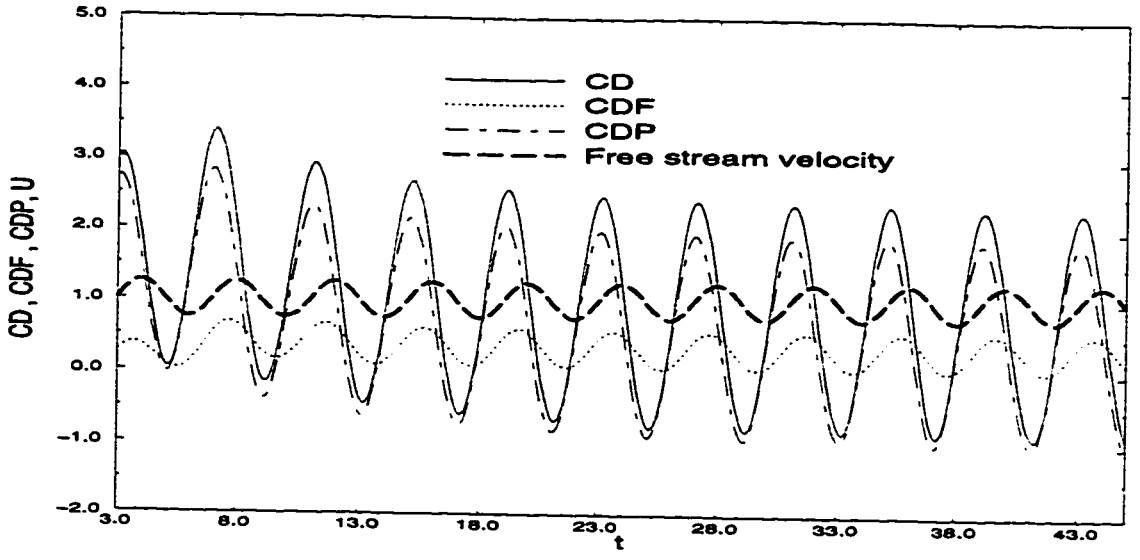

Figure 5.37: The time variation of the C_D, C_{DF}, C_{DP} in case of A-9.

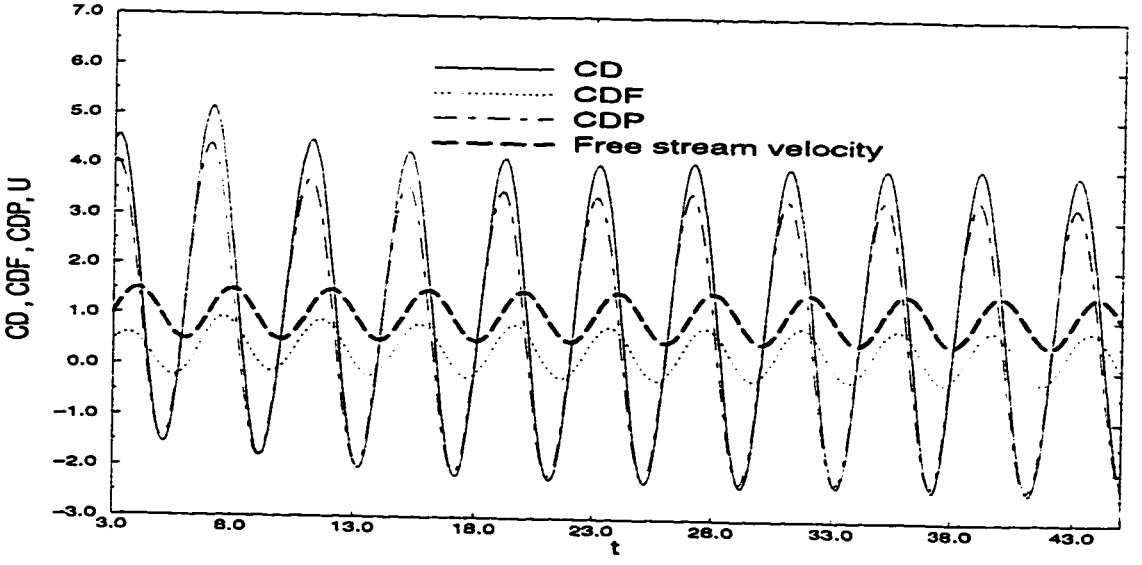

Figure 5.38: The time variation of the C_D, C_{DF}, C_{DP} in case of A-10.

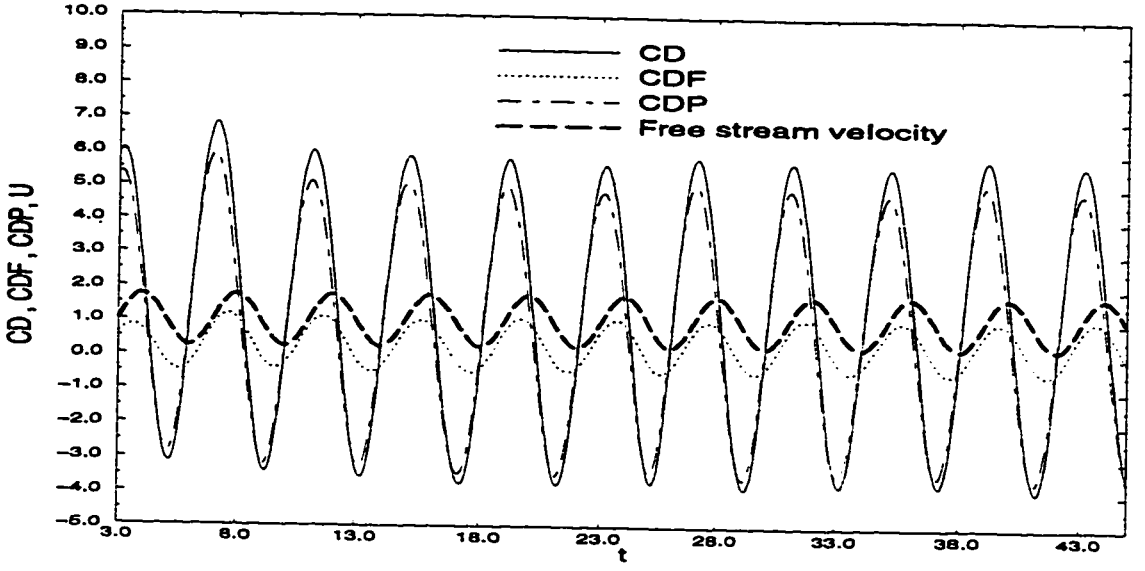

Figure 5.39: The time variation of the C_D, C_{DF}, C_{DP} in case of A-11.

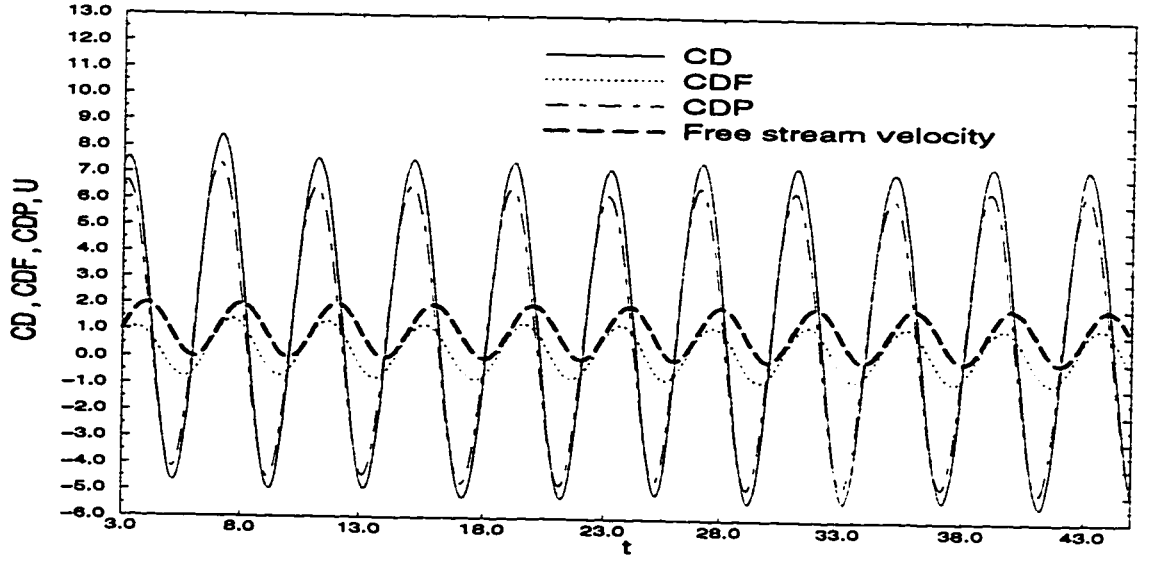

Figure 5.40: The time variation of the C_D, C_{DF}, C_{DP} in case of A-12.

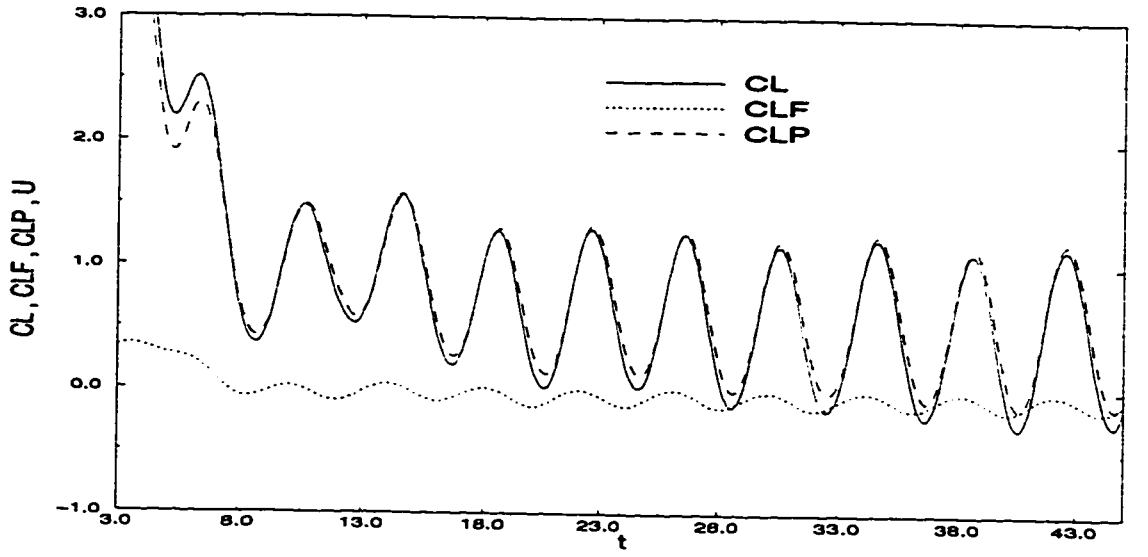

Figure 5.41: The time variation of the C_L, C_{LF}, C_{LP} in case of A-9.

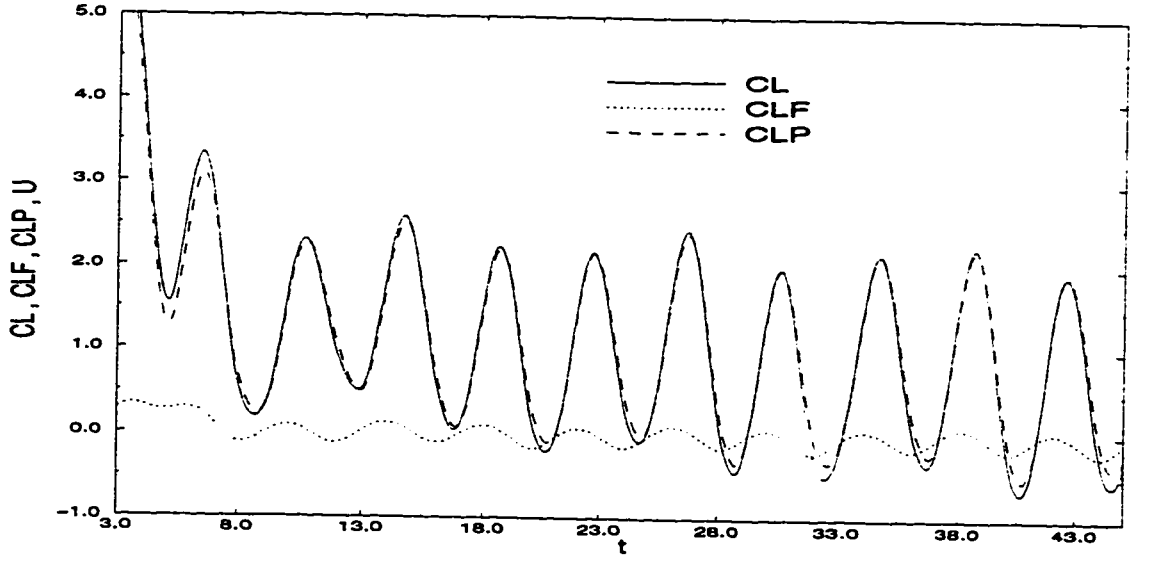

Figure 5.42: The time variation of the C_L, C_{LF}, C_{LP} in case of A-10.

5.3.4 The Effect of Amplitude on the Streamlines and Isotherms

The streamlines patterns and isotherms were plotted for three values of the amplitudes ($\beta = 0.25,\ 0.5$ and 1.0) for Strouhal number S $= \pi/4$. Figures 5.43a-f show the time variation of the streamlines patterns for case(A-6). The figures give the details of the flow field structure during one complete cycle of fluctuations. Figure 5.43a shows the streamlines when the free stream is moving to the right at maximum velocity. The values of the dimensionless stream function (ψ) corresponding to the streamlines from the top of the diagram to the tube surface are given in the figure caption and the same values are used in all other streamline plots. The figure shows no formation of vortices or bubbles at the rear end of the tube. The buoyancy effect tends to shift the streamlines up in the wake region. Figure 5.43b shows the streamlines at a time when the free stream velocity is decreasing. The rear stagnation point is moved up stream with the formation of a vortex in the wake. As the free stream velocity further decreases two vortices appear in the wake region as shown in figure 5.43c. One of these vortices is growing in size, compared to the previous figure, while the other is starting to form. Figure 5.43d shows the streamlines when the free stream velocity is minimum. The large distance between the streamlines reflects the smaller velocity everywhere. The vortex formed in the wake is getting larger reaching maximum size when the free stream velocity is minimum. The vor-

tex is shed away from the tube wake as the free stream velocity is increased again (see Figure 5.43f).

The slope of the streamlines upstream and downstream of the tube is greatly affected by the buoyancy force (represented by Grashof number) as well as the changes of the free stream velocity. Lower stream velocity results in higher slopes. Figure 5.43f which represent the streamlines at the end of the cycle is very much the same as that at the beginning (see Figure 5.43a). The minor differences reflect the continuous development of the flow field away from the tube surface because of vortex shedding and interactions.

The thermal field is represented by plotting the constant temperature lines (isotherms) around the tube surface. The values of ϕ plotted are $\phi = 0.1(0.1)1.0$. The isotherms for case (A-6) are shown in Figures 5.44a-f. The temperature distribution is shown for a complete cycle of free stream fluctuations. Figure 5.44a shows the isotherms when the free stream velocity is maximum (at the beginning of the cycle). The effect of gravity is shifting warm fluid upward as shown in the figure. The figure also shows a warm fluid body moving away from the tube surface which is caused by vortex shedding. As the free stream velocity decreases, the effect of vortex growth and shedding on the isotherms is shown in Figures 5.44b-e where the isotherms extend further from the tube surface until they separate indicating warm fluid bodies detaching from the tube surface. To clearly show how the amplitude

is affecting the velocity and thermal fields, the streamlines and isotherms for cases (A-5) and (A-8) are presented. Figures 5.45a-d show the streamlines for case (A-5). The figure indicate the same pattern of vortex growth and shedding as presented in Figures 5.43a-f. The main difference between the streamlines in case (A-5) and case (A-6) is in the number of vortices forming. While one vortex is forming and detaching in case (A-5), two were alternatively forming, growing in size and then shed away in case (A-6). Another difference can be seen when considering the effect of buoyancy forces. Since the minimum velocity that will be reached in case (A-5) is higher than that in case (A-6), this causes higher effect of buoyancy forces in case (A-6) when the free stream velocity is minimum in both cases. The isotherms for case (A-5) are shown in figure 5.46a-d. The figure shows lumps of fluid detaching from the tube surface with the isotherms affected by buoyancy forces. Figure 5.46a shows a bulk of warm fluid moving away from the tube wake which is the same occurring at the end of the cycle shown in figure 5.46d.

The final case discussed is case (A-8). This case is an extreme case in which the free stream velocity will stall in the middle of the cycle. Figures 5.47a-d represent the streamlines for one complete cycle. The figure shows a small bubble forming at the top part of the tube at t = 32. At the next time step, the free stream velocity becomes less and the vortex grows in the wake as shown in Figure 5.47b. As time increases another vortex starts forming below the previous one at the rear of the

tube. Figure 5.47c shows the streamlines when the free stream velocity is zero. The large distances between the streamlines away from the tube reflects the very small velocity while the fluid motion near the tube is dominated by the vortical motion. The vortices then detach as the free stream velocity increases. The isotherms for case (A-8) is shown in Figures 5.48a-d. The figure shows lumps of warm fluid detaching from the tube and moving away while another lump is about to detach due to the effect of vortex shedding and interactions.

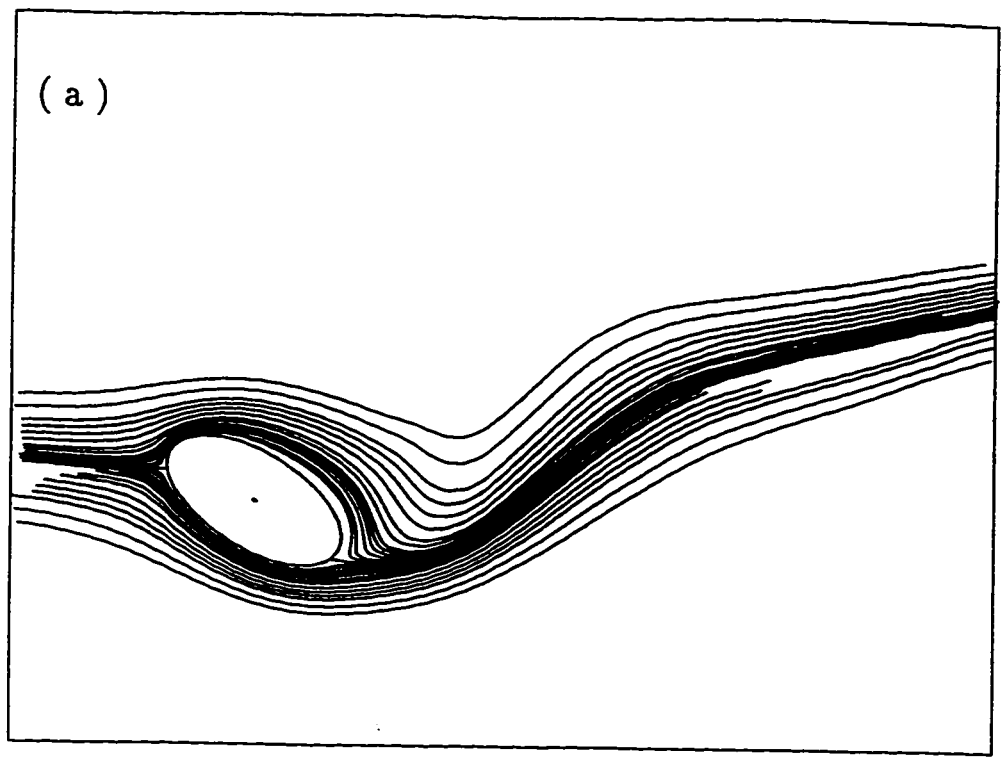
(a)

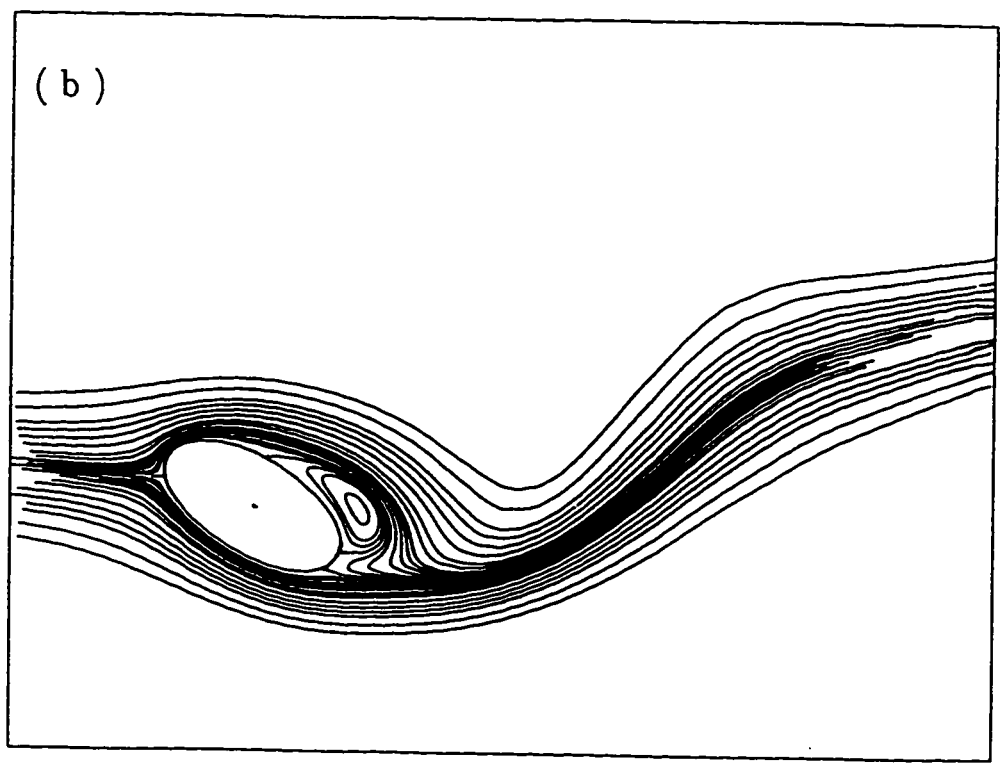
(b)

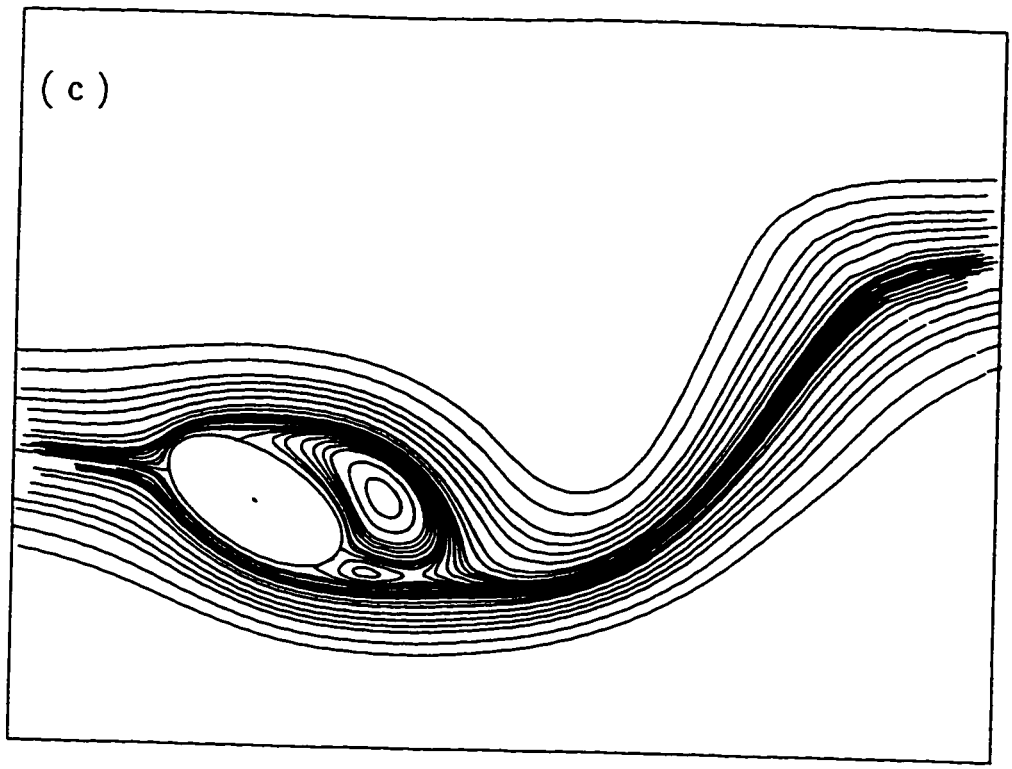
(c)

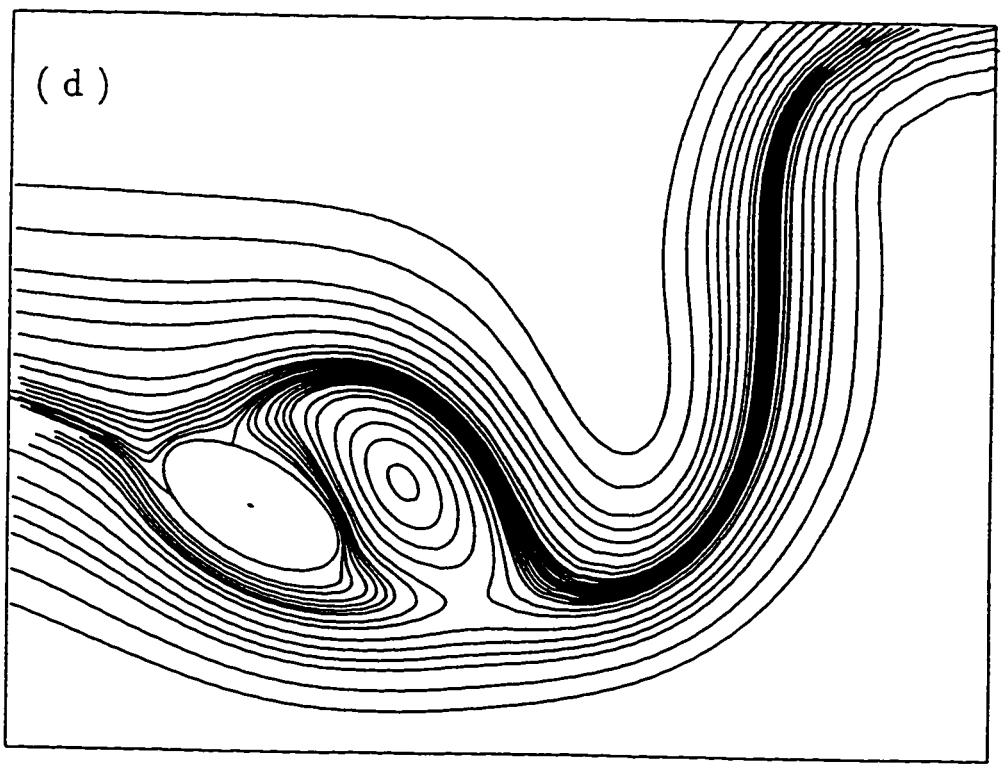
(d)

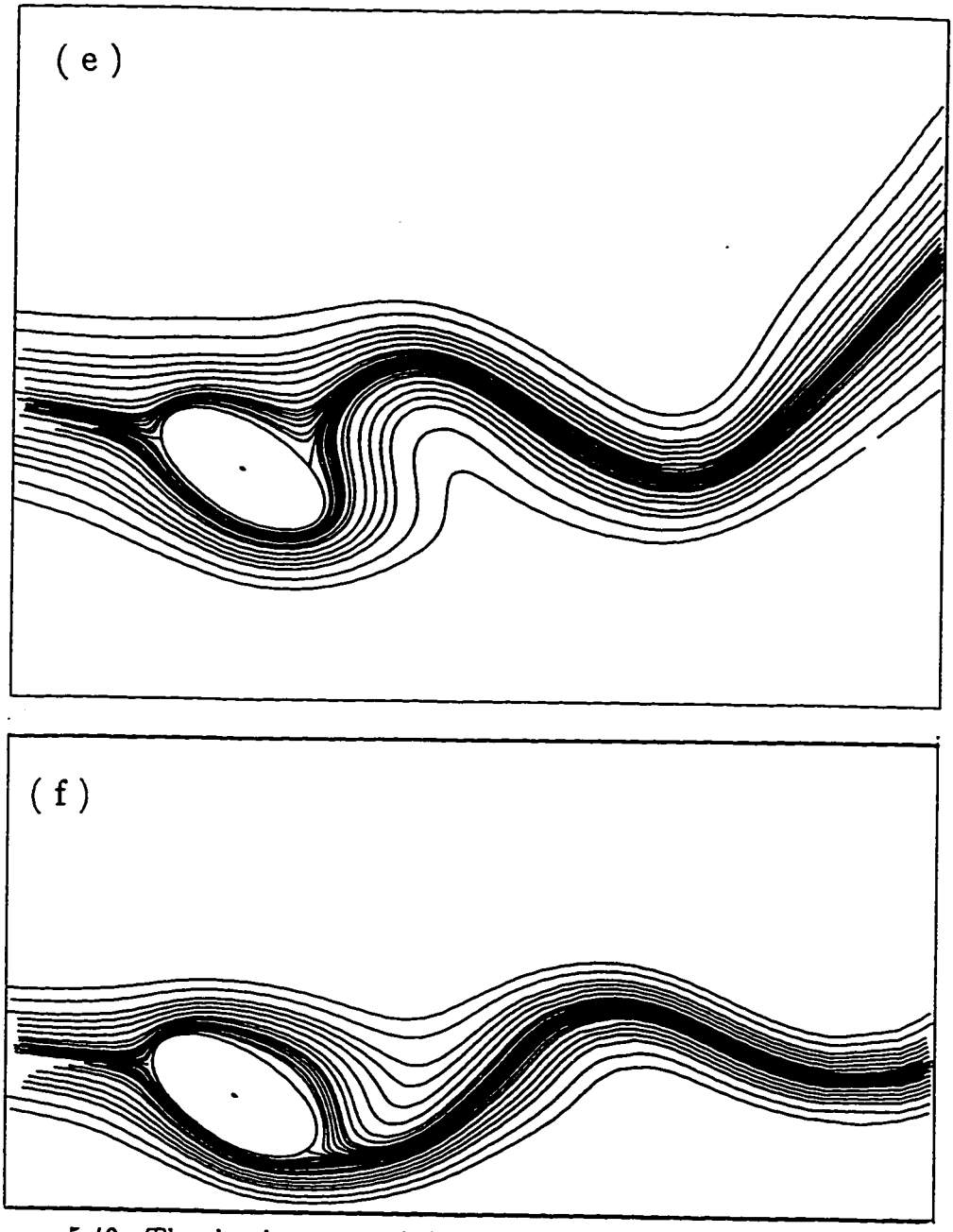

Figure 5.43: The development of the streamline patterns for the case of Re=100, Gr= 20000, Ar = 0.5, $\lambda = 30°$, $\beta = 0.5$ and $S = \pi/4$ during one complete cycle : (a) t = 32; (b) t = 33; (c) t = 34; (d) t = 36; (e) t = 38; (f) t = 40. The streamlines plotted are ψ = 2.0, 1.5, 1.0, 0.75, 0.5, 0.4, 0.3, 0.2, 0.15, 0.1, 0.08, 0.06, 0.04, 0.02, 0.0, -0.02, -0.04, -0.06, -0.08, -0.1, -0.15, -0.2, -0.3, -0.4, -0.5, -0.75, -1.0, -1.5, -2.0 .

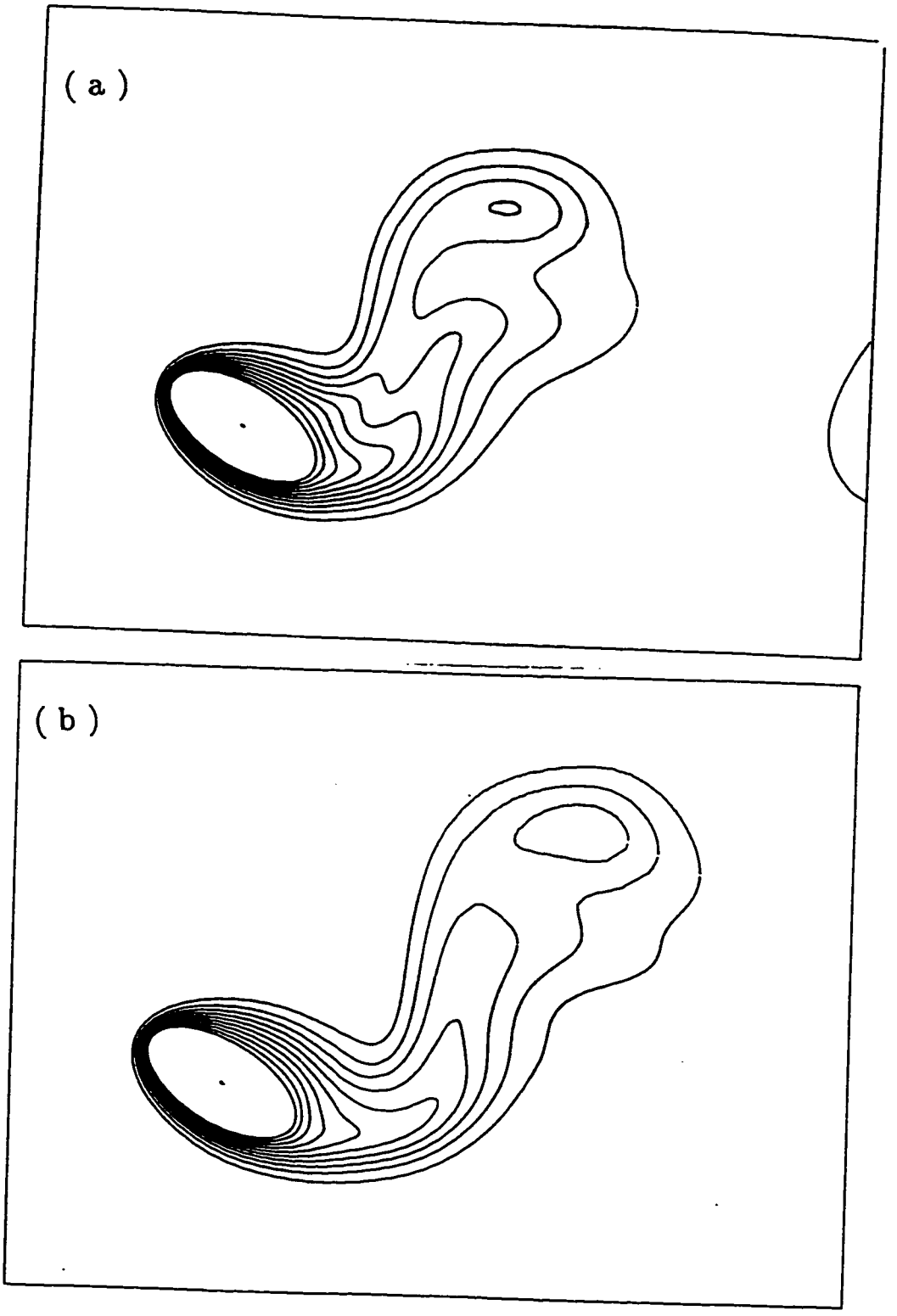
(a)
(b)

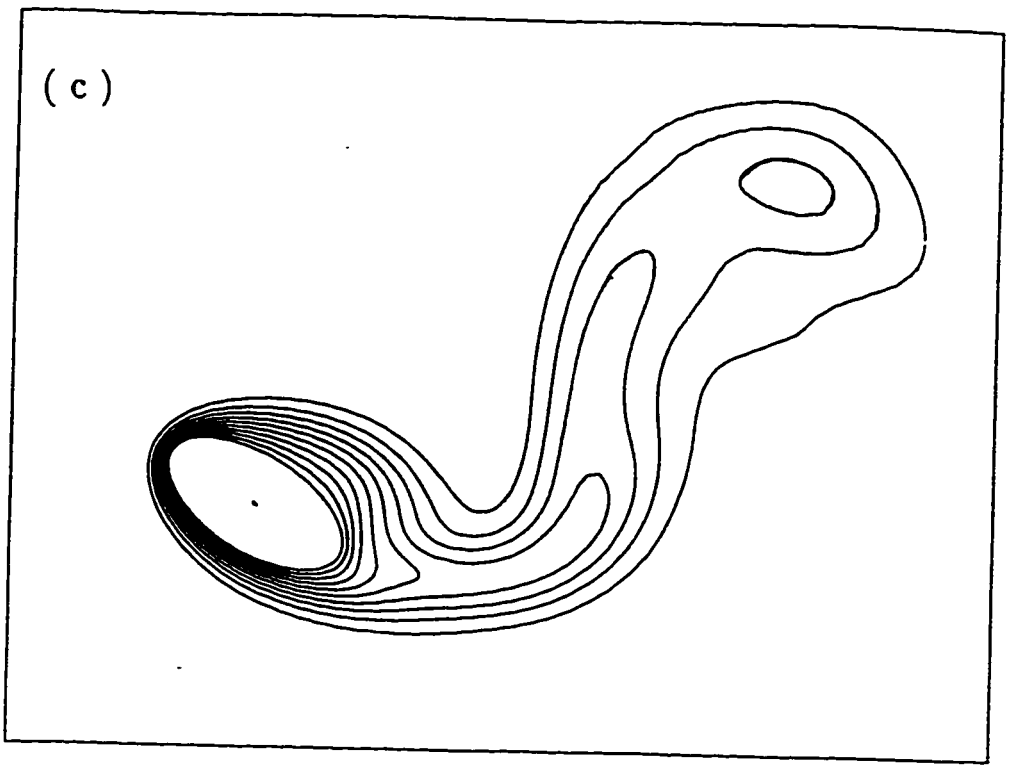
(c)

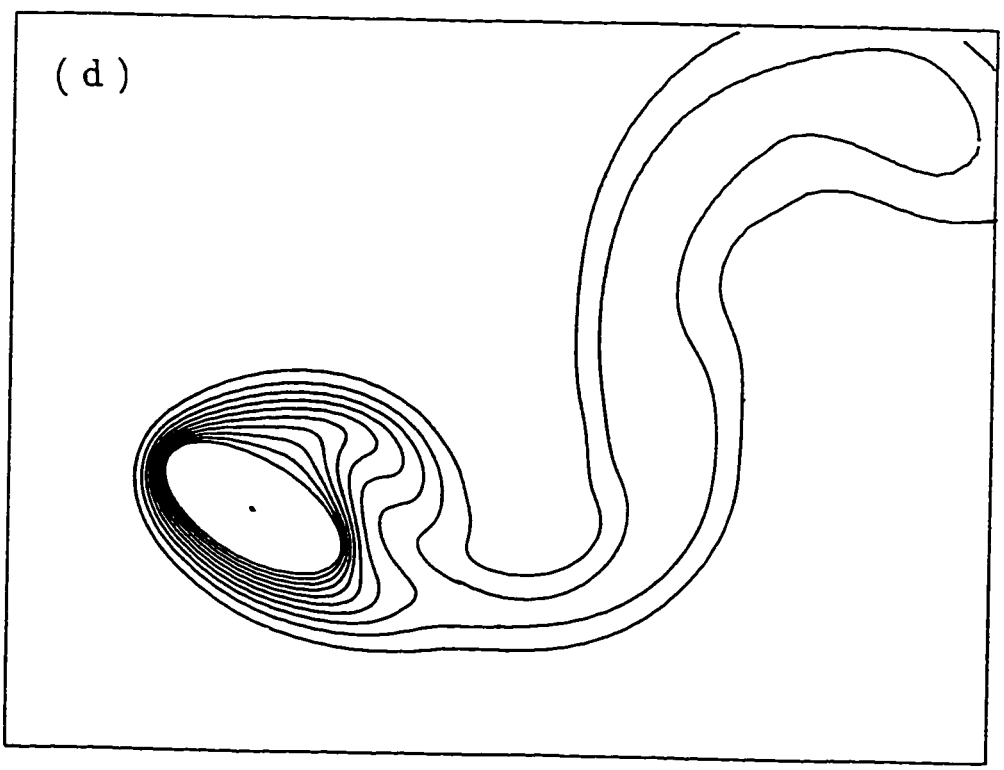
(d)

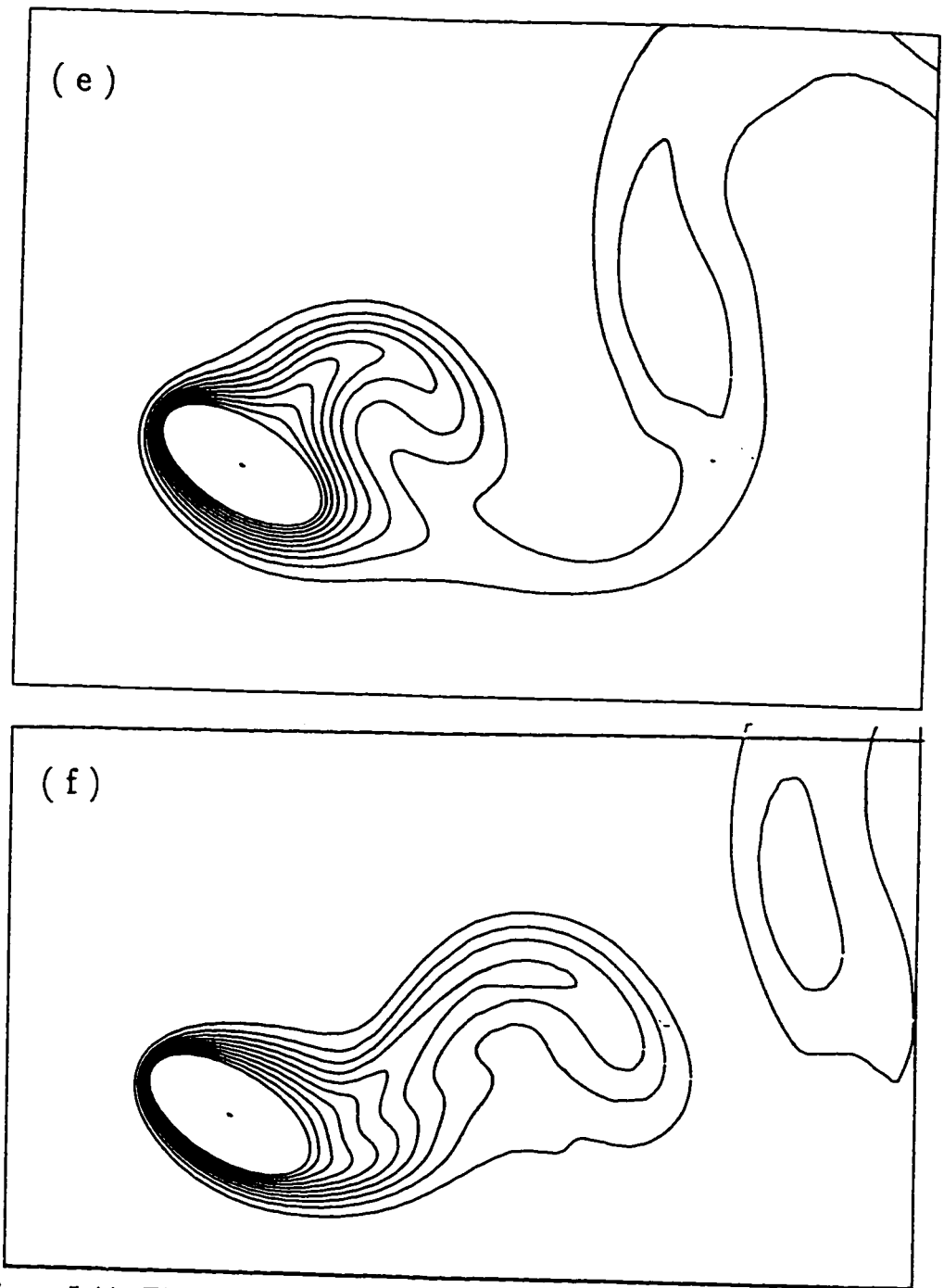

Figure 5.44: Time Development of the isotherm contours for the case of Re=100, Gr= 20000, Ar = 0.5, $\lambda = 30°$, $\beta = 0.5$ and $S = \pi/4$ during one complete cycle : (a) t = 32; (b) t = 33; (c) t = 34; (d) t = 36; (e) t = 38; (f) t = 40. The isotherms plotted are $\phi = 0.1(0.1)1.0$.

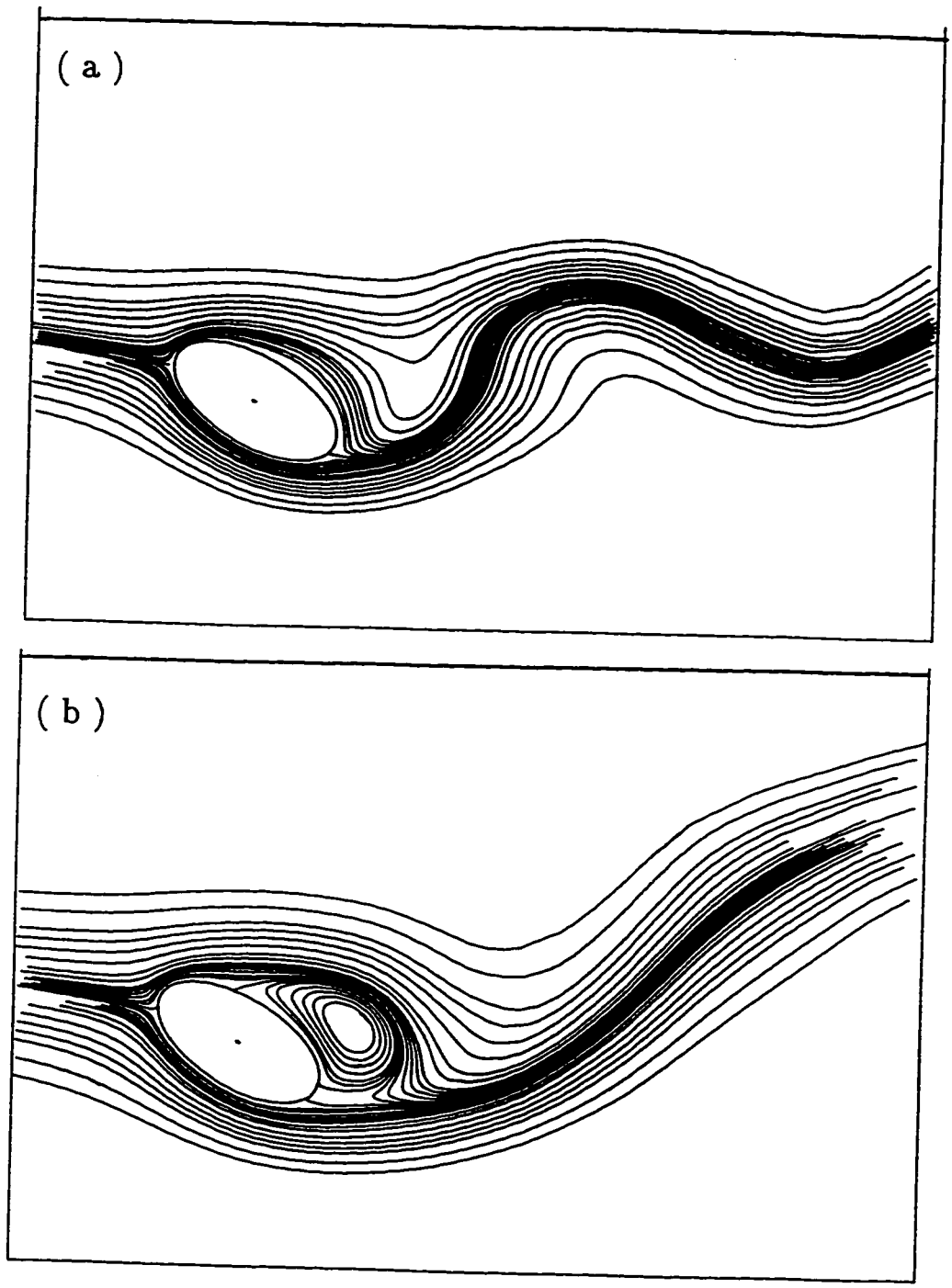
(a)
(b)

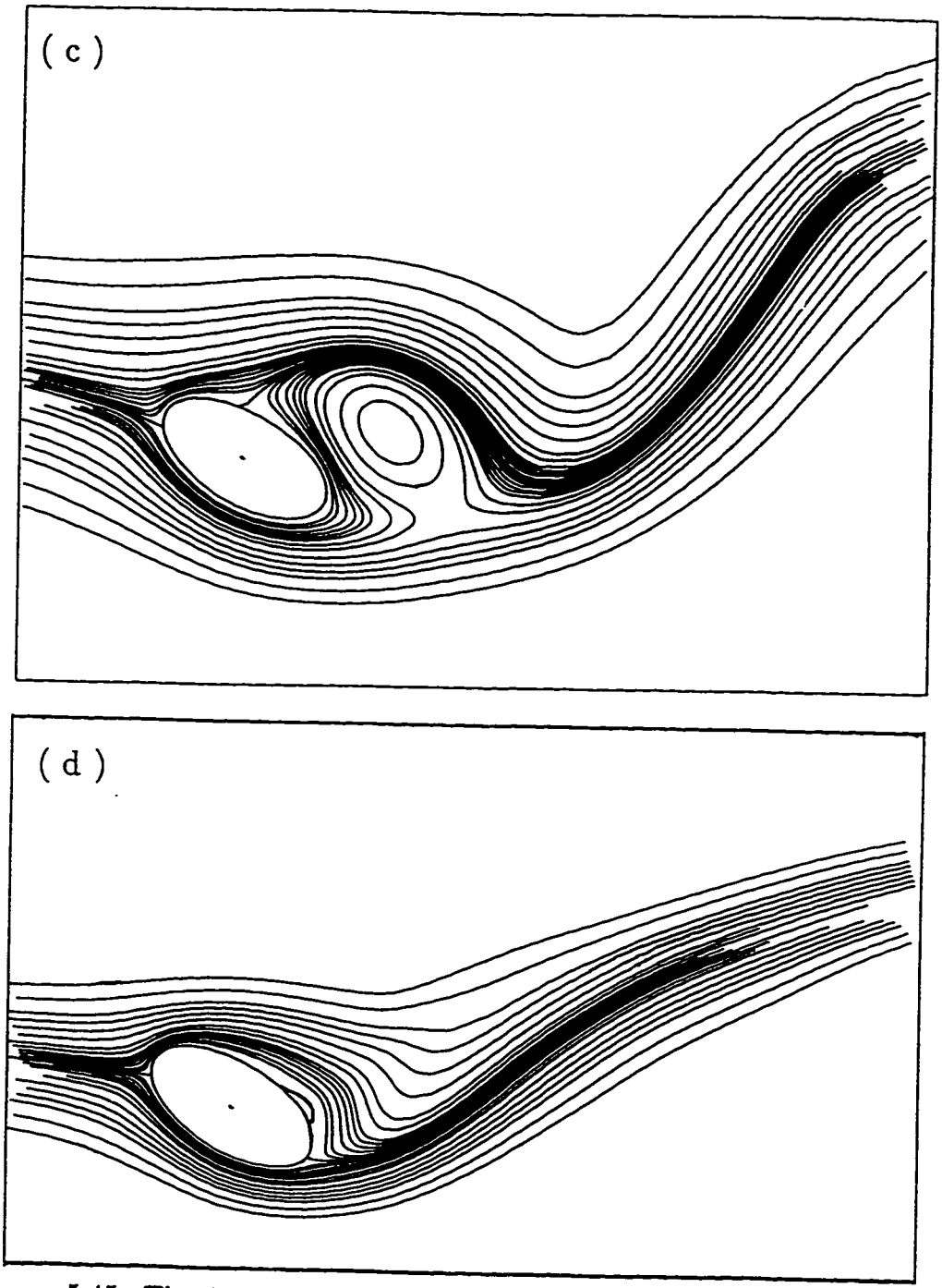

Figure 5.45: The development of the streamline patterns for the case of Re=100, Gr= 20000, Ar = 0.5, $\lambda = 30°$, $\beta = 0.25$ and $S = \pi/4$ during one complete cycle : (a) t = 32; (b) t = 34; (c) t = 36; (d) t = 40.

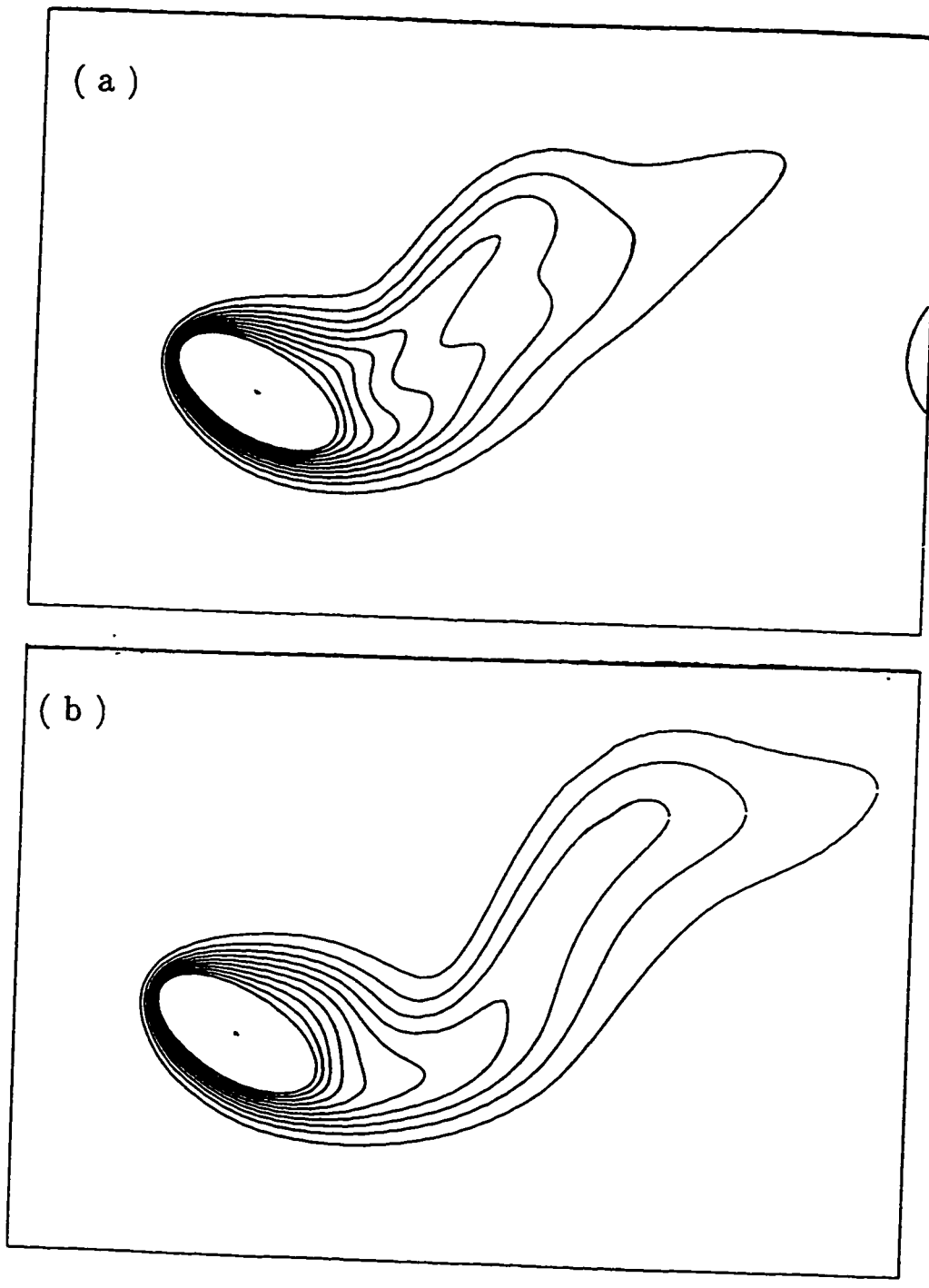
(a)
(b)

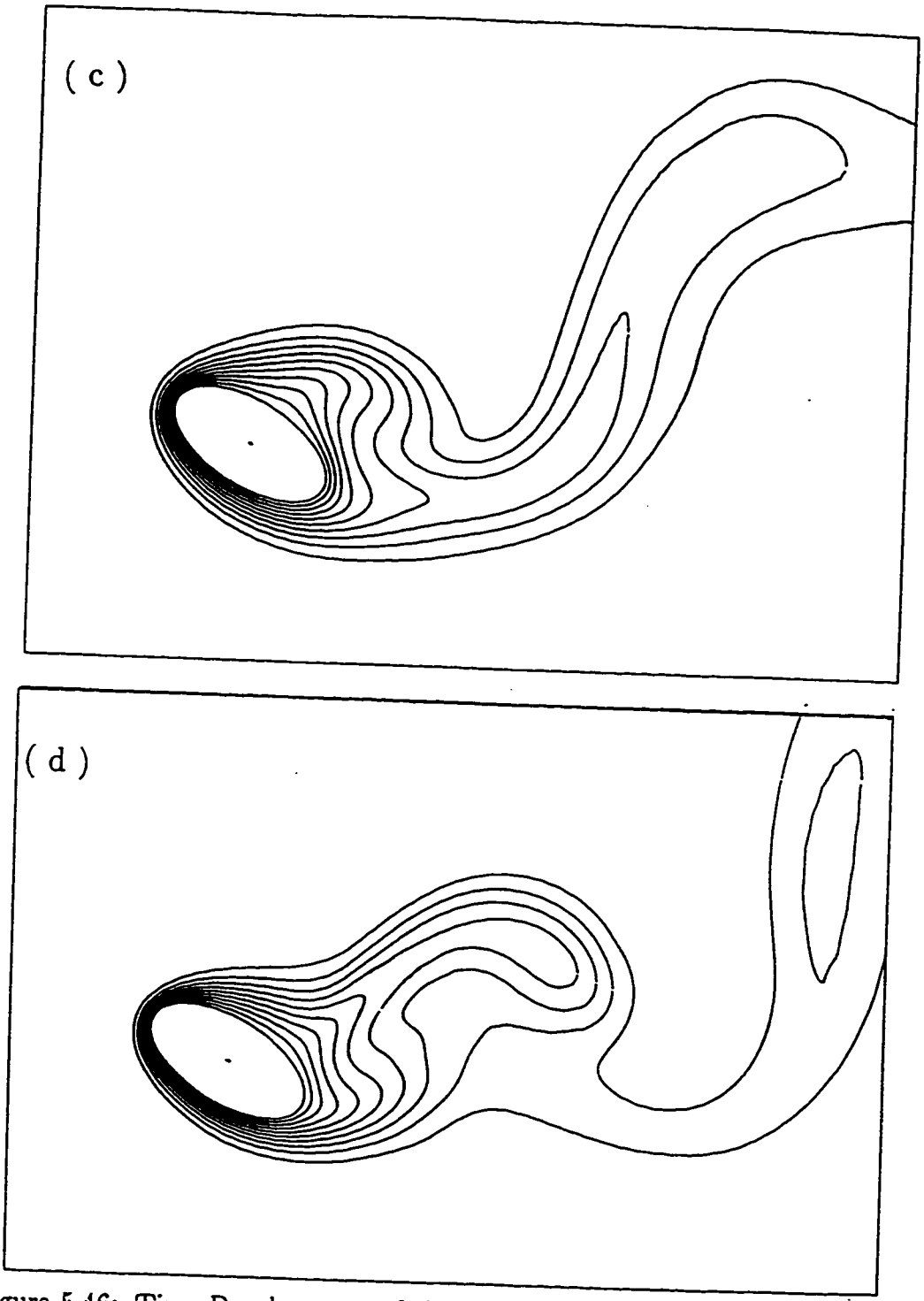

Figure 5.46: Time Development of the isotherm contours for the case of Re=100, Gr= 20000, Ar = 0.5, $\lambda = 30°$, $\beta = 0.25$ and $S = \pi/4$ during one complete cycle : (a) t = 32; (b) t = 34; (c) t = 36; (d) t = 40.

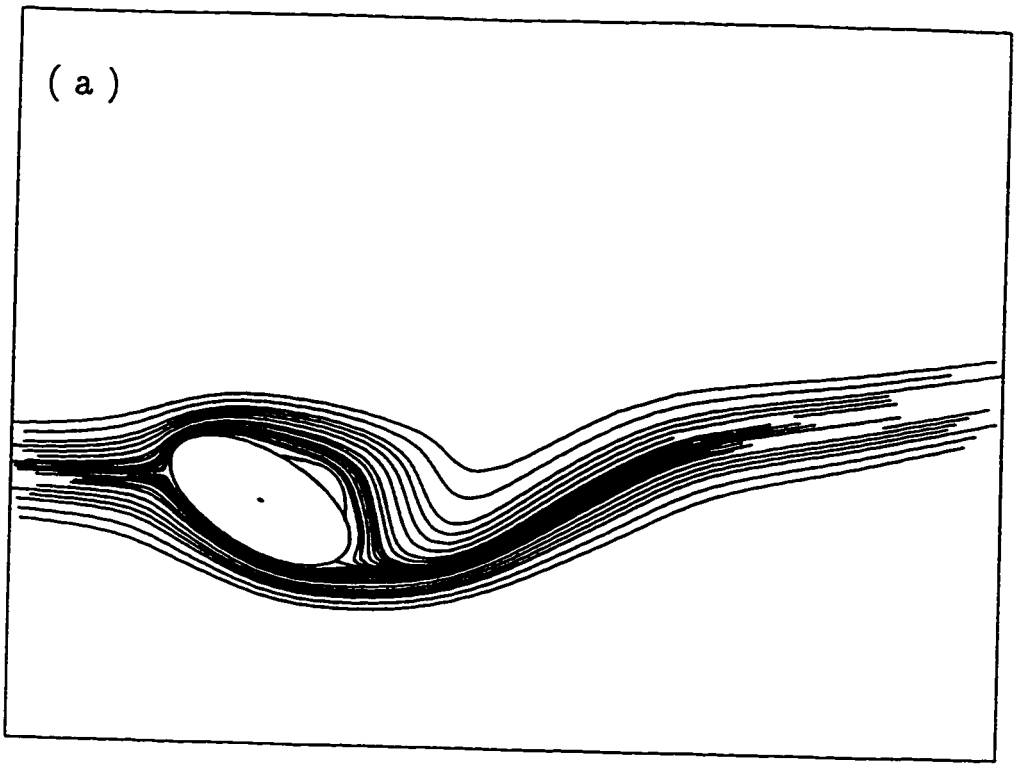
(a)

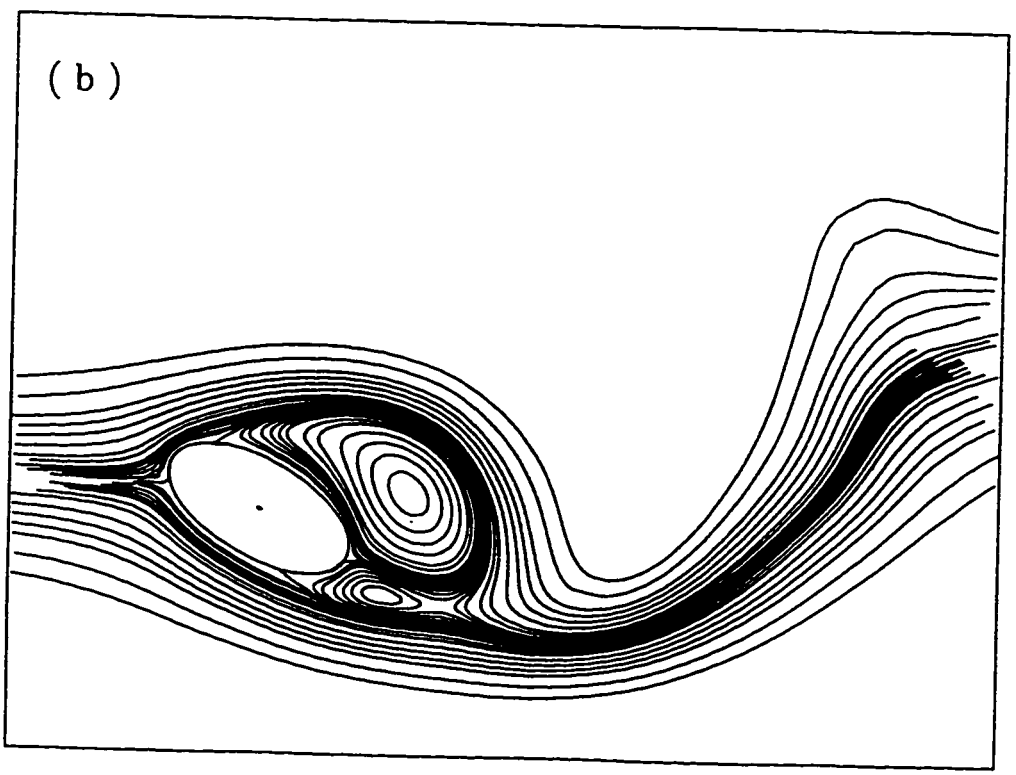
(b)

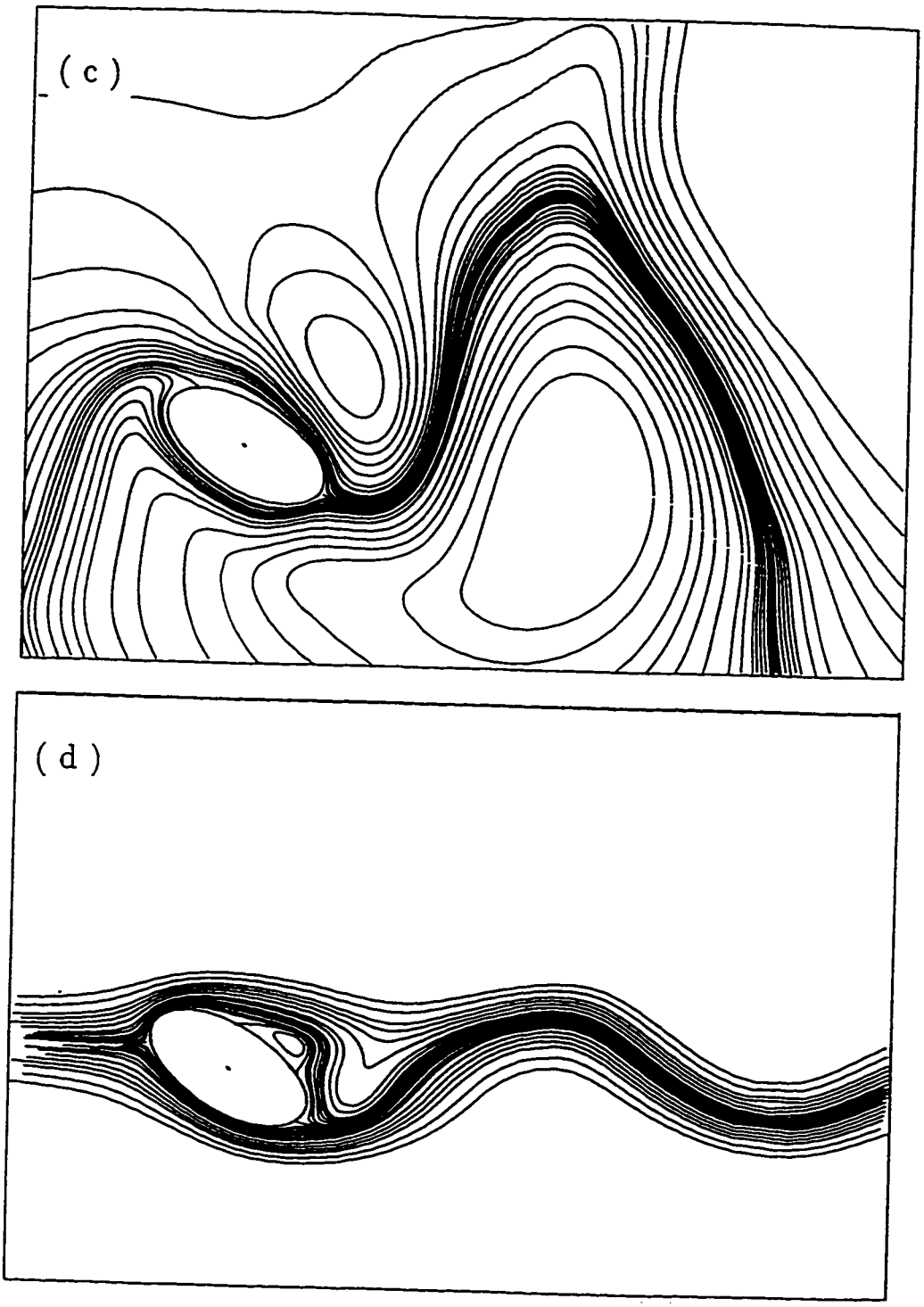

Figure 5.47: The development of the streamline patterns for the case of Re=100, Gr= 20000, Ar = 0.5, $\lambda = 30^o$, $\beta = 1.0$ and $S = \pi/4$ during one complete cycle : (a) t = 32; (b) t = 34; (c) t = 36; (d) t =40.

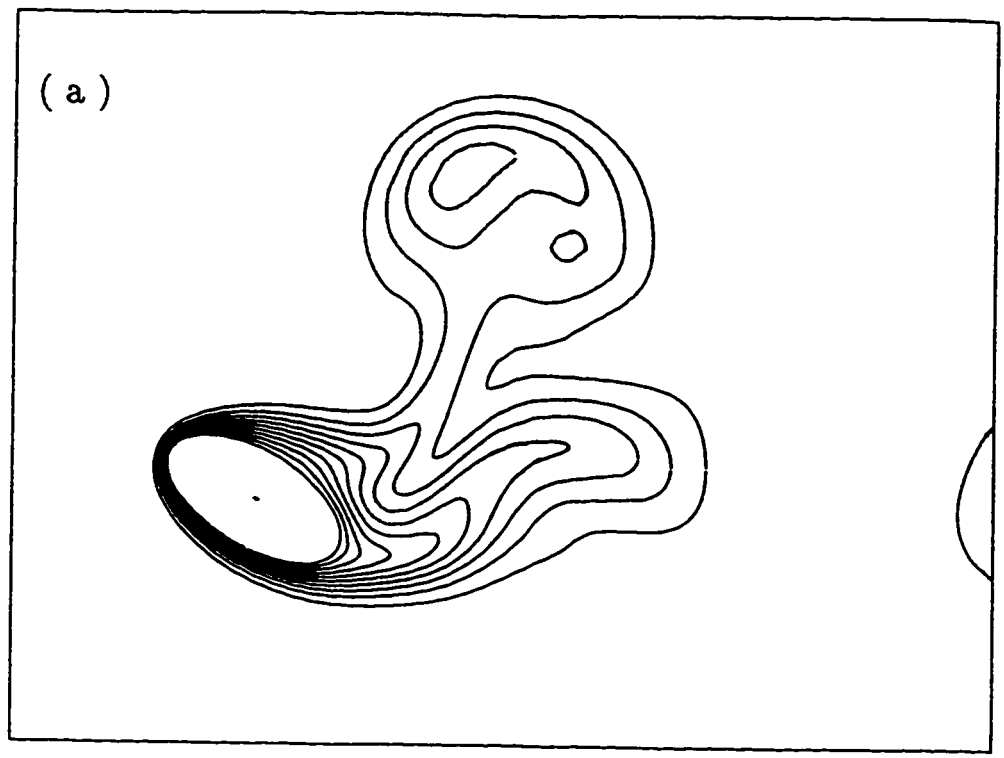
(a)

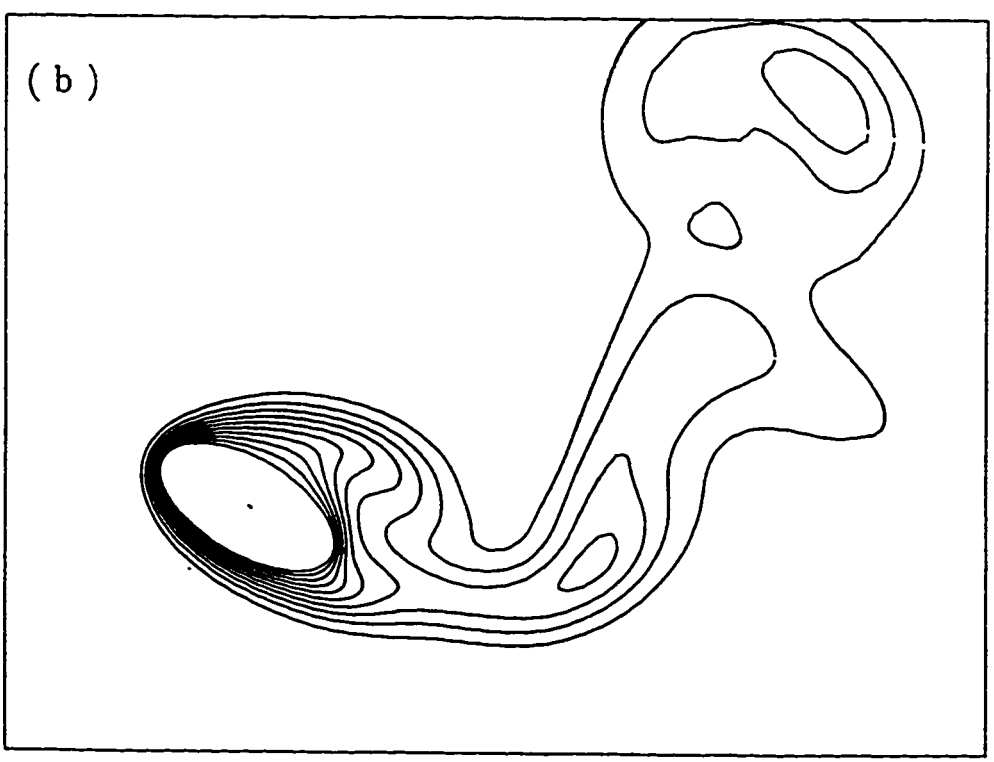
(b)

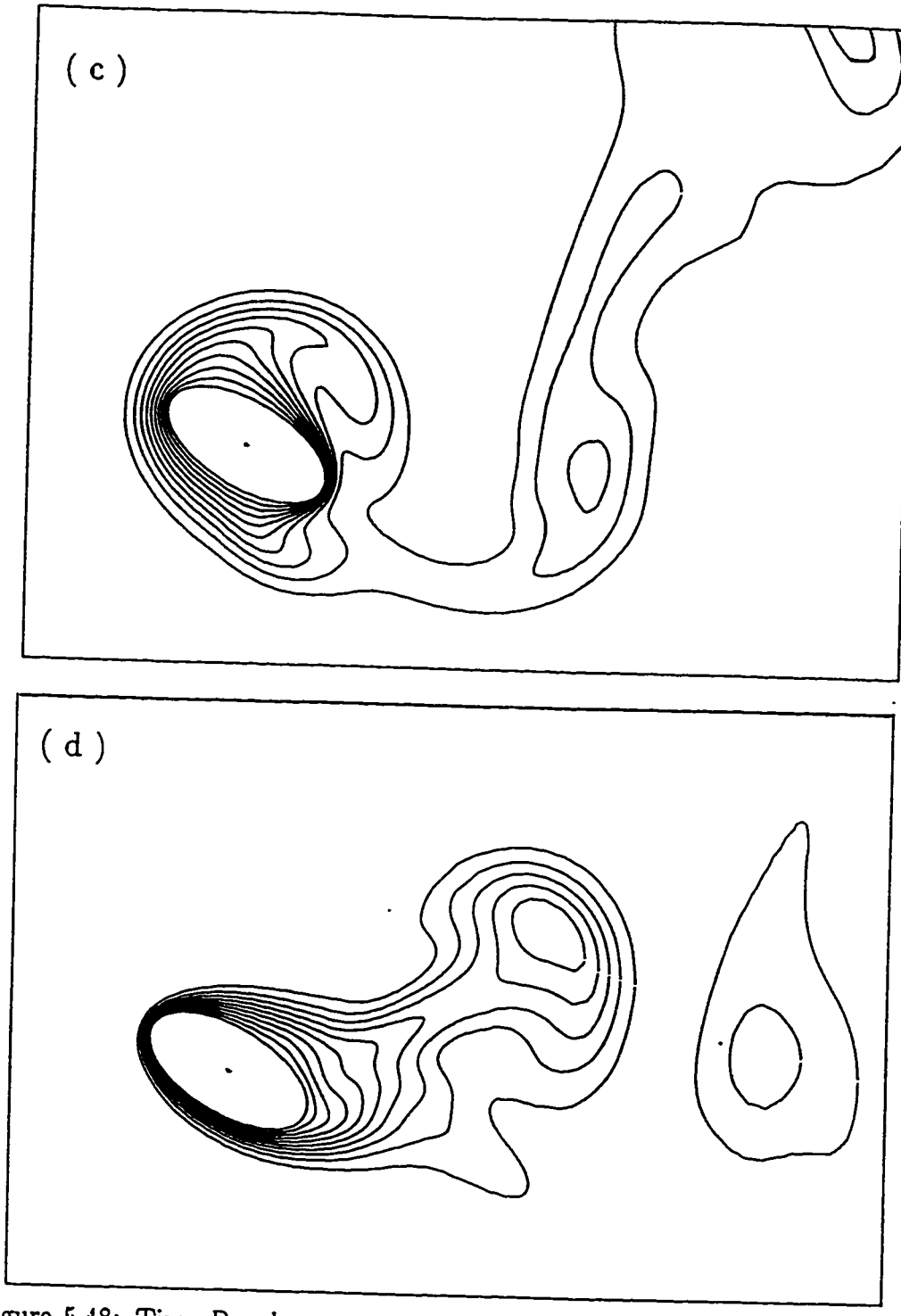

Figure 5.48: Time Development of the isotherm contours for the case of Re=100, Gr= 20000, Ar = 0.5, $\lambda = 30^{o}$ $\beta = 1.0$ and $S = \pi/4$ during one complete cycle : (a) t = 32; (b) t = 34; (c) t = 36; (d) t = 40.

5.4 The Effect of Strouhal Number

The effect of Strouhal number on the flow and thermal fields, average and local Nusselt numbers and pressure and vorticity distribution is studied. The study will consider values of S ranging from S = $\pi/4$ to 2π.

5.4.1 The Effect of Strouhal Number on the Average Nusselt Number

Table 5.4 gives the values of $\overline{\overline{Nu}}$ for the fluctuating and steady free stream cases. In comparison with the steady stream case, the low Strouhal number fluctuations (S = $\pi/4$, $\pi/3$, $\pi/2$) resulted in an increase in $\overline{\overline{Nu}}$, however, further increase of S tends to decrease $\overline{\overline{Nu}}$ to values below that of the flow with no fluctuations. It is important to mention here that with higher values of S, the quasi-steady state is reached faster.

Figure 5.49 shows the time variation of the average Nusselt number $\overline{Nu}$ following the sudden temperature rise of the tube surface temperature for different Strouhal numbers when $\beta = 0.5$. The figure shows that $\overline{Nu}$ has its maximum value at t=0. This value, then, decreases with an increase in time until reaching a quasi-steady values. The figure shows $\overline{Nu}$ variation for S = $\pi/3$, $\pi/2$, π together with the steady stream Nusselt number. It is important to notice that the amplitude of $\overline{Nu}$ fluctuations gets less when the frequency of the free stream fluctuations increases.

Figures 5.50 to 5.52 show the time variation of $\overline{Nu}$ together with a comparison between its time-average and the steady stream case. Figure 5.50 shows an increase in the heat transfer rate due to the free stream fluctuations for low Strouhal number values (S=$\pi/3$). However, Figures 5.51 and 5.52 show that $\overline{\overline{Nu}}$ decreases below the steady values as Strouhal number gets higher.

Table 5.4: The effect of Strouhal number on the time-averge Nusselt number.

Code #	Re	Gr	λ	Ar	S	β	$\overline{\overline{Nu}}$	$\overline{Nu}$ ($\beta = 0$)	% Increase
B-1	100	20000	30°	0.5	$\frac{\pi}{4}$	0.25	6.41	6.23	2.83 %
B-2	100	20000	30°	0.5	$\frac{\pi}{4}$	0.50	6.57	6.23	5.58 %
B-3	100	20000	30°	0.5	$\frac{\pi}{3}$	0.25	6.42	6.23	2.16 %
B-4	100	20000	30°	0.5	$\frac{\pi}{3}$	0.50	6.42	6.23	3.24 %
B-5	100	20000	30°	0.5	$\frac{\pi}{2}$	0.25	6.01	6.23	2.01 %
B-6	100	20000	30°	0.5	$\frac{\pi}{2}$	0.50	6.43	6.23	3.10 %
B-7	100	20000	30°	0.5	π	0.25	6.15	6.23	−1.03%
B-8	100	20000	30°	0.5	π	0.5	5.12	6.23	−1.7 %
B-9	100	20000	30°	0.5	2π	0.25	6.09	6.23	−2.2 %
B-10	100	20000	30°	0.5	2π	0.50	6.04	6.23	−3.03 %

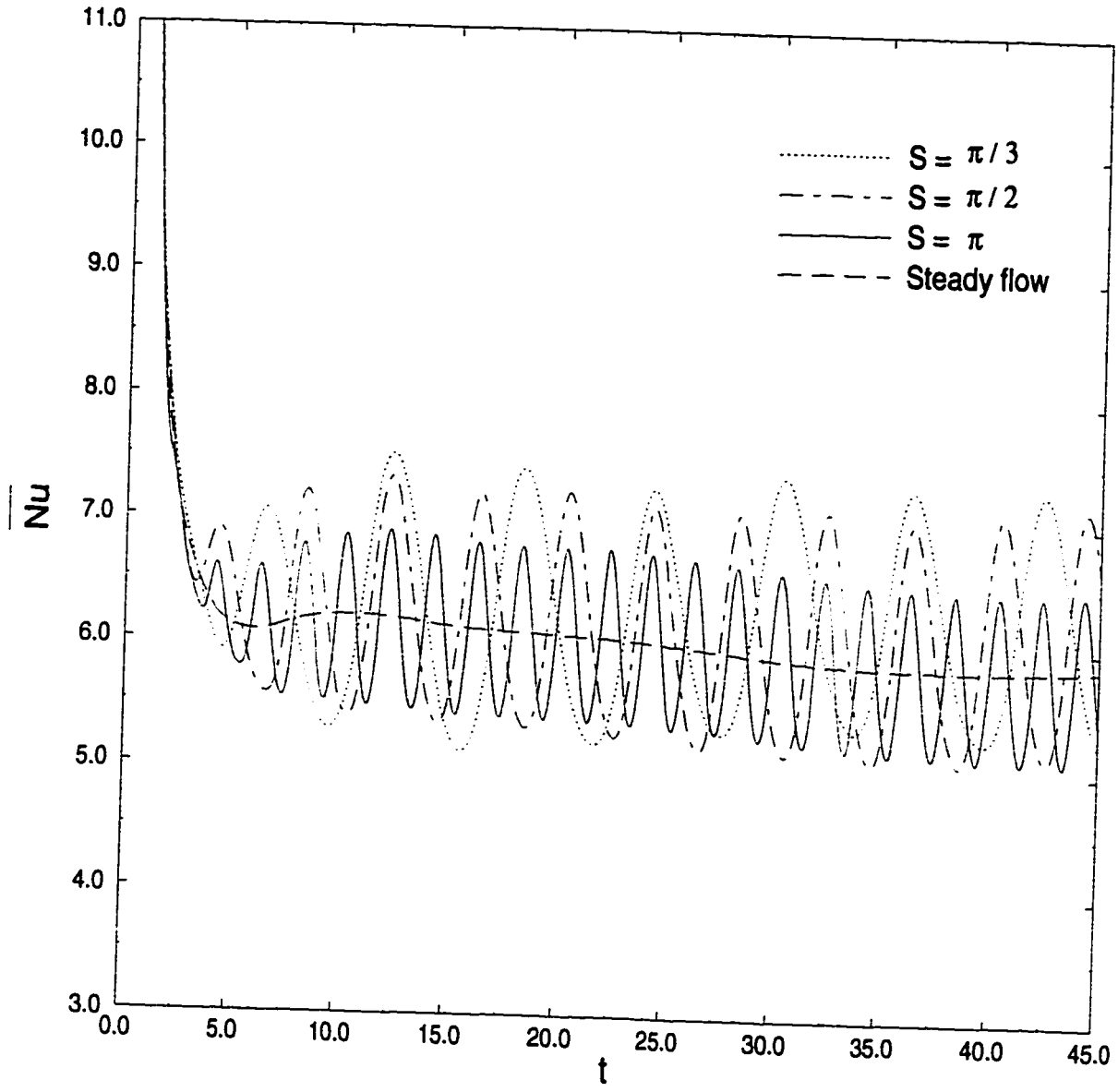

Figure 5.49: The time variation of $\overline{Nu}$ following the sudden temperature rise for various Strouhal numbers in case of Re=100, Gr=20000, Ar=0.5, $\lambda = 30.0°$ and $\beta = 0.5$.

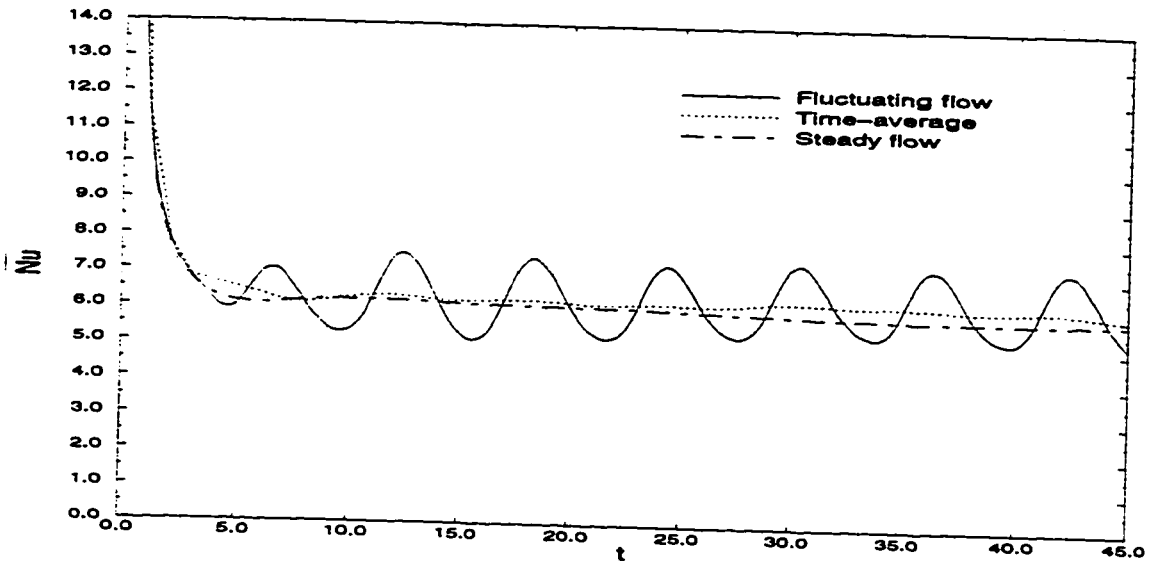

Figure 5.50: The variation of $\overline{Nu}$ for case B-4 and comparison with the case of steady free stream.

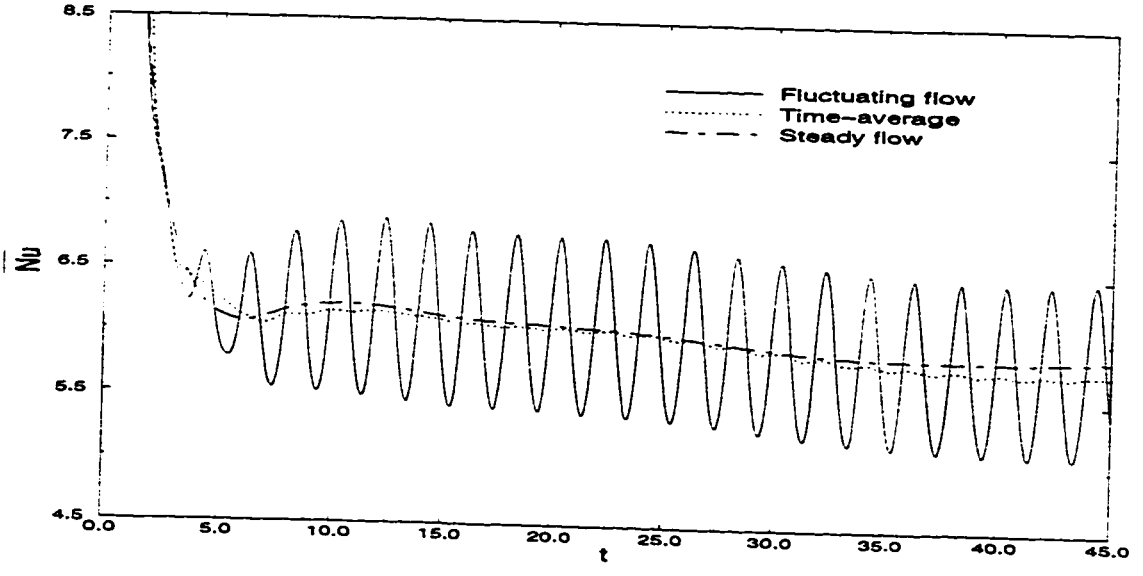

Figure 5.51: The variation of $\overline{Nu}$ for case B-8 and comparison with the case of steady free stream.

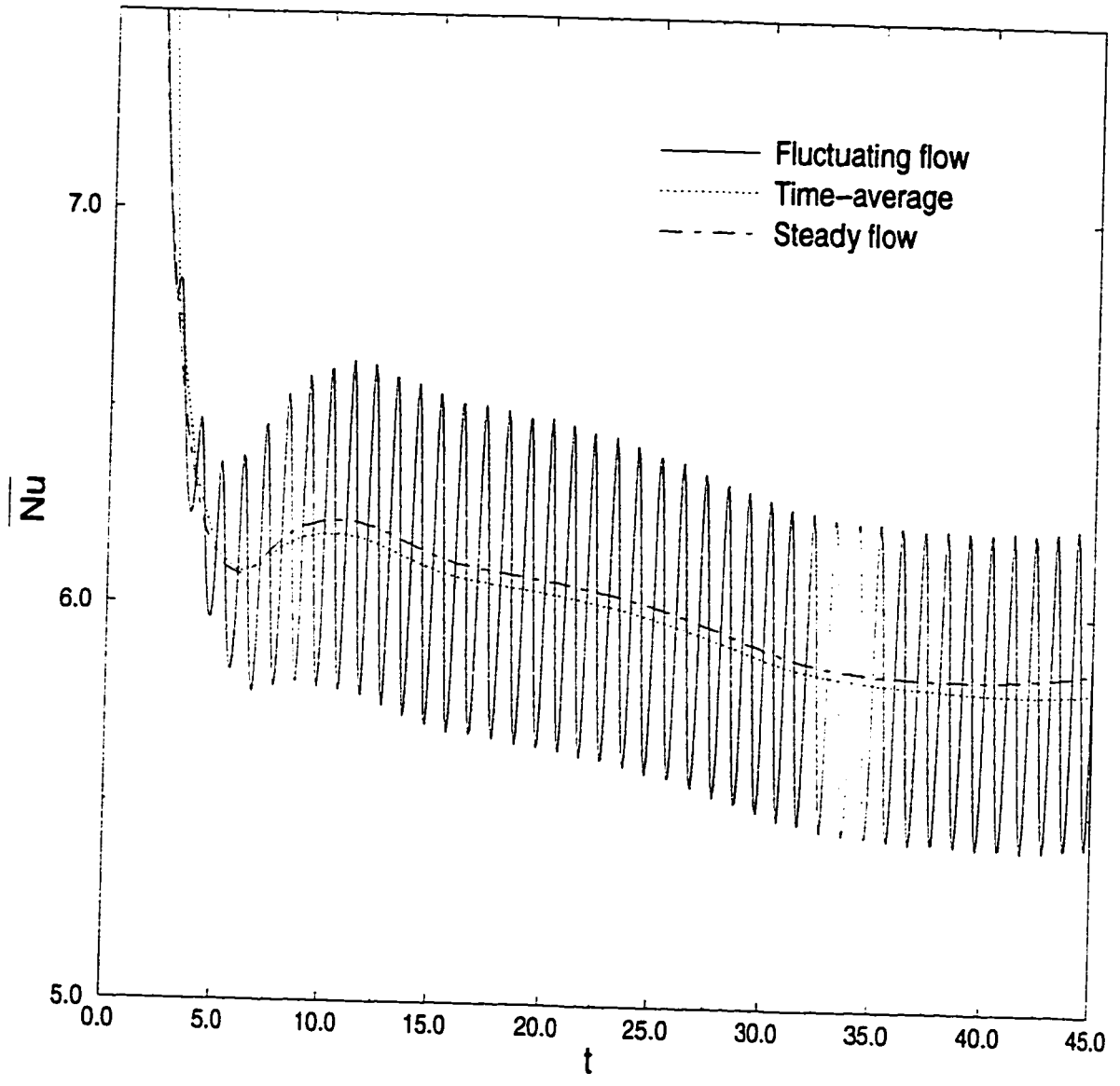

Figure 5.52: The variation of $\overline{Nu}$ for case B-10 and comparison with the case of steady free stream.

5.4.2 The Effect of Strouhal Number on the Local Nusselt Number, Pressure and Vorticity Distributions

Figures 5.53 and 5.54 show the effect of increasing Strouhal number (S) on the local Nusselt number distribution around the tube surface for cases (B-4) (B-6) and (B-8) together with the steady flow case. Figure 5.53 corresponds to maximum free stream velocity (U_{max}). In this figure Nu is higher than the steady values for the cases S = $\pi/3$ and $\pi/2$ while for S = π, the Nu values are lower than the steady values on most of the tube surface. On the other hand, Figure 5.54 shows the local Nusselt number distribution at the minimum free stream velocity (U_{min}). It is clear from the figure that Nu for the steady stream case is higher on most of the tube surface except for the rear part (η = 0° to 90°). The reason for that is the large velocity gradient caused by the vortical flow. Figures 5.55 and 5.56 show the surface vorticity distribution at maximum and minimum free stream velocities.

The local Nusselt number and the vorticity distributions during one complete cycle are presented in Figures 5.57 and 5.58 for S = π. Figure 5.57 shows the variation of Nu during the twelfth cycle (t=32 - 34). Nu is higher for higher velocities on almost all the tube surface except in the wake region (η = 0° – 90°) similar to the previous case. This behavior can be explained based on Figure 5.58 where the vorticity distribution is plotted for the same cycle. From the figure, one can see that at high free stream velocities, $|\zeta_s|$ is higher except at the rear of the tube surface

where the values of $|\zeta_s|$ are higher for lower velocities.

The pressure distribution around the tube surface is plotted for different Strouhal numbers at maximum and minimum free stream velocities as shown in Figures 5.59 and 5.60. The pressure distribution at maximum free stream velocity is not affected by Strouhal number values in the range $\eta = 100^o - 250^o$ while in the other regions a higher S values cause the absolute minimum pressure to be higher. The value of minimum pressure for $S = \pi/3$ was -3.6 while for $S = \pi$ the value was -5.4. As S increases the location of minimum pressures also shifts toward the rear end of the tube. Figure 5.60 represents the pressure distribution when the free stream velocity is minimum for different Strouhal numbers together with a comparison with the no fluctuation case.

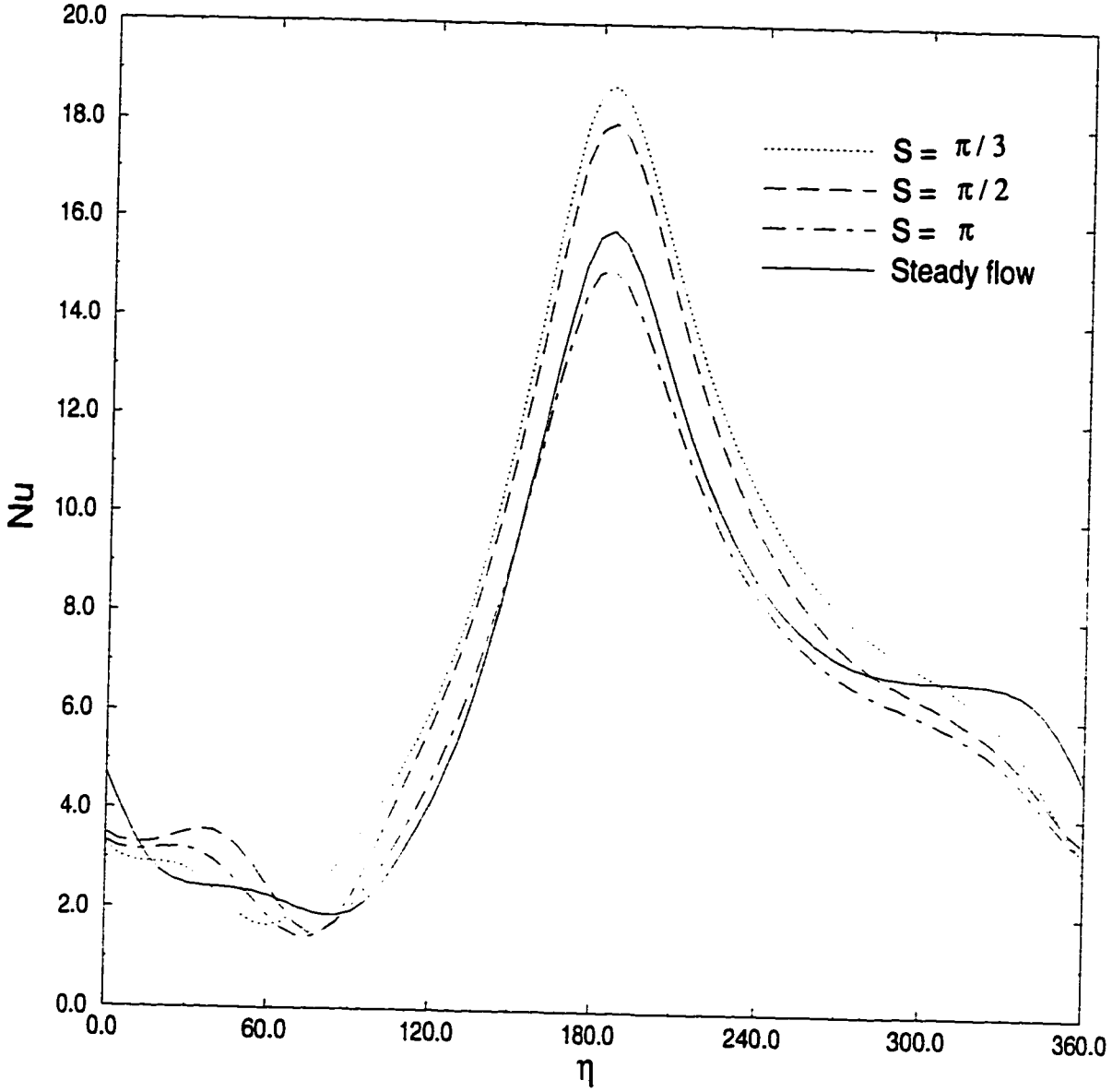

Figure 5.53: The effect of Strouhal number on the local Nusselt number distribution at maximum free stream velocity for the case of Re=100, Gr=20000, Ar=0.5, $\lambda = 30^o$ and $\beta = 0.5$.

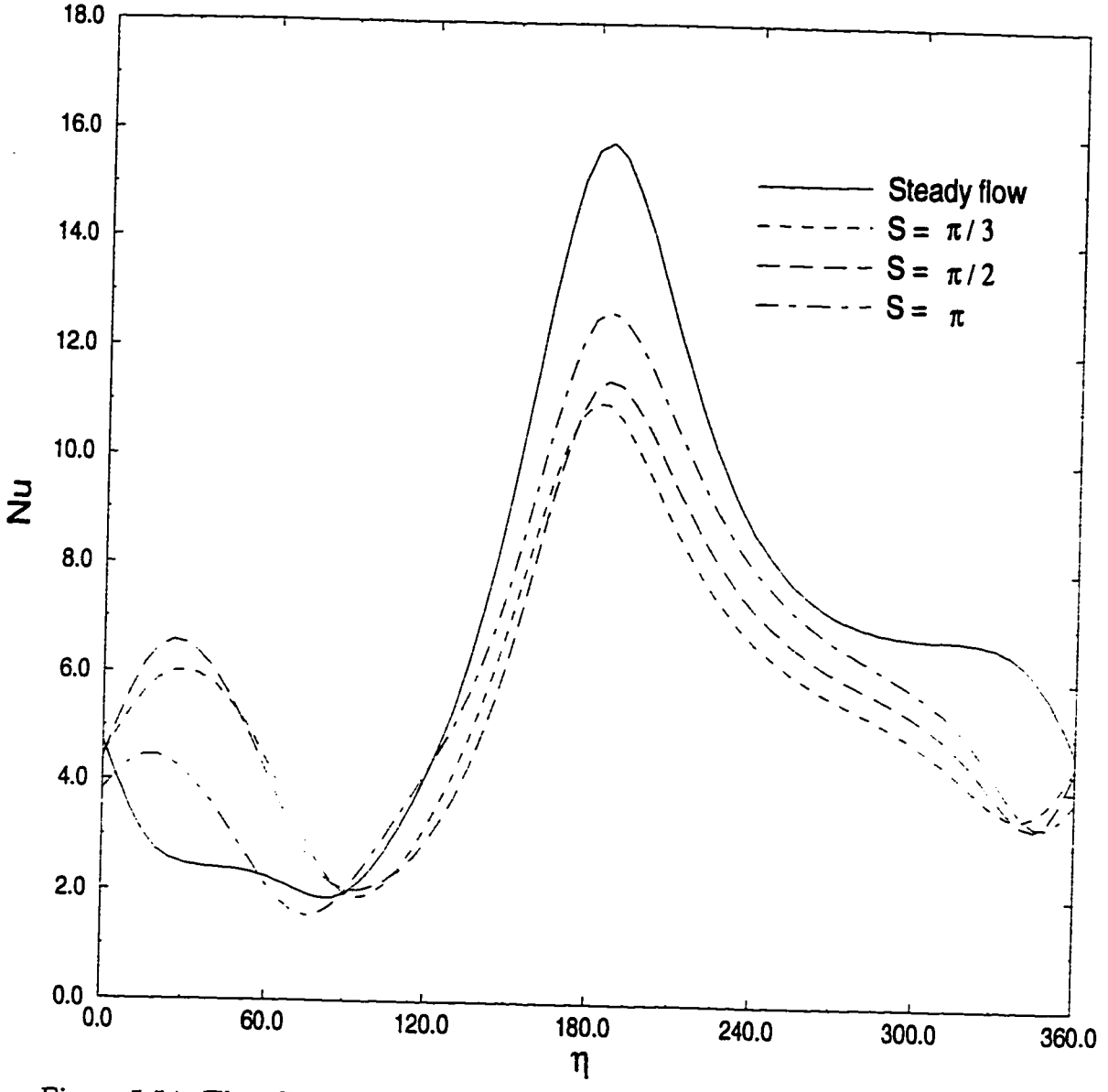

Figure 5.54: The effect of Strouhal number on the local Nusselt number distribution at minimum free stream velocity for the case of Re=100, Gr=20000, Ar=0.5, $\lambda = 30^o$ and $\beta = 0.5$.

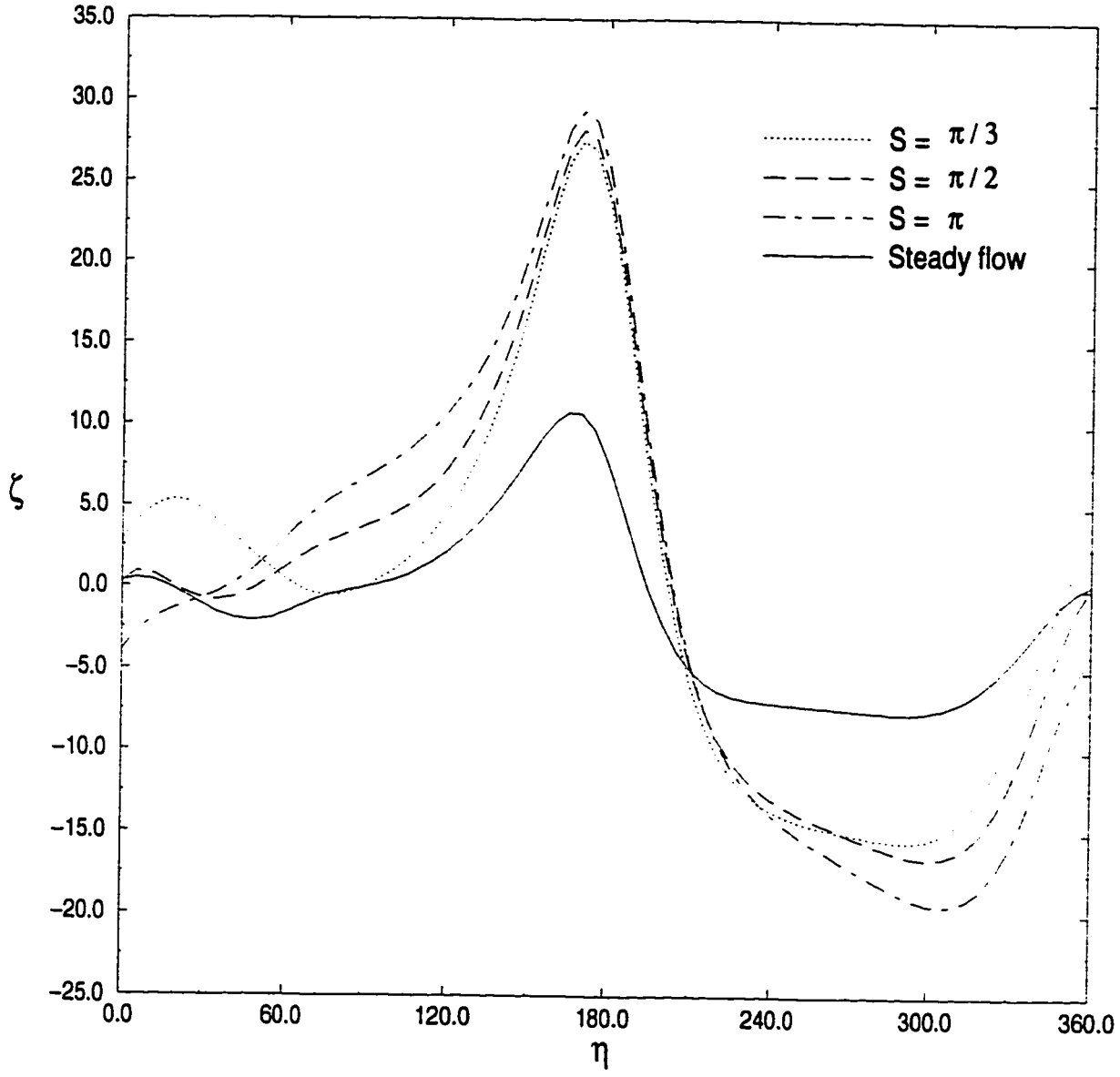

Figure 5.55: The effect of Strouhal number on the vorticity distribution at maximum free stream velocity for the case of Re=100, Gr=20000, Ar=0.5, $\lambda = 30^o$ and $\beta = 0.5$.

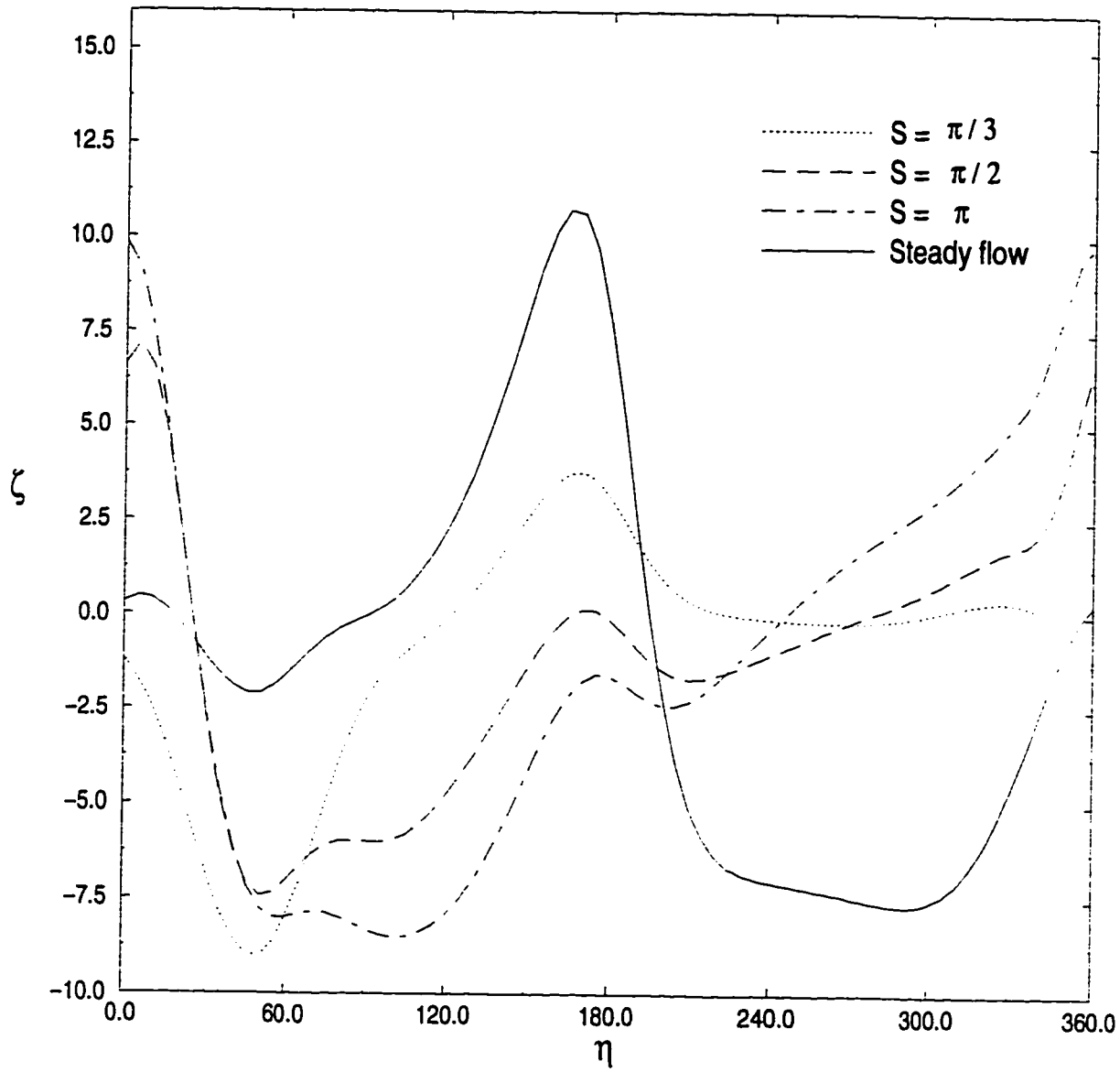

Figure 5.56: The effect of Strouhal number on the vorticity distribution at minimum free stream velocity for the case of Re=100, Gr=20000, Ar=0.5, $\lambda = 30^o$ and $\beta = 0.5$.

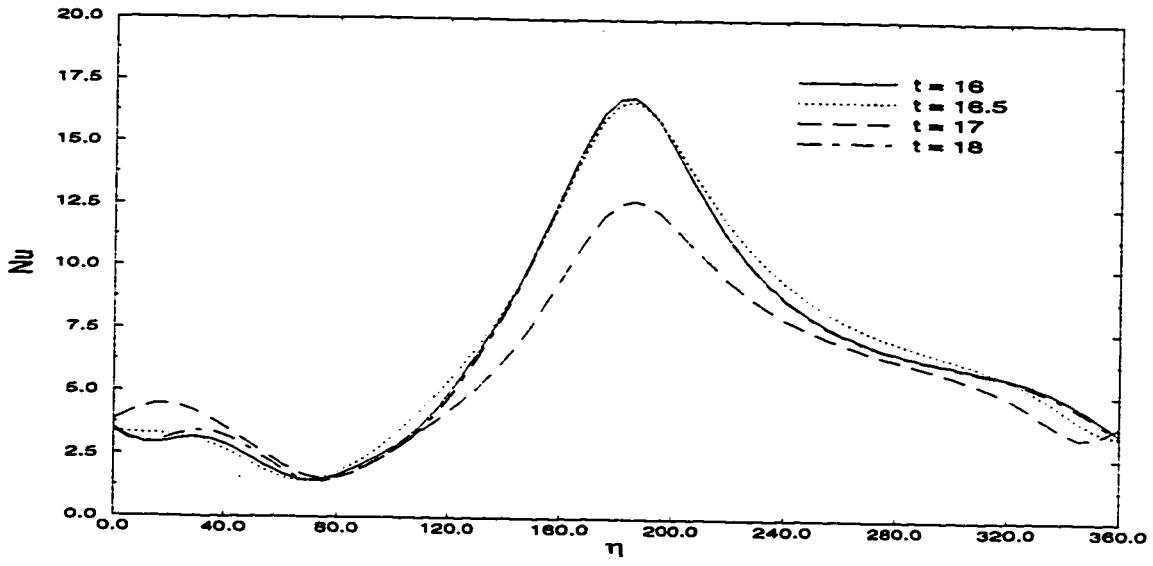

Figure 5.57: The local Nusselt number distribution at various times during one complete cycle in case B-8.

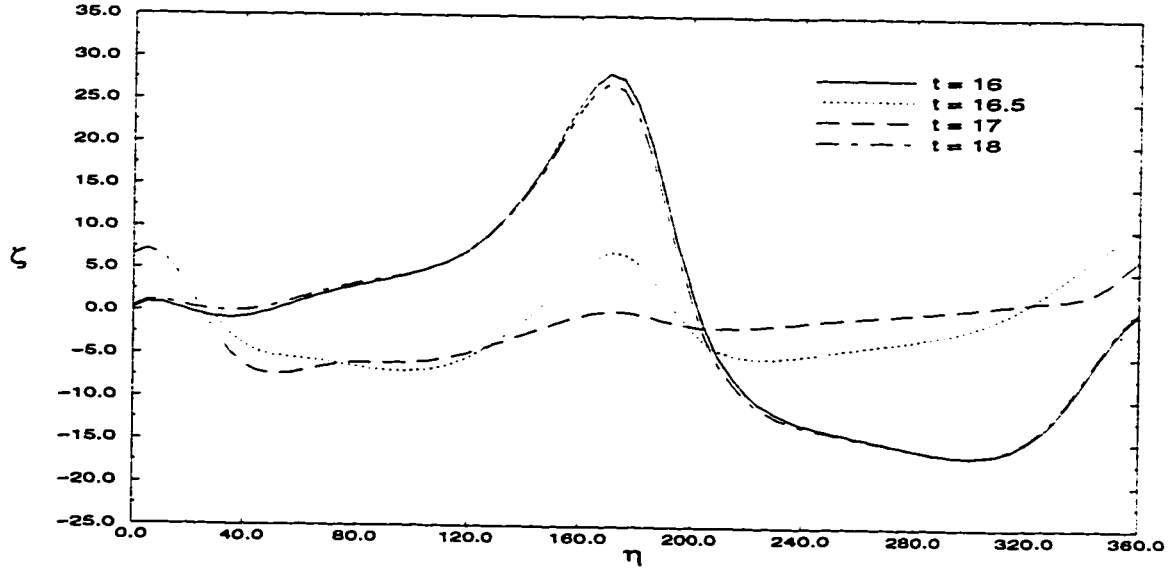

Figure 5.58: The surface vorticity distribution at various times during one complete cycle in case B-8.

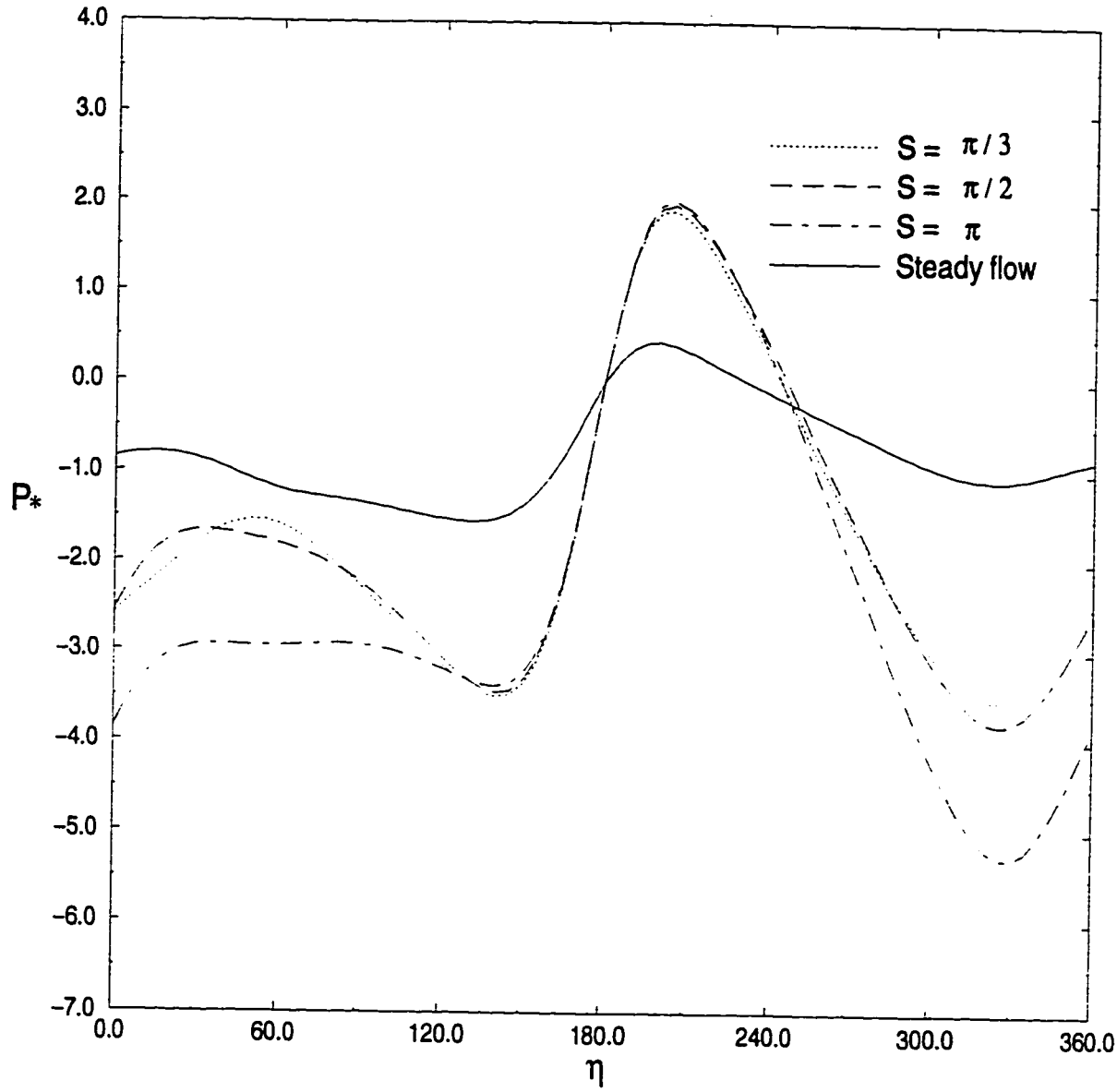

Figure 5.59: The effect of Strouhal number on the pressure distribution at maximum free stream velocity for the case of Re=100, Gr=20000, Ar=0.5, $\lambda = 30^o$ and $\beta = 0.5$.

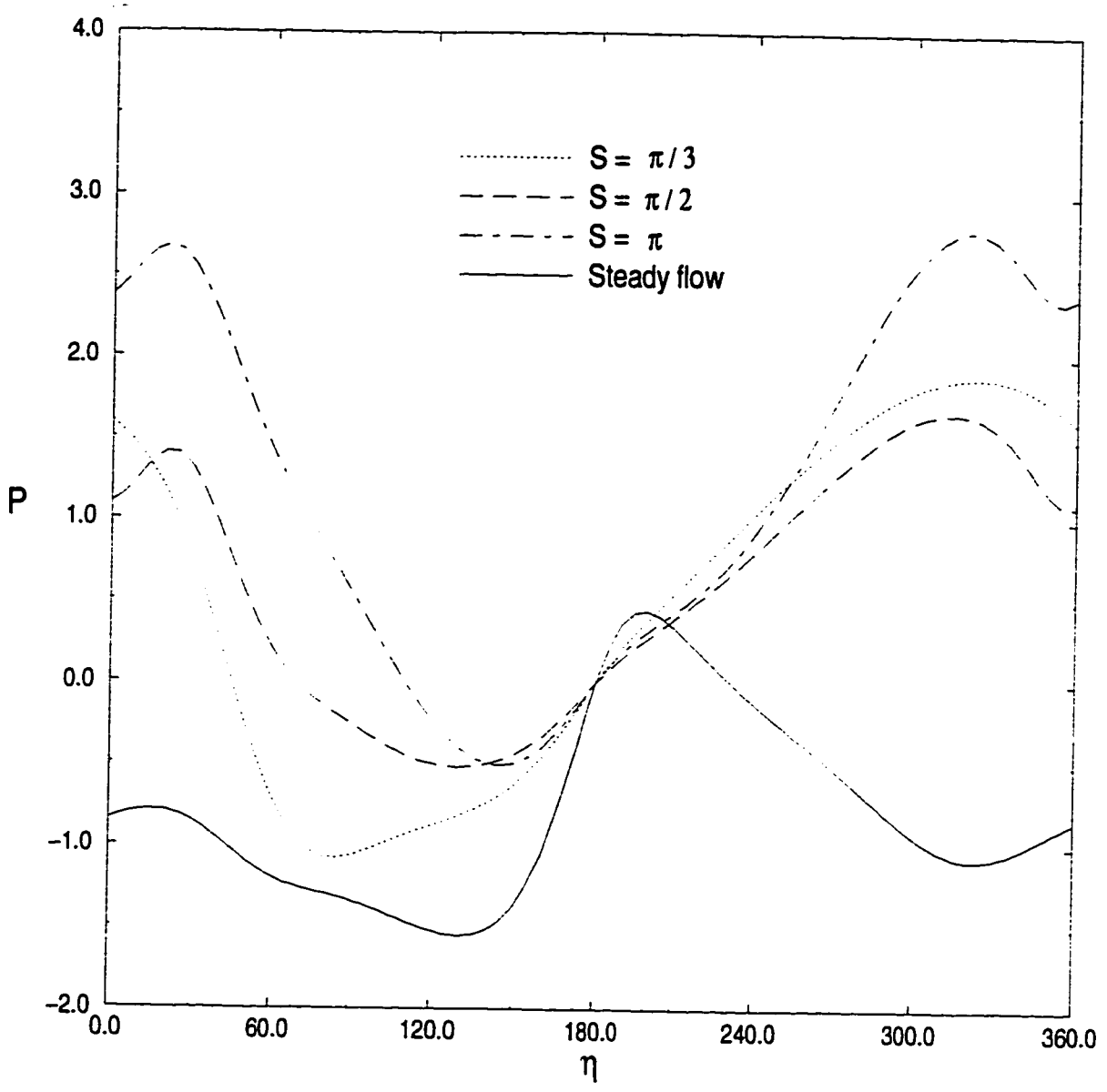

Figure 5.60: The effect of Strouhal number on the pressure distribution at minimum free stream velocity for the case of Re=100, Gr=20000, Ar=0.5. $\lambda = 30^o$ and $\beta = 0.5$.

5.4.3 The Effect of Strouhal Number on the Drag and Lift Forces

Figures 5.61 and 5.62 show the time variation of the drag and lift coefficients for different S values. The variation of C_D in Figure 5.61 is fluctuating with a frequency equal to the free stream fluctuations. Figure 5.62 shows the variation of the coefficient of the transverse forces acting on the tube surface. Similar to C_D, the frequency of C_L is the same as that of the free stream velocity. The effect of vortex shedding is causing the peaks of C_L to vary with time. Figure 5.63 shows the time variation of C_D, C_L for S $= 2\pi$ with the the steady free stream C_D and C_L. The quasi-steady state has been reached for both C_D and C_L as shown in the figure.

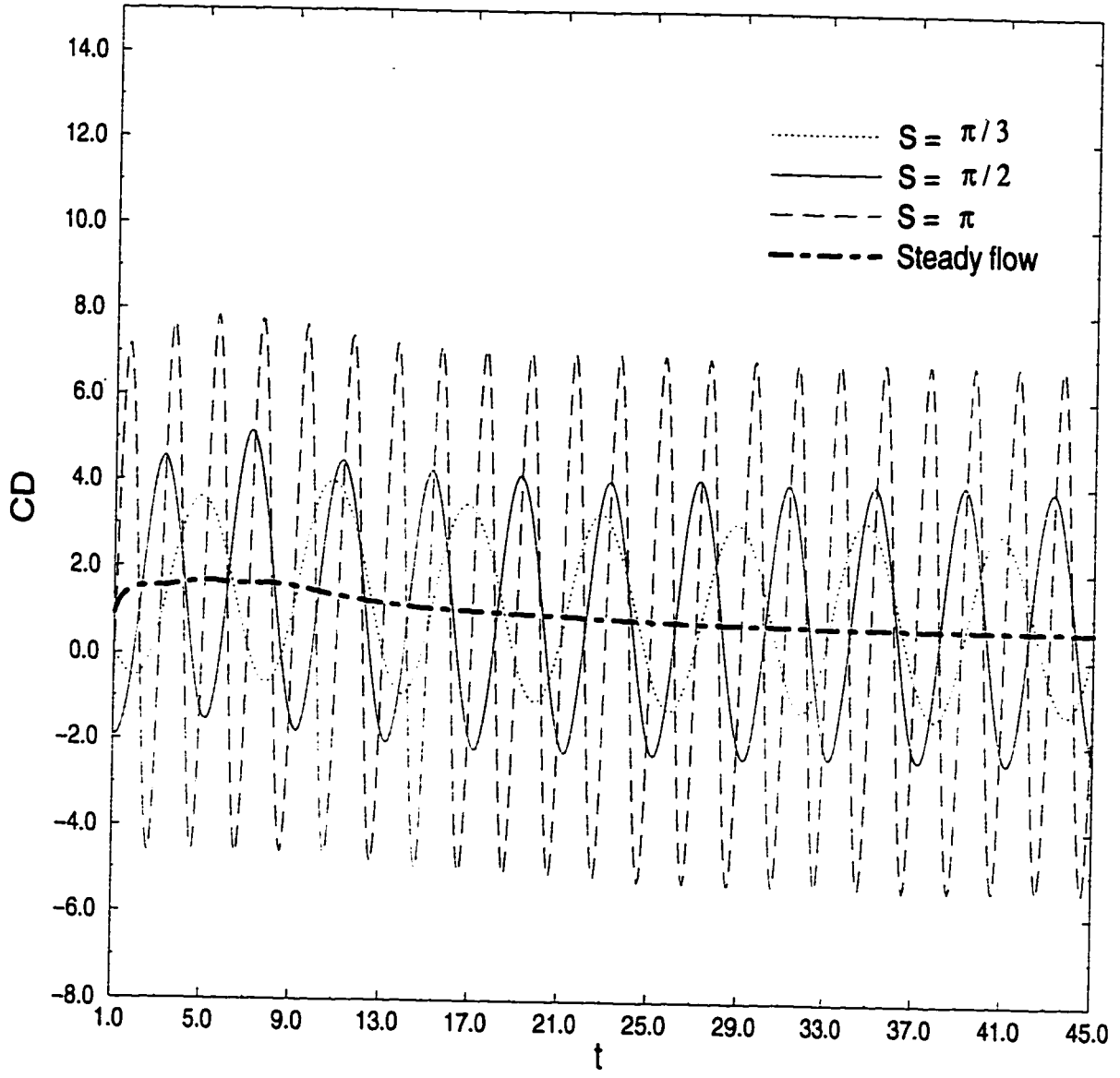

Figure 5.61: The time variation of the in-line force coefficient for various Strouhal numbers in case of Re=100, Gr=20000, Ar=0.5, $\lambda = 30.0^o$ and $\beta = 0.5$.

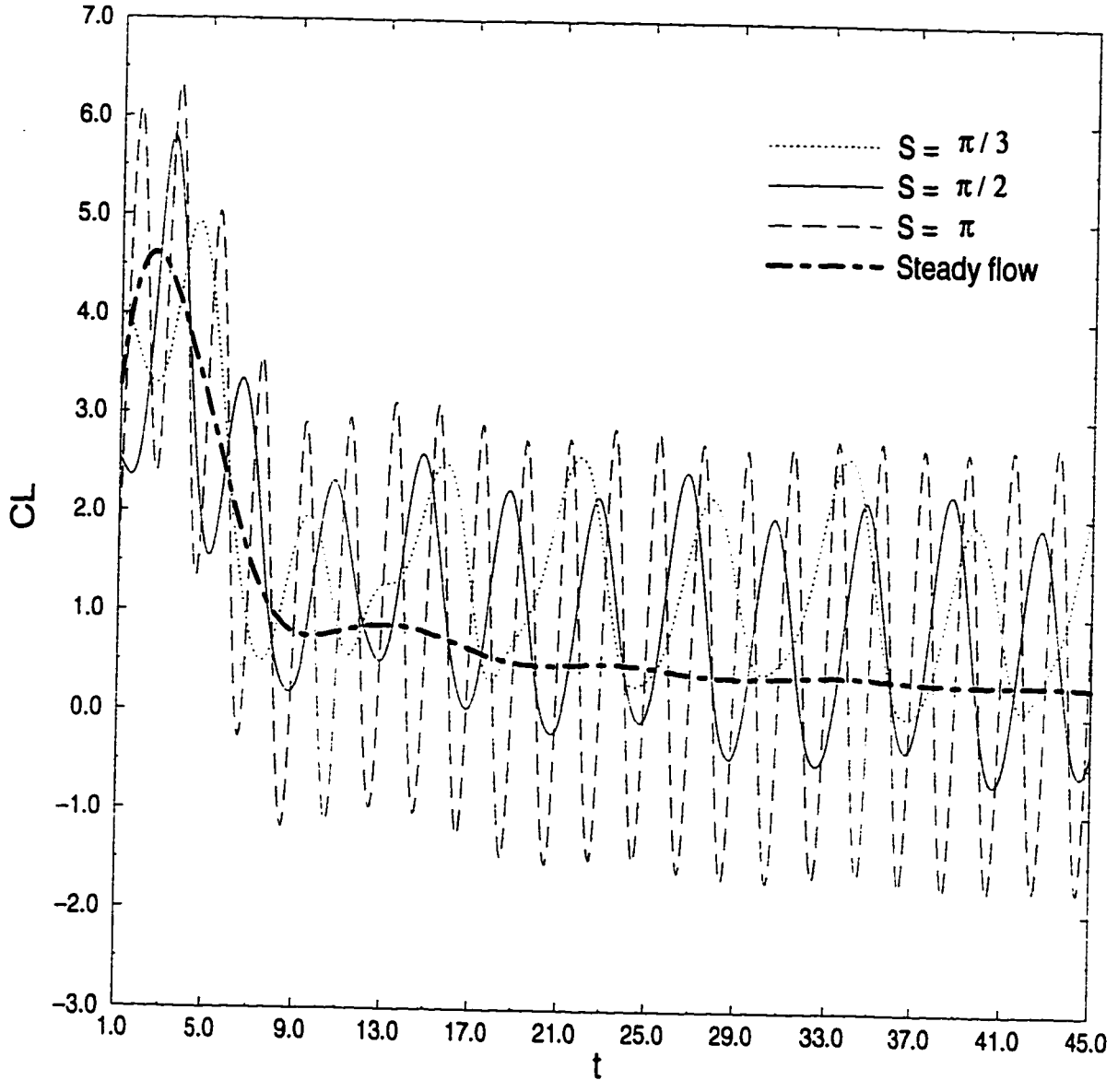

Figure 5.62: The time variation of the transverse force coefficient for various Strouhal numbers in case of Re=100, Gr=20000, Ar=0.5, $\lambda = 30.0^o$ and $\beta = 0.5$.

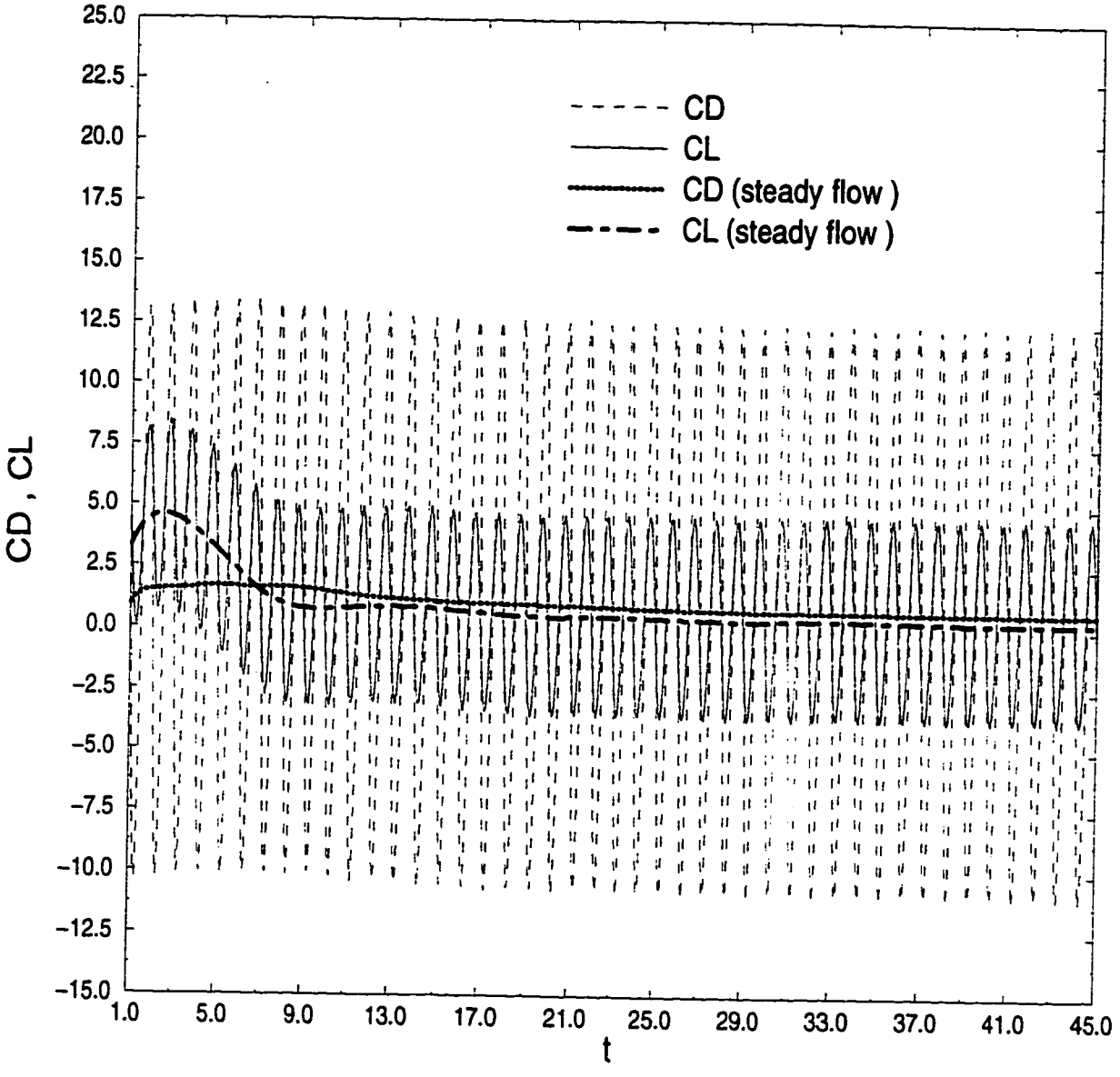

Figure 5.63: The time variation of the $C_D, C_L$for steady and fluctuating free stream in case of Re=100, Gr=20000, Ar= 0.5, $\lambda = 30°$ and $\beta = 0.5$, $S = 2\pi$.

5.4.4 The Effect of Strouhal Number on the Streamlines and Isotherms

To show the effect of frequency on the velocity field, the streamlines are plotted for two Strouhal numbers ($S = \pi/2$, π). The time variation of the streamline patterns for case (B-6) is shown in Figure 5.64a-d covering one complete cycle. Figure 5.64a represents the streamlines at the beginning of the cycle where the free stream velocity is maximum. The figure shows the early stages of vortex formation near the rear end of the tube. As the free stream velocity decreases the vortex grows in size and moves upstream on the top surface of the tube (see Figure 5.64b) and then detaches while another vortex starts at the same place as the previous one. Figure 5.64c shows the streamlines at minimum free stream velocity. At this time, both vortices reach their maximum size. When this figure is compared with Figure 5.43d for $S = \pi/4$, it is shown that due to the higher inertial forces caused by the higher frequency, the vortical flow in the wake of the present case ($S=\pi/2$) is pushed away from the tube for larger distances. In the next time step the free stream velocity increases and both vortices detach from the tube surface (see Figure 5.64d). The streamlines at the end of the cycle (Figure 5.64d) looks very much similar to those at the beginning with minor differences. These differences are due to the continuos development of the flow field away from the tube especially in the wake region. Figures 5.65a-d show the corresponding isotherms for the same case. Similar to the streamlines

behavior, vortex shedding and interactions are causing warm fluid lumps to detach and move away from the tube surface. When the isotherms for this case is compared to the isotherms for S = $\pi/4$ shown in Figures 5.44a-d, one can deduce that since the frequency is lower in case of S=$\pi/4$ the effect of vortex shedding and interaction are more pronounced.

The streamlines for case (B-8) are shown in Figures 5.66a-d. The time required for one complete cycle in the case of S = π is 2. In this case the streamlines are plotted after the completion of 16 complete cycles. This large number of cycles causes the quasi-steady to be reached. This becomes very clear when comparing the streamlines in Figures 5.66a and 5.66d at the beginning and end of the cycle. The effect of vortices formation and shedding on the isotherms is shown in Figures 5.67a-d.

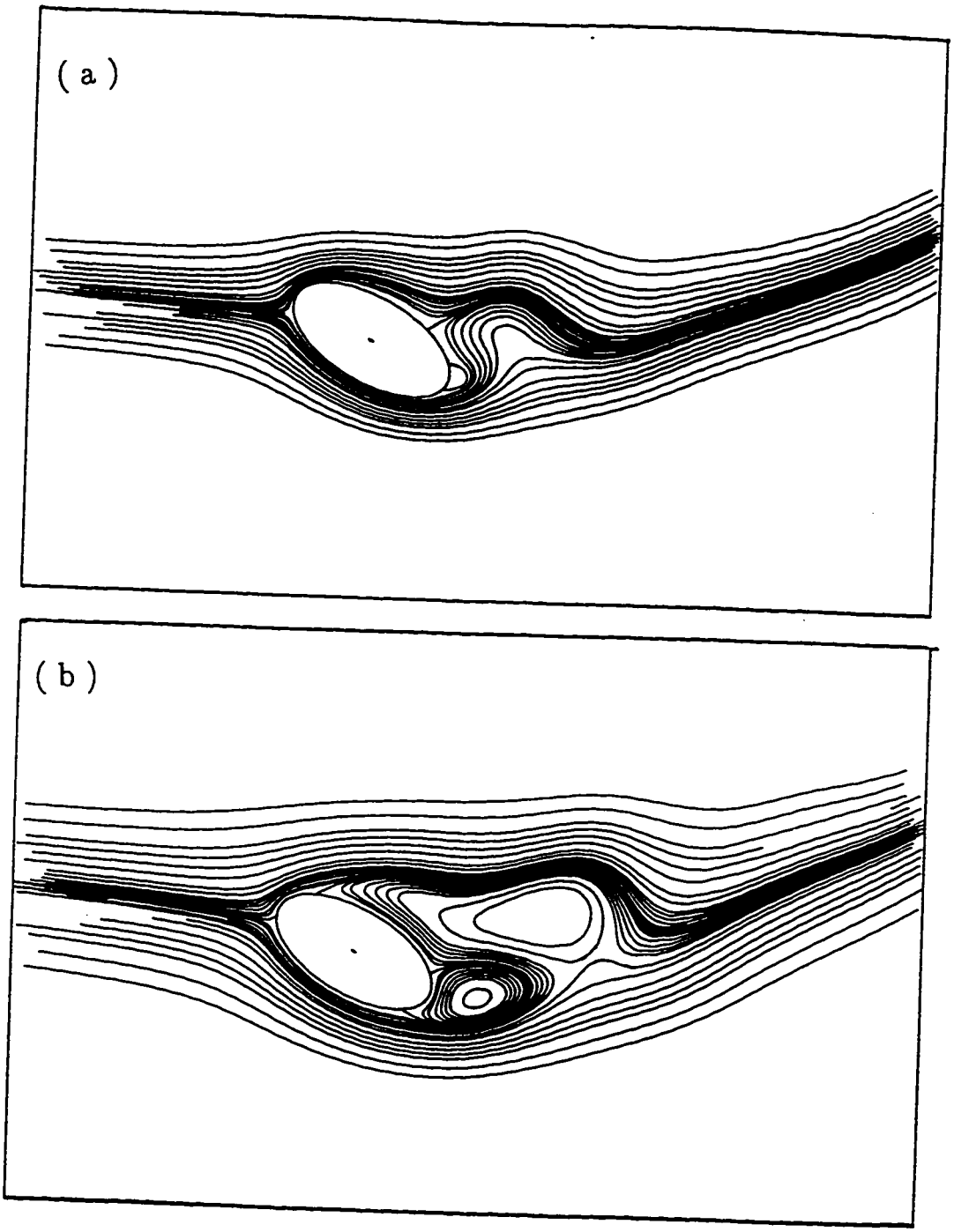
(a)
(b)

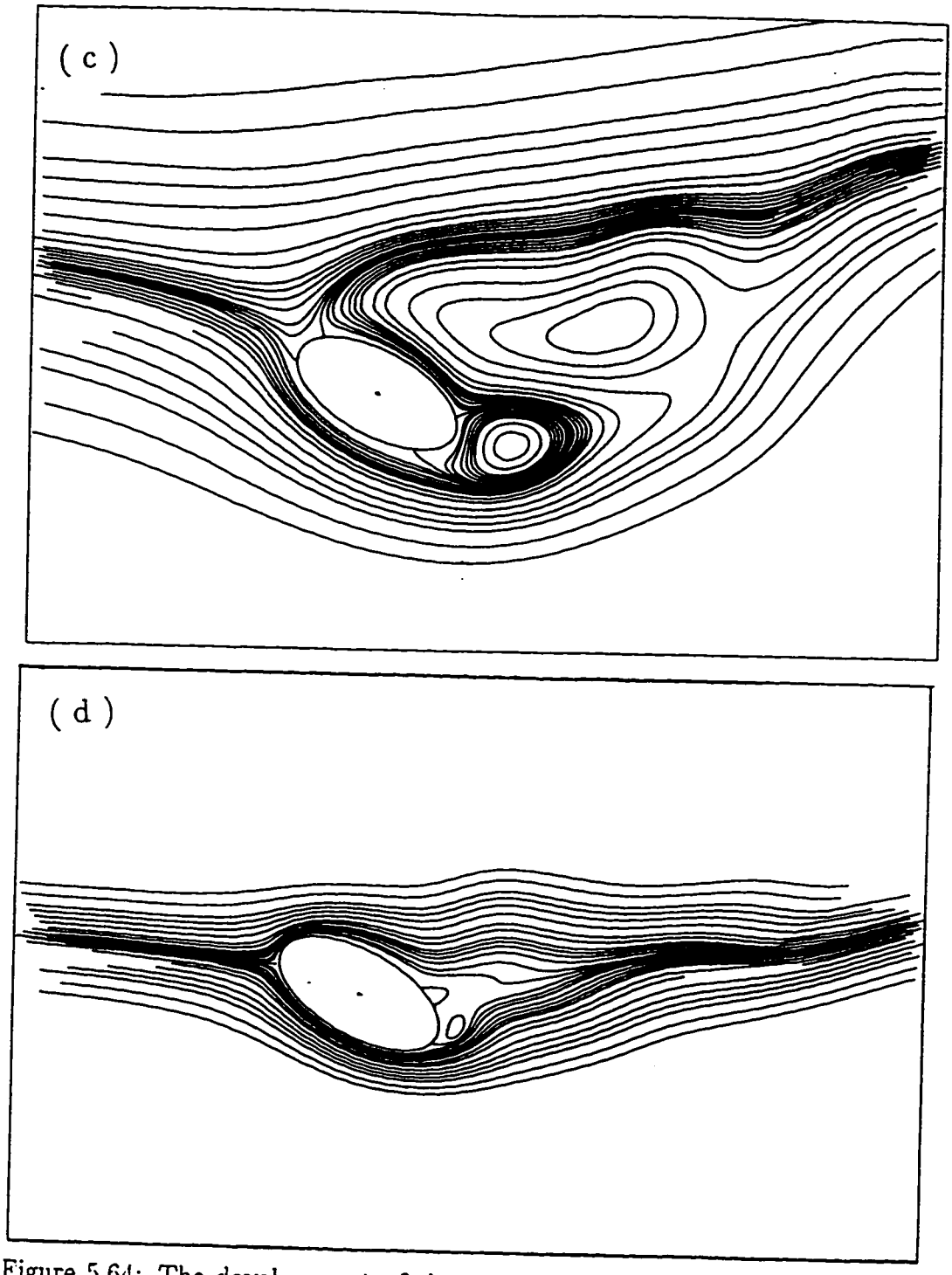

Figure 5.64: The development of the streamline patterns for the case of Re=100, Gr= 20000, Ar = 0.5, $\lambda = 30°$, $\beta = 0.5$ and $S = \pi/2$, during one complete cycle : (a) t = 32; (b) t = 33; (c) t = 34; (d) t = 36.

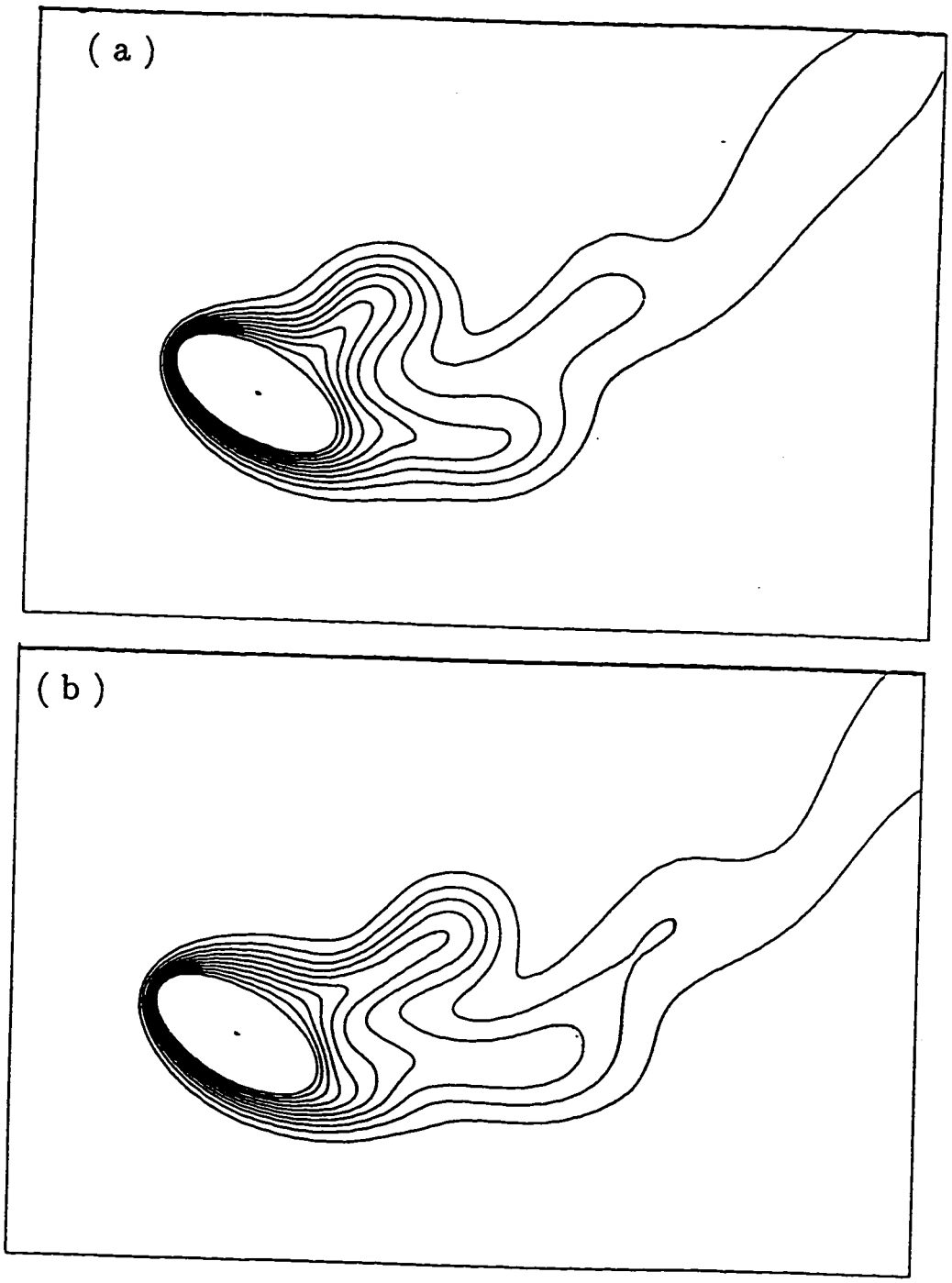
(a)
(b)

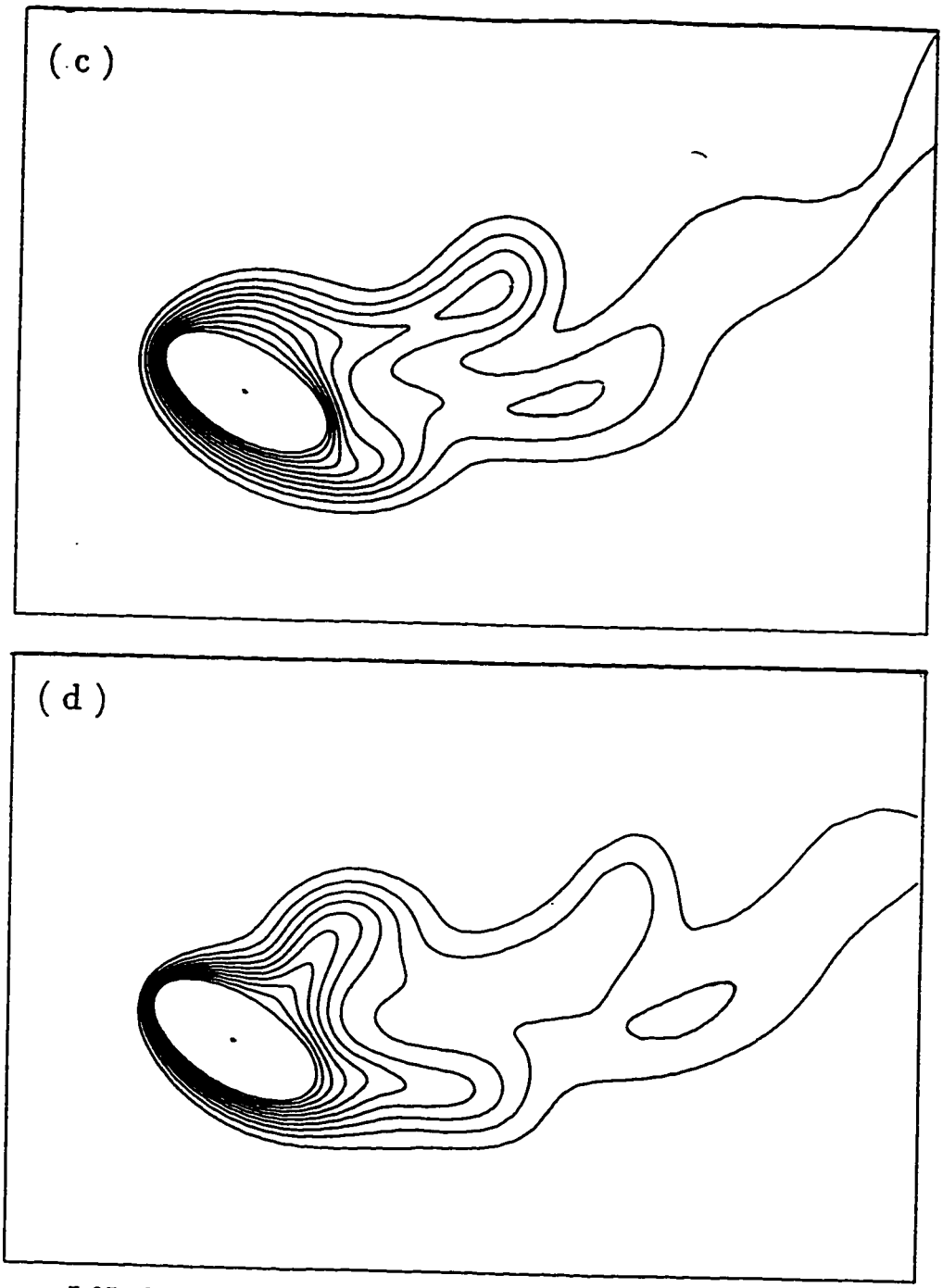

Figure 5.65: Time Development of the isotherm contours for the case of Re=100, Gr= 20000, Ar = 0.5, $\lambda = 30^{o}$ $\beta = 0.5$ and $S = \pi/2$ during one complete cycle : (a) t = 32; (b) t = 33; (c) t = 34; (d) t = 36.

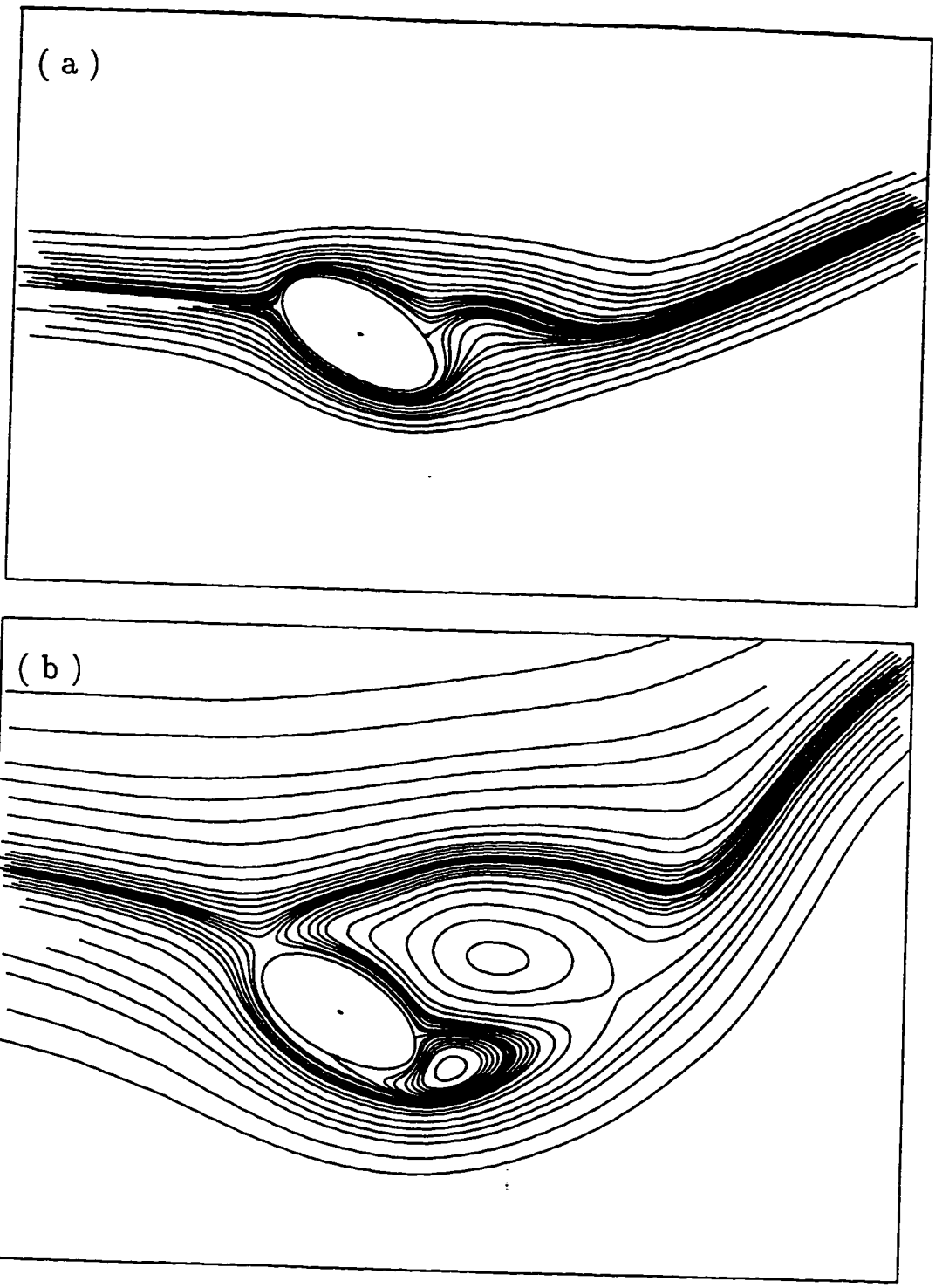
(a)
(b)

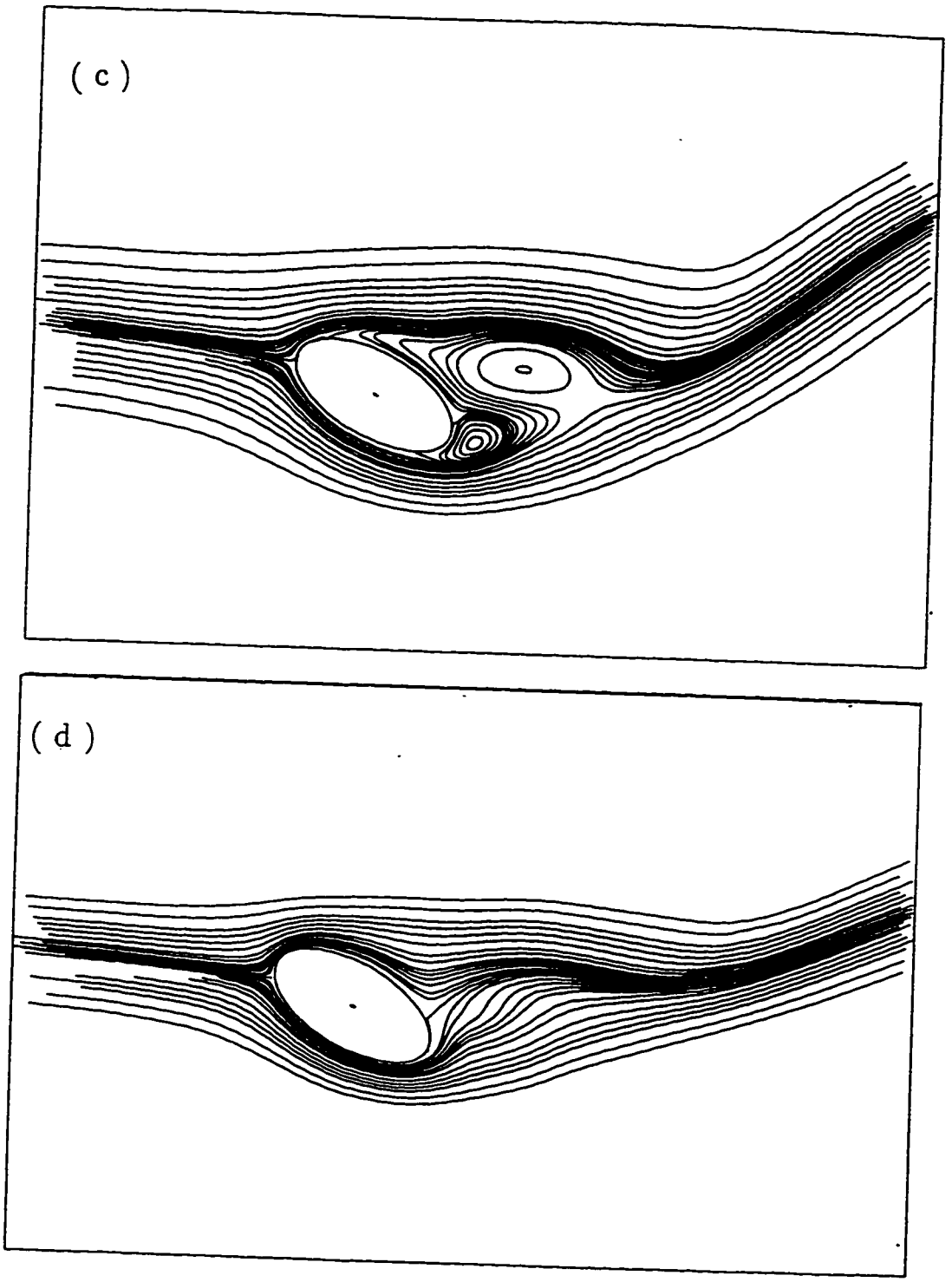

Figure 5.66: The development of the streamline patterns for the case of Re=100, Gr= 20000, Ar = 0.5, $\lambda = 30°$, $\beta = 0.5$ and $S = \pi$, during one complete cycle : (a) t = 32; (b) t = 32.5; (c) t = 33; (d) t = 34.

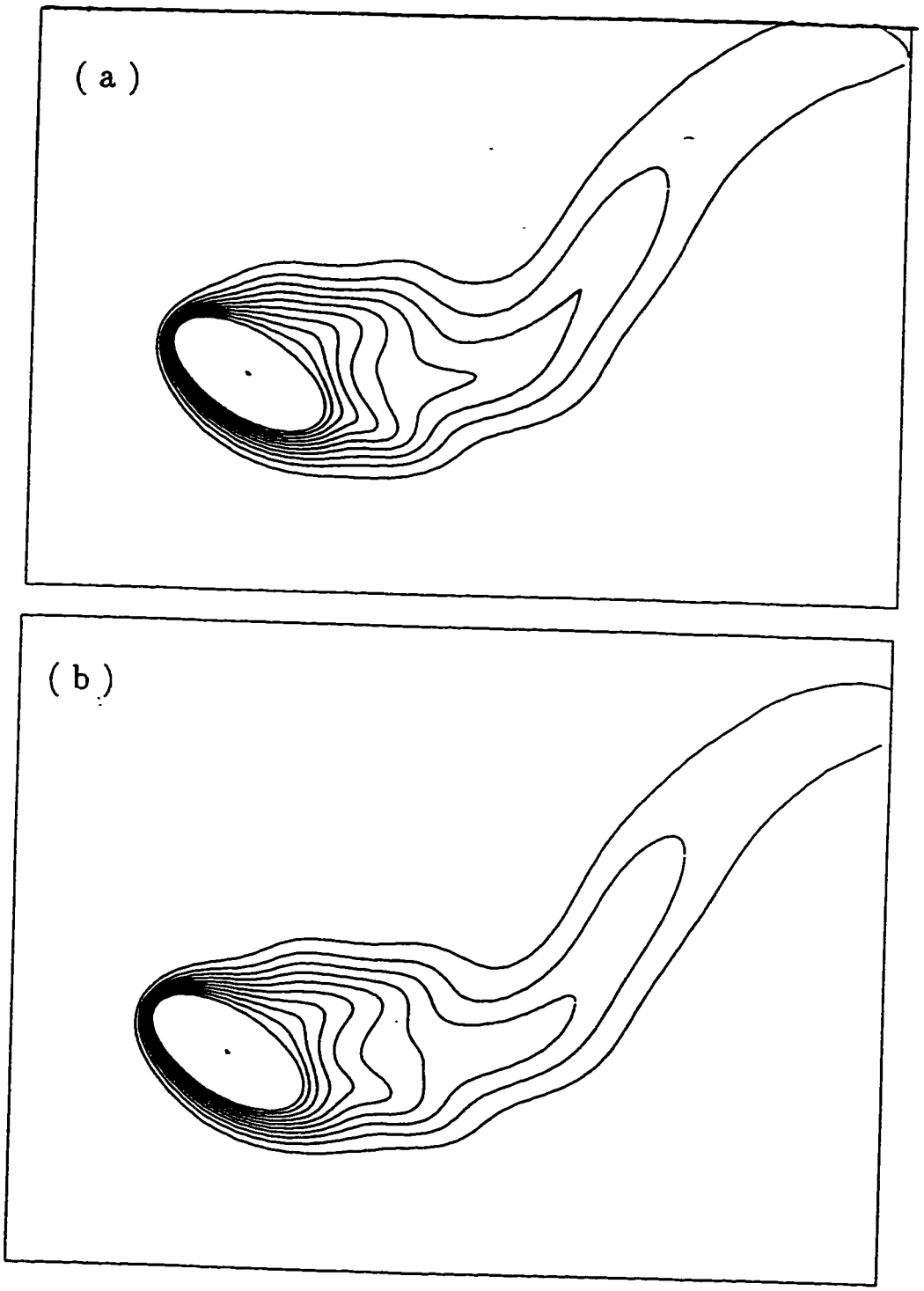
(a)
(b)

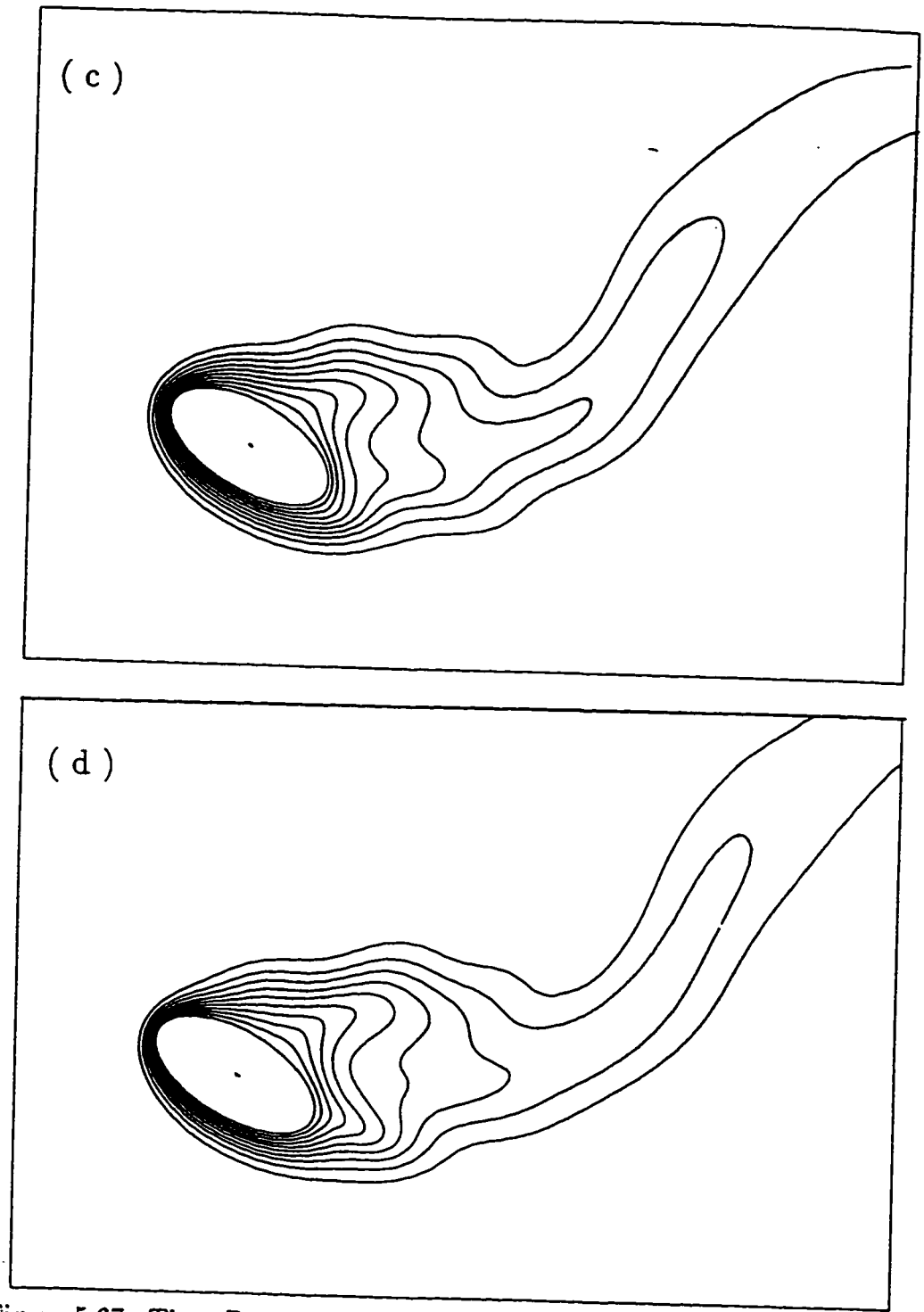

Figure 5.67: Time Development of the isotherm contours for the case of Re=100, Gr= 20000, Ar = 0.5, $\lambda = 30^{o}$ $\beta = 0.5$ and $S = \pi$ during one complete cycle : (a) t = 32; (b) t = 32.5; (c) t = 33; (d) t = 34.

5.5 The Effect of Reynolds Number

The effect of Reynolds number on the flow and thermal fields, average and local Nusselt numbers, pressure and vorticity distributions is studied in this section. The study considers values of Re ranging from Re=20 to Re=500.

5.5.1 The Effect of Reynolds Number on the Average Nusselt Number

The numerical values of $\overline{\overline{Nu}}$ for different Re values are given in Table 5.5.1. In the low Reynolds number cases of Re $\leq$ 50, introducing fluctuations in the free stream results in small increase in $\overline{\overline{Nu}}$, while further increase of Re tends to increase $\overline{\overline{Nu}}$ much higher. The two higher Re cases of 100 and 500 show that the effect of fluctuations becomes more pronounced with increasing Re. Within the range of variables considered, the maximum increase of $\overline{\overline{Nu}}$ was found for Re=500 and reached 12.6 % .

Figure 5.68 shows the time variation of the average Nusselt number $\overline{Nu}$ following the sudden temperature rise of the tube surface temperature for different Reynolds number values. The figure shows that when Re increases $\overline{Nu}$ increases as expected and $\overline{Nu}$ fluctuates with time at the same frequency as the free stream. One should emphasis here that the periodic variation has been achieved for the case of Re=50, however. for other cases specially when Re=500 the thermal field was still developing

for this low Strouhal number ($S = \pi/4$) when computation are terminated. Figures 5.69 and 5.70 show the increase in heat transfer due to the fluctuations in the free stream. This heat transfer enhancement increases as Re increases.

Table 5.5: The percentage increase in $\overline{\overline{Nu}}$ caused by different amplitudes and frequencies for differenrt Reynolds numbers compared to the steady stream case.

Code #	Re	Gr	λ	b/a	S	β	$\overline{\overline{Nu}}$	$\overline{Nu}$ $\beta = 0$	% increase
C-1	20	10000	30°	0.5	$\frac{\pi}{4}$	0.25	4.46	4.43	0.60 %
C-2	20	10000	30°	0.5	$\frac{\pi}{4}$	0.50	4.50	4.43	1.58 %
C-3	20	10000	30°	0.5	$\frac{\pi}{2}$	0.25	4.45	4.43	0.45 %
C-4	20	10000	30°	0.5	$\frac{\pi}{2}$	0.50	4.48	4.43	1.11 %
C-5	50	10000	30°	0.5	$\frac{\pi}{4}$	0.25	4.79	4.73	1.29 %
C-6	50	0000	30°	0.5	$\frac{\pi}{4}$	0.50	4.85	4.73	2.70 %
C-7	50	10000	30°	0.5	$\frac{\pi}{2}$	0.25	4.78	4.73	1.06 %
C-8	50	10000	30°	0.5	$\frac{\pi}{2}$	0.50	4.83	4.73	2.15 %
C-9	100	10000	30°	0.5	$\frac{\pi}{4}$	0.25	6.25	6.09	2.76 %
C-10	100	10000	30°	0.5	$\frac{\pi}{4}$	0.50	6.43	6.09	5.60 %
C-11	100	10000	30°	0.5	$\frac{\pi}{2}$	0.25	6.22	6.09	2.26 %
C-12	100	10000	30°	0.5	$\frac{\pi}{2}$	0.50	6.29	6.09	3.40 %
C-13	150	10000	30°	0.5	$\frac{\pi}{4}$	0.25	7.31	6.79	7.6 %
C-14	150	10000	30°	0.5	$\frac{\pi}{4}$	0.50	7.517	6.79	10.7 %

Code #	Re	Gr	λ	b/a	S	β	$\overline{\overline{Nu}}$	$\overline{Nu}$ $\beta = 0$	% increase
C-15	150	10000	30°	0.5	$\frac{\pi}{2}$	0.25	7.18	6.79	5.77 %
C-16	150	10000	30°	0.5	$\frac{\pi}{2}$	0.50	7.38	6.79	8.6 %
C-17	200	10000	30°	0.5	$\frac{\pi}{4}$	0.25	8.31	7.57	9.8 %
C-18	200	10000	30°	0.5	$\frac{\pi}{4}$	0.50	8.53	7.57	12.3 %
C-19	200	10000	30°	0.5	$\frac{\pi}{2}$	0.25	8.14	7.57	7.5 %
C-20	200	10000	30°	0.5	$\frac{\pi}{2}$	0.50	8.34	7.57	10.2 %
C-21	500	10000	30°	0.5	$\frac{\pi}{4}$	0.25	13.78	12.91	6.8 %
C-22	500	10000	30°	0.5	$\frac{\pi}{4}$	0.50	14.76	12.91	14.3 %
C-23	500	10000	30°	0.5	$\frac{\pi}{2}$	0.25	13.56	12.91	5.1 %
C-24	500	10000	30°	0.5	$\frac{\pi}{2}$	0.50	14.54	12.91	12.6 %

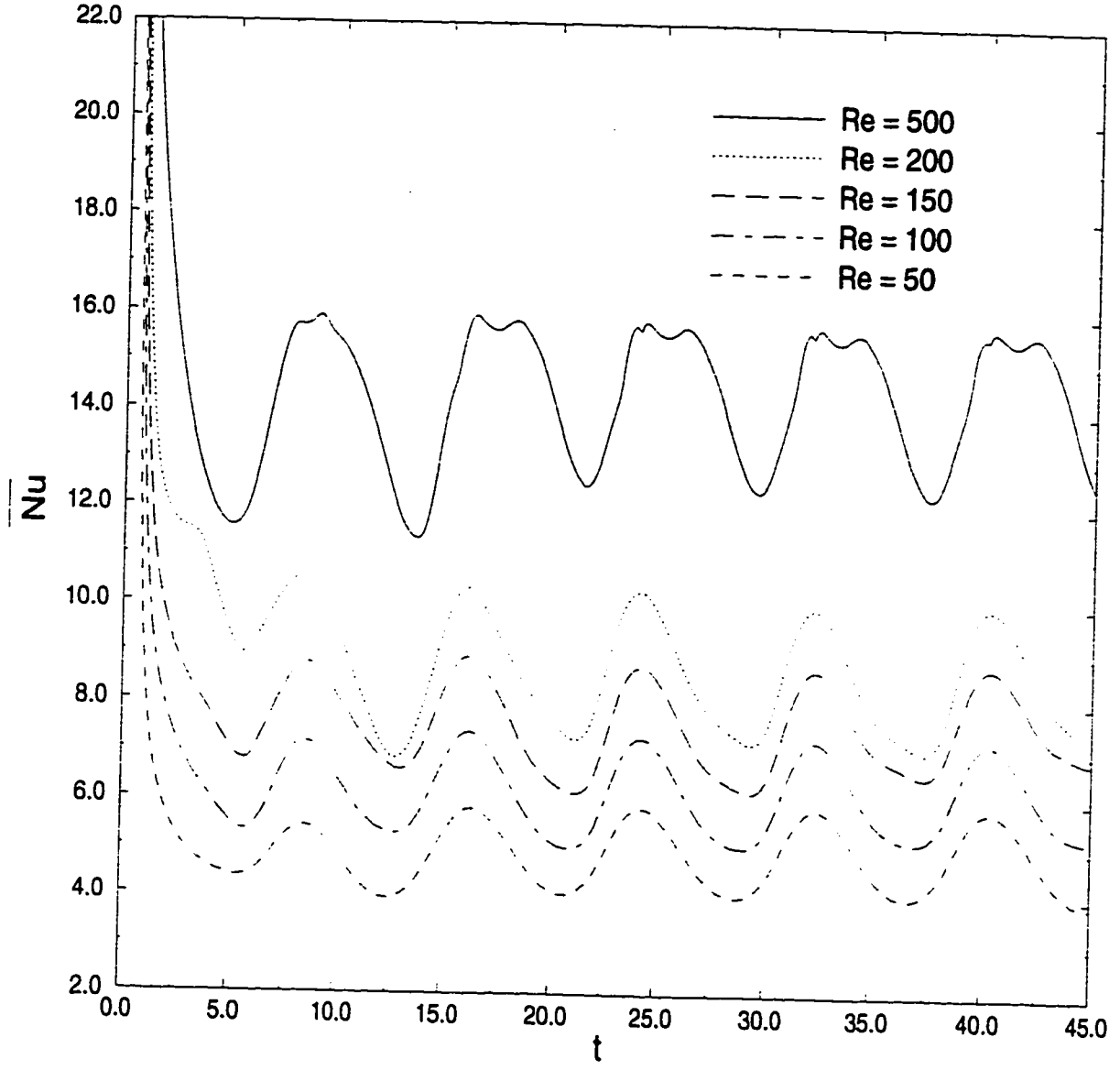

Figure 5.68: The time variation of $\overline{Nu}$ following the sudden temperature rise for various Reynolds numbers in case of Gr=10000, Ar=0.5, $\lambda = 30.0^o$ and $\beta = 0.5$, $S = \pi/4$.

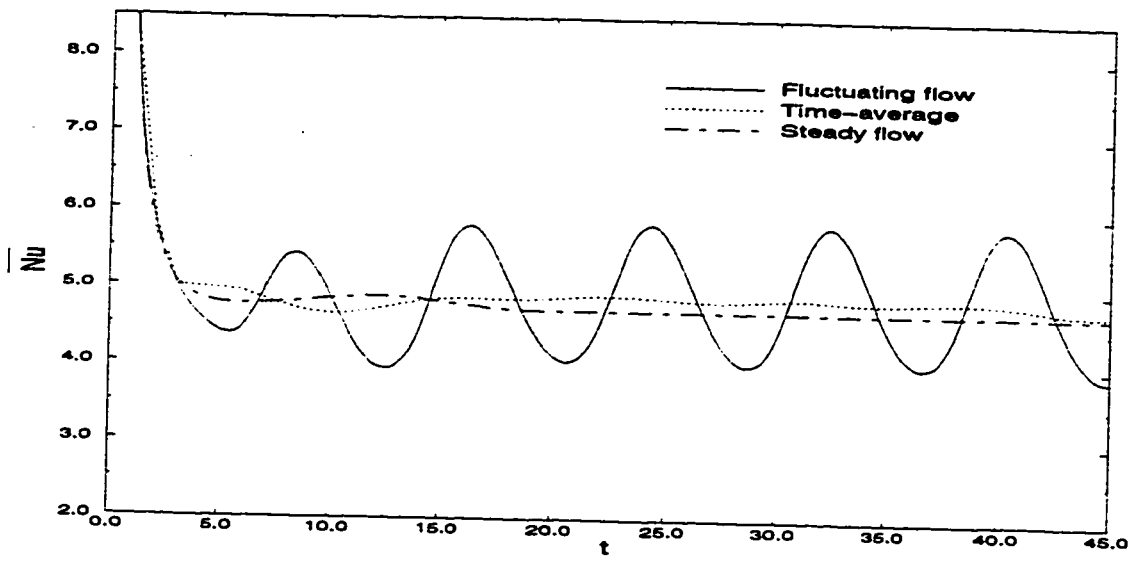

Figure 5.69: The variation of $\overline{Nu}$ for case C-6 and comparison with the steady free stream case.

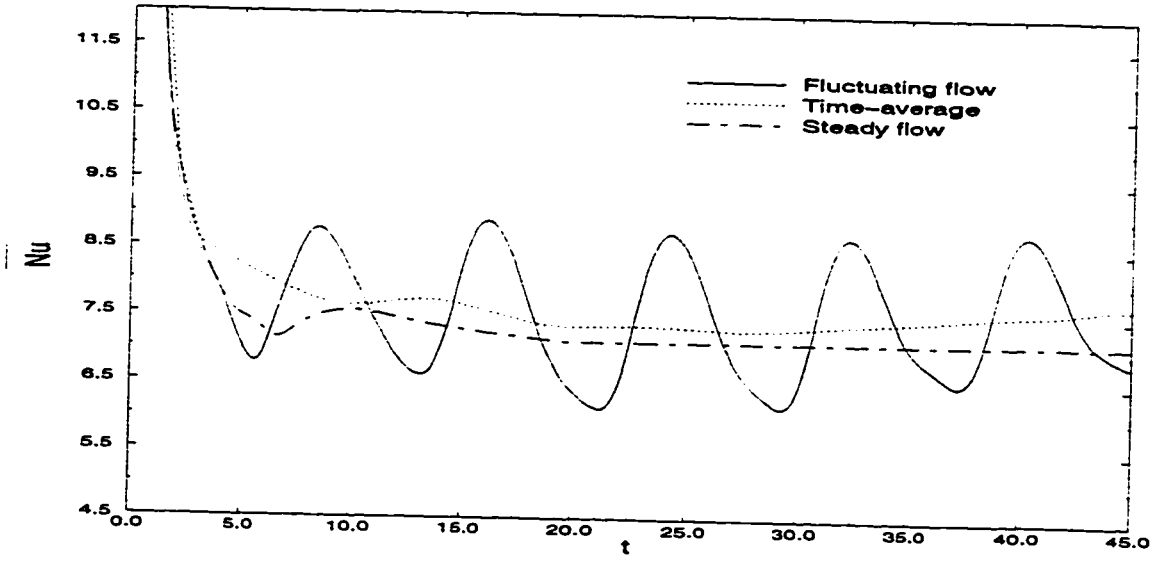

Figure 5.70: The variation of $\overline{Nu}$ for case C-14 and comparison with the steady free stream case.

5.5.2 The Effect of Reynolds Number on the Local Nusselt Number, Pressure and Vorticity Distributions

Figure 5.71 shows the local Nusselt number distribution at different Re values. High Re values causes higher heat transfer rates all over the tube surface. The vorticity distribution for this case is shown in Figure 5.72 where the highest $|\zeta_s|$ values occurring at Re = 500 which means higher velocity gradients at the tube surface and consequently higher heat transfer rates.

Figures 5.73 and 5.74 show the local Nusselt distribution for different times togother with a comparison with the steady stream distribution for Re=50 and Re=150 respectively. In both figures t=16 represents the start of the third cycle where the free stream velocity is maximum while t = 20 corresponds to the minimum stream velocity. Compared to the steady stream case, Nu values are higher almost over all the tube surface when the free stream velocity is maximum except for the rear portion where vortical velocity causes a different behavior. This same reason causes Nu to be higher at the rear portion when the free stream velocity is minimum compared to no fluctuation values.

Figures 5.75 and 5.76 show the vorticity distribution and its variation over half a cycle for the same two cases. The figure shows that the surface vorticity variation is much less when the stream velocity is minimum. A similar behavior also occurs for the local Nusselt number distribution (see Figure 5.74)

Figures 5.77 and 5.78 show the local Nusselt number and vorticity distributions respectively for Re = 500 for one complete cycle at different time steps. It is clear that when the free stream velocity is maximum the Nu curve possesses two peaks. The highest is near the front end ($\eta = 183^o$) and the other is occurring at the rear end ($\eta = 50^o$). As the free stream velocity decreases to its minimum the front peak decreases while the rear one gets considerably higher. The vorticity distribution given in Figure 5.78 shows that for t = 16, $|\zeta_s|$ is higher in the tube front while for t = 20 (at minimum free stream velocity) $|\zeta_s|$ is higher near the tube end matching the behavior of Nu distribution.

The pressure distributions around the tube surface for different Re values when the free stream velocity is either maximum or minimum are shown in in Figures 5.79 and 5.80. The pressure variation around the surface gets less as the stream velocity decreases.

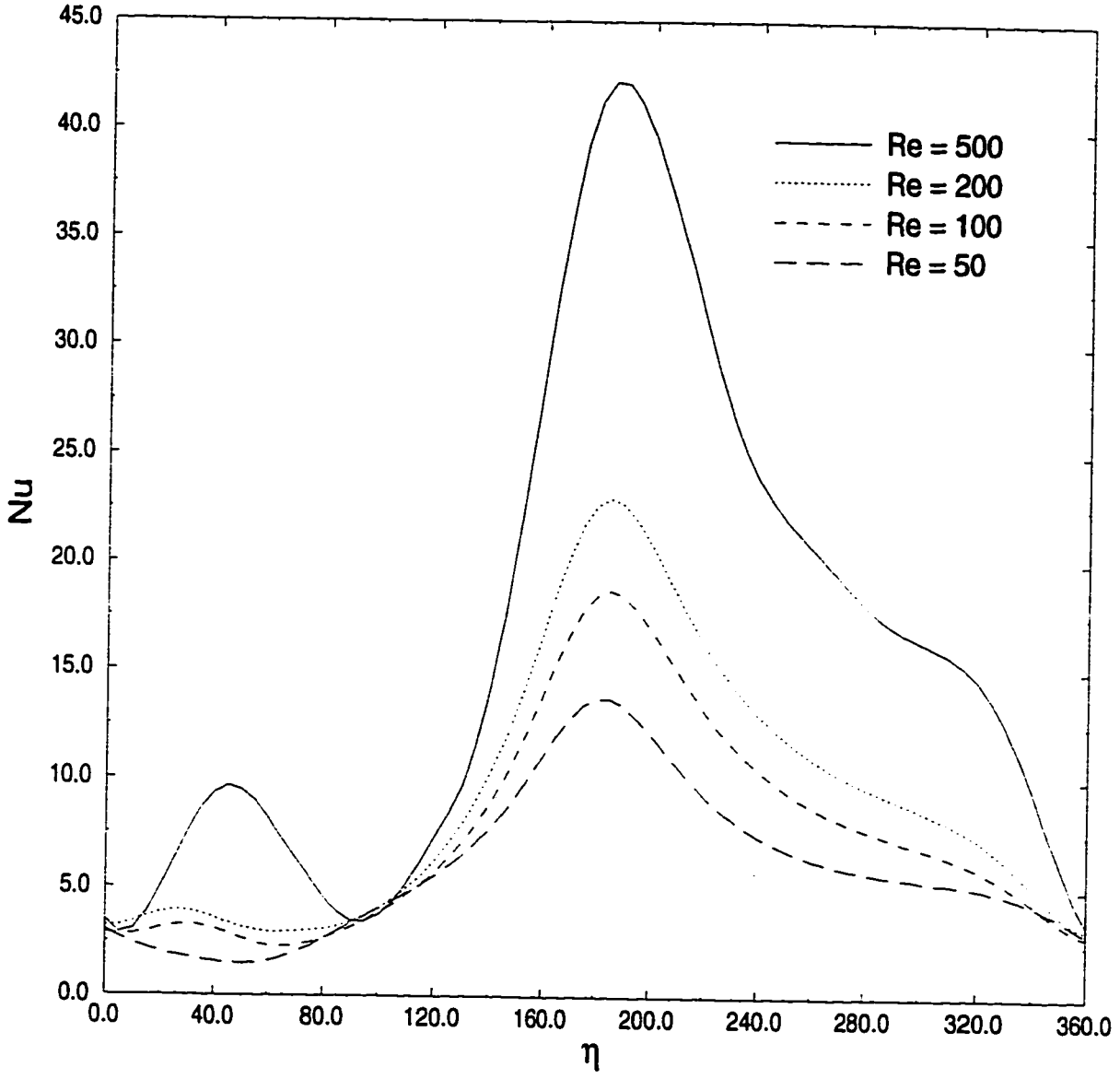

Figure 5.71: The effect of Reynolds number on the local Nusselt number distribution at maximum free stream velocity for the case of Gr = 10000, Ar = 0.5 , $\lambda = 30°$, $\beta = 0.5$ and $S = \pi/4$.

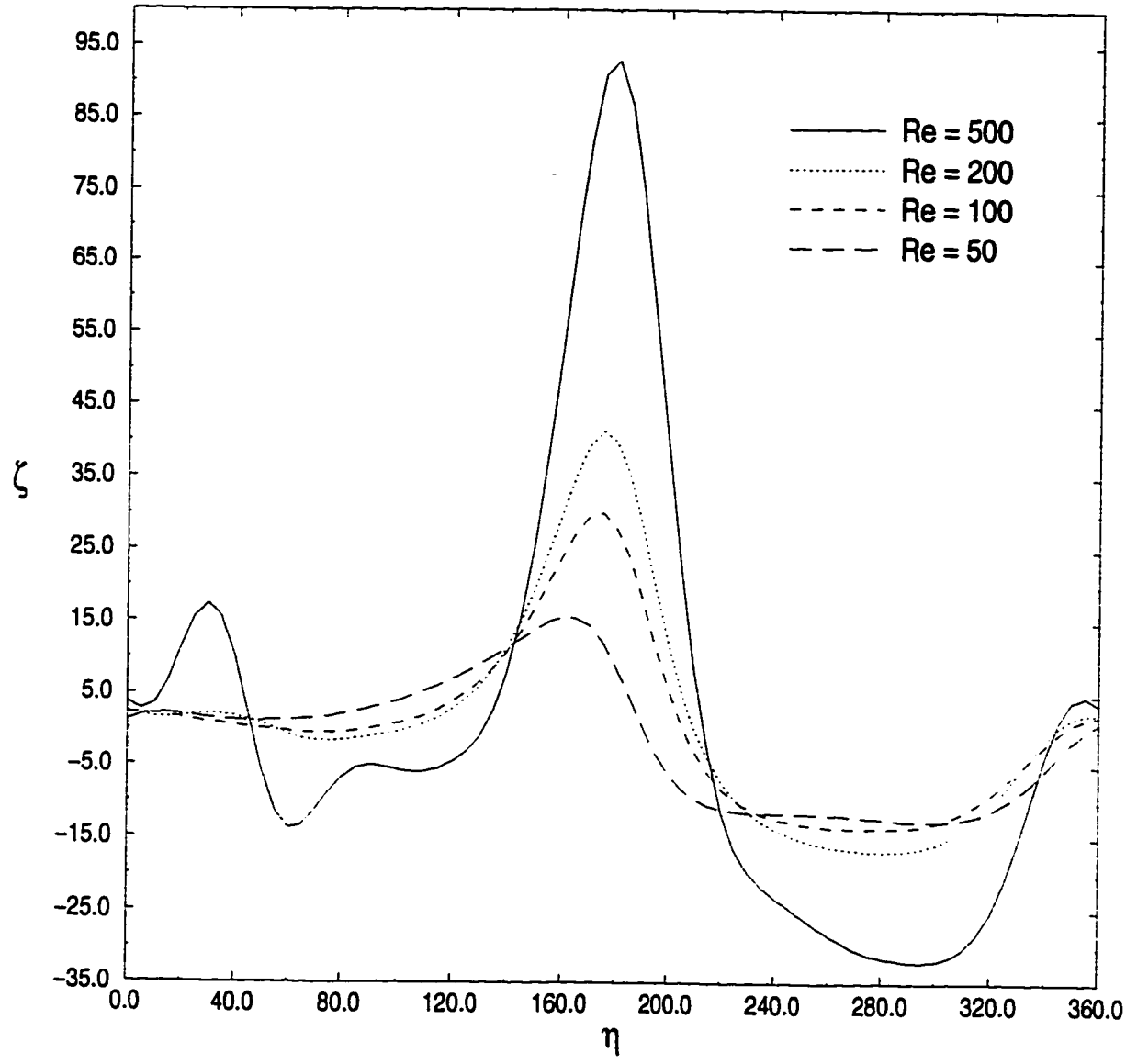

Figure 5.72: The effect of Reynolds number on the vorticity distribution at maximum free stream velocity for the case of Gr=10000, Ar=0.5, $\lambda = 30^o$, $\beta = 0.5$ and $S = \pi/4$.

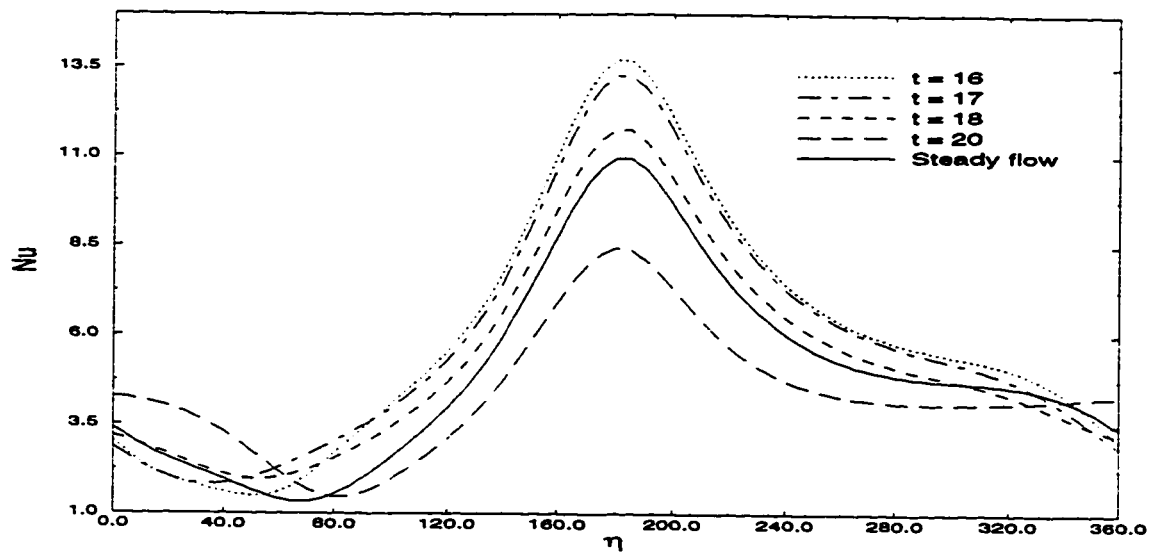

Figure 5.73: The local Nusselt number distribution at various times during one complete cycle in case C-6 and comparison with the steady free stream.

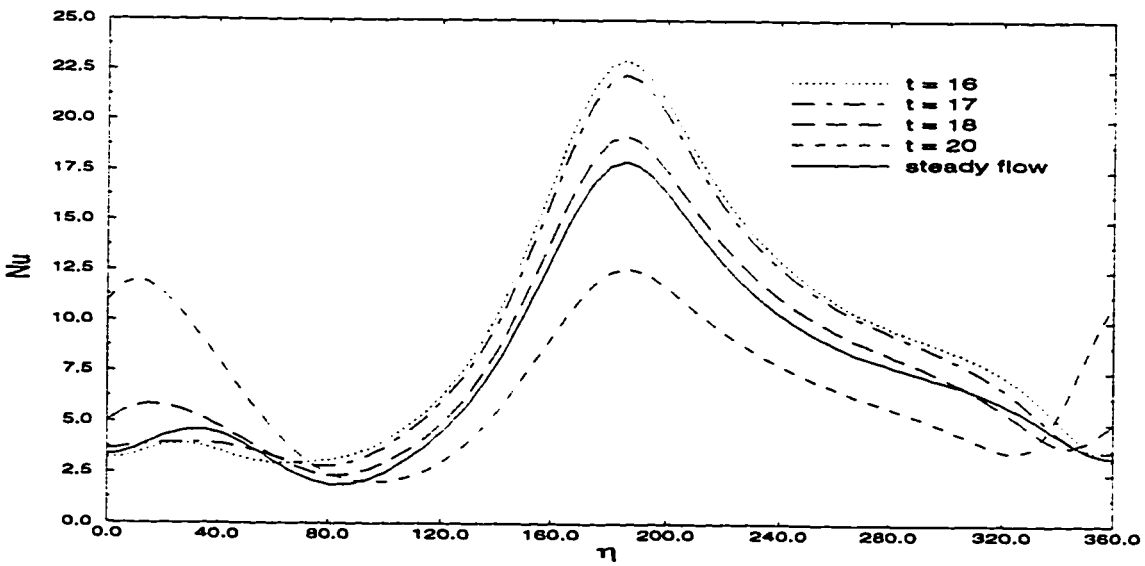

Figure 5.74: The local Nusselt number distribution at various times during one complete cycle in case C-14 and comparison with the steady free stream.

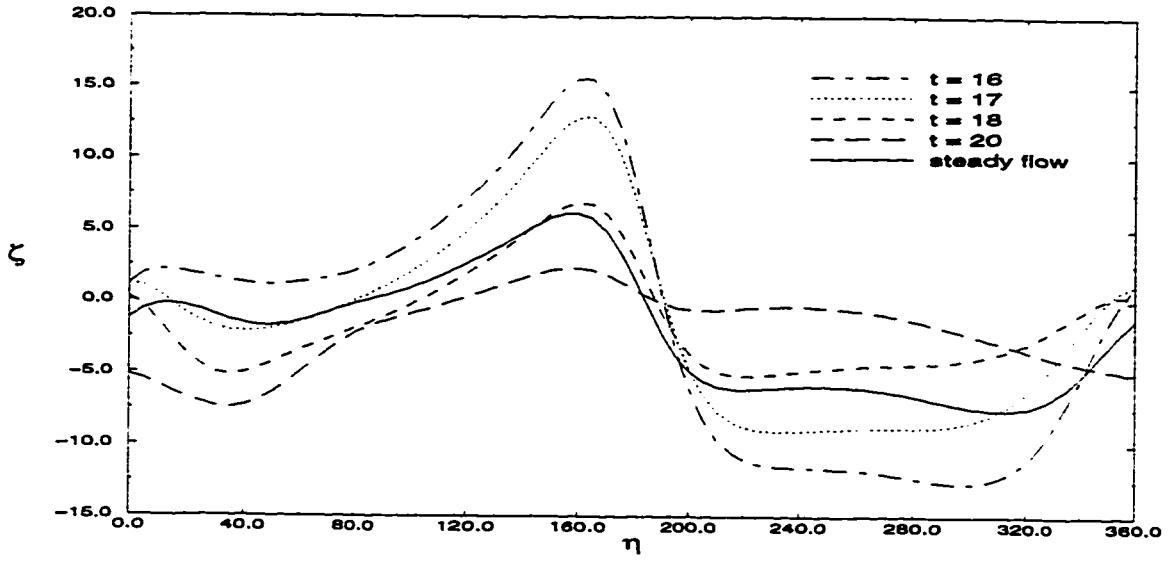

Figure 5.75: The surface vorticity distribution at various times during one complete cycle in case C-6 and comparison with the steady free stream.

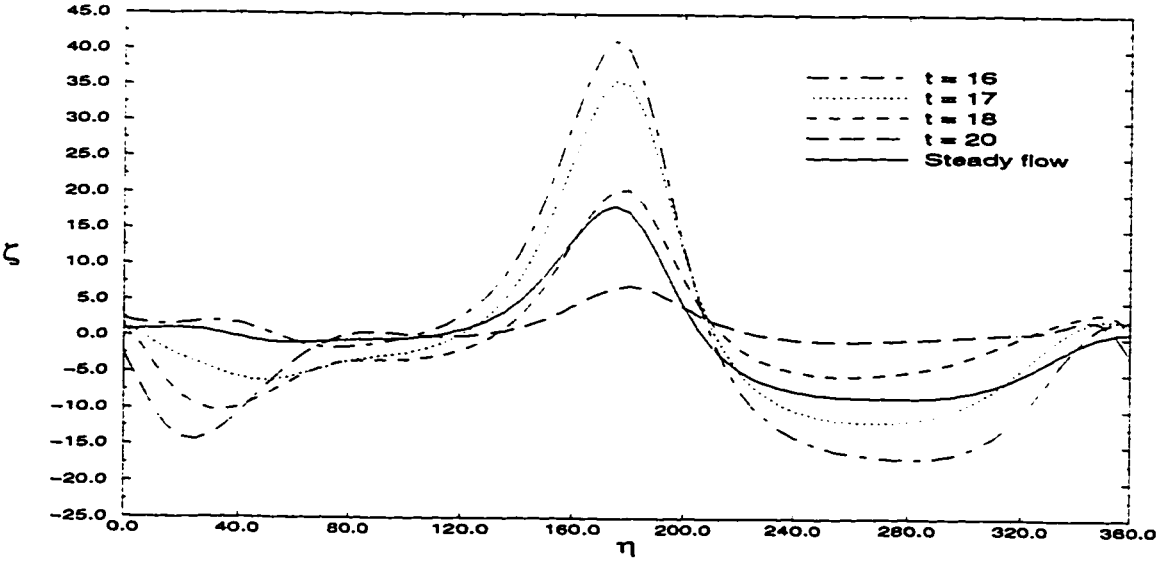

Figure 5.76: The surface vorticity distribution at various times during one complete cycle in case C-14 and comparison with the steady free stream.

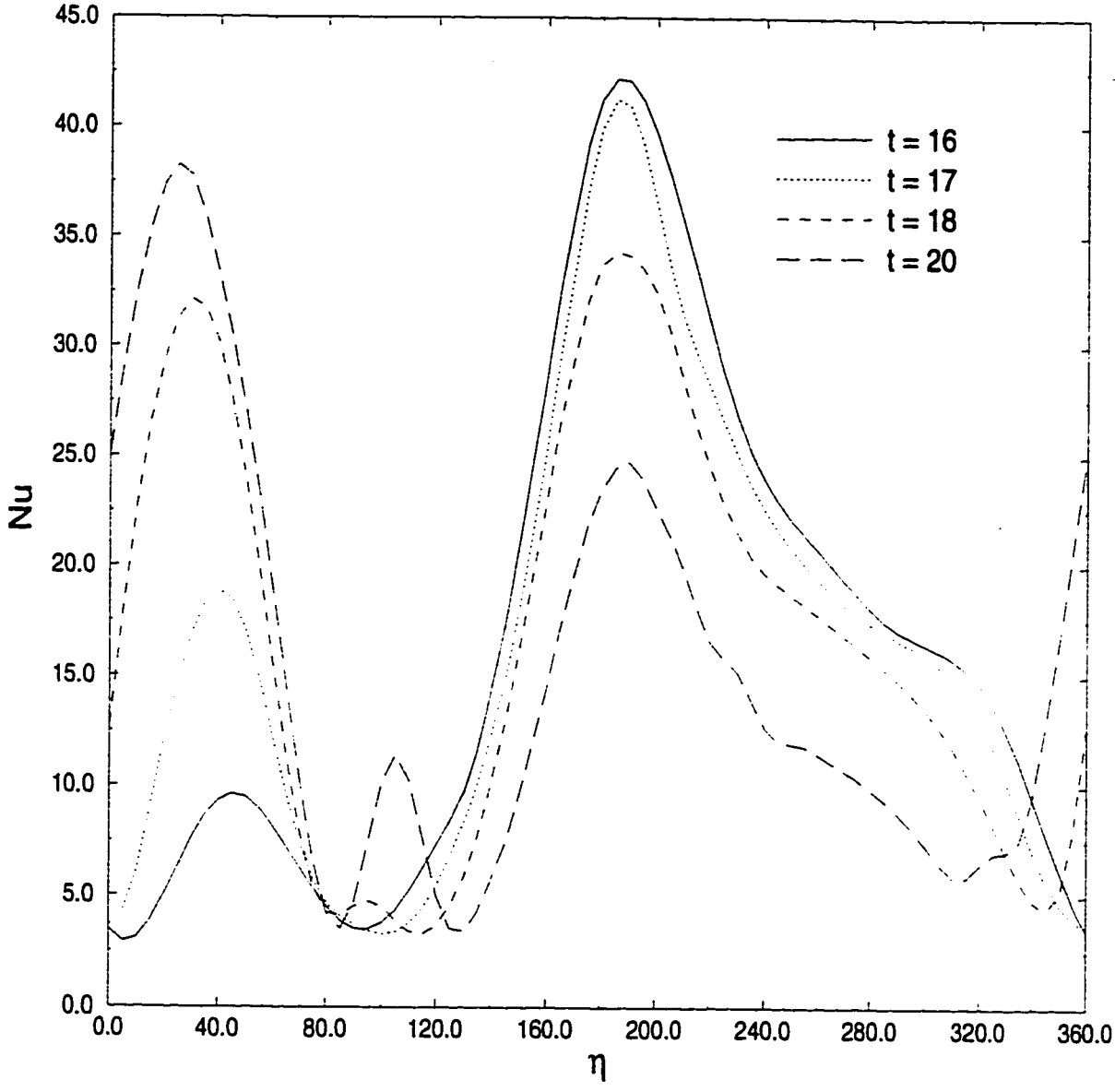

Figure 5.77: The local Nusselt number distribution at various times during one complete cycle in case C-21.

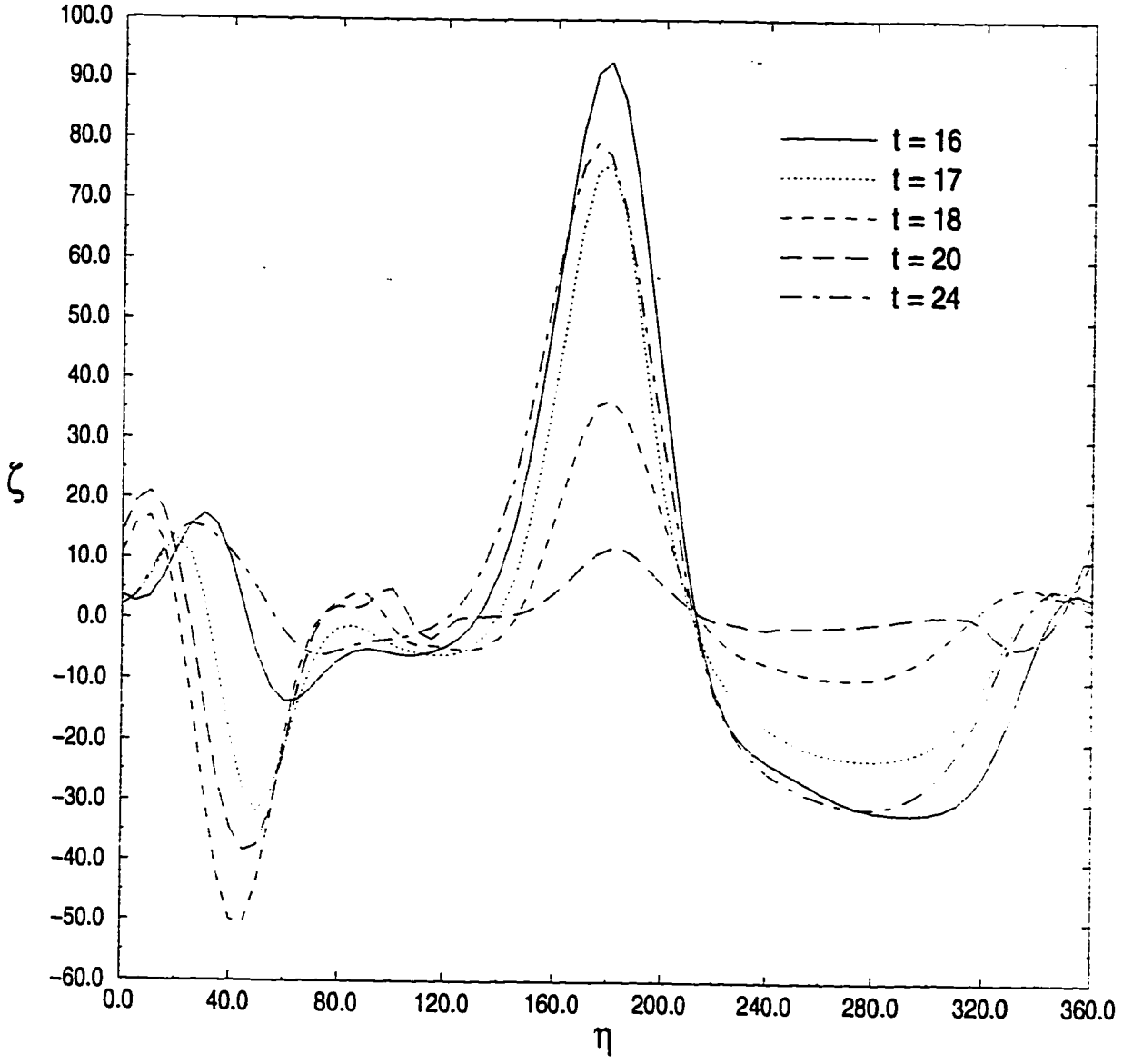

Figure 5.78: The surface vorticity distribution at various times during one complete cycle in case C-21.

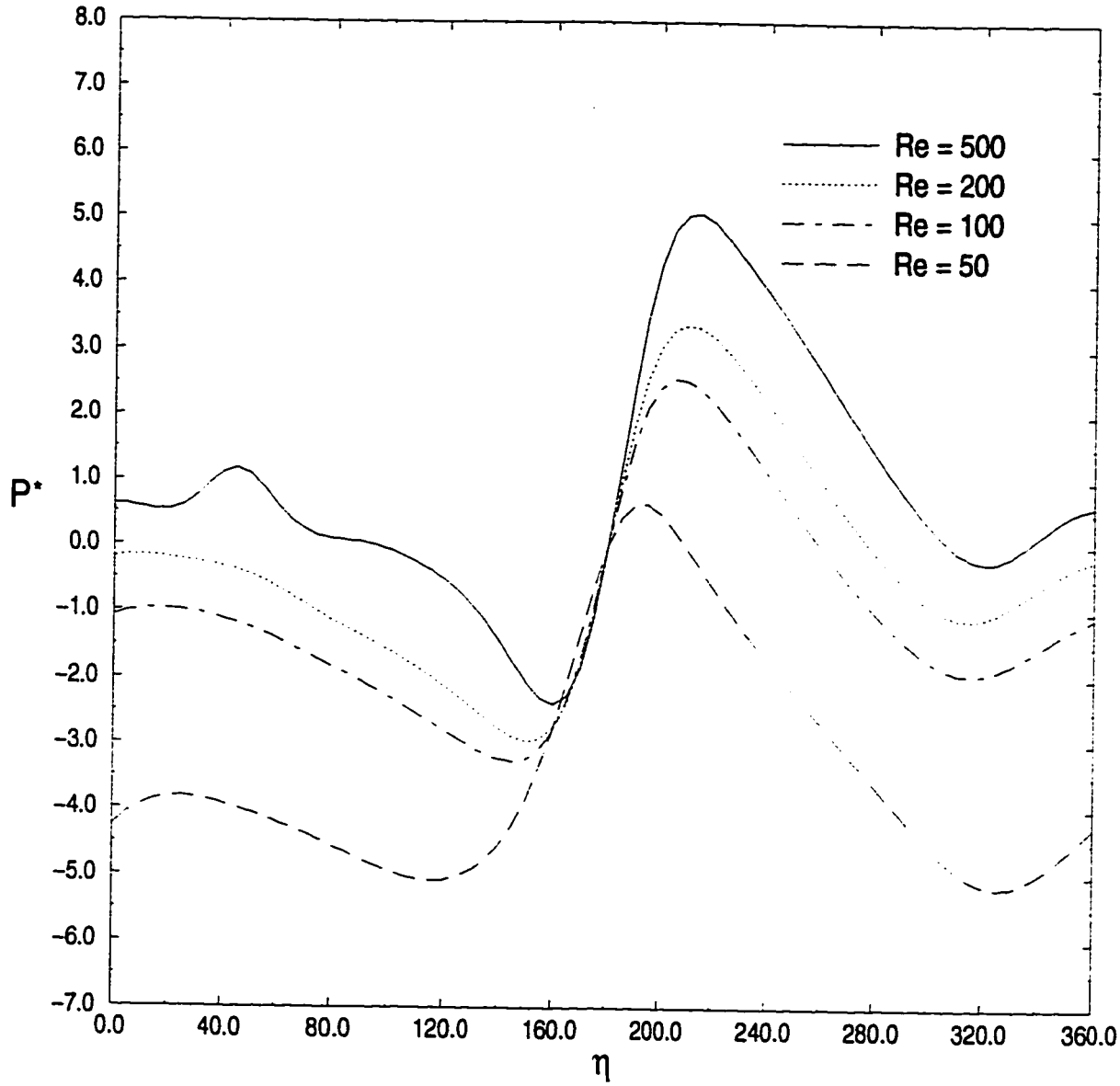

Figure 5.79: The effect of Reynold number on the pressure distribution at maximum free stream velocity for the case of Gr=10000, Ar=0.5, $\lambda = 30^o$, $\beta = 0.5$ and $S = \pi/4$.

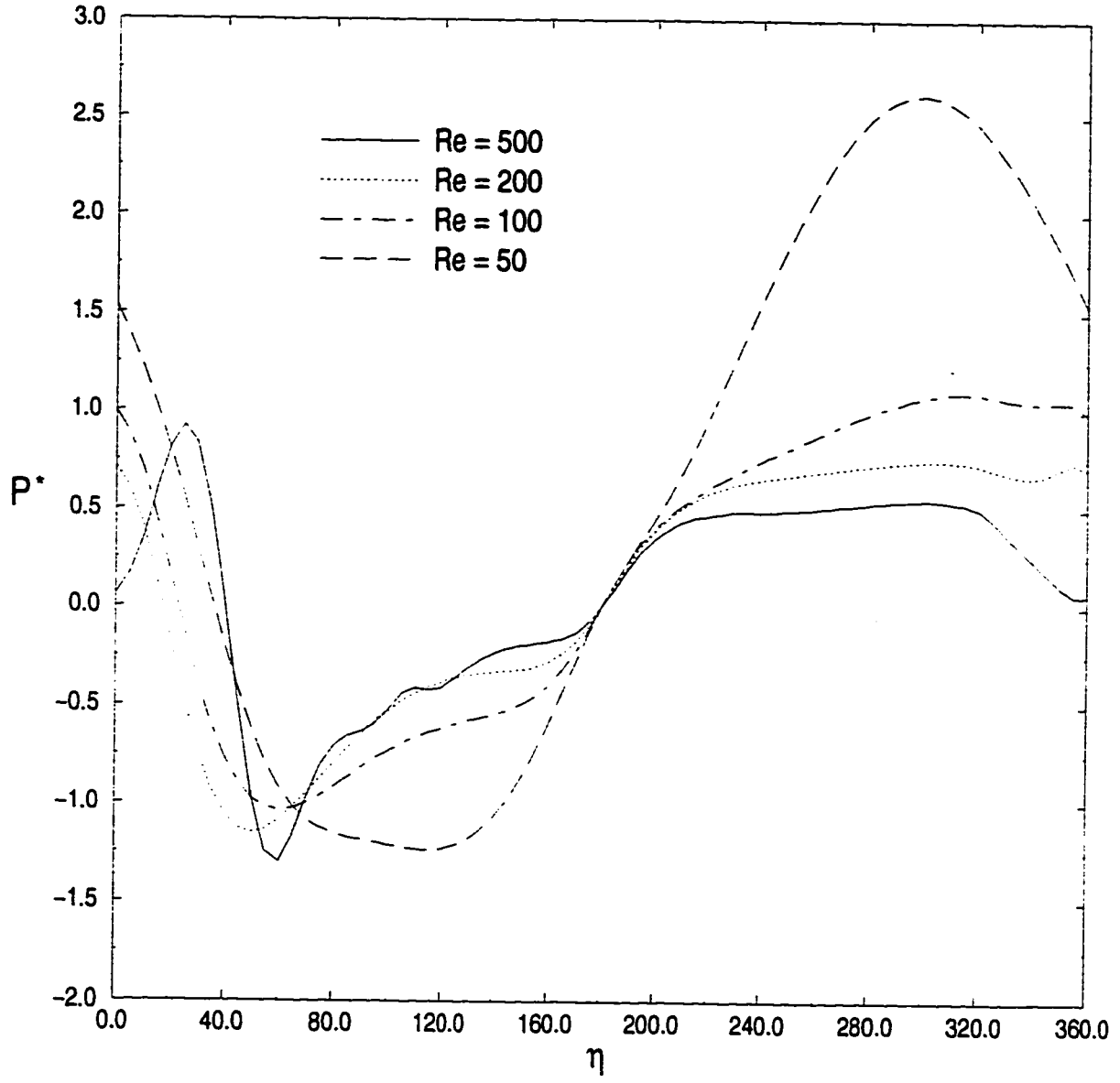

Figure 5.80: The effect of Re on the pressure distribution at minimum free stream velocity, for Gr=10000, Ar= 0.5, $\lambda = 30^o$, $\beta = 0.5$ and $S = \pi/4$.

5.5.3 The Effect of Reynolds Number on the Streamlines and Isotherms

The instantaneous streamline patterns are plotted for the two cases of Re=50 and Re=200. Figures 5.81a-d show the time variation of the streamlines patterns for case (C-6) where time varies from 32 to 40. This gives the details at the flow field during the fourth cycle after the start of the fluid motion. Figure 5.81a shows the streamlines when the free stream is moving to the right at maximum velocity. In this case, the high Grashof number (Gr=10,000) causes the upward flow in the wake region. As the velocity decreases, the fluid deceleration results in the formation of a weak vortex as shown in Figure 5.81b. The formed vortex decays with time with the continuous decrease of the main stream velocity as shown in Figure 5.81c. At this time U=U_{min} and the buoyancy forces become much higher than inertial forces giving rise to the large slope of the upward flow in the wake region. In this case, the streamlines at the start of the cycle and at its end are very much similar as can be seen in Figures 5.81a and 5.81d. This indicates that at low Re values a quasi-steady state was reached following the third cycle. The isotherms for this case are shown in Figures 5.82a-d. At the start af the cycle the effect of high Grashof number tend to shift the isotherms steeply upward as shown in Figure 5.82a matching the behavior of the velocity field. Figure 5.82d shows a lump of hot fluid separating and moving upward.

The time variation of the streamline patterns for the case (C-18) of Re=200 and Gr=10^4 is shown in Figures 5.83a-d for values of t between t=32 to 40. The chosen interval represents the fifth complete cycle following the start of fluid motion. Figures 5.83a, c and d represent the situation at the beginning, middle and end of the cycle, respectively. Vortices start to form when free stream velocity decelerates, then they grow in size reaching maximum size when the velocity is minimum. This is followed by a decay as the free stream velocity accelerates. By comparing Figures 5.83a and d the differences between the start and end of the cycle are minor.

The isotherms for the same case Re = 200 are plotted in Figures 5.84a-d. In general, the figures show that for Re=200, the separation of warm fluid is more pronounced. This can be explained based on the fact that the ratio between the buoyancy forces and inertial forces are much less than the previous case since $Gr/Re^2 = 0.25$ for case (C-16) while $Gr/Re^2 = 4$ in case (C-6). The figures also show that the isotherms for higher Re values are closer to the tube surface reflecting a higher temperature gradient. The analysis of the above two cases show that higher values of Re causes more vortex formation creating a vortical dominating flow near the rear end of the tube. Such superposed velocity field alters the heat transfer characteristics in that region. To show the details of vortex formation and shedding on both velocity and thermal fields the streamlines and isotherms patterns are plotted for the case of Re=500 and Gr=10^4 (which is almost a forced convection case)

between t=40 and t=41. This time period represents the start of the sixth cycle after the start of the fluid motion. Figure 5.85a shows the formation of one vortex in the wake with a fluid bubble at the rear end. Figure 5.85b shows the streamlines at t=40.2 where the vortex becomes larger while the small bubble is getting larger. At t=40.4 the big vortex decayed while the smaller one is growing as shown in Figure 5.85c. Figure 5.85e shows the detachment of this vortex and an upper vortex starts to form at t=41 as shown in Figure 5.85f. The isotherms for the same case are shown in Figures 5.86a-f. The first plot (5.86a) shows a high temperature gradient every where except at the middle of the top surface as well as the rear end. The figure also shows a detached fluid bulk moving away from the tube surface. Figure 5.86c shows another fluid bulk getting ready to detach and the process continues.

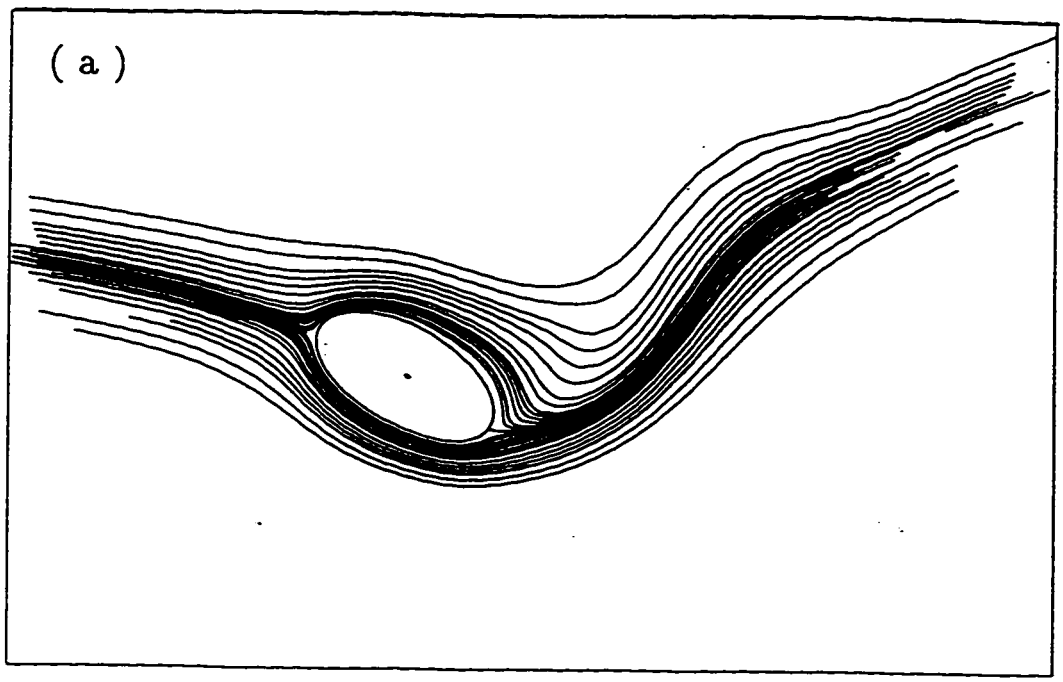
(a)

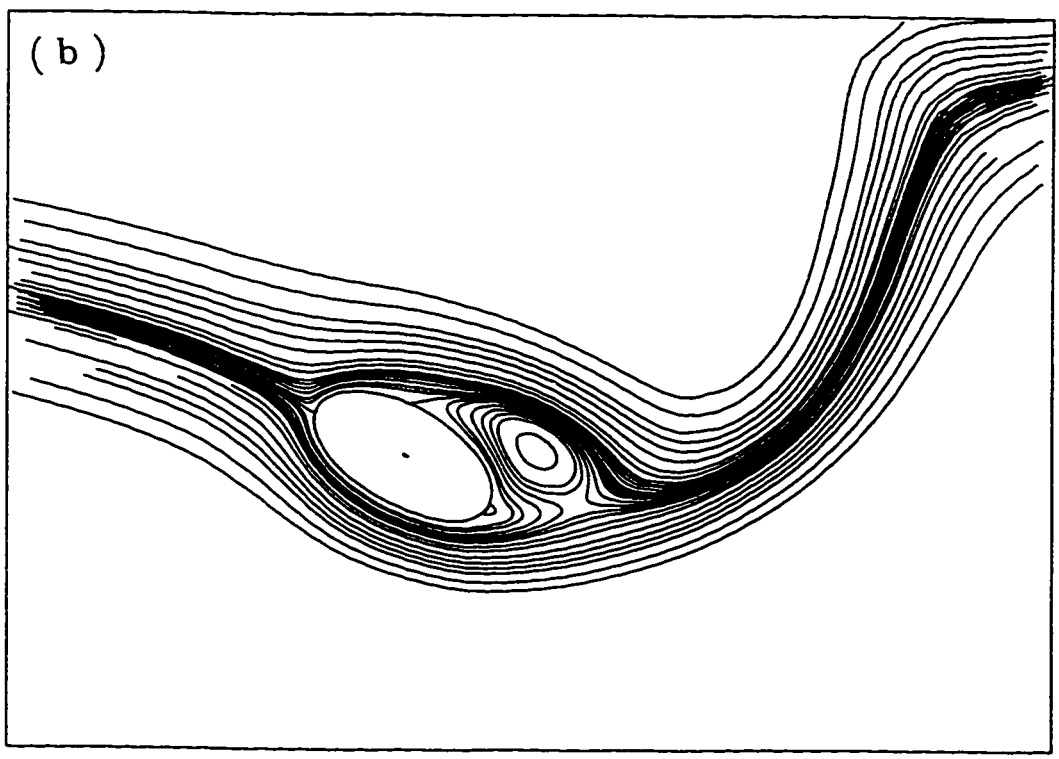
(b)

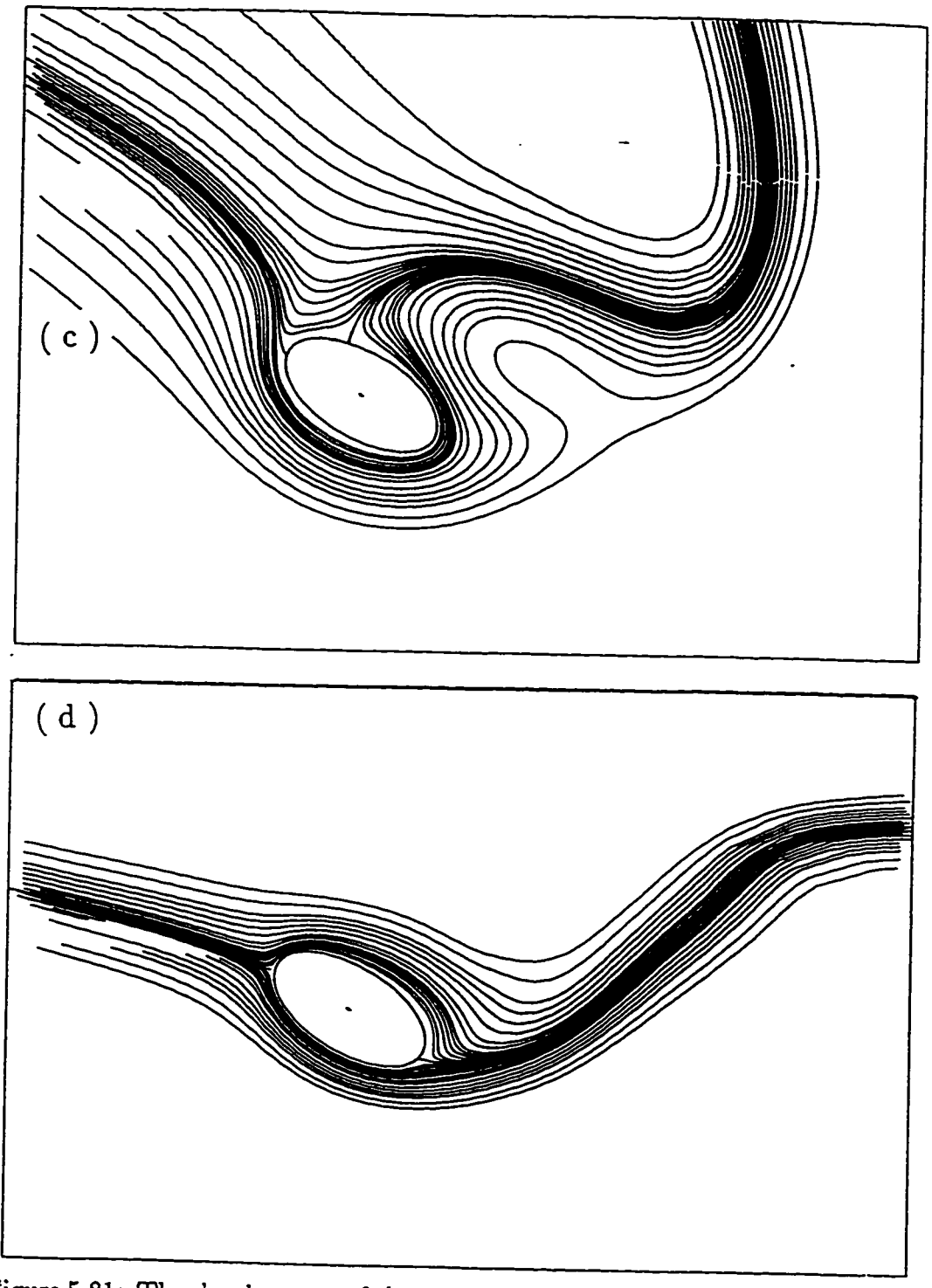

Figure 5.81: The development of the streamline patterns for the case of Re=50, Gr= 10000, Ar = 0.5, $\lambda = 30°$, $\beta = 0.5$ and $S = \pi/4$ during one complete cycle : (a) t = 32; (b) t = 34; (c) t = 36; (d) t = 40.

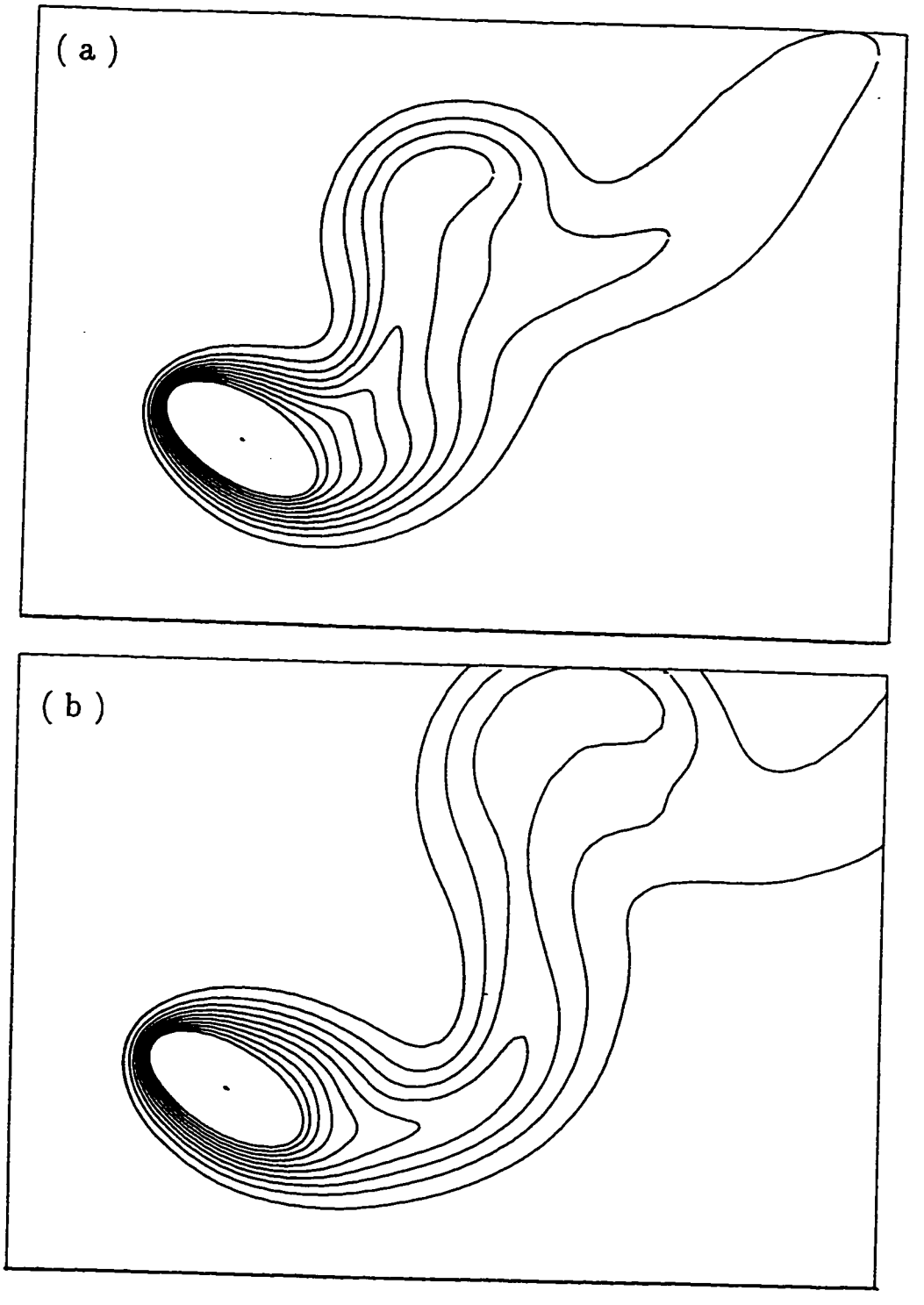
(a)
(b)

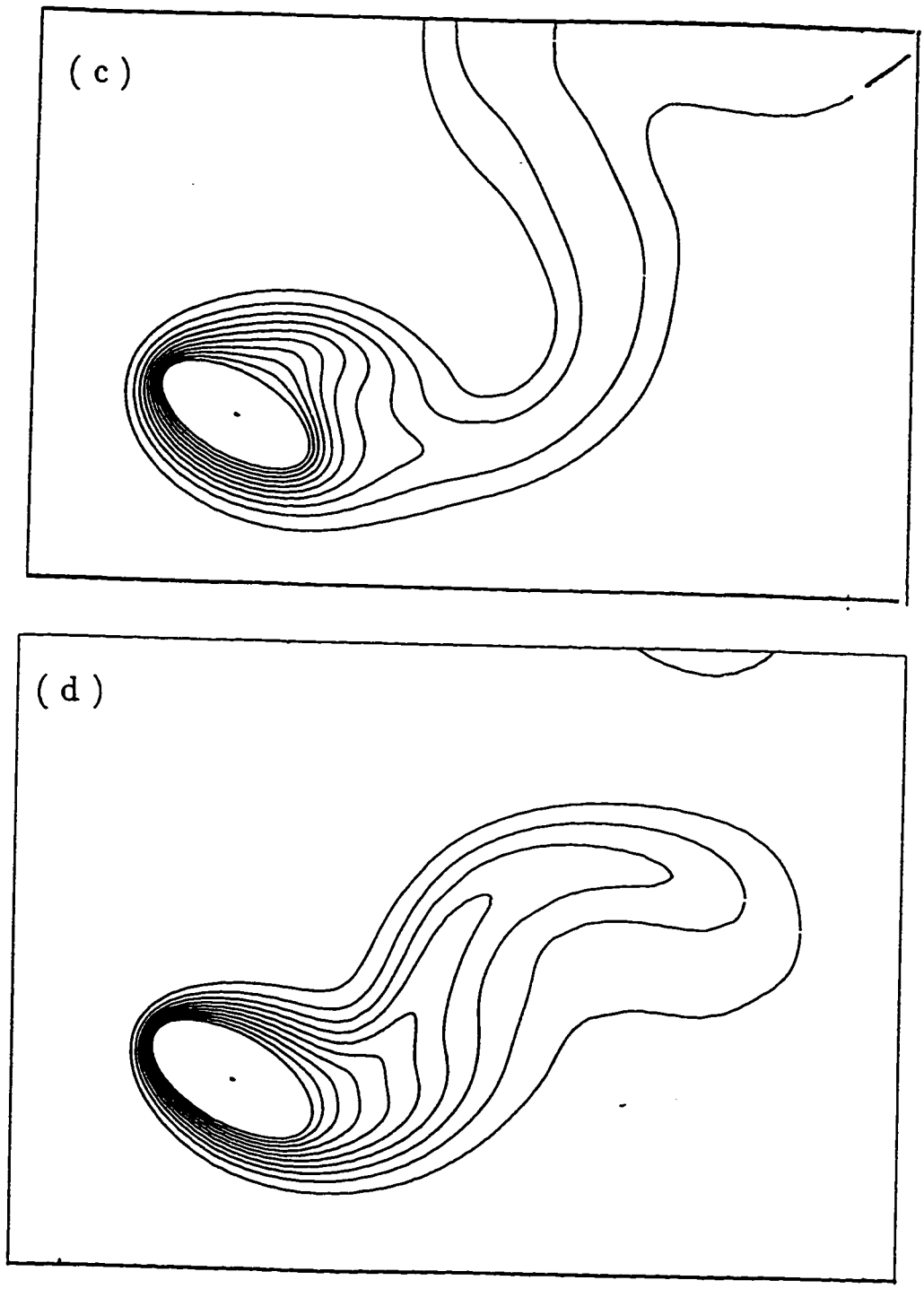

Figure 5.82: Time Development of the isotherm contours for the case of Re=50, Gr= 10000, Ar = 0.5, $\lambda = 30^o$, $\beta = 0.5$ and $S = \pi/4$ during one complete cycle : (a) t = 32; (b) t = 34; (c) t = 36; (d) t = 40.

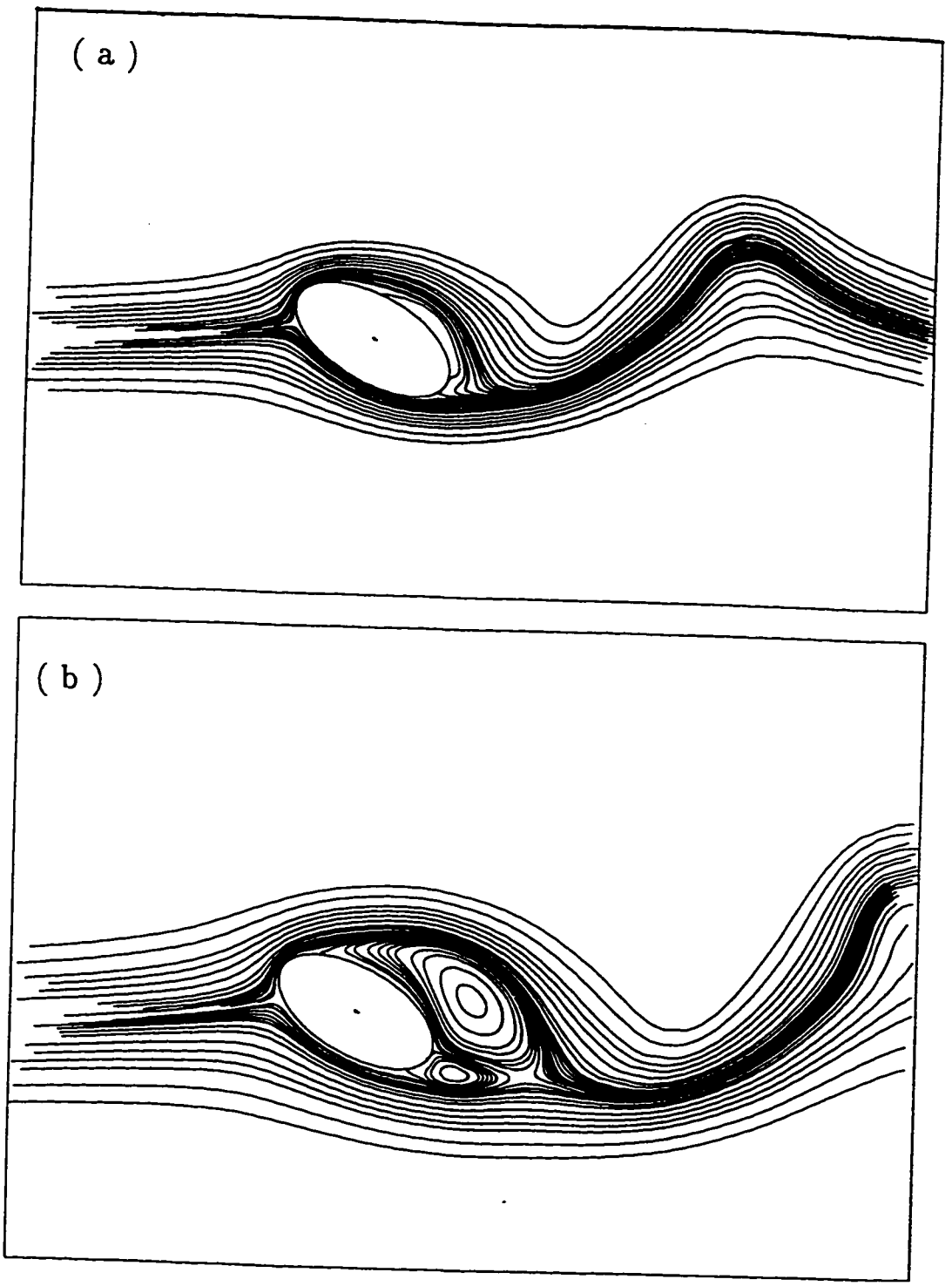
(a)
(b)

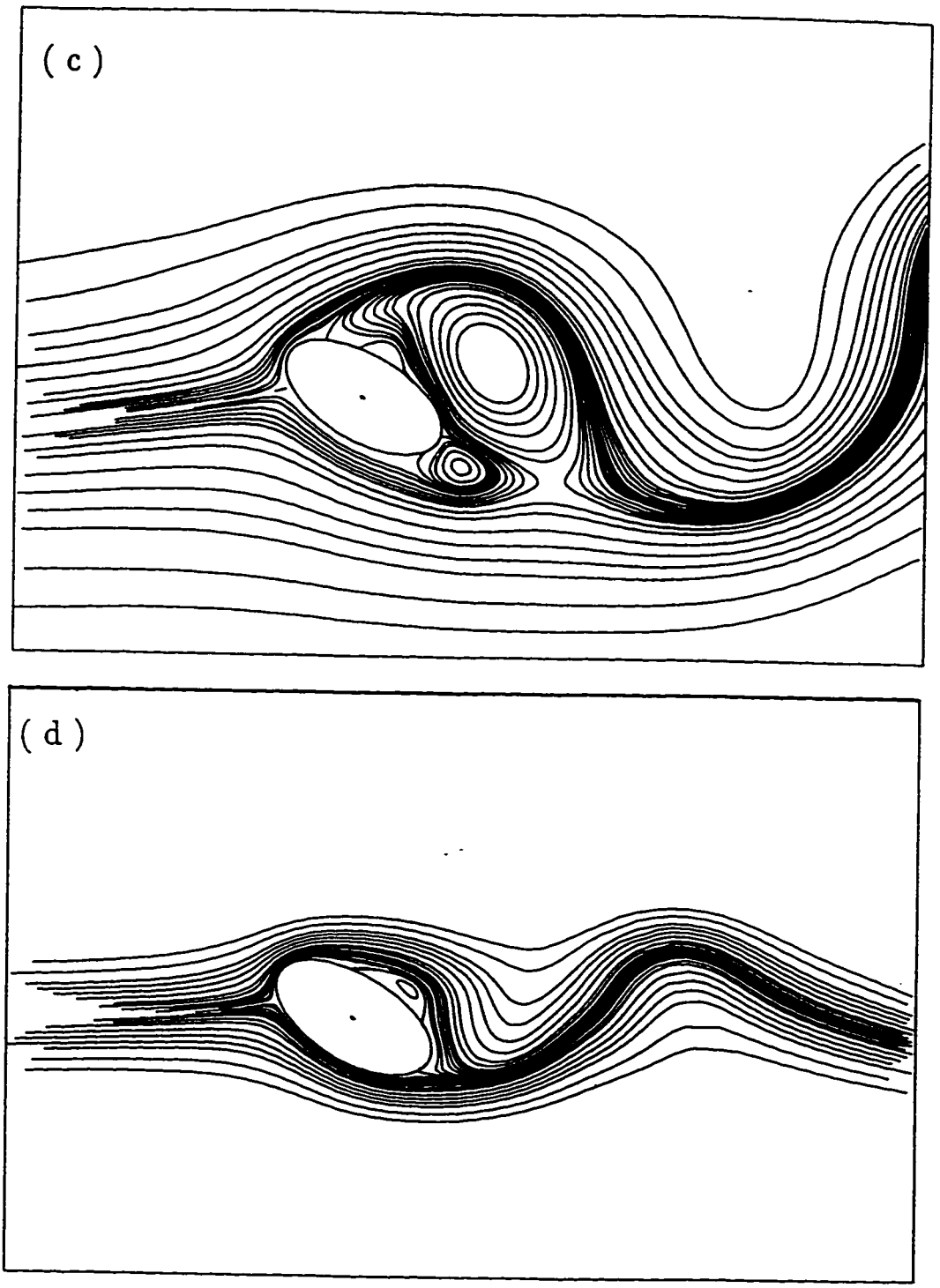

Figure 5.83: The development of the streamline patterns for the case of Re=200, Gr= 10000, Ar = 0.5, $\lambda = 30°$, $\beta = 0.25$ and $S = \pi/4$ during one complete cycle : (a) t = 32; (b) t = 34; (c) t = 36; (d) t = 40.

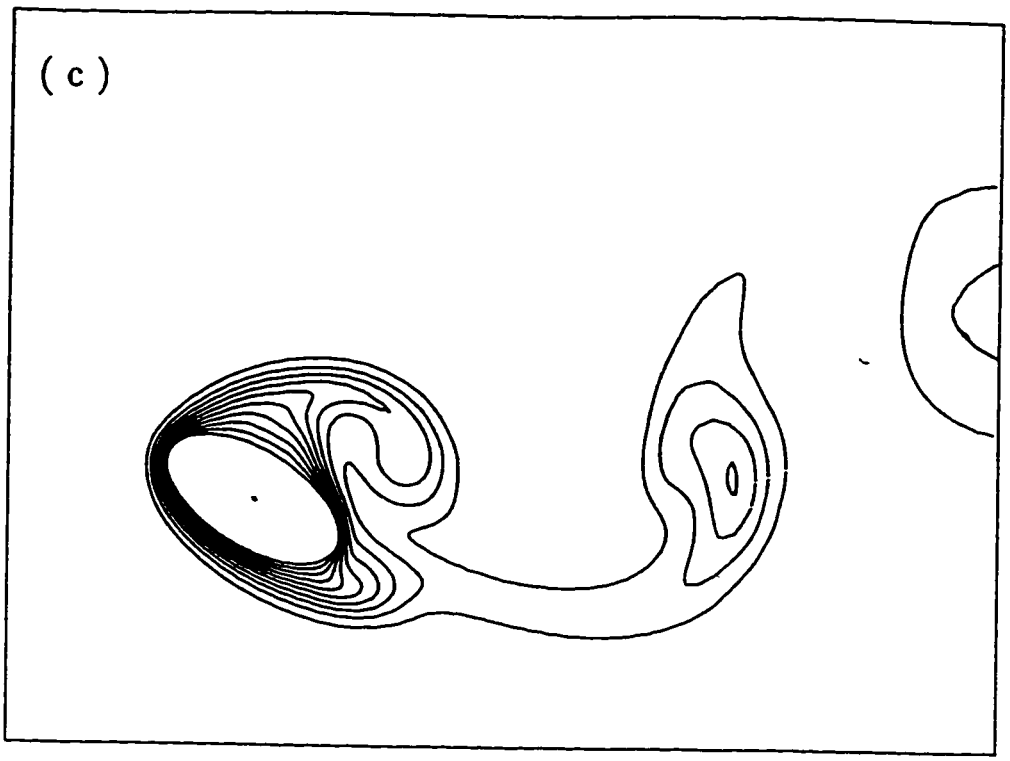
(c)

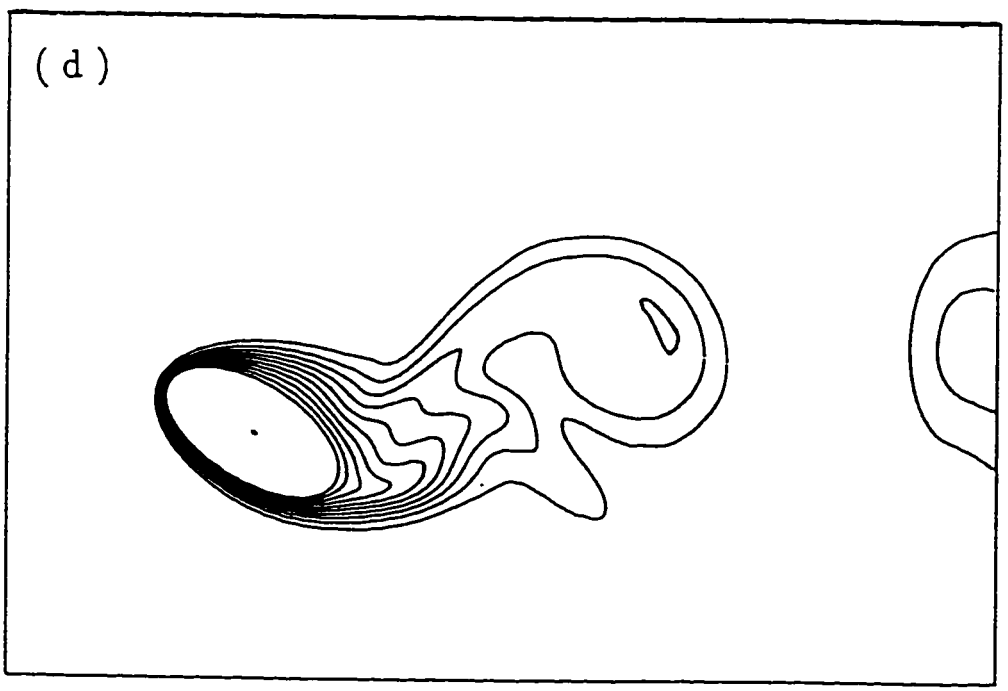
(d)

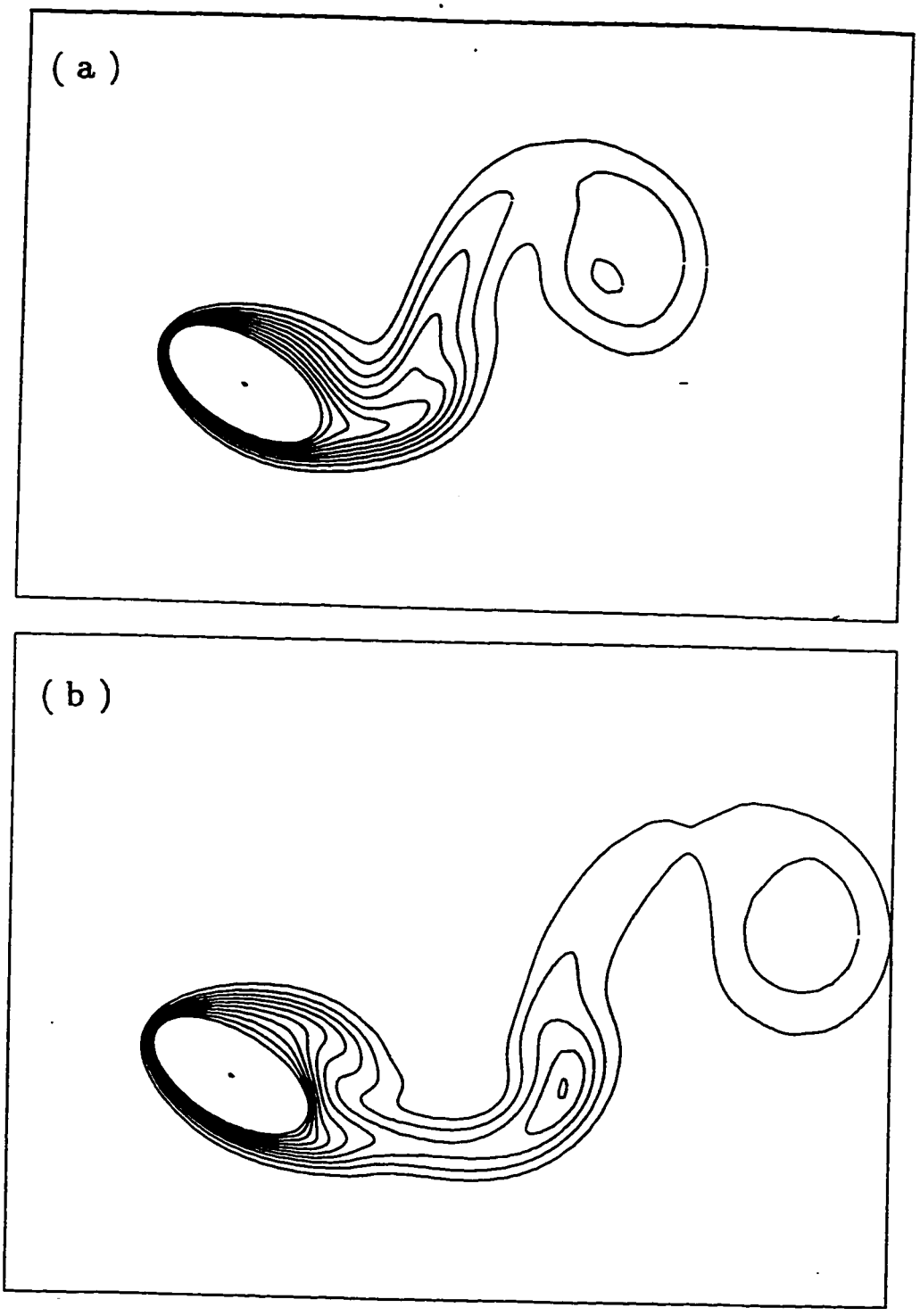

Figure 5.84: Time Development of the isotherm contours for the case of Re=200, Gr= 10000, Ar = 0.5, $\lambda = 30°$, $\beta = 0.5$ and $S = \pi/4$ during one complete cycle : (a) t = 32; (b) t = 34; (c) t = 36; (d) t = 40.

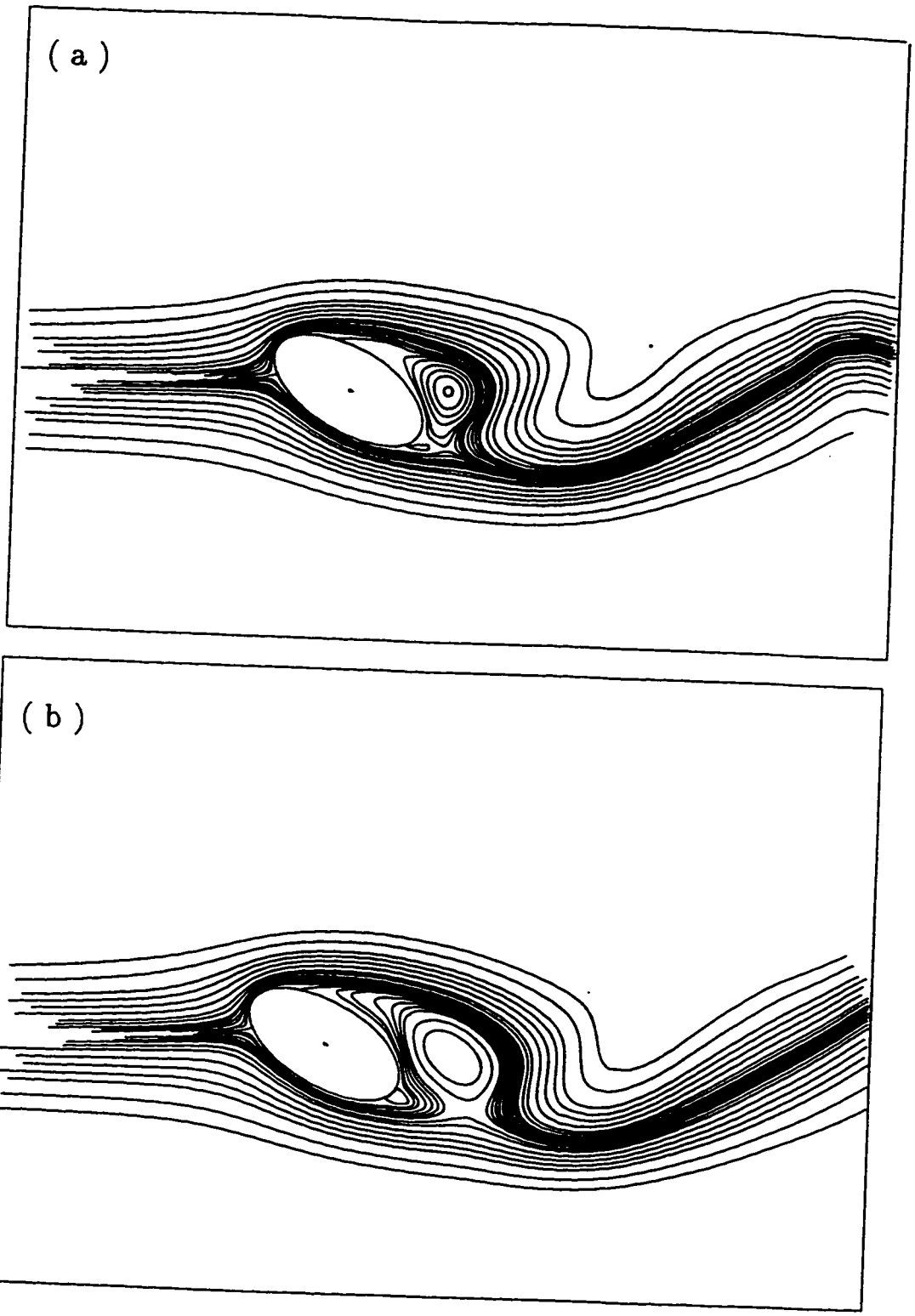
(a)
(b)

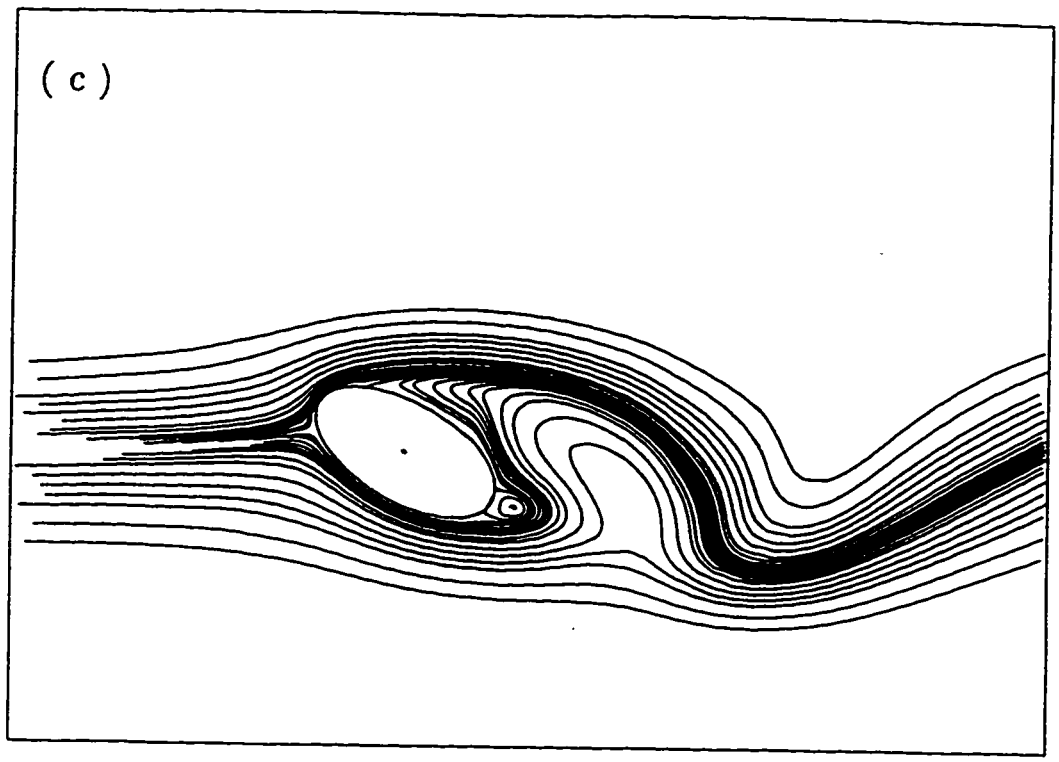
(c)

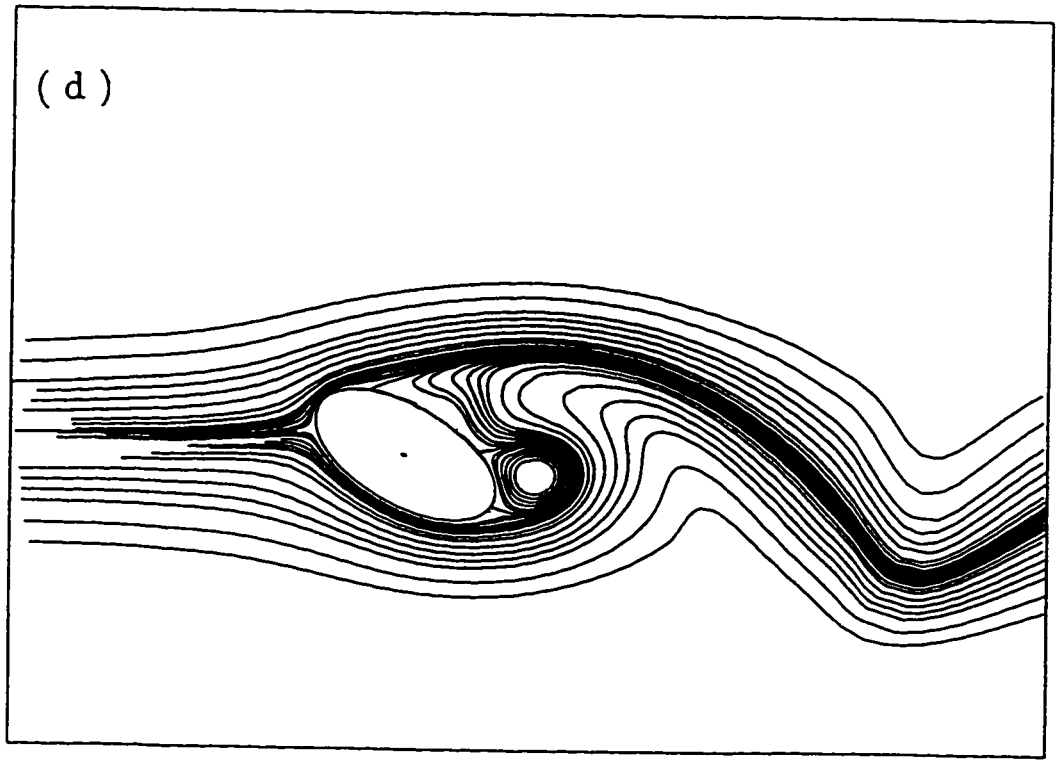
(d)

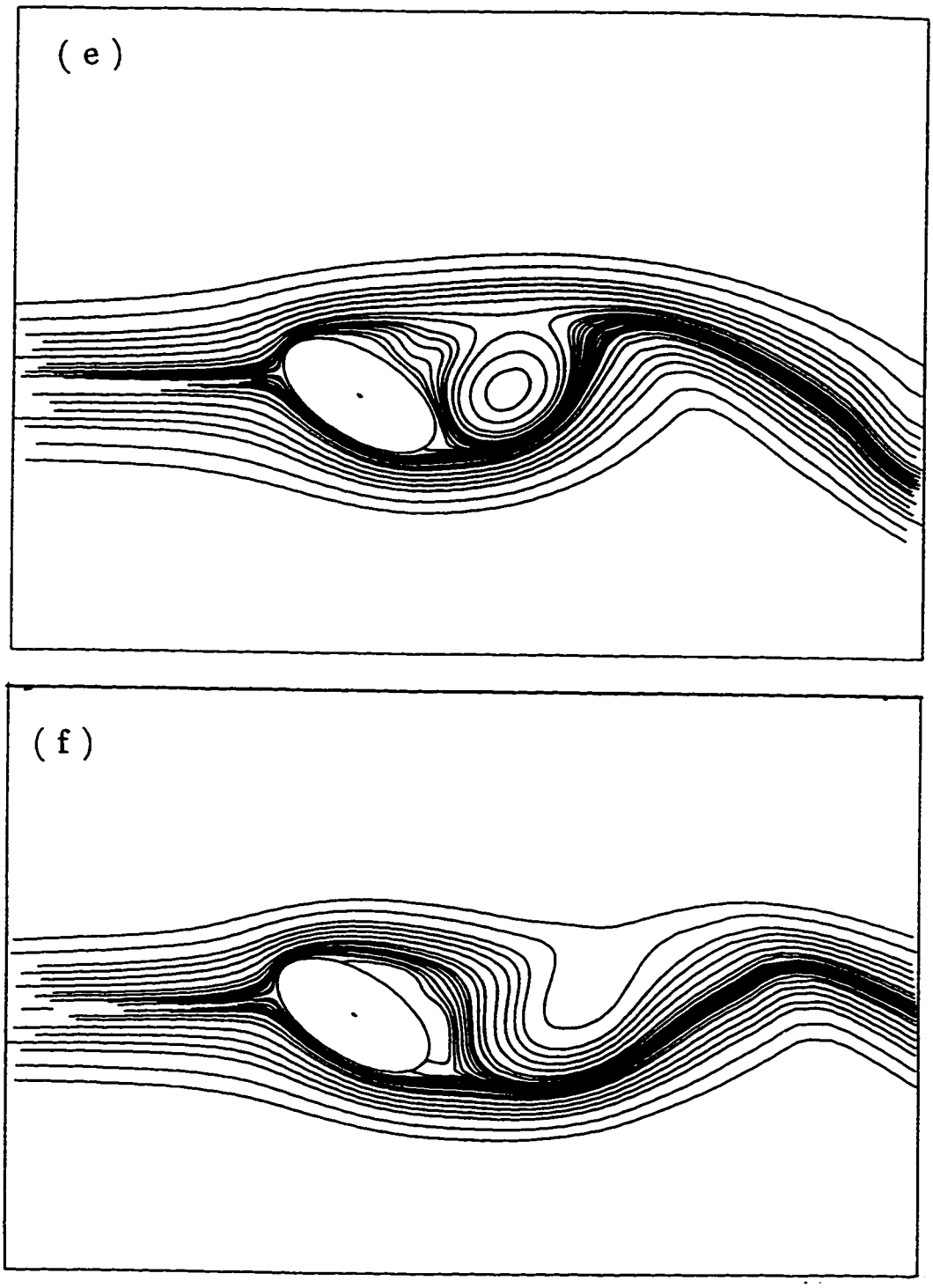

Figure 5.85: The development of the streamline patterns for the case of Re=500, Gr= 10000, $Ar = 0.5$, $\lambda = 30°$, $\beta = 0.5$ and $S = \pi/4$, during one time step : (a) t = 40; (b) t = 40.2; (c) t =40.4; (d) t = 40.6; (e) t = 40.8; (f) t = 41 .

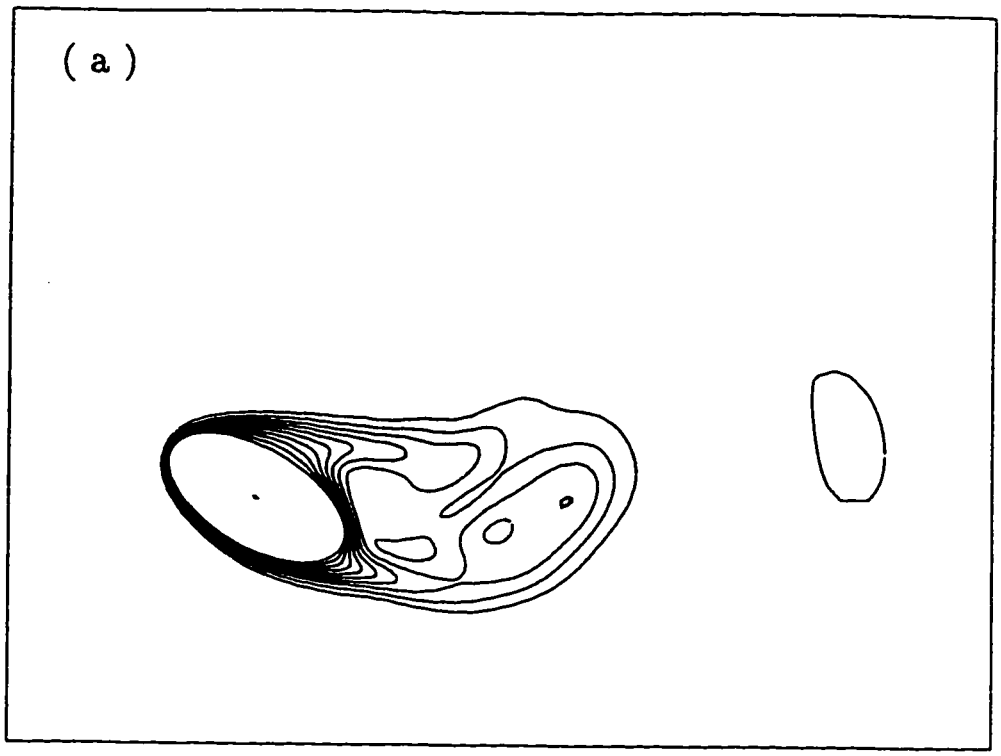
(a)

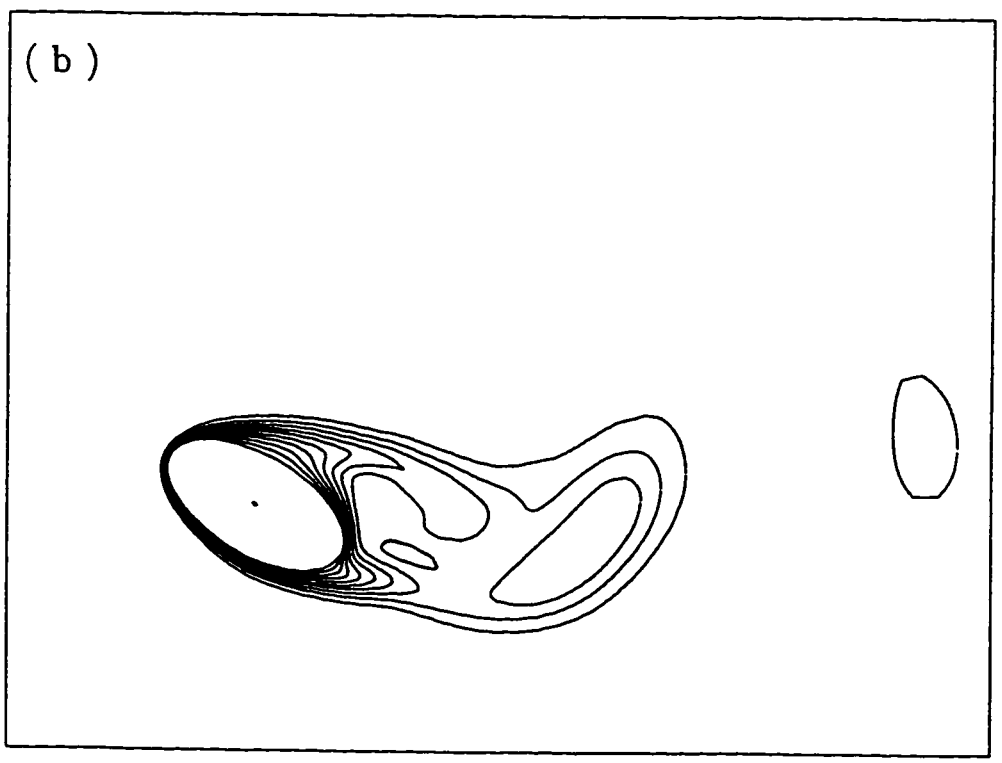
(b)

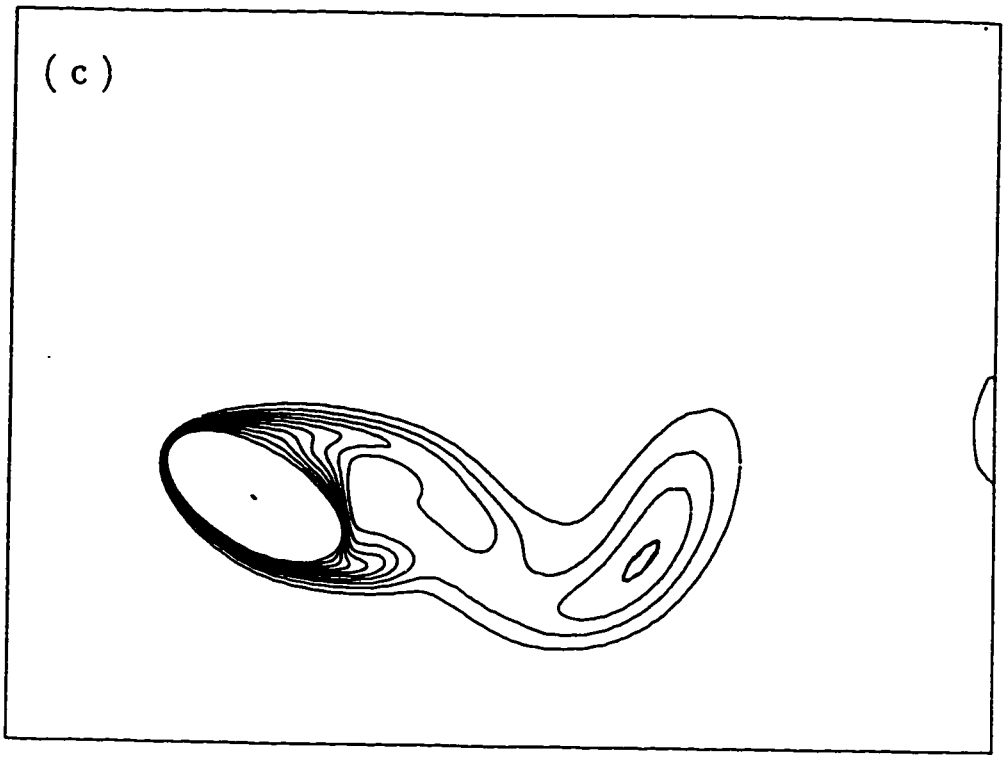
(c)

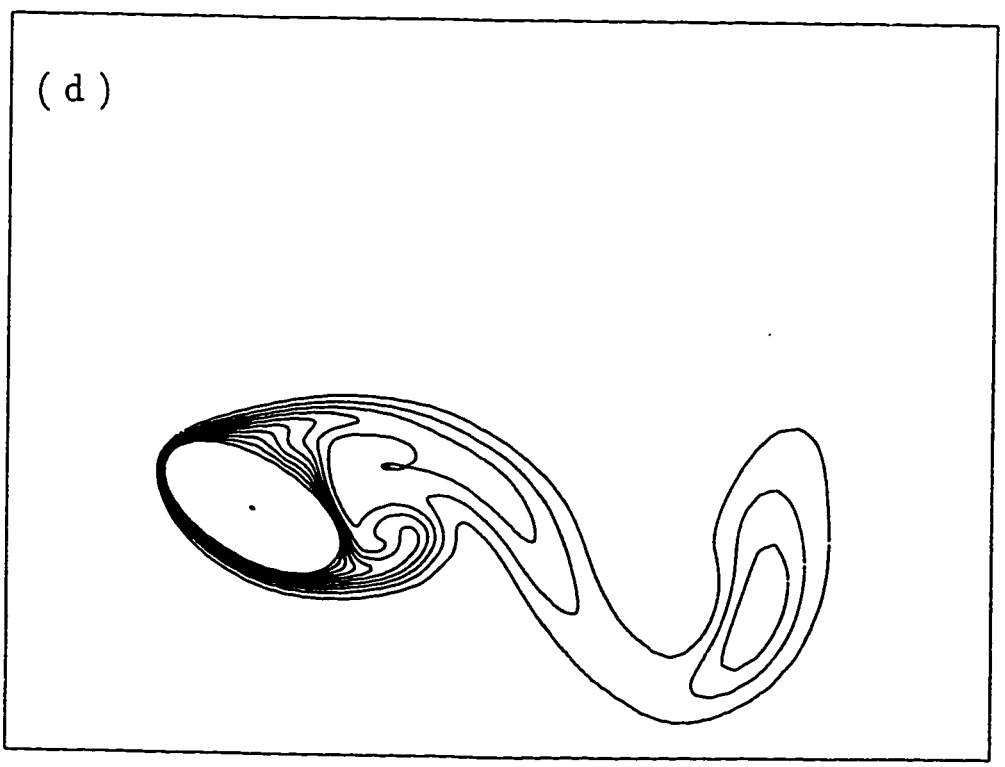
(d)

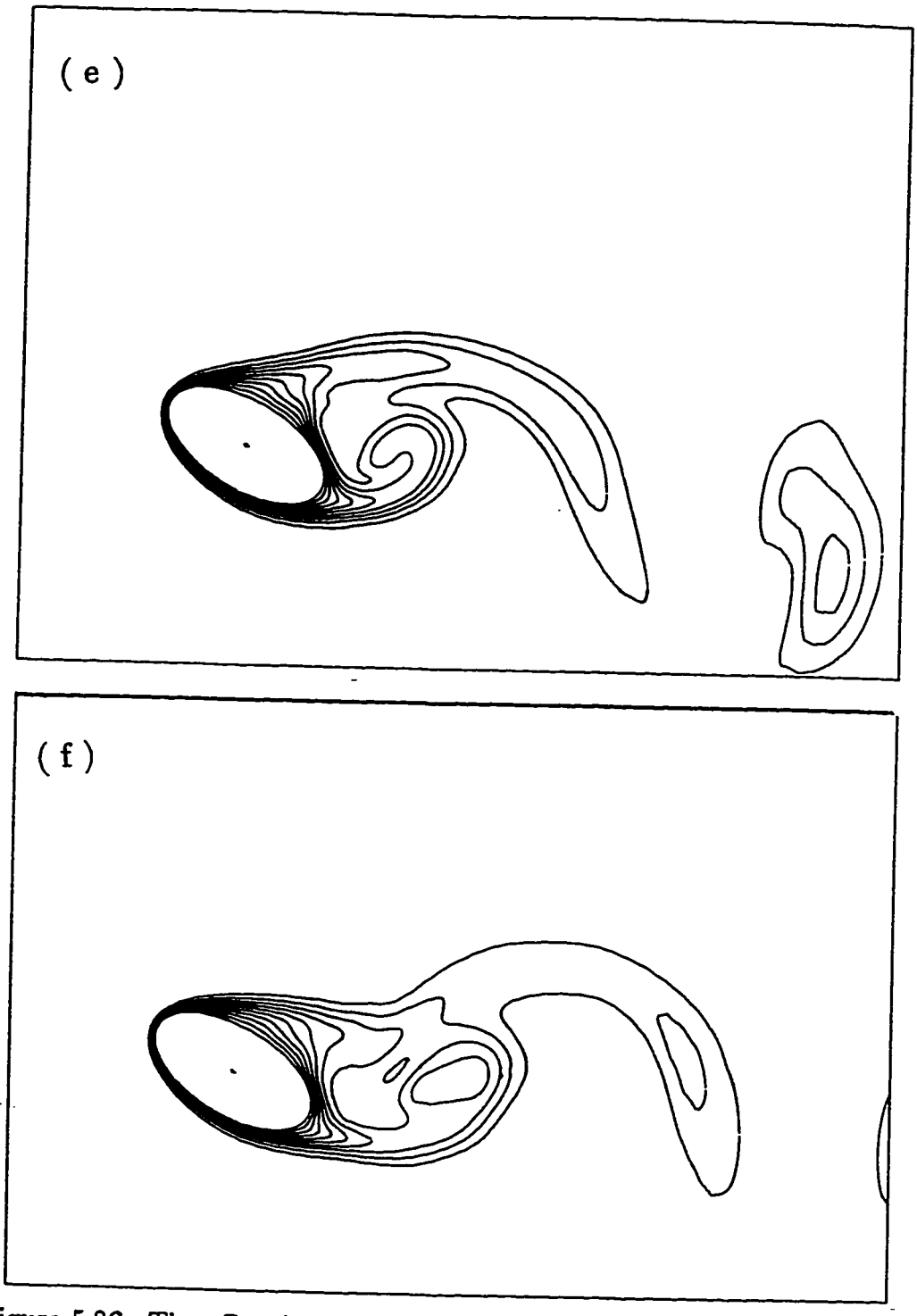

Figure 5.86: Time Development of the isotherm contours for the case of Re=500, Gr= 10000, Ar = 0.5, $\lambda = 30°$, $\beta = 0.5$ and $S = \pi/4$ during one time step : (a) t = 40; (b) t = 40.2; (c) t = 40.4; (d) t = 40.6; (e) t = 40.8; (f) t = 41.

5.6 The Effect of Grashof Number

In this section the effect of Gr on the flow and thermal fields, average and local Nusselt numbers, pressure and vorticity distributions is presented. The study covers values of Gr ranging from 0 to 50,000.

5.6.1 Effect of Grashof Number on the Average Nusselt Number

The numerical values of $\overline{\overline{Nu}}$ for different Gr values are given in Table 5.6 for all cases considered. It is clear from the table that the maximum increase in heat rates due to fluctuations occurs in the case of forced convection. Although increasing Gr tends to achieve higher heat rates, it suppresses the heat transfer enhancement due to free stream fluctuations.

Figure 5.87 shows the time variation of the average Nusselt number $\overline{Nu}$ following the sudden temperature rise of the tube surface for different Gr values. As the value of Gr increase $\overline{Nu}$ increases as expected since the buoyant stream tends to increase the effective Reynolds number. One can deduce from the figure that as Gr increases, more time is needed for the fluctuation of the $\overline{Nu}$ to reach a quasi-steady state.

The time average Nusselt number, $\overline{\overline{Nu}}$ is compared with the steady free stream Nusselt number for different Gr values as shown in figures 5.88 to 5.91. One can deduce that for the pure forced convection case, imposing fluctuation in the ap-

proaching stream enhances the heat transfer rate as shown in Figure 5.88. When Gr increases heat transfer rate is further increased while the heat transfer enhancement when compared to the steady stream case is higher than that in forced convection. Figure 5.91 clearly shows that when Gr reaches high values (Gr=50,000), the heat transfer enhancement due to main stream fluctuations is decreased (in comparison with Gr=30,000).

Table 5.6: The percentage increase in $\overline{\overline{Nu}}$ caused by different amplitudes and frequencies for different Grashof numbers compared to the steady stream case.

Code #	Re	Gr	λ	b/a	S	β	$\overline{\overline{Nu}}$	$\overline{Nu}$ $\beta = 0$	% increase
D-1	100	0	30°	0.5	$\frac{\pi}{4}$	0.25	6.07	5.9	2.93 %
D-2	100	0	30°	0.5	$\frac{\pi}{4}$	0.50	5.80	6.23	5.66 %
D-3	100	0	30°	0.5	$\frac{\pi}{2}$	0.25	6.04	5.9	2.40 %
D-4	100	0	30°	0.5	$\frac{\pi}{2}$	0.50	6.15	5.9	4.30 %
D-5	100	30000	30°	0.5	$\frac{\pi}{4}$	0.25	6.43	6.21	3.64 %
D-6	100	30000	30°	0.5	$\frac{\pi}{4}$	0.50	6.63	6.21	6.83 %
D-7	100	30000	30°	0.5	$\frac{\pi}{2}$	0.25	6.35	6.21	2.41 %
D-8	100	30000	30°	0.5	$\frac{\pi}{2}$	0.50	6.50	6.21	5.80 %
D-9	100	50000	30°	0.5	$\frac{\pi}{4}$	0.25	6.73	6.57	2.43 %
D-10	100	50000	30°	0.5	$\frac{\pi}{4}$	0.50	6.97	6.57	6.10 %
D-11	100	50000	30°	0.5	$\frac{\pi}{2}$	0.25	6.71	6.57	2.10%
D-12	100	50000	30°	0.5	$\frac{\pi}{2}$	0.50	6.95	6.57	5.78 %

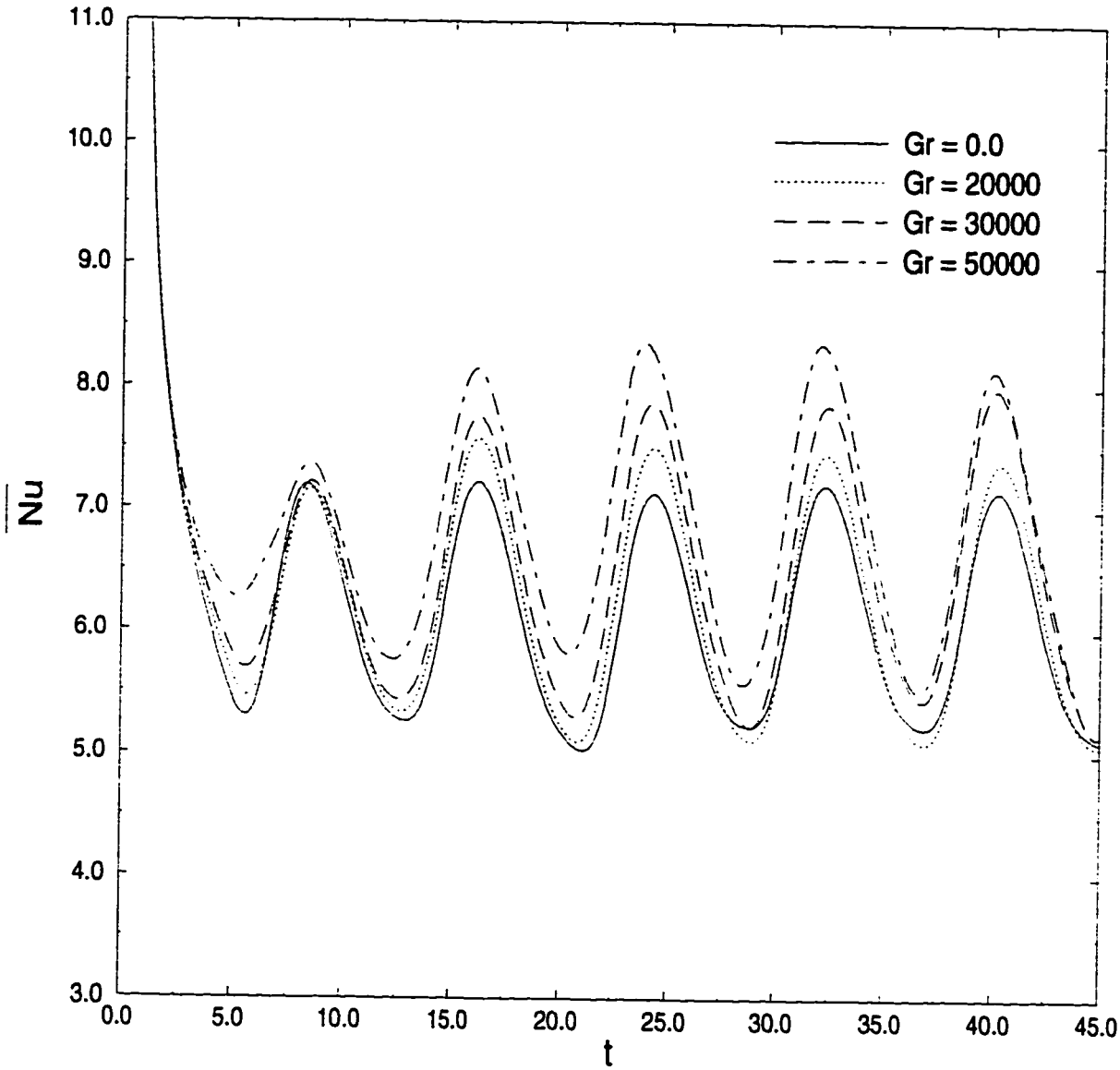

Figure 5.87: The time variation of $\overline{Nu}$ following the sudden temperature rise for various Grashof numbers for the case of Re=100, Ar=0.5, $\lambda = 30.0^o$, $\beta = 0.5$ and $S = \pi/4$.

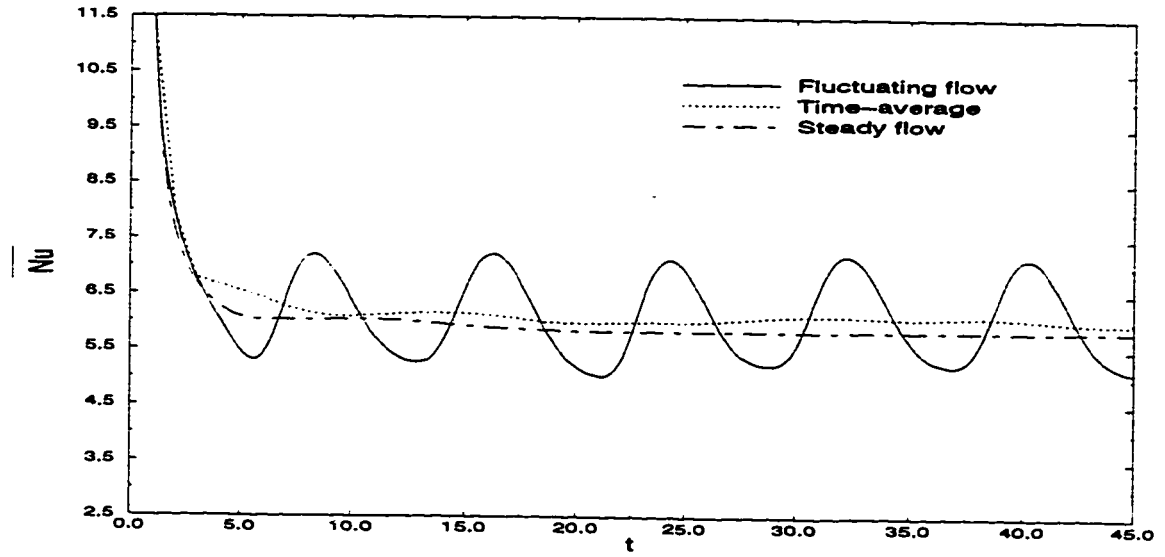

Figure 5.88: The variation of $\overline{Nu}$ for case of D-2 and comparison with the steady free stream.

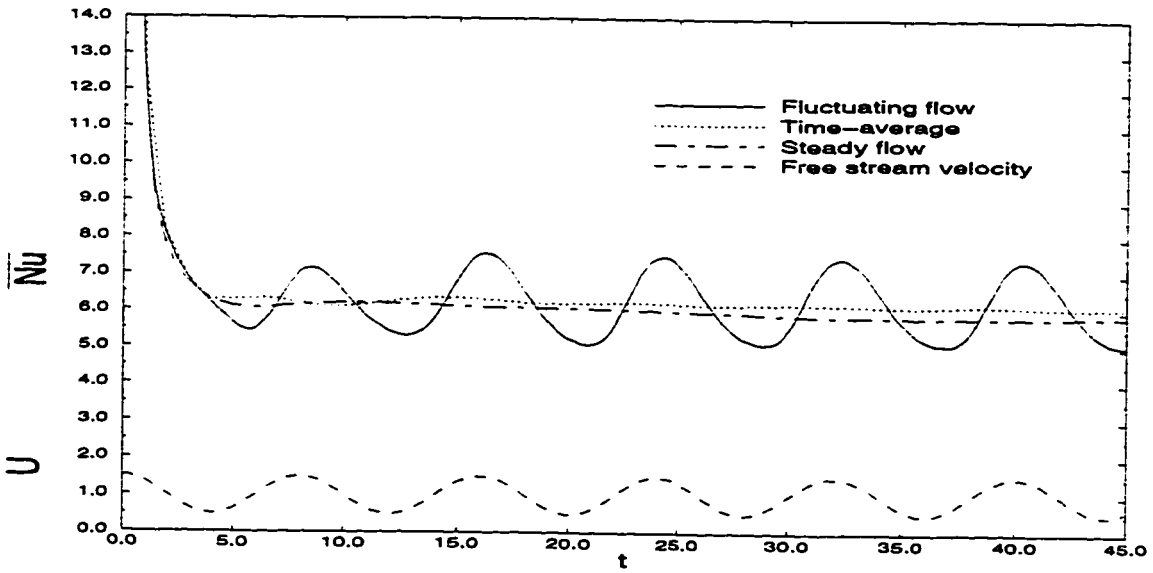

Figure 5.89: The variation of $\overline{Nu}$ for case of A-5 and comparison with the steady free stream.

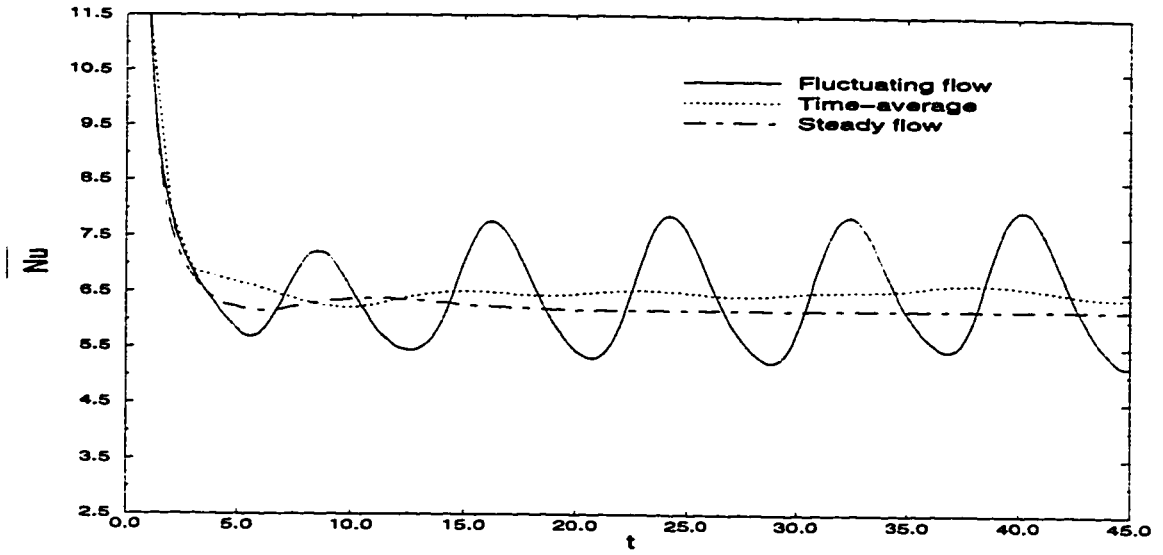

Figure 5.90: The variation of $\overline{Nu}$ for case of D-6 and comparison with the steady free stream.

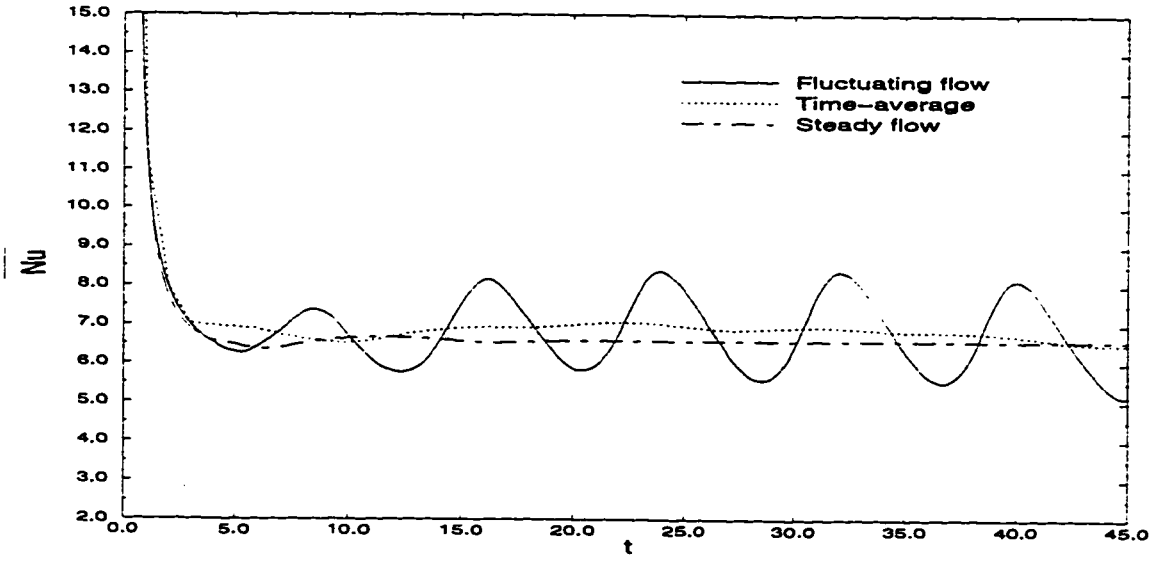

Figure 5.91: The variation of $\overline{Nu}$ for case of D-12 and comparison with the steady free stream.

5.6.2 The effect of Grashof Number on the Local Nusselt Number, Pressure and Vorticity Distributions

Figures 5.92 and 5.93 show the local Nusselt number distribution for different Gr values when the free stream velocity is maximum and minimum, respectively. When the free stream velocity is maximum there is a slight increase in the heat transfer rate between the lowest and highest Gr values. The maximum local Nusselt number for Gr=50,000 occurs at $\eta = 180^o$ while this value is shifted towards $\eta = 190^o$ for Gr = 0. When the free stream velocity is minimum (Figure 5.93) the maximum local Nu occurs at $\eta = 180^o$ and the minimum occurs at η between 60^o and 100^o depending on the value of Gr. Moreover, the increase of Gr causes Nu to increase on the entire surface except in the region between $\eta = 0^o$ and $\eta = 60^o$ at which the effect is reversed. The surface vorticity distributions are plotted in figures 5.94 and 5.95 for maximum and minimum free stream velocities. Figure 5.95 shows that $|\zeta_s|$ increases with the increase of Gr over most of the tube surface indicating a higher velocity gradient, as expected, as a result of the increase in the buoyancy forces. Such a velocity increase leads to an increase in the heat transfer rate.

The local Nusselt number distribution around the tube surface at different times together with a comparison with the steady stream case are plotted in Figures 5.96, 5.97 and 5.98 for Gr = 0, 30,000, and 50,000 respectively. The forced convection case is shown in Figure 5.96. In this figure the local Nusselt number increases

and decreases with the free stream velocity except in the tube wake where vortex formation and shedding is the dominating factor in deciding the heat transfer rate. To understand this phenomenon, the vorticity distributions for the same case and same times are plotted in Figure 5.99. It is depicted from the figure that the absolute value of the surface vorticity is higher for higher free stream velocity in most of the tube surface except in the region $0^o \leq \eta \leq 80^o$. In this region the highest value of $|\zeta_s|$ is occurring when the free stream velocity is minimum and this gives a high velocity gradient and as a result a high heat transfer rate.

The pressure distribution is plotted for different Gr values in Figures 5.100 and 5.101 for maximum and minimum free stream velocity respectively. From Figure 5.100, one can deduce that increasing Grashof number results in a considerable pressure reduction around the tube surface. The zones of minimum pressure occurred in all cases between $120^o \leq \eta \leq 160^o$. However the exact location is a function of Grashof number. For example, the minimum pressure take place at $\eta = 155^o$, 136^o and 123^o for Gr = 0, 20000 and 30000 respectively. The buoyancy forces become more effective in increasing the pressure at the tube front near $\eta = 180^o$. Figures 5.102 and 5.103 show the pressure distribution at different times with a comparison to the no fluctuation case for Gr = 0 and Gr = 30000 respectively. Figure 5.102 shows that for the pure forced convection case the pressure drop around the tube increases sharply as the free stream velocity increases. Figure 5.103 shows the pres-

sure variations around the tube surface at different times with comparison to steady flow pressure distributions.

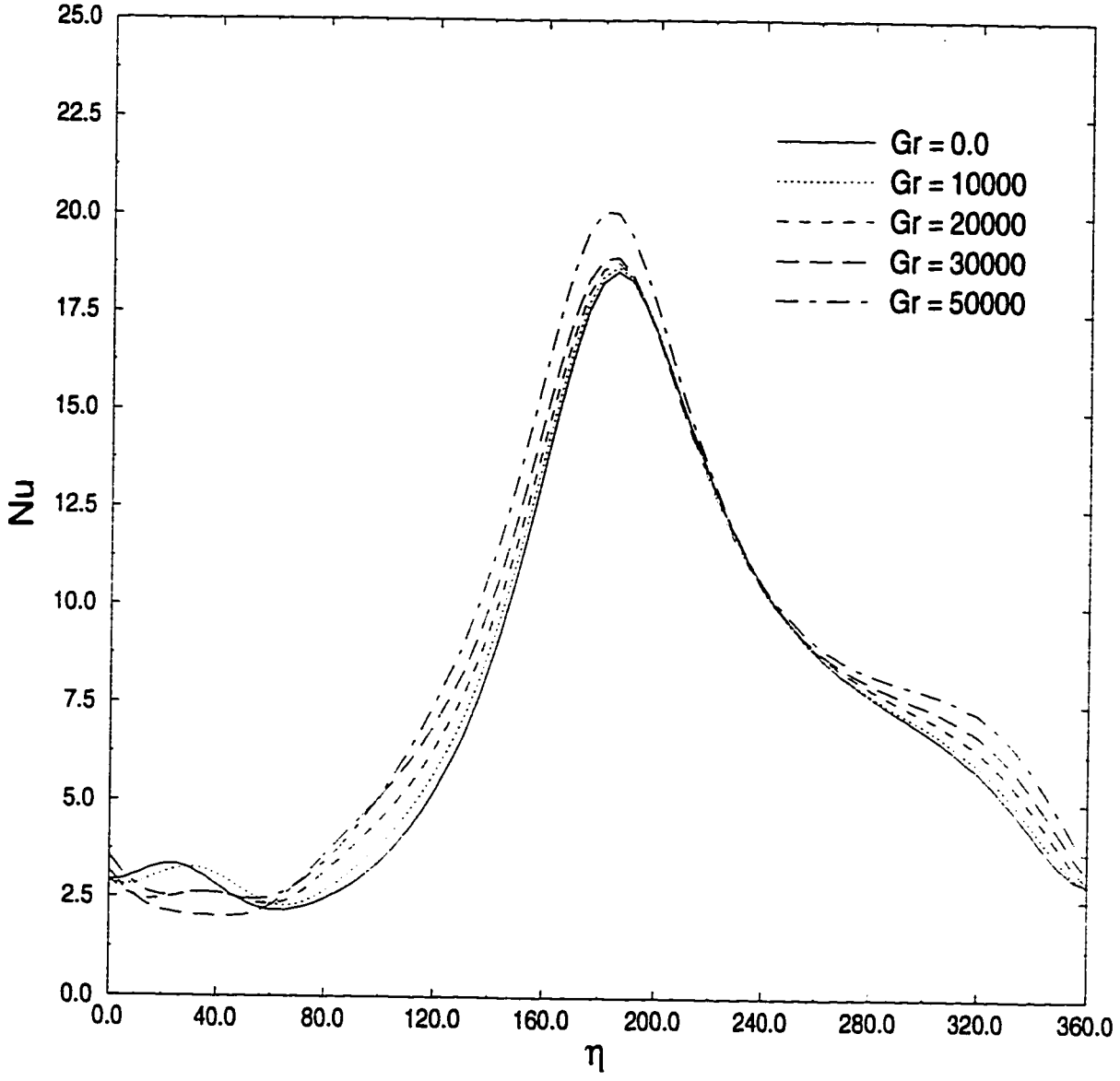

Figure 5.92: The effect of Grashof number on the local Nusselt number distribution at maximum free stream velocity for the case of Re=100, Ar=0.5, $\lambda = 30^o$, $\beta = 0.5$ and $S = \pi/4$.

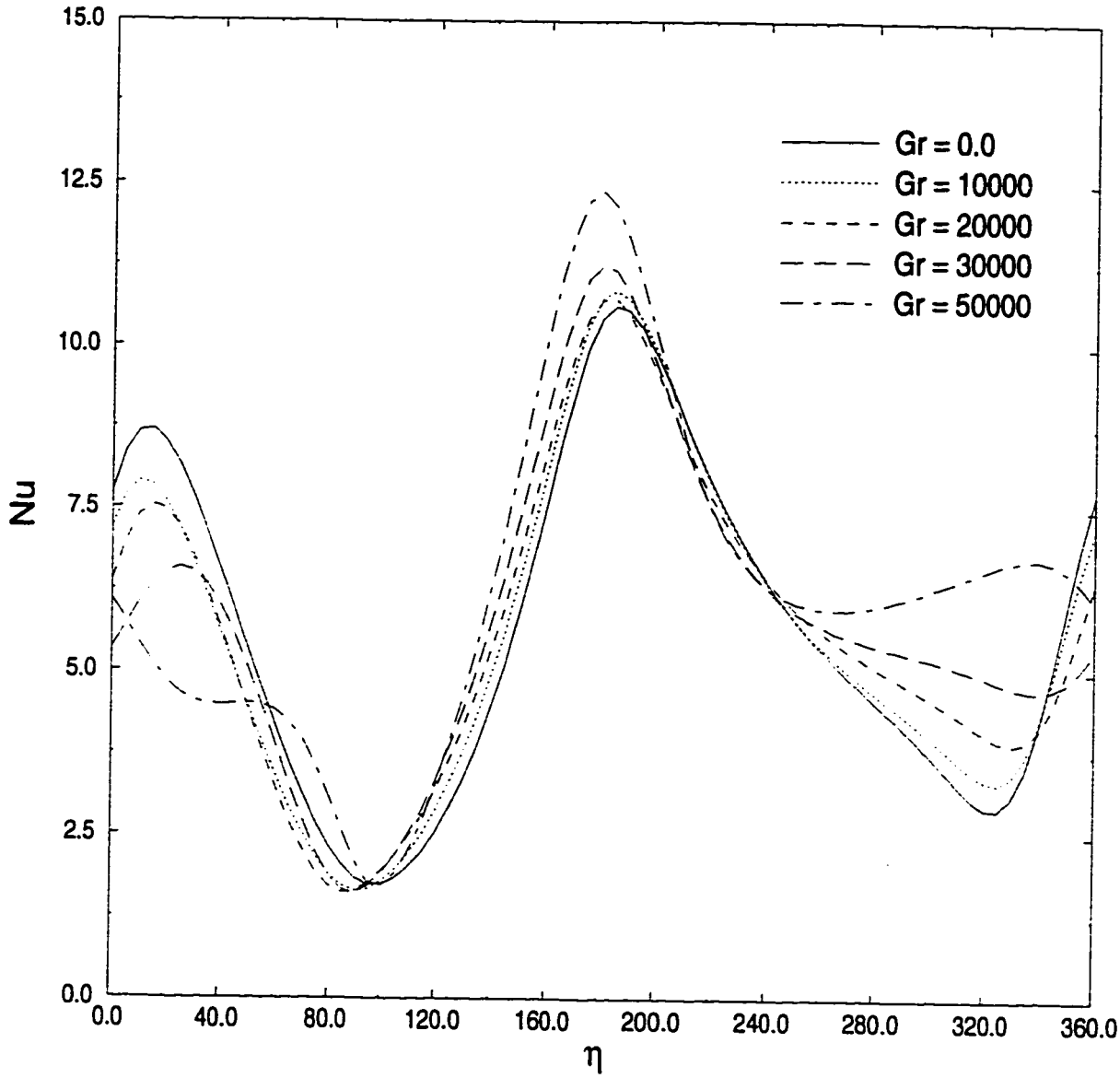

Figure 5.93: The effect of Grashof number on the local Nusselt number distributions at minimum free stream velocity for the case of Re=100, Ar=0.5, $\lambda = 30°$, $\beta = 0.5$ and $S = \pi/4$.

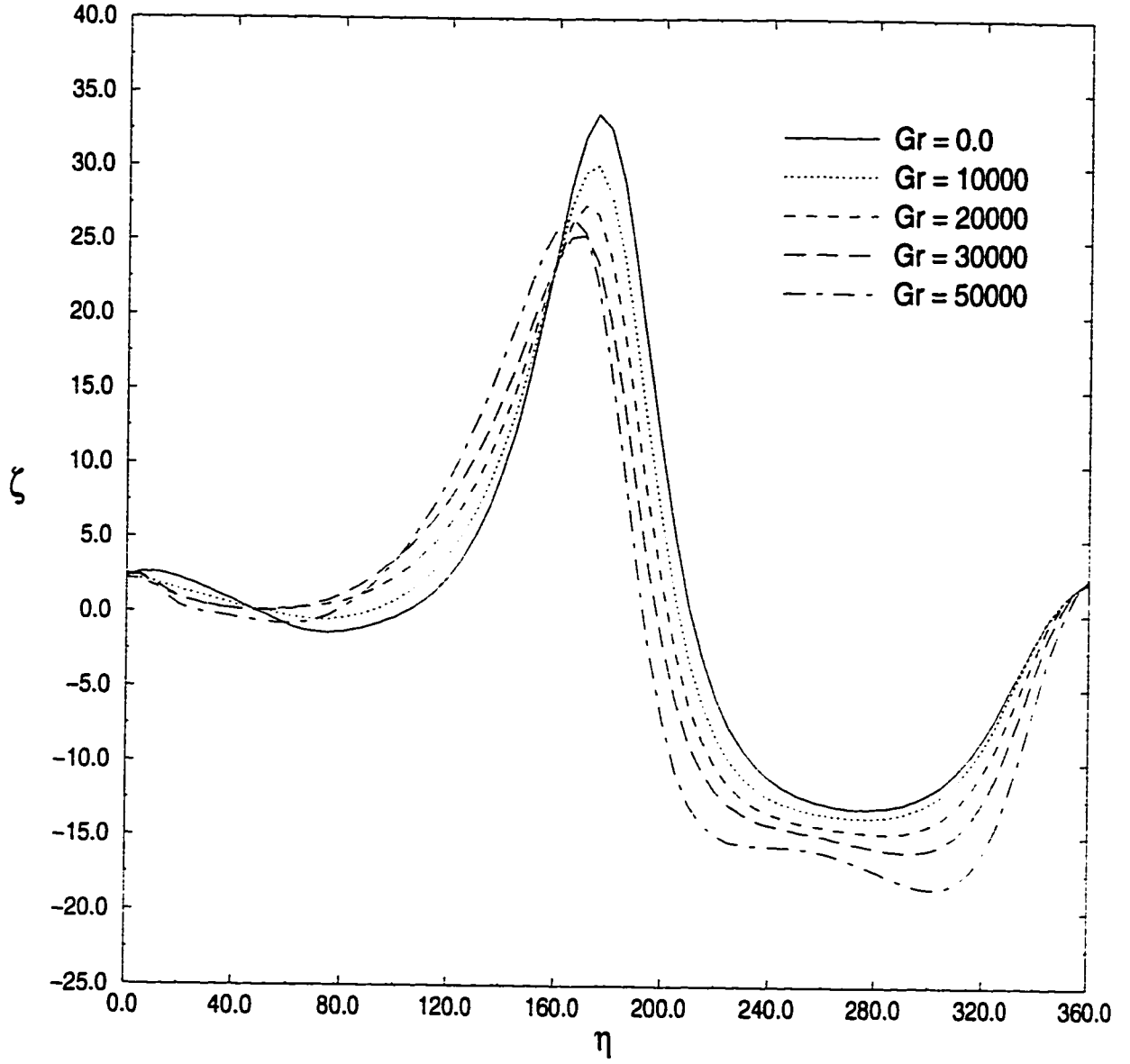

Figure 5.94: The effect of Grashof number on the vorticity distribution at maximum free stream velocity for the case of Re=100, Ar = 0.5 and $\lambda = 30^o$, $\beta = 0.5$ and $S = \pi/4$.

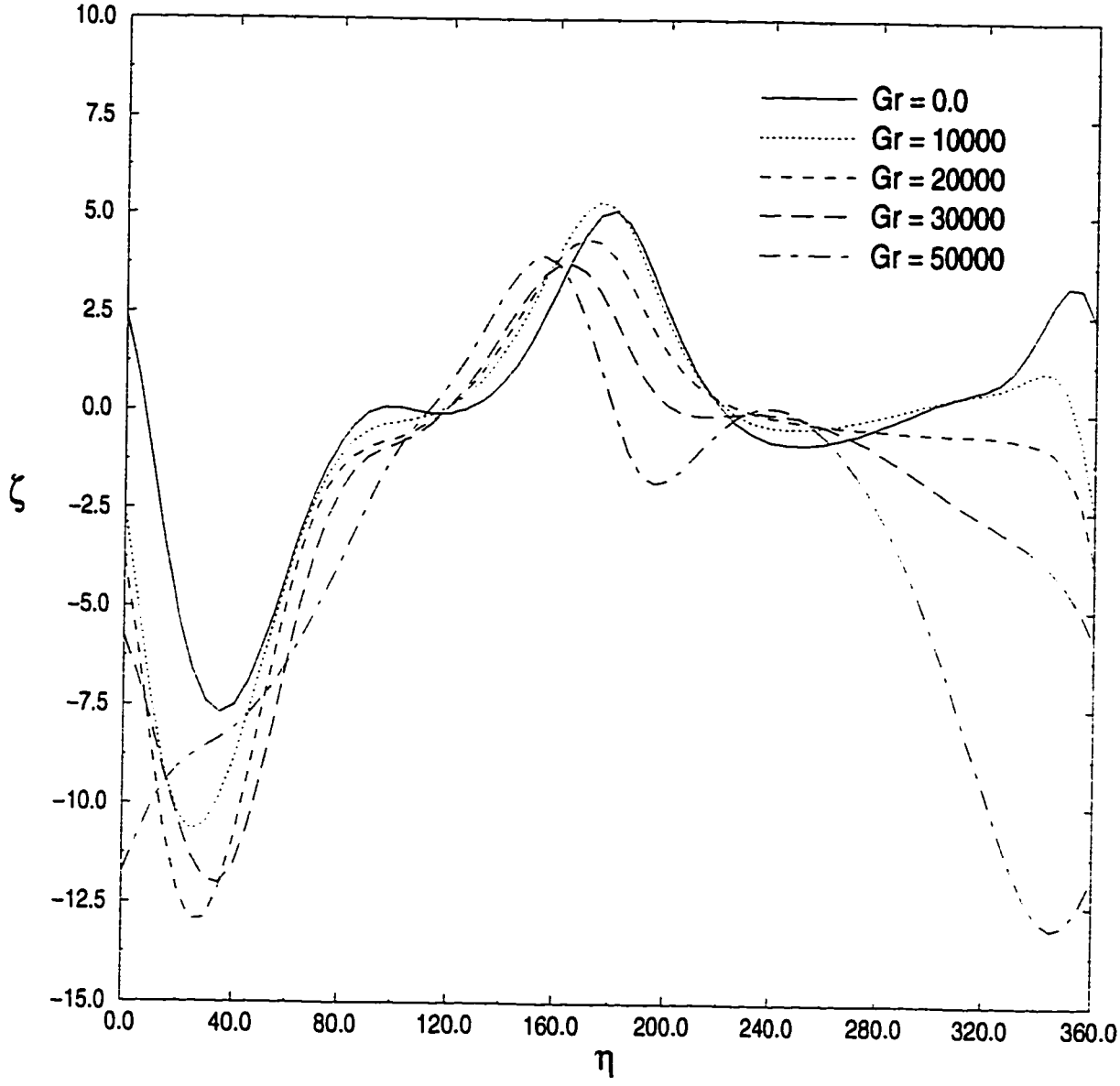

Figure 5.95: The effect of Grashof number on the vorticity distribution at minimum free stream velocity for the case of Re=100, Ar=0.5, $\lambda = 30°$, $\beta = 0.5$ and $S = \pi/4$.

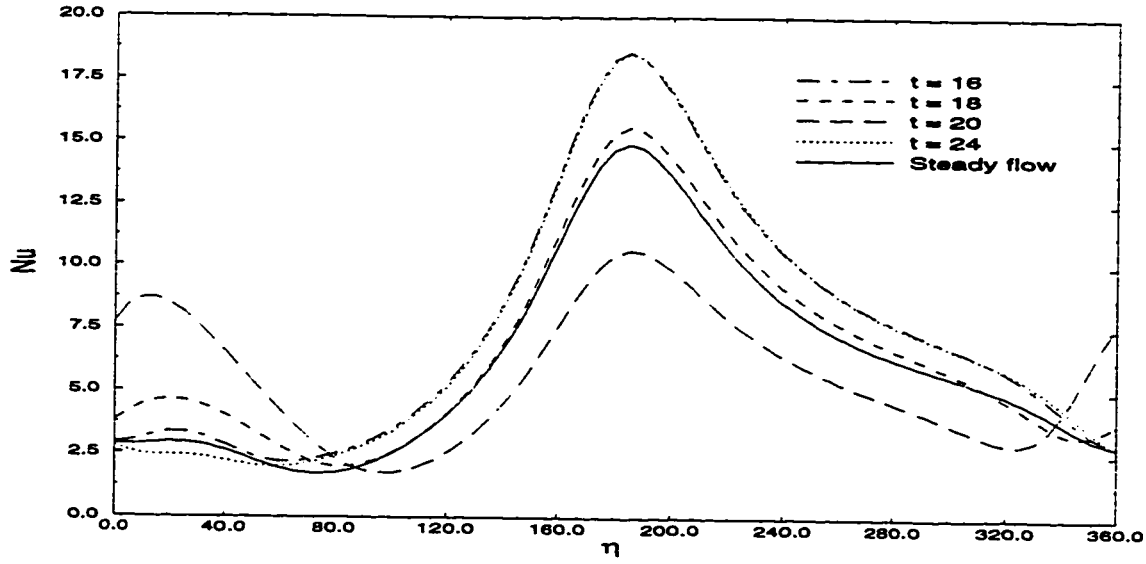

Figure 5.96: The local Nusselt number distribution at various times during one complete cycle in case D-2 and comparison with the steady free stream.

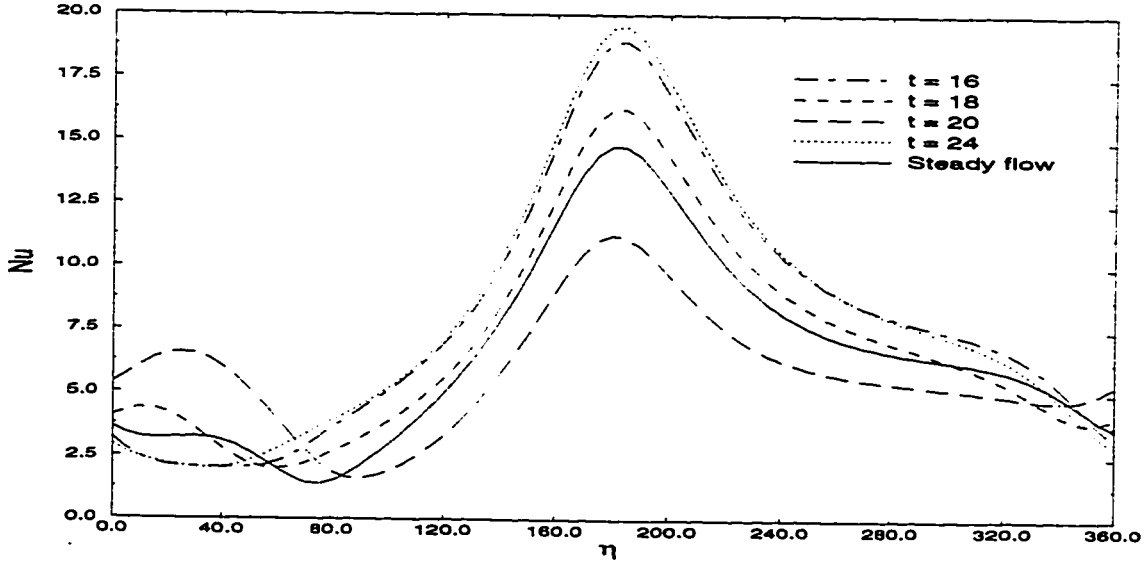

Figure 5.97: The local Nusselt number distribution at various times during one complete cycle in case D-6 and comparison with the steady free stream.

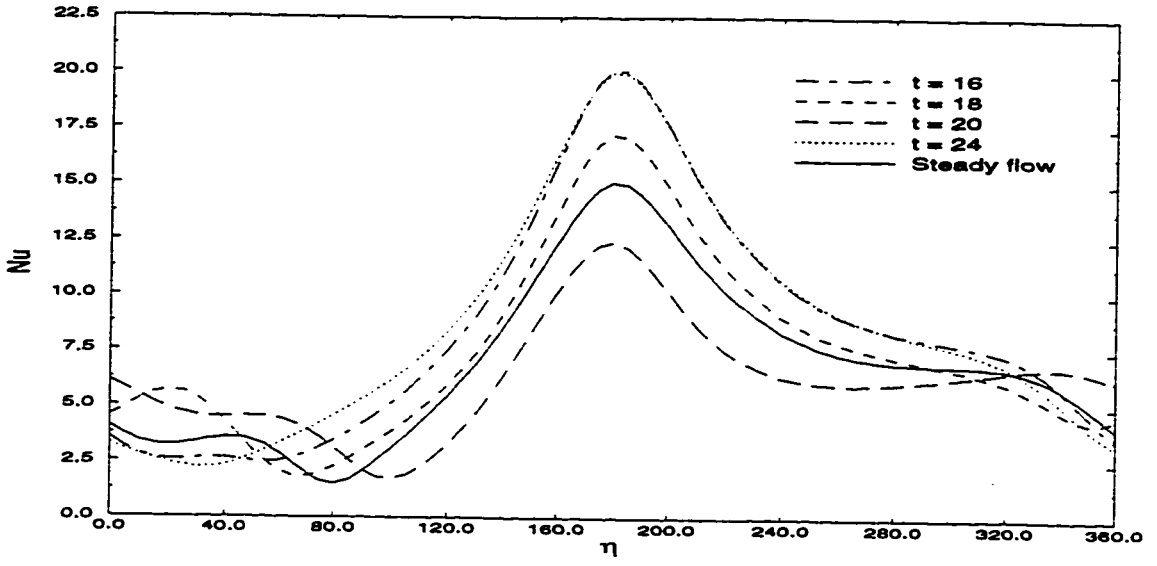

Figure 5.98: The local Nusselt number distribution at various times during one complete cycle in case D-9 and comparison with the steady free stream.

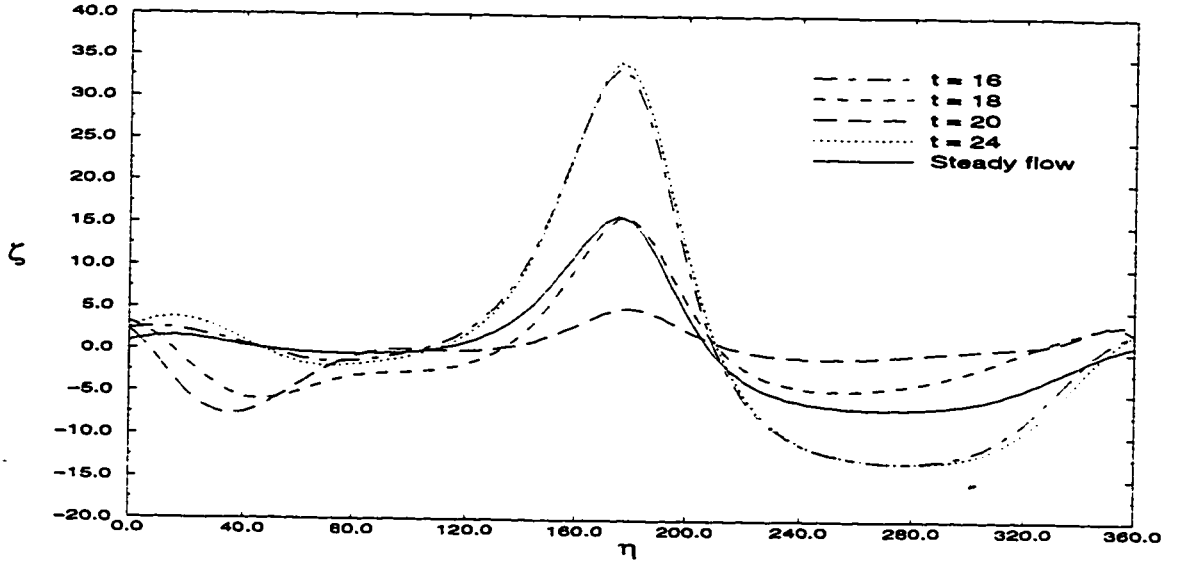

Figure 5.99: The surface vorticity distribution at various times during one complete cycle in case D-2 and comparison with the steady free stream.

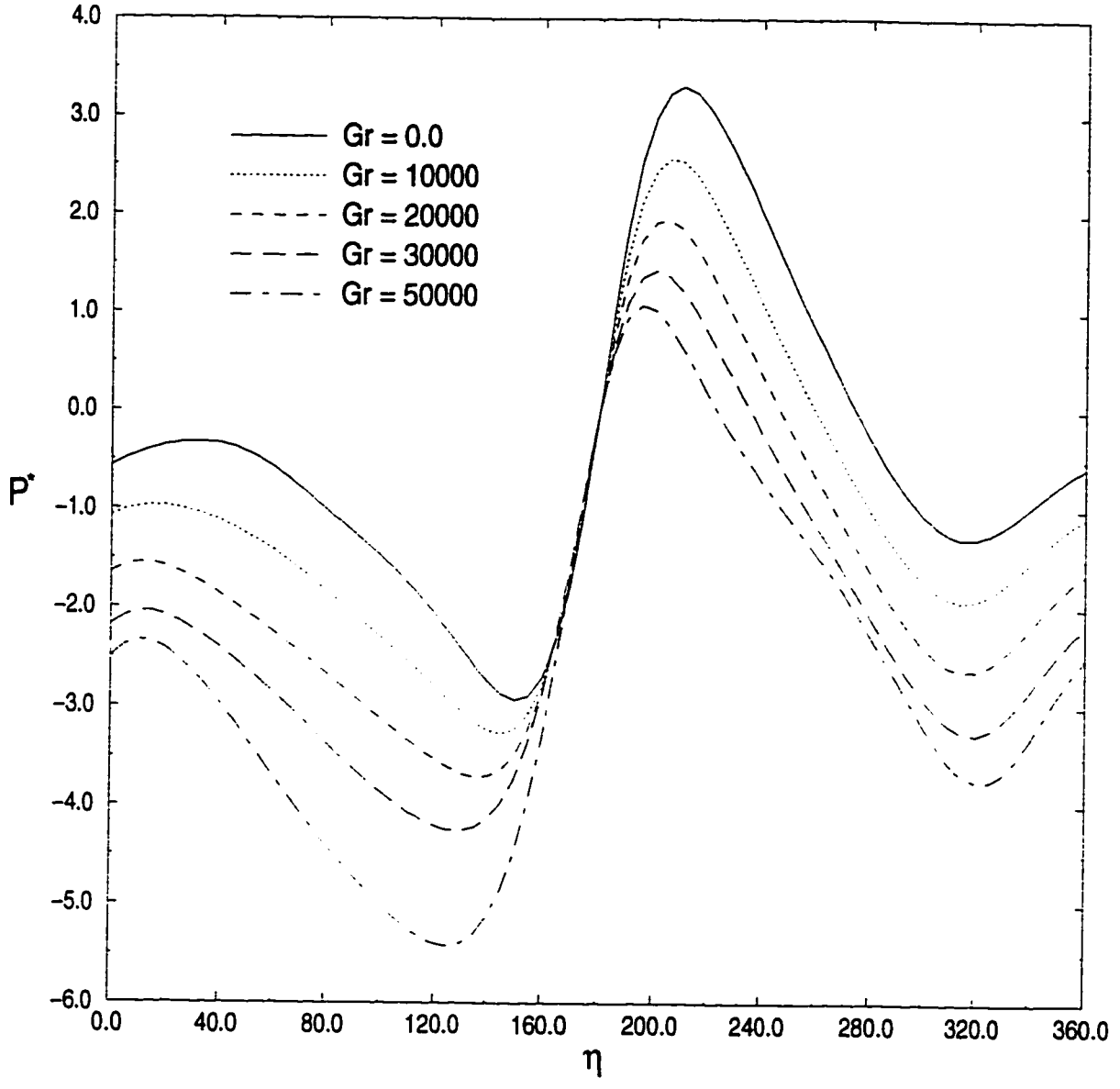

Figure 5.100: The effect of Grashof number on the pressure distribution at maximum free stream velocity for the case of , Re=100, Ar=0.5, $\lambda = 30^o$ $\beta = 0.5$ and $S = \pi/4$.

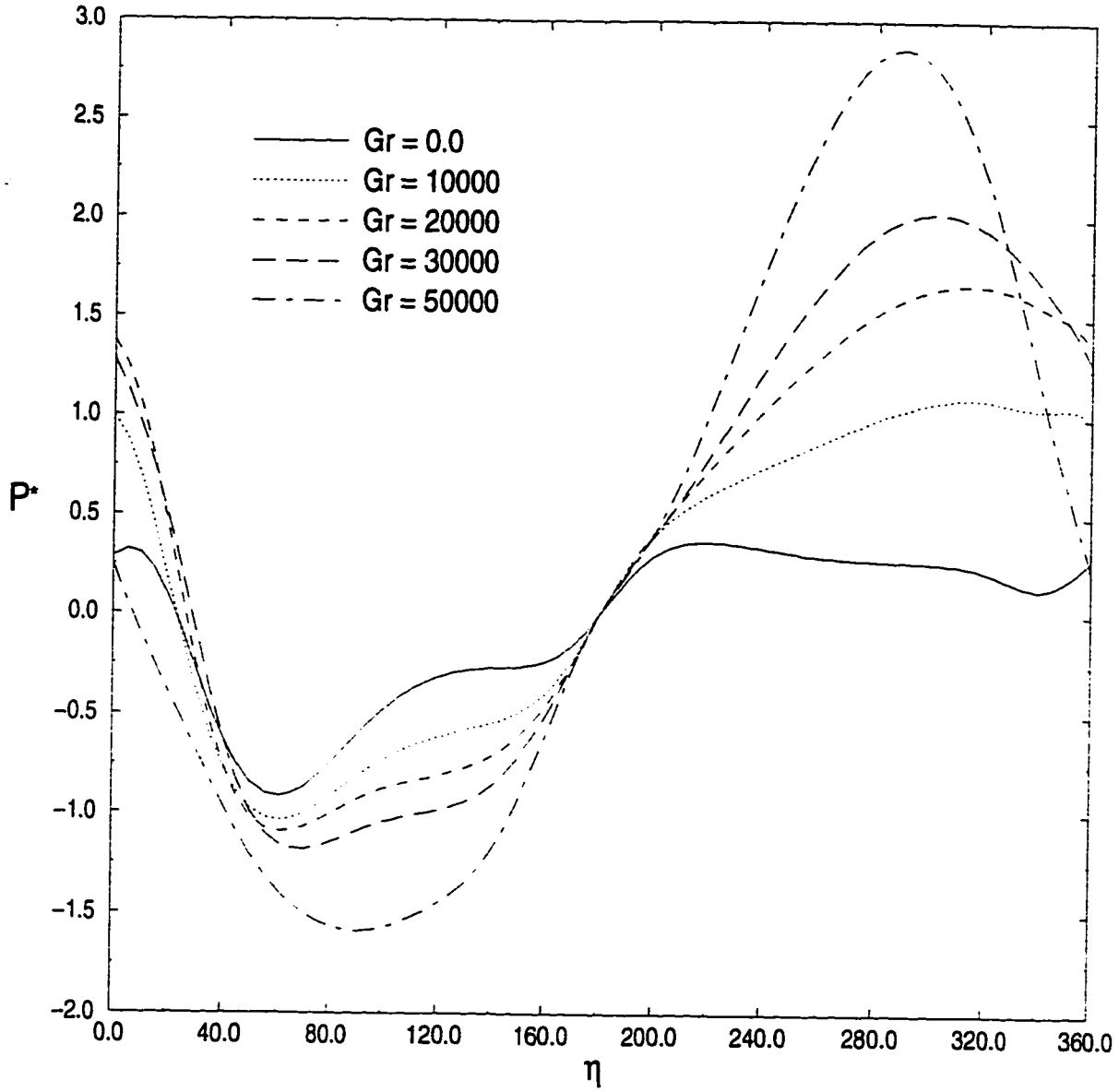

Figure 5.101: The effect of Grashof number on the pressure distribution at minimum free stream velocity for the case of Re=100, Ar = 0.5 and $\lambda = 30^o$ $\beta = 0.5$ and $S = \pi/4$.

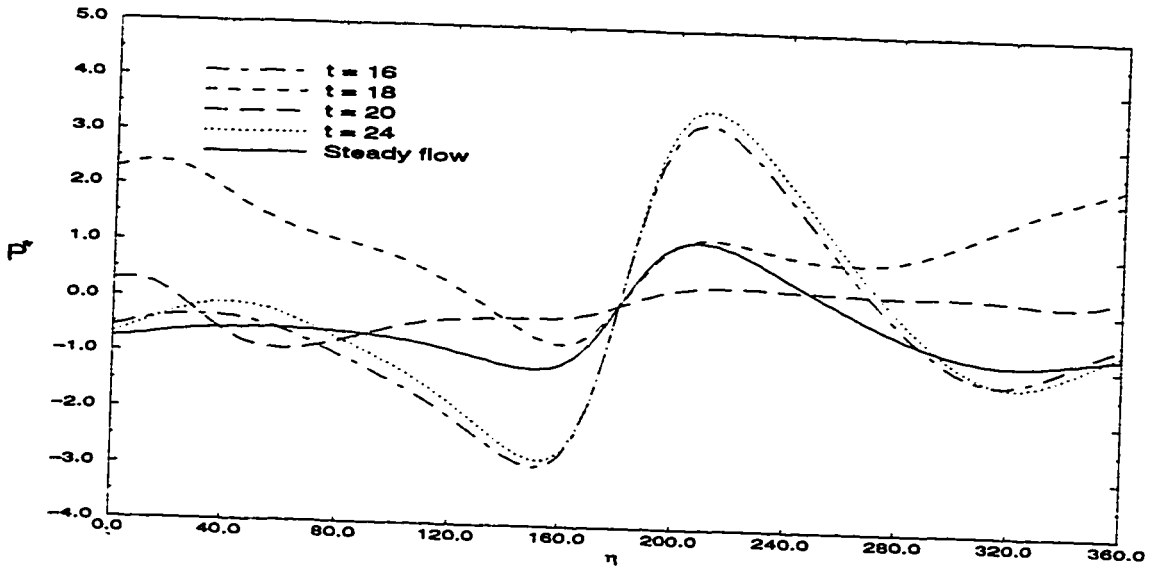

Figure 5.102: The pressure distribution at various times during one complete cycle in case D-2 and comparison with the steady free stream.

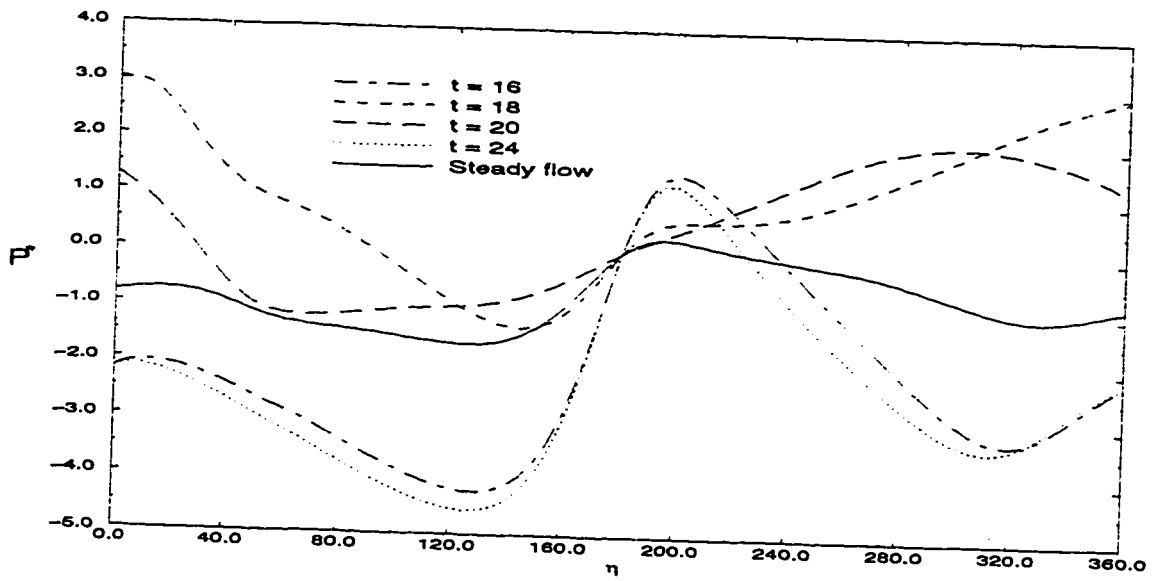

Figure 5.103: The local Nusselt number distribution at various times during one complete cycle in case D-6 and comparison with the steady free stream.

5.6.3 The Effect of Grashof Number on the Streamlines and Isotherms

The stream lines for Gr = 0 and $\lambda = 90^o$ are shown for different times in Figures 5.104a-d. Figure 5.104a shows the streamlines when the free stream is moving to the right at maximum velocity. The figure shows two pairs of vortices, the first is growing near the tube surface and the other is decaying downstream. One can see the growth of the first pair and the movement and decay of the other pair in Figures 5.104b. Figure 5.104b shows the streamlines when the free stream velocity reaches its minimum. The large distances between streamlines away from the tube and also within the vortices reflects the small flow velocities in these regions. Another interesting phenomena here is the unique pattern of vortex shedding which occurs in pairs in a symmetrical flow field.

The isotherms for the same case are shown in Figures 5.105a-d where the absence of buoyancy forces creates a symmetrical thermal field. The figures show the details of how vortex detachment affecting the thermal field. Figures 5.106a-d show the streamline patterns for the same case but for Gr= $3x10^4$. The asymmetry in the streamlines appearing in the figure is a result of buoyancy forces. Figure 5.106a shows two different size vortices on the downstream surface of the tube at t=32, instead of four vortices when Gr=0. A comparison between Figures 5.104a and 5.106a shows the higher velocities prevailing in the wake region. Figure 5.106b shows

a completely different vortex pattern (in comparison with Figure 5.104b). Although the number of vortices is the same, the size, shape and strength of each is quite different. The attached vortex in this figure created higher velocities and velocity gradient at the tube surface. Figure 5.106c shows the situation when U=U_{min} while Figure 5.106d shows the end of the cycle.

The isotherms for this case are shown in Figures 5.107a-d. The vortical motion mentioned in Figure 5.106b creates higher temperature gradients in the back of the tube (see Figure 5.107b) in comparison with the symmetrical case (see Figure 5.105b).

In general, increasing Grashof number tends to suppress vortex formation and shedding.

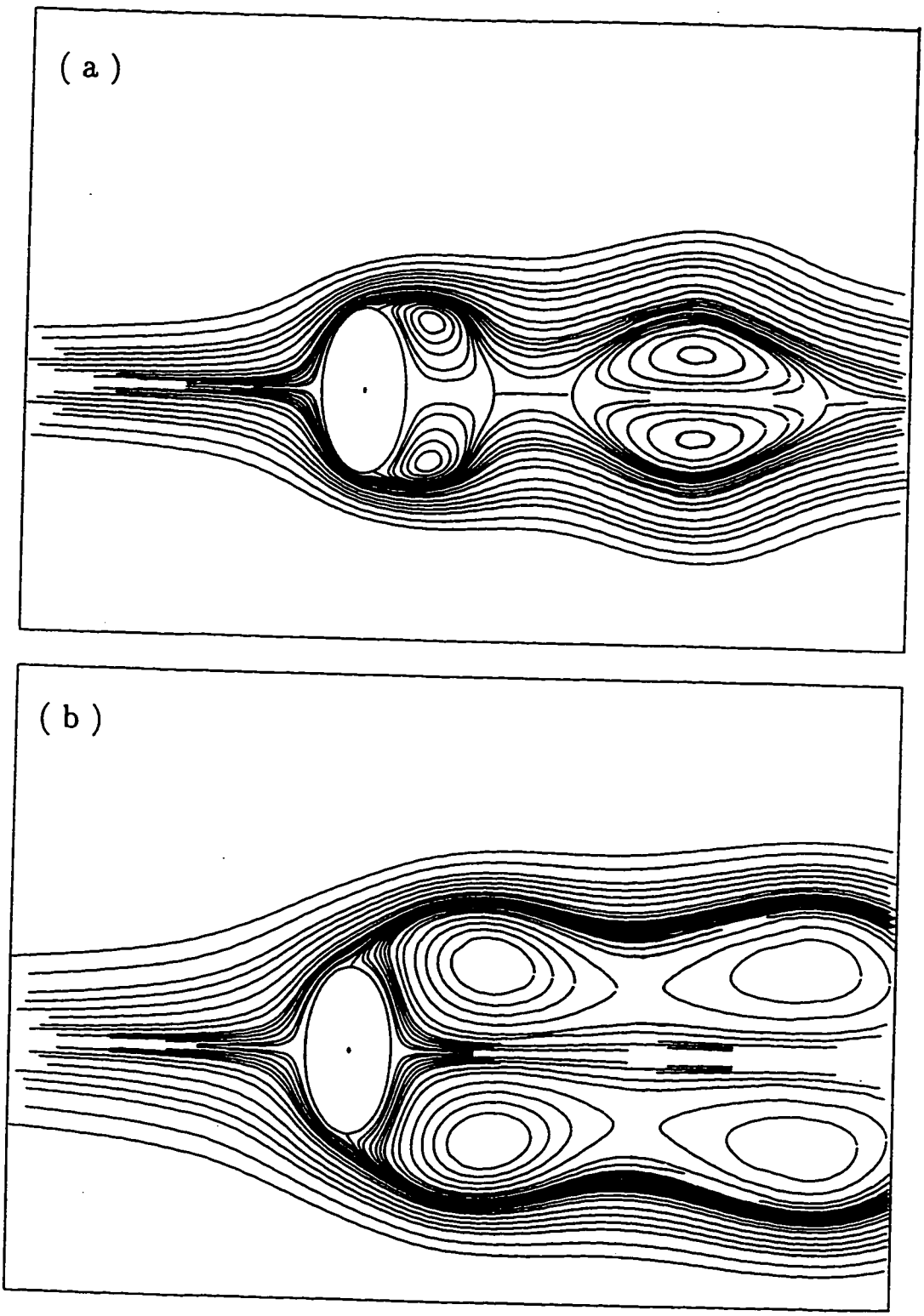
(a)
(b)

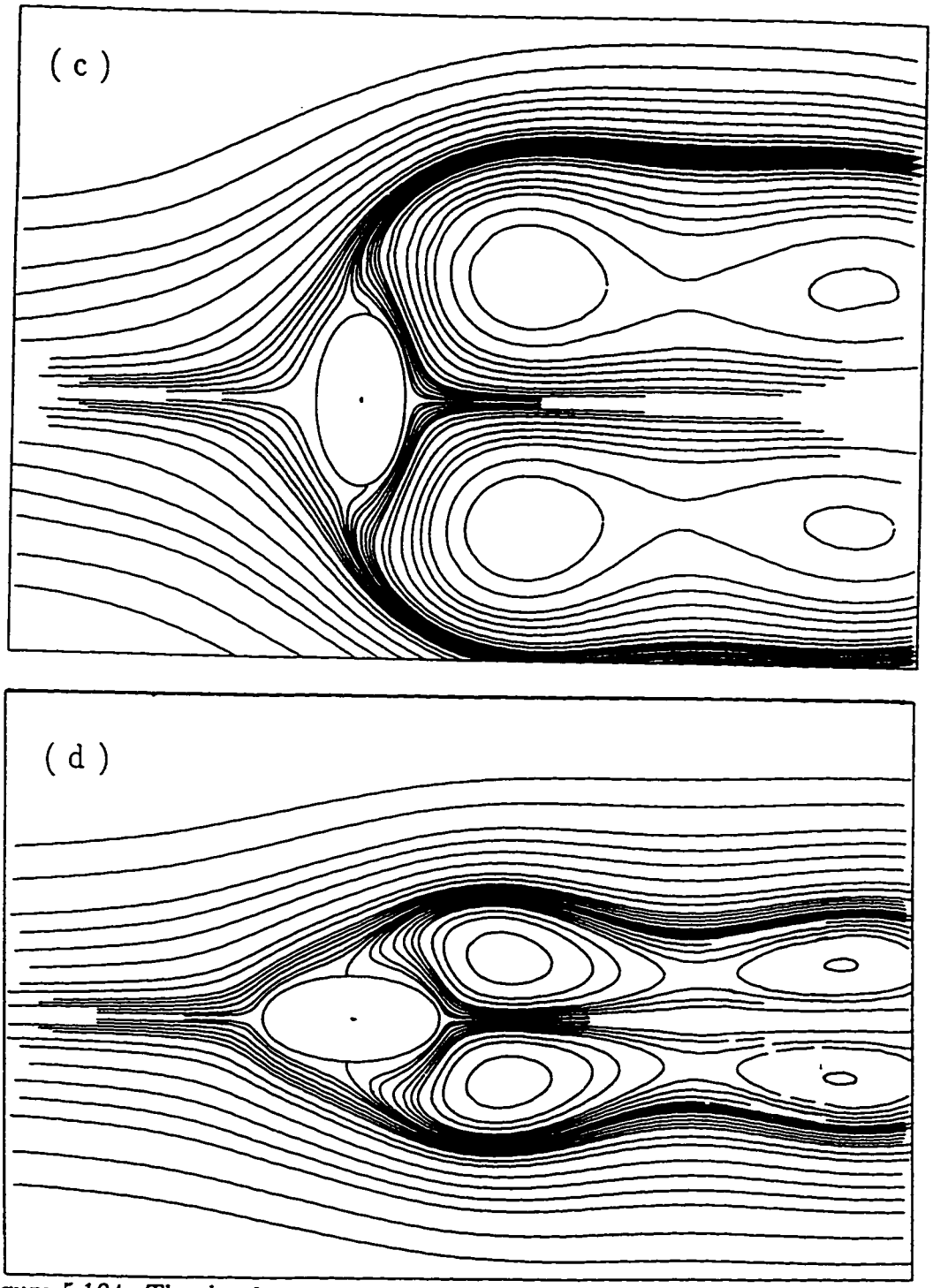

Figure 5.104: The development of the streamline patterns for the case of Re=100, Gr=0, Ar=0.5, $\lambda = 90°$, $\beta = 0.5$ and $S = \pi/4$, during one complete cycle : (a) t = 32; (b) t = 34; (c) t = 36; (d) t = 40.

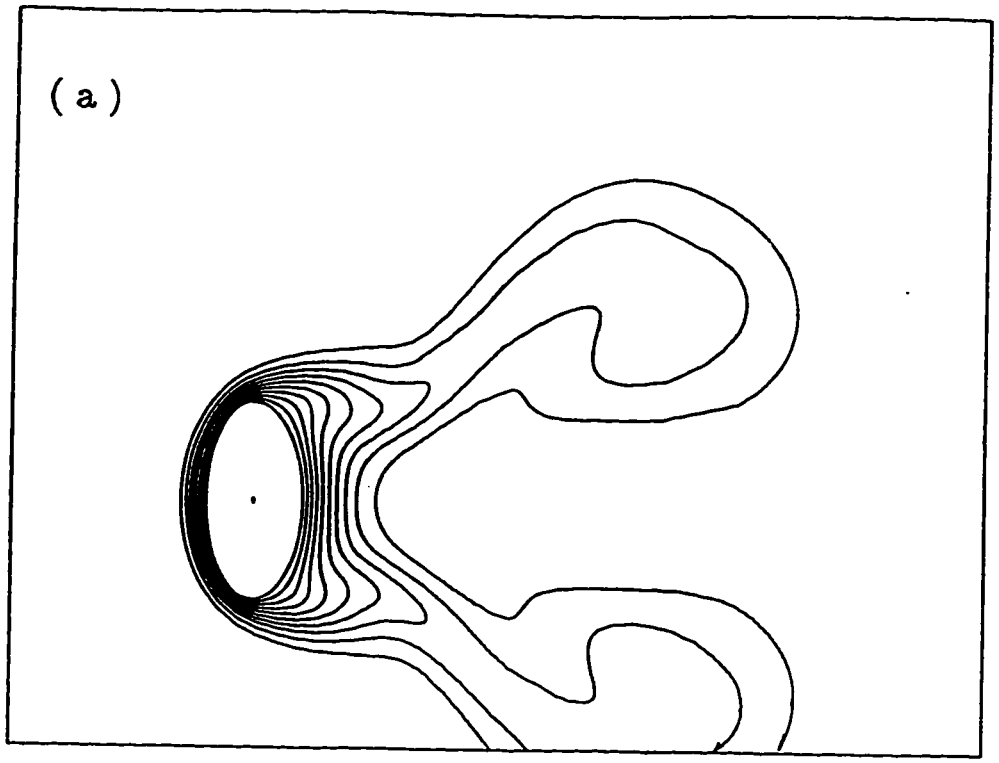
(a)

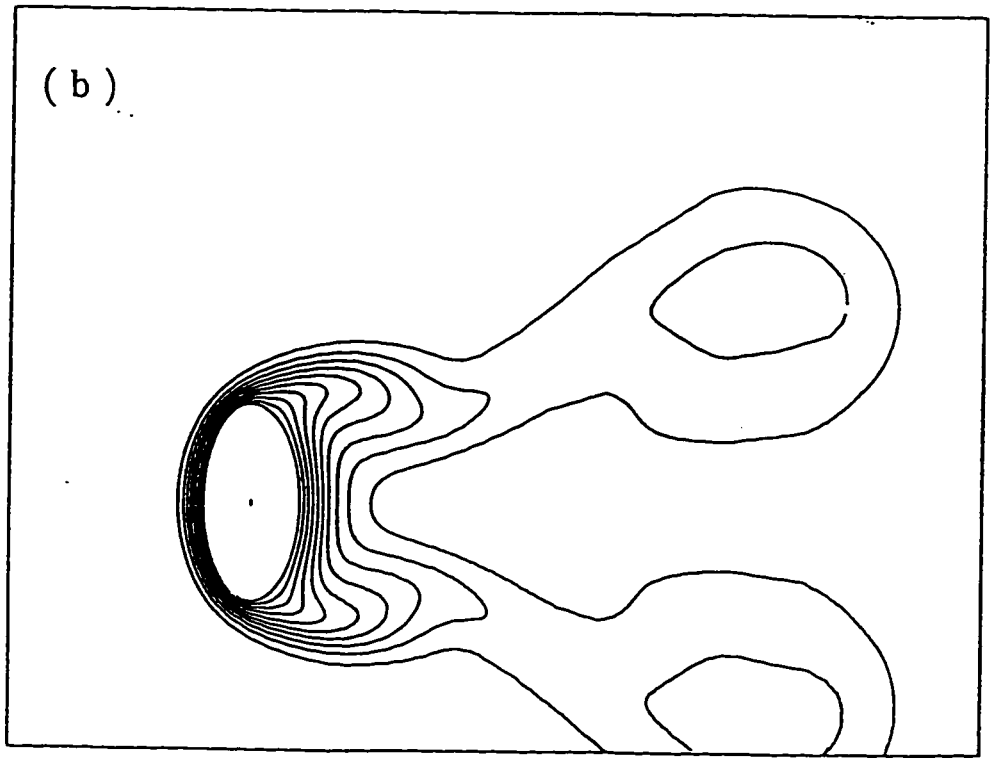
(b)

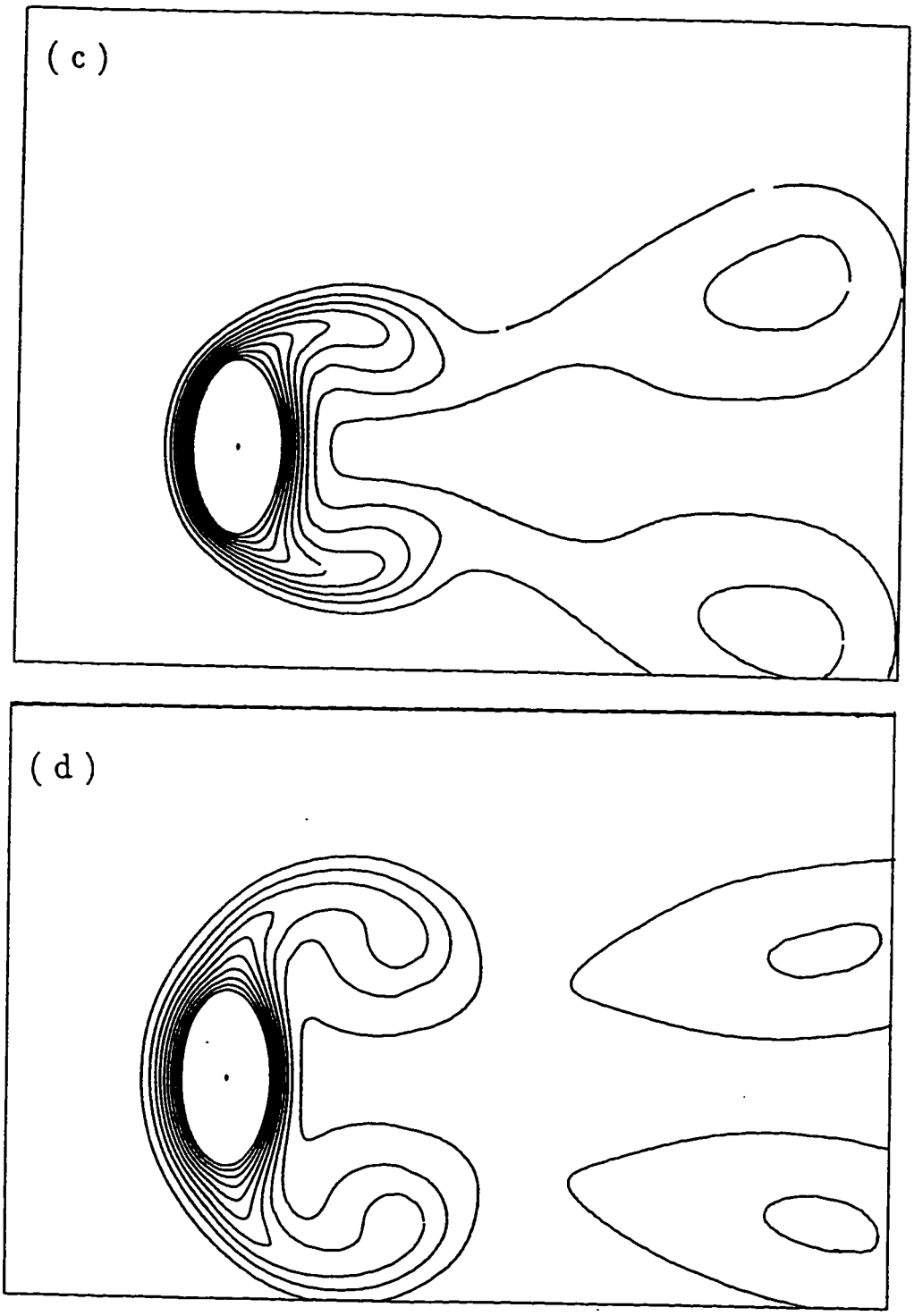

Figure 5.105: Time Development of the isotherm contours for the case of Re=100, Gr=0, Ar=0.5, $\lambda = 90°$, $\beta = 0.5$ and $S = \pi/4$ during one complete cycle : (a) t = 32; (b) t = 34; (c) t = 36; (d) t = 40.

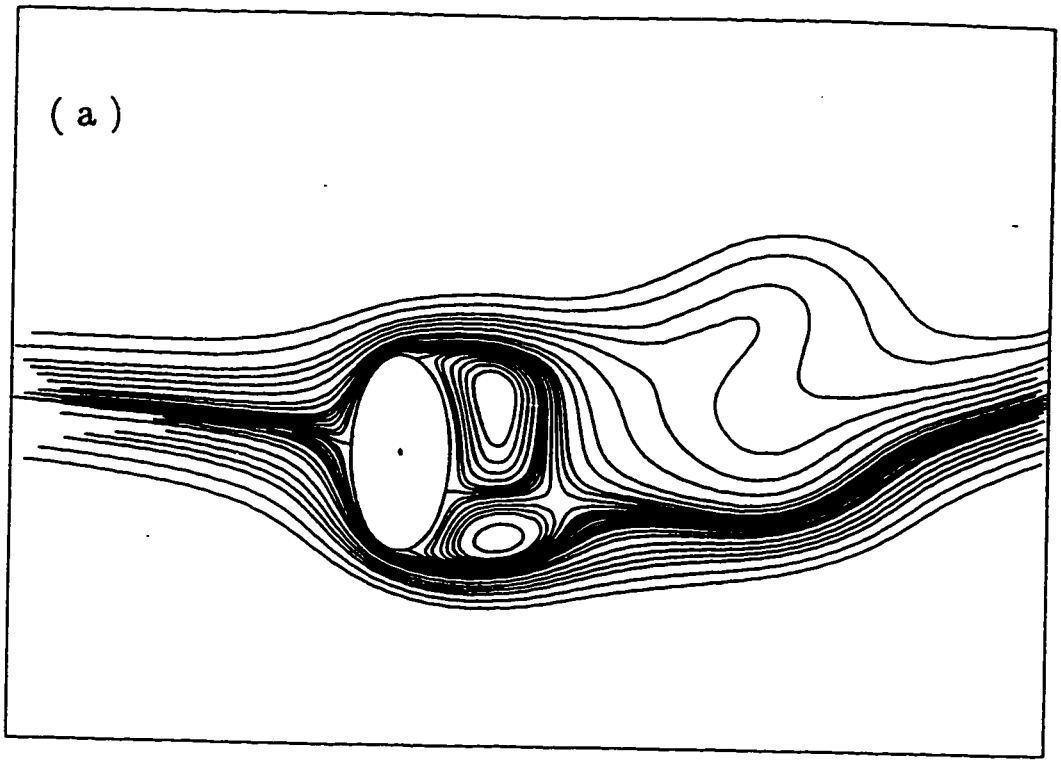
(a)

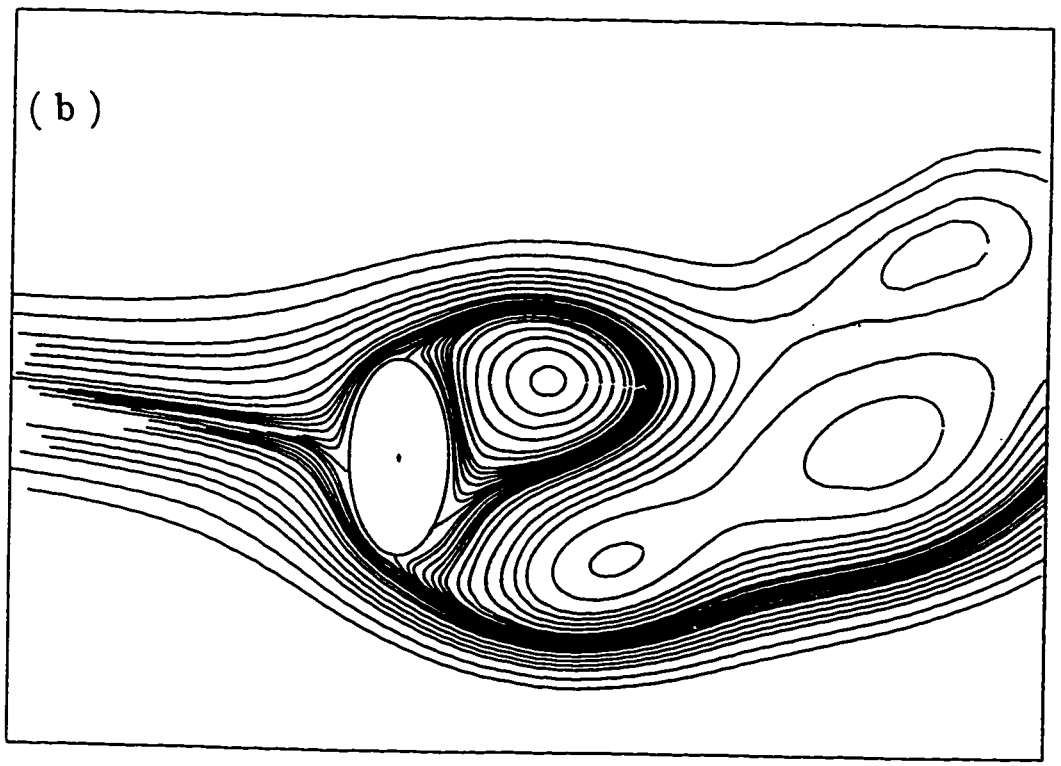
(b)

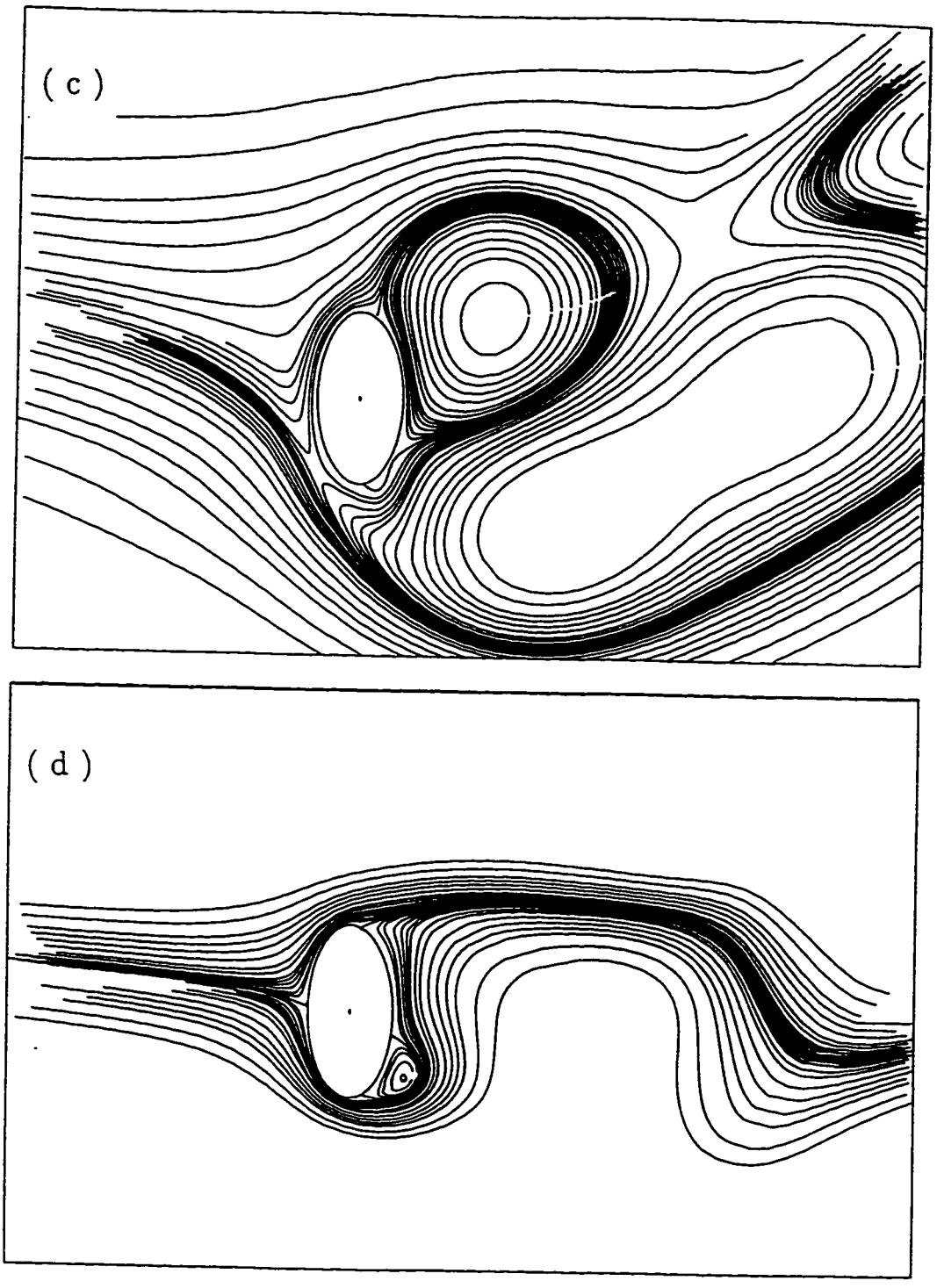

Figure 5.106: The development of the streamline patterns for the case of Re=100, Gr=30000, Ar=0.5, $\lambda = 90°$, $\beta = 0.5$ and $S = \pi/4$, during one complete cycle : (a) t = 32; (b) t = 34; (c) t = 36; (d) t = 40.

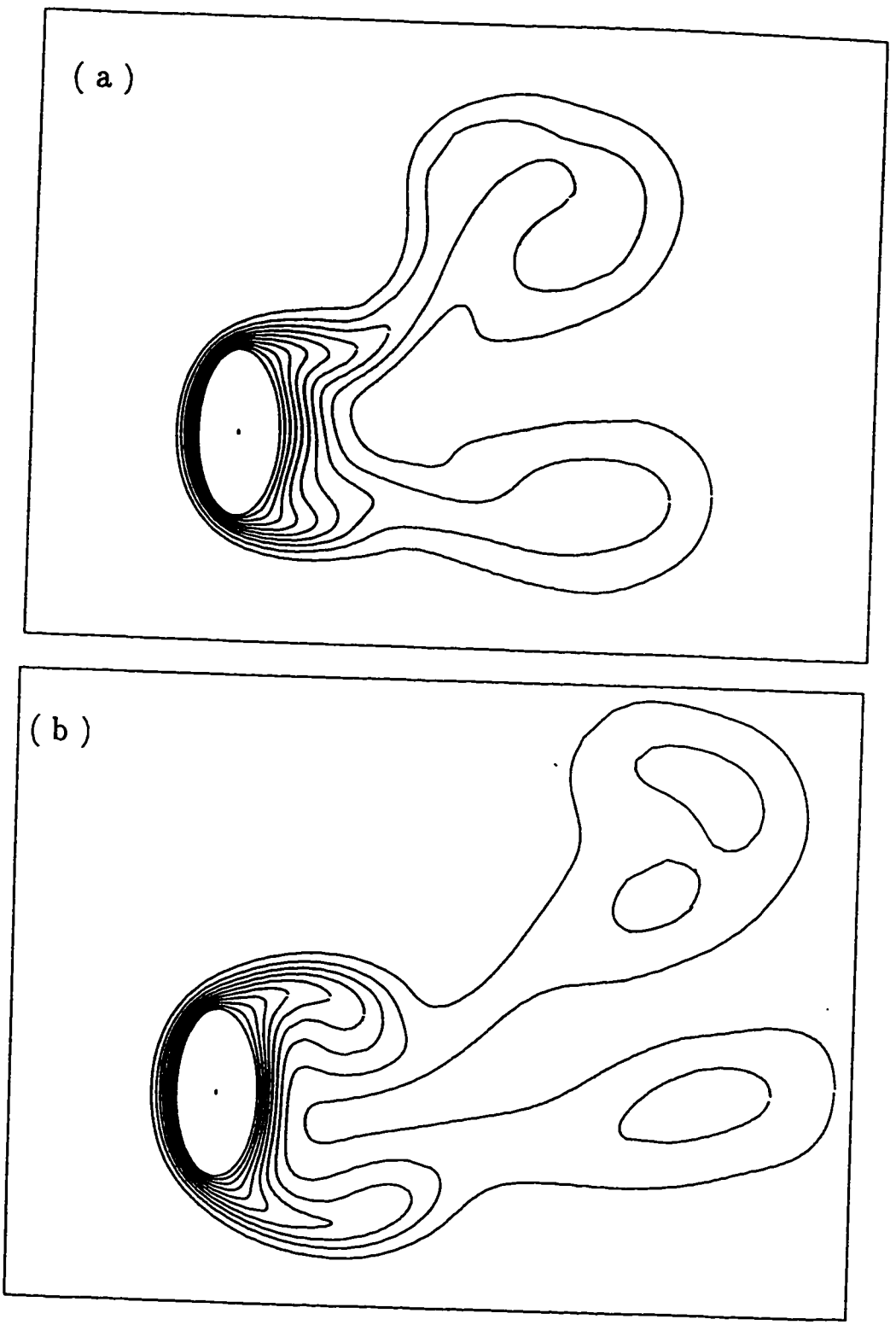
(a)
(b)

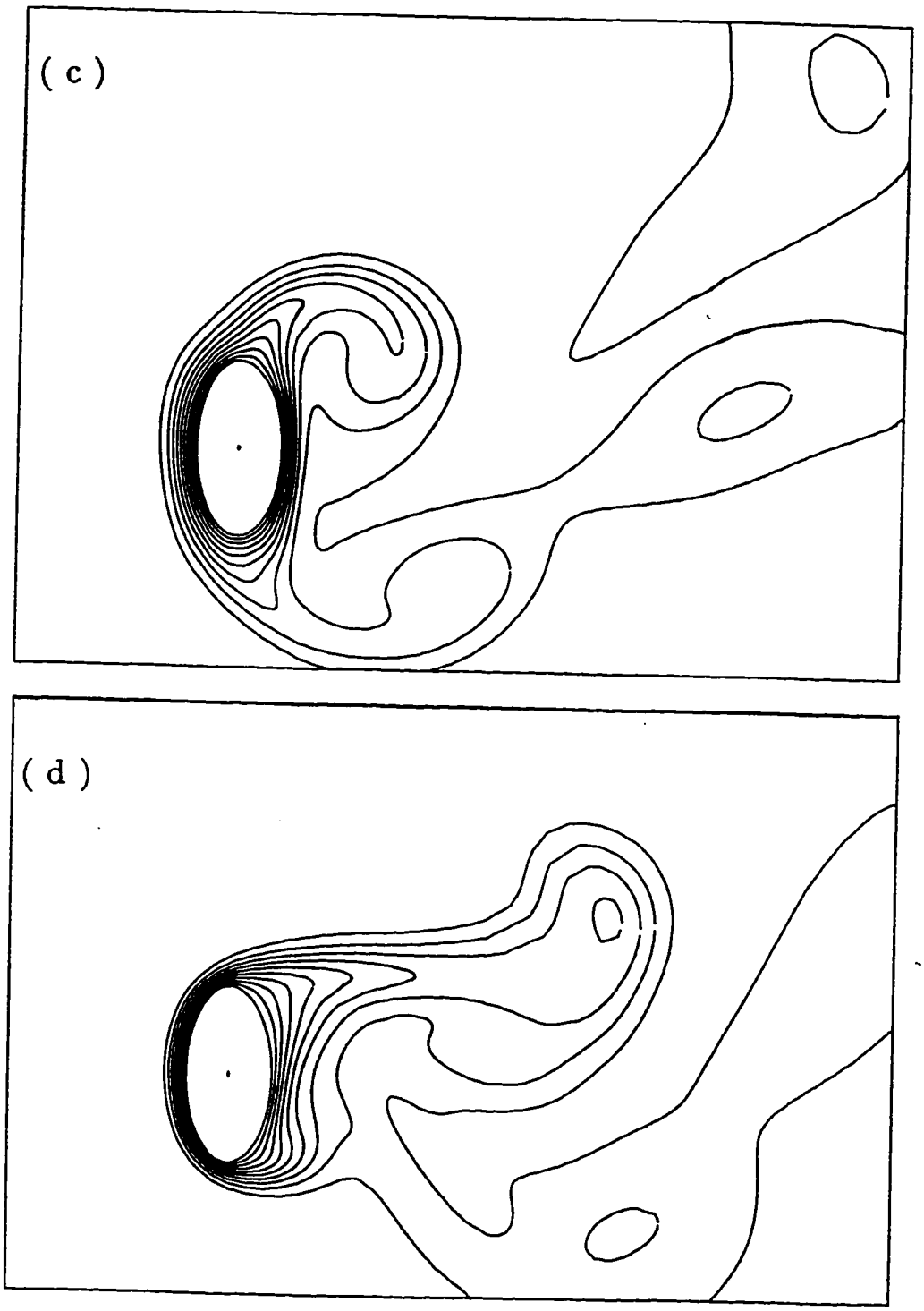

Figure 5.107: Time Development of the isotherm contours for the case of Re=100, Gr=30000, Ar=0.5, $\lambda = 90^o$, $\beta = 0.5$ and $S = \pi/4$ during one complete cycle : (a) t = 32; (b) t = 34; (c) t = 36; (d) t = 40.

5.7 The Effect of Angle of Inclination

In this section, the effect of angle of inclination (λ) on the velocity and thermal fields, average and local Nusselt numbers and pressure and vorticity distributions is presented. The values of λ considered vary between 0^o and 150^o with a step of 30^o. The case of $\lambda = 180^o$ was excluded since it is the same as $\lambda = 0$.

5.7.1 The Effect of Angle of Inclination on the Average Nusselt Number

Table 5.7 gives the percentage of heat transfer enhancement when the value of $\overline{\overline{Nu}}$ is compared to the steady free stream values. From the table, one can conclude that the heat transfer enhancement due to free stream fluctuations increases with the increase of λ up to $\lambda = 90^o$ after which increasing λ tends to reduce the heat transfer enhancement.

The time variation of the average Nusselt number is shown in Figure 5.108 for different angles of inclination. From the figure, one can deduce that the value of λ affects the amplitude of $\overline{Nu}$ fluctuations. For example, for $\lambda = 90^o$ the amplitudes of $\overline{Nu}$ fluctuations are lower than that for any other value of λ. The figure also shows that for $\lambda = 0$, the periodic variation has been achieved in the fluctuations of $\overline{Nu}$ while for $\lambda = 90^o$ still larger time is needed to achieve the quasi-steady state.

To study the enhancement in heat transfer rate due to the imposed fluctuations

in free stream for different λ, the variation of $\overline{Nu}$ and its time average together with the steady stream case are plotted in Figures 5.109 to 5.112. The figures are drawn for $\lambda = 0^o$, 60^o, 90^o and 150^o respectively. One can conclude from these figures that the enhancement in heat transfer is greatly affected by the angle of inclination. Figure 5.109 indicates that there is no enhancement in the heat transfer rate for $\lambda = 0$. On the contrary, $\overline{\overline{Nu}}$ can be slightly less than that for the case of no fluctuations. As λ increases the enhancement in heat transfer due to fluctuations also increases. Figure 5.110 shows that there is a noticeable increase in the heat transfer rate and this increase becomes less when $\lambda = 150^o$.

Table 5.7: The percentage increase in $\overline{\overline{Nu}}$ for different angles of inclination compared to the steady stream case.

Code #	Re	Gr	λ	b/a	S	β	$\overline{\overline{Nu}}$	$\overline{Nu}$ $\beta = 0$	% increase
E-1	100	20000	0^o	0.5	$\frac{\pi}{4}$	0.5	6.16	6.28	−0.2 %
E-2	100	20000	60^o	0.5	$\frac{\pi}{4}$	0.5	6.67	6.11	9.1 %
E-3	100	20000	90^o	0.5	$\frac{\pi}{4}$	0.5	6.45	6.40	0.7 %
E-4	100	20000	120^o	0.5	$\frac{\pi}{4}$	0.5	6.67	6.11	9.1 %
E-5	100	20000	150^o	0.5	$\frac{\pi}{4}$	0.5	6.25	6.23	0.4 %

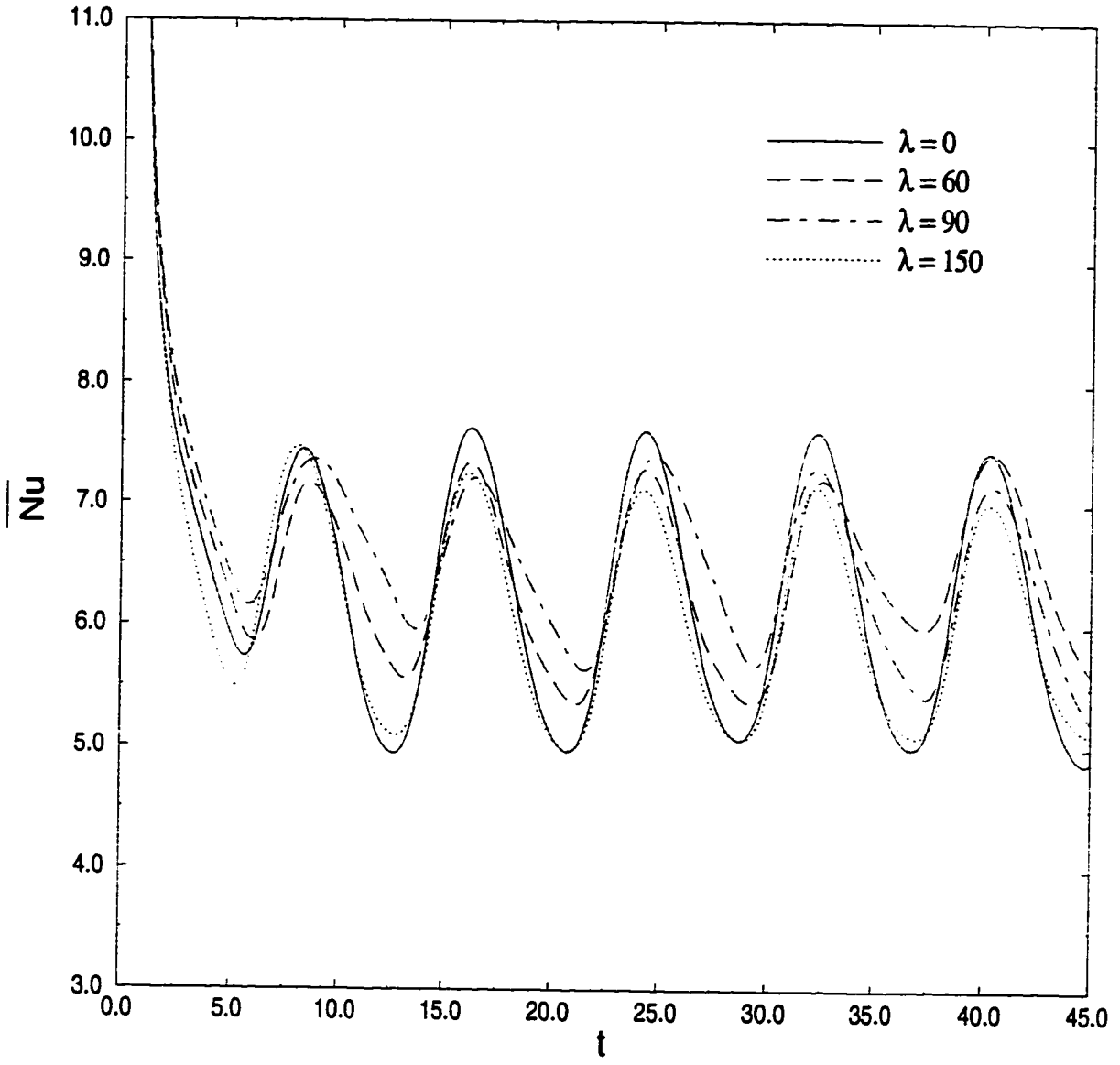

Figure 5.108: The time variation of $\overline{Nu}$ following the sudden temperature rise for various angles of inclination for the case of Re=100, Gr=20000, Ar=0.5, $\beta = 0.5$ and $S = \pi/4$.

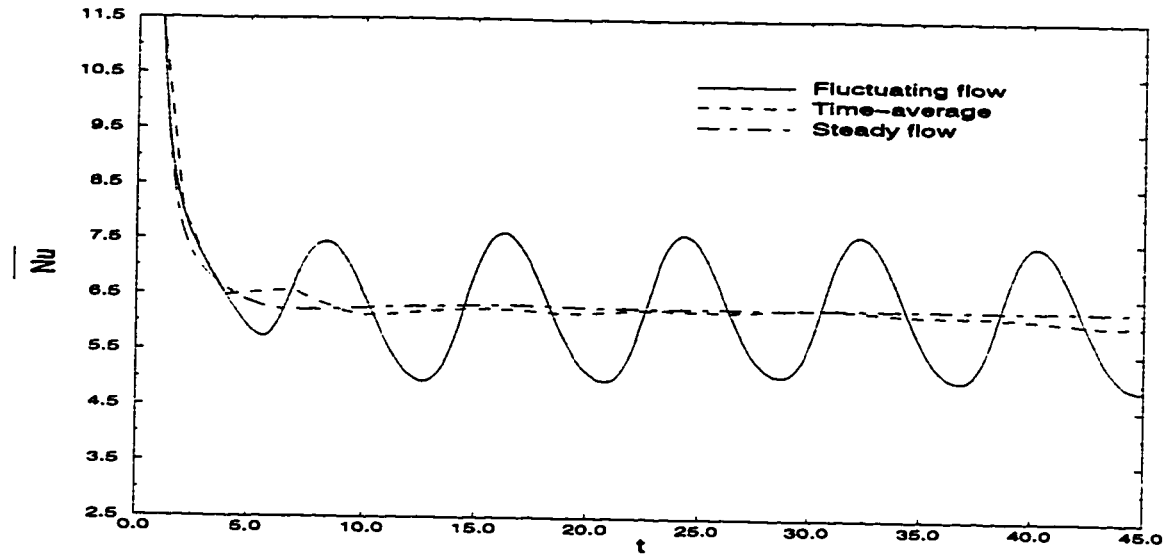

Figure 5.109: Time variation of $\overline{Nu}$ for case E-1 and comparison with the steady free stream.

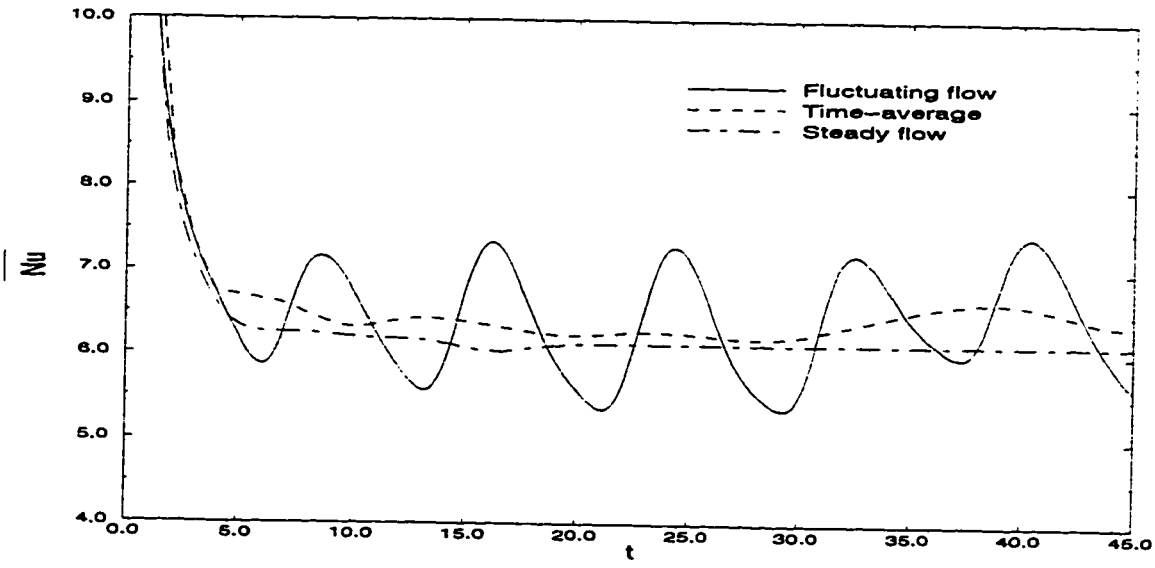

Figure 5.110: Time variation of $\overline{Nu}$ for case E-2 and comparison with the steady free stream.

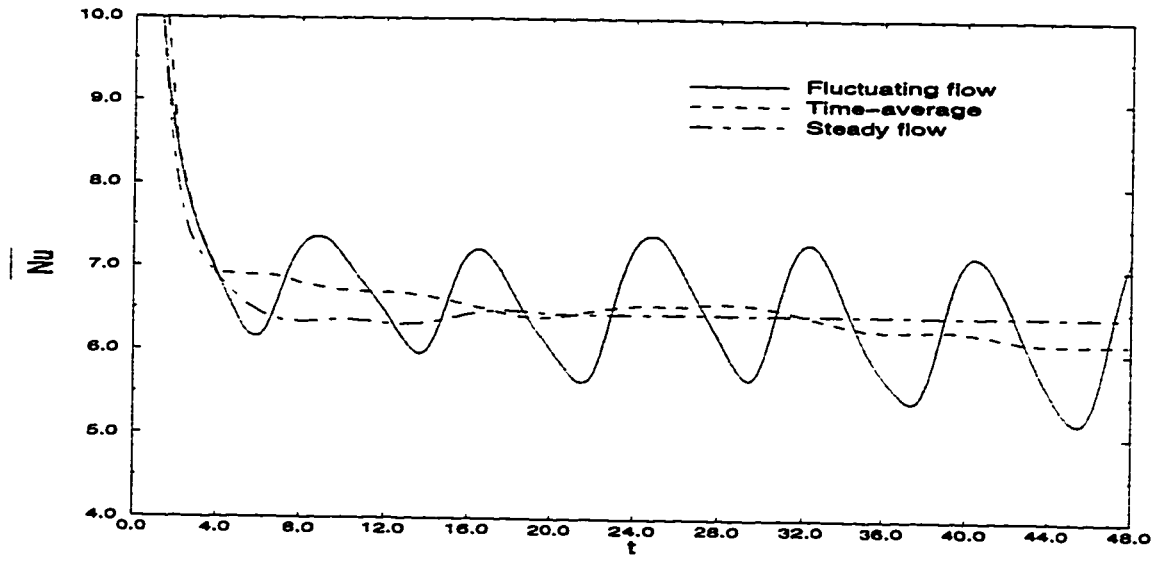

Figure 5.111: Time variation of $\overline{Nu}$ for case E-3and comparison with the steady free stream.

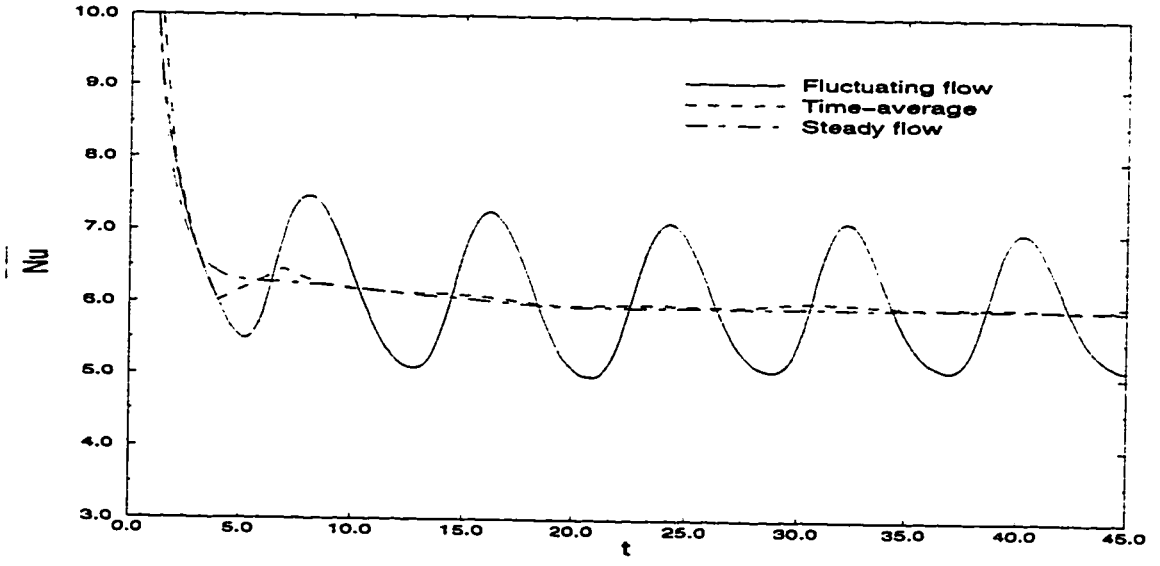

Figure 5.112: Time variation of $\overline{Nu}$ for case E-5 and comparison with the steady free stream.

5.7.2 The Effect of Angle of Inclination on the Local Nusselt Number, Pressure and Vorticity Distributions

Figures 5.113 and 5.114 show the local Nusselt number distribution for different λ values at U = U_{max} and U = U_{min} respectively. Figure 5.113 shows that the angle of inclination is greatly affecting the local Nusselt number distribution. For λ ranging from 0^o to 60^o, it is found that the maximum local Nusselt number value occurs at η between 160^o and 200^o. However for $\lambda = 150^o$ the maximum Nu value occurs at $\eta = 350^o$. The local Nusselt number distribution for $\lambda = 90^o$ shows four local peaks occurring at $\eta = 50^o$, 117^o, 200^o, and 340^o. This leads to a conclusion that for maximum free stream velocity the maximum heat transfer rate always occures in the area facing the approaching free stream. The vorticity distributions for the same λ values at U = U_{max} are shown in Figure 5.115. The figure shows that the maximum $|\zeta_s|$ occurs in the range between $\eta = 160^o$ and 200^o for $\lambda = 0^o$, 30^o and 60^o. However for $\lambda = 150^o$ the maximum $|\zeta_s|$ occurs at $\eta = 350^o$. This explains the behavior of the local Nusselt number distribution around the tube surface at maximum free stream velocity since maximum value of Nu occurs at the same location of maximum $|\zeta_s|$.

Figures 5.114 and 5.116 show the local Nusselt number and vorticity distributions when the free stream velocity is minimum for same λ values while Figures 5.117, 5.118, 5.119 and 5.120 show the local Nusselt number distributions at different times

together with the steady stream values for $\lambda = 0^o$, 60^o, 90^o and 150^o. Figure 5.117 indicates that when U = U_{max} the Nu values are higher over the whole surface except for small region at the trailing edge similar to what has been previously described. For the case of $\lambda = 90^o$ which is shown in Figure 5.119, one can deduce that at this angle of inclination the maximum heat transfer rate occurs on the tube part facing the free stream at any velocity except for U = U_{min} at which the opposite occurs. The figure also shows that when U=U_{min}, The Nu distribution is almost uniform on the upstream surface ($\eta = 180^o - 360^o$) and the only peak occurs at $\eta = 80^o$ on the downstream surface. However, for $\lambda = 150^o$ it was found that maximum Nu occurs at $\eta = 340^o$ while minimum Nu occurs at η between 80^o and 120^o for all values of U. The vorticity distributions around the tube surface at different times are shown in Figures 5.121, 5.122, 5.123 and 5.124 for $\lambda = 0^o$, 60^o, 90^o and 150^o respectively.

Figures 5.125 and 5.126 show the pressure distribution around the tube surface for different λ values at maximum and minimum free stream velocities. The value of λ is greatly influencing the pressure distributions. With $\lambda = 90^o$, it was found that there is a considerable increase in the pressure compared to $\lambda = 0^o$ on almost all the tube surface. The pressure distributions at different times for the fluctuating flow and the steady stream cases are shown in Figures 5.127 and 5.128 for $\lambda = 90^o$ and 150^o respectively.

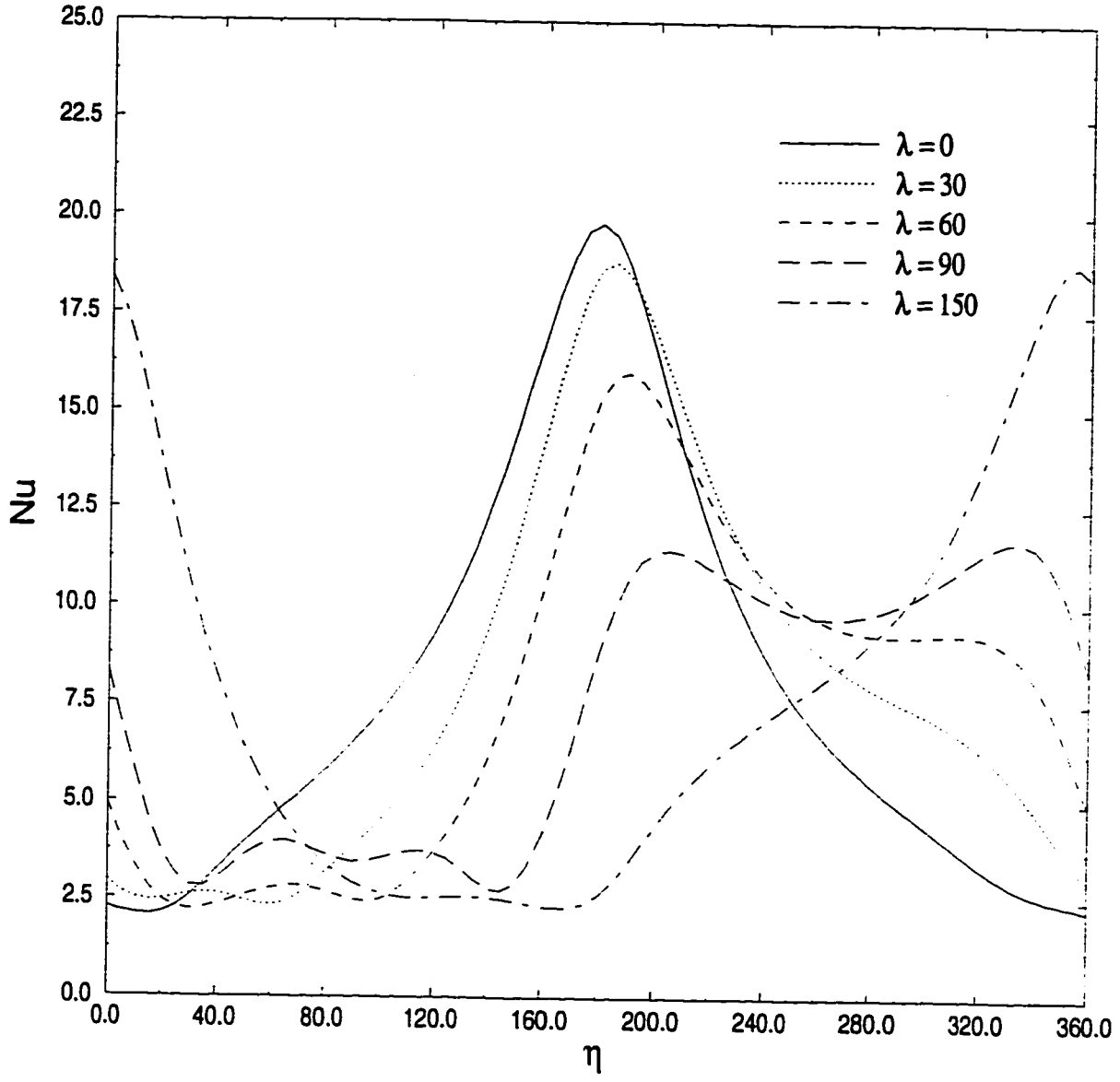

Figure 5.113: The effect of the angle of inclination on the local Nusselt number distribution at maximum free stream velocity for the case of Re=100, Gr =20000, Ar=0.5, $\beta = 0.5$ and $S = \pi/4$.

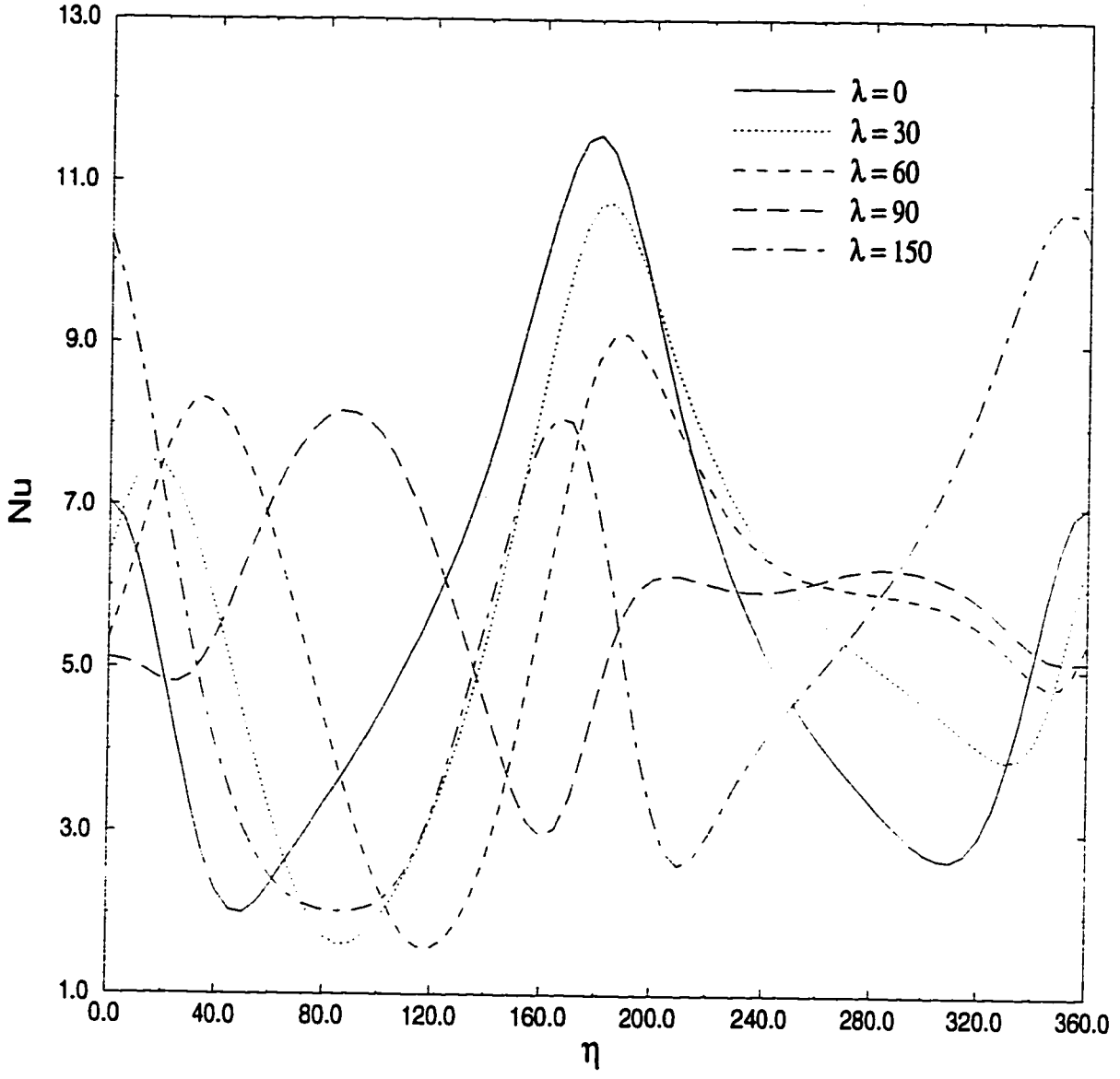

Figure 5.114: The effect of the angle of inclination on the local Nusselt number distribution at minimum free stream velocity for the case of Re=100, Gr=20000, Ar=0.5, $\beta = 0.5$ and $S = \pi/4$.

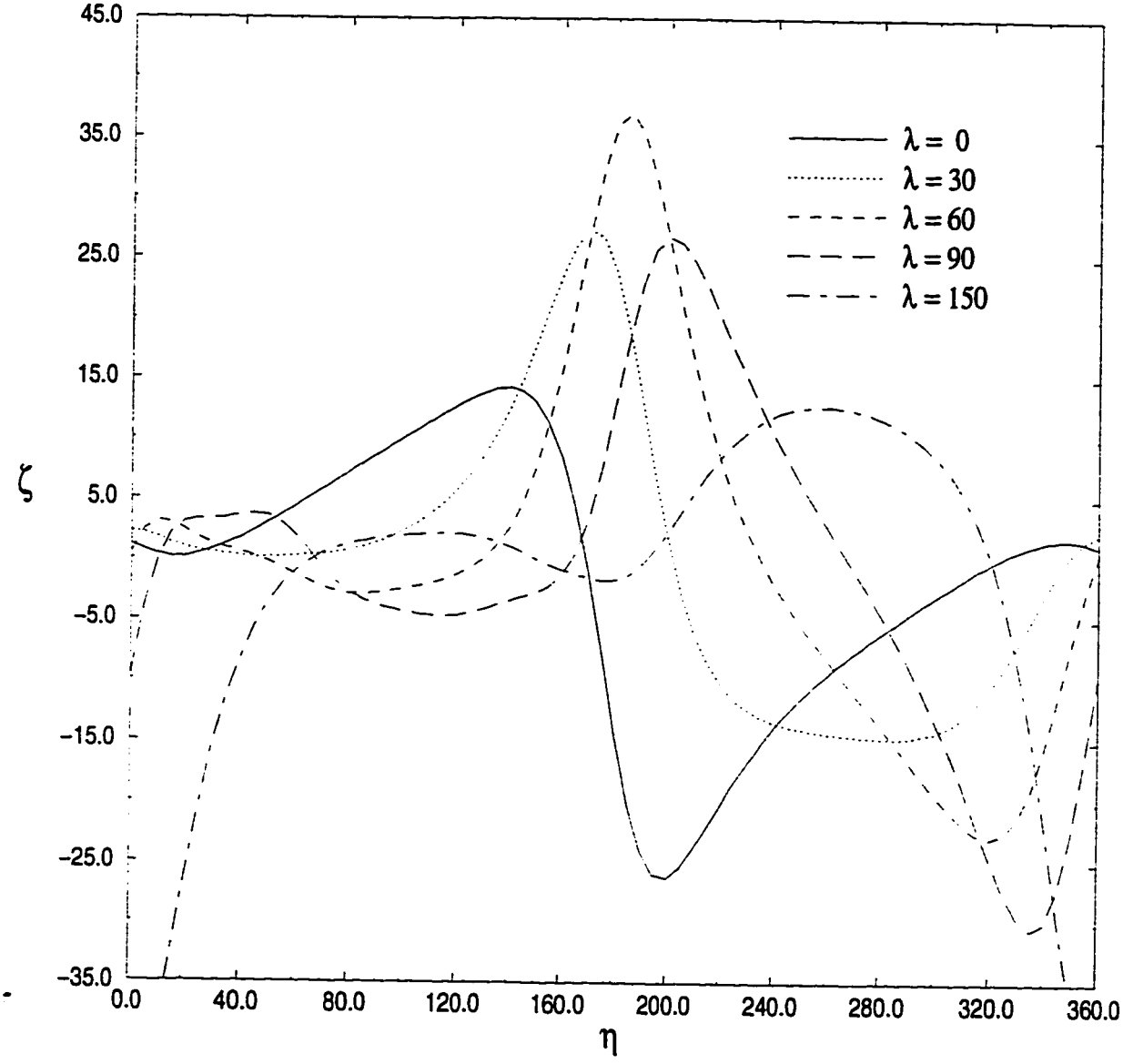

Figure 5.115: The effect of the angle of inclination on the vorticity distribution at maximum free stream velocity for the case of Re=100, Gr=20000, Ar=0.5, $\beta = 0.5$ and $S = \pi/4$.

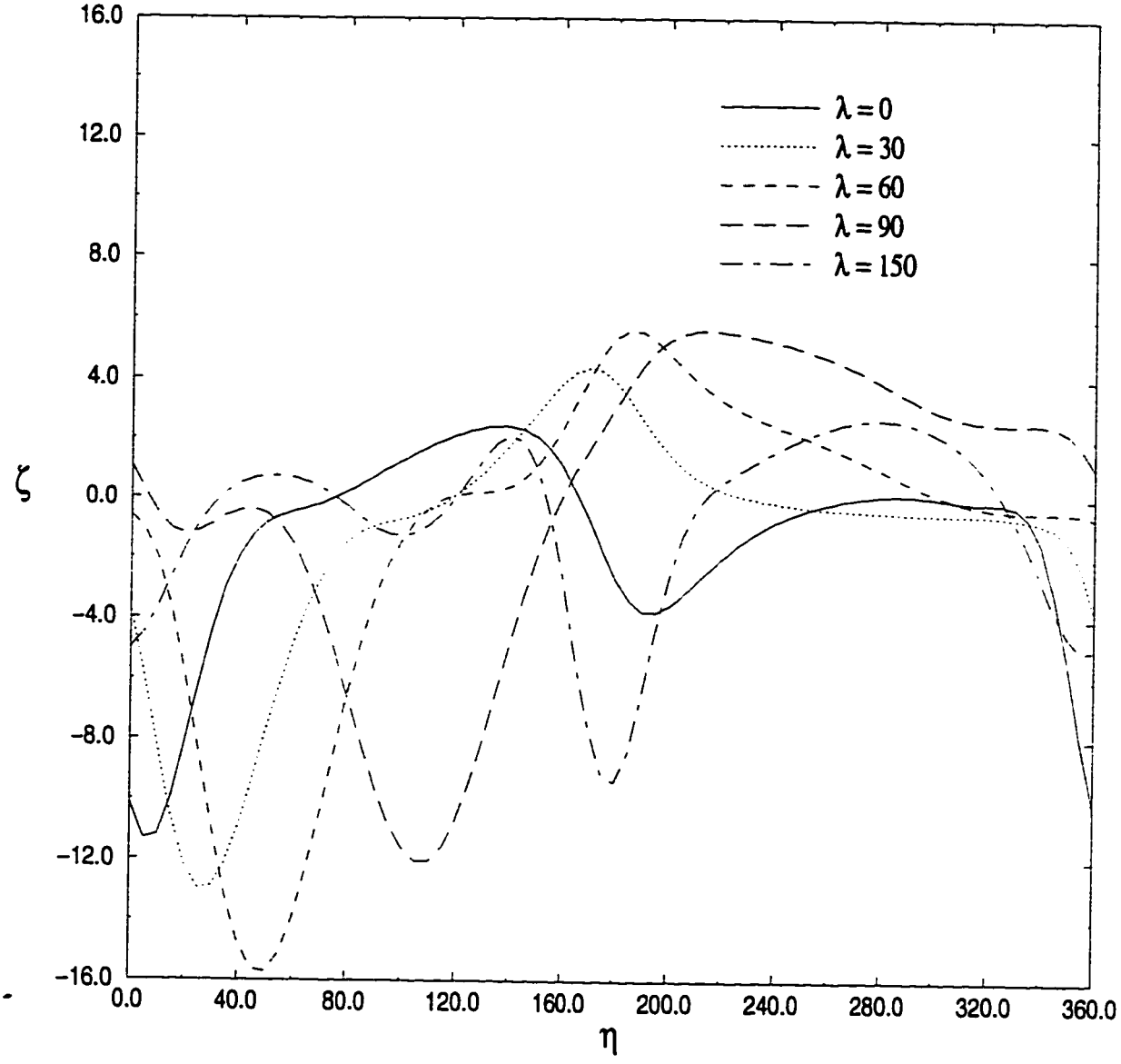

Figure 5.116: The effect of the angle of inclination on the vorticity distribution at minimum free stream velocity for the case of Re=100, Gr=20000, Ar=0.5, $\beta = 0.5$ and $S = \pi/4$.

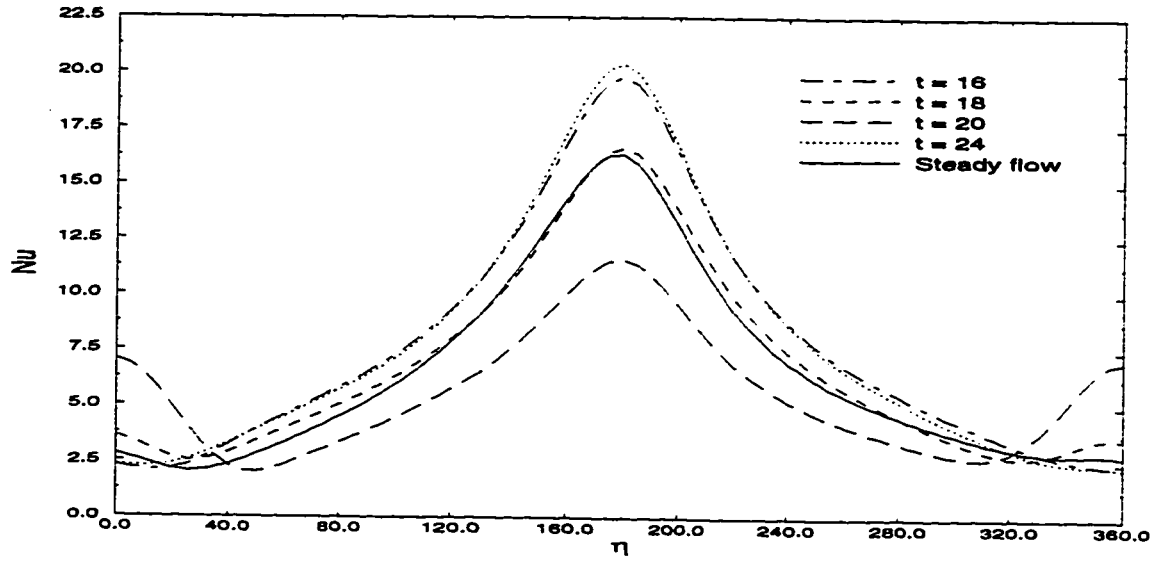

Figure 5.117: The local Nusselt number distribution at various times during one complete cycle in case E-1 and comparison with the case of steady free stream.

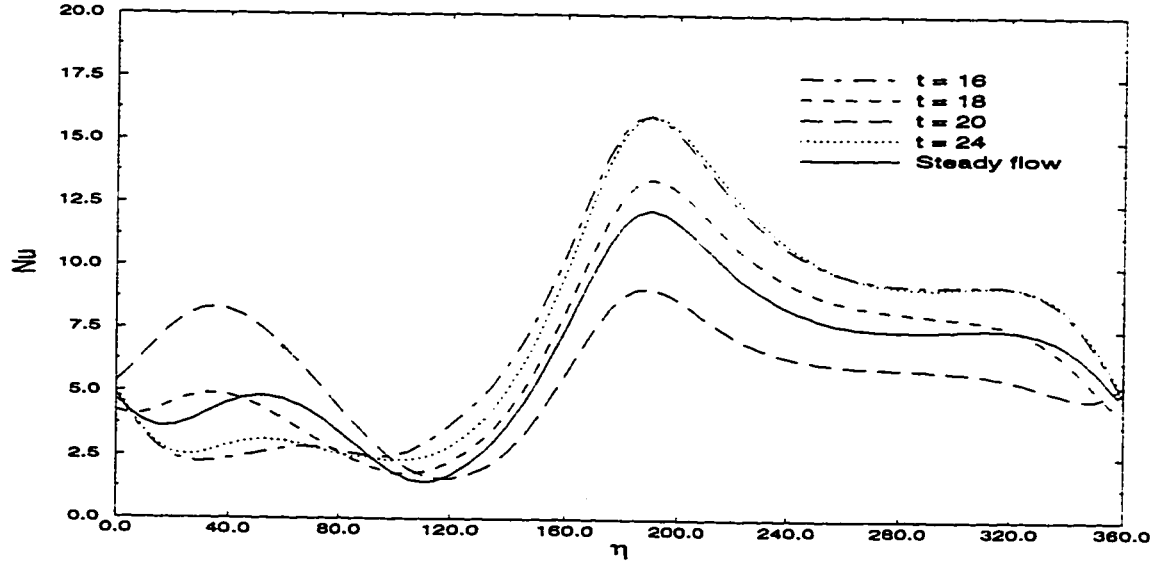

Figure 5.118: The local Nusselt number distribution at various times during one complete cycle in case E-2 and comparison with the case of steady free stream.

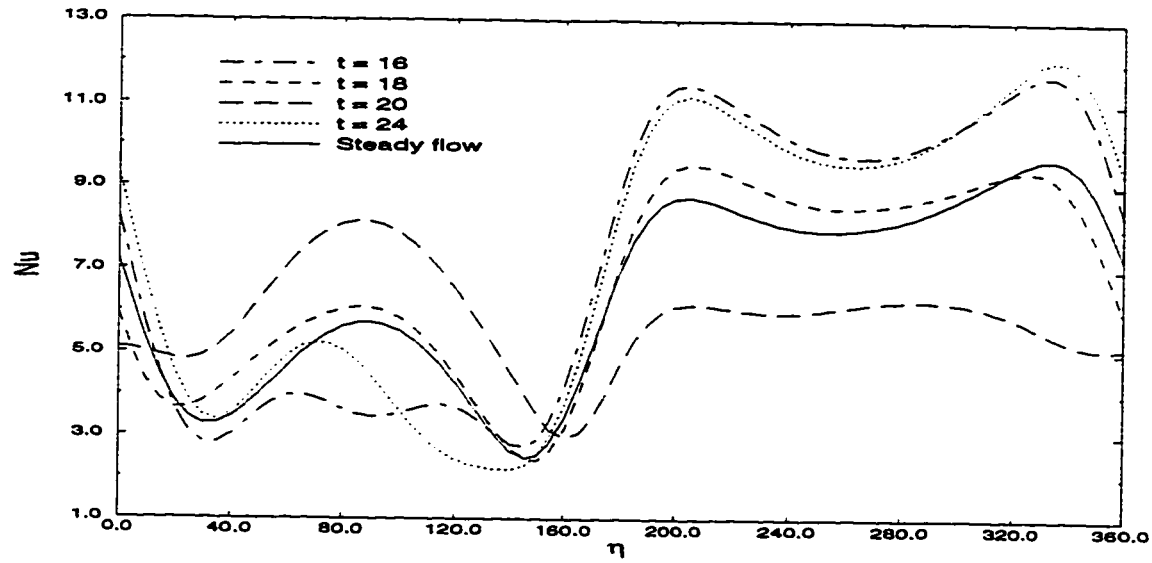

Figure 5.119: The local Nusselt number distribution at various times during one complete cycle in case E-3 and comparison with the case of steady free stream.

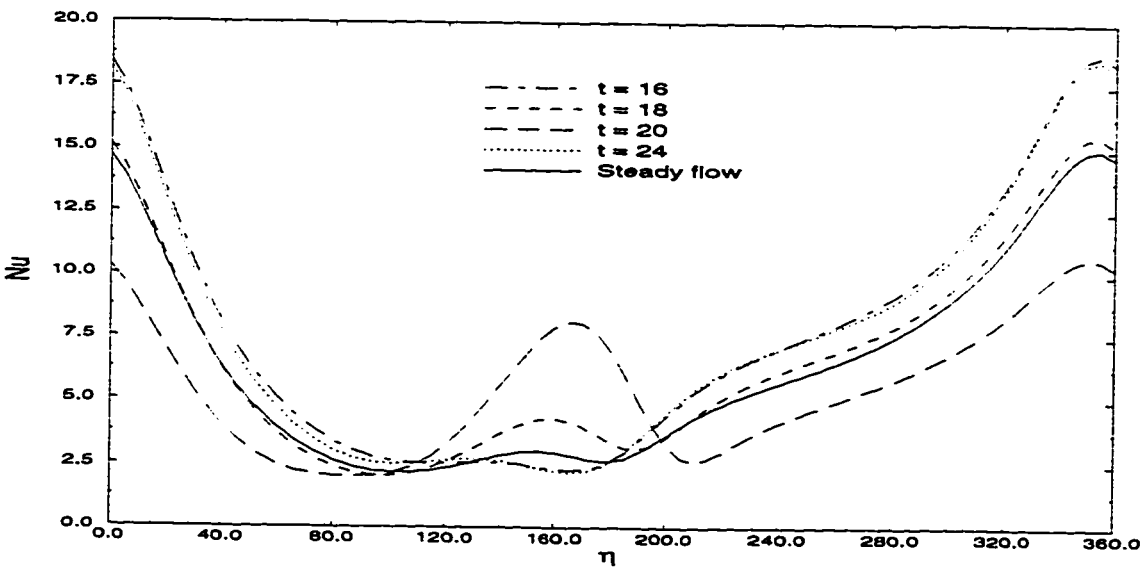

Figure 5.120: The local Nusselt number distribution at various times during one complete cycle in case E-5 and comparison with the case of steady free stream.

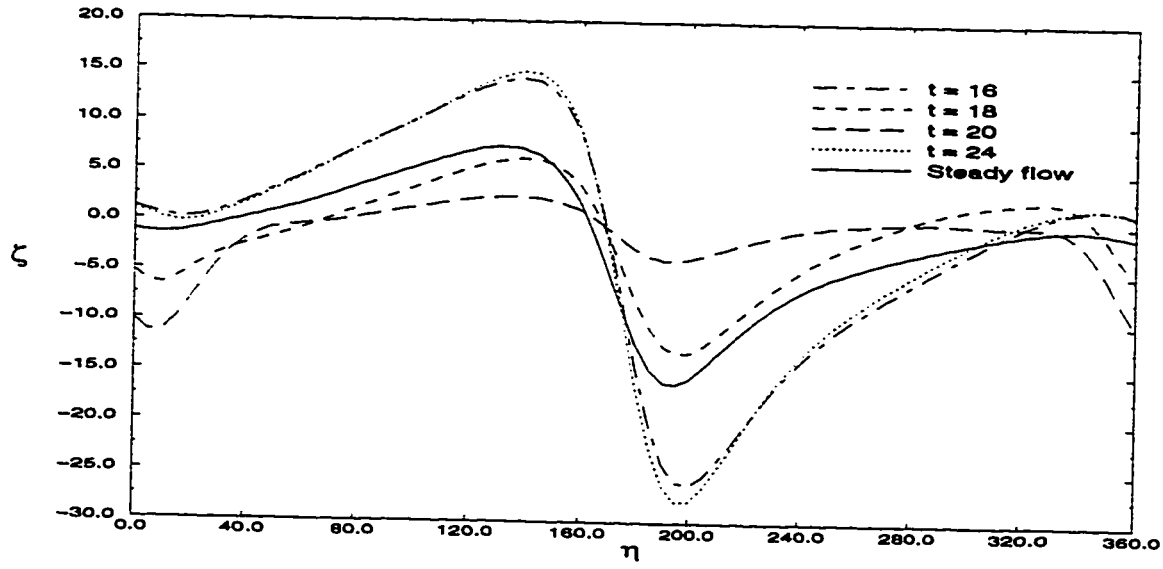

Figure 5.121: The surface vorticity distribution at various times during one complete cycle in case E-1 and comparison with the case of steady free stream.

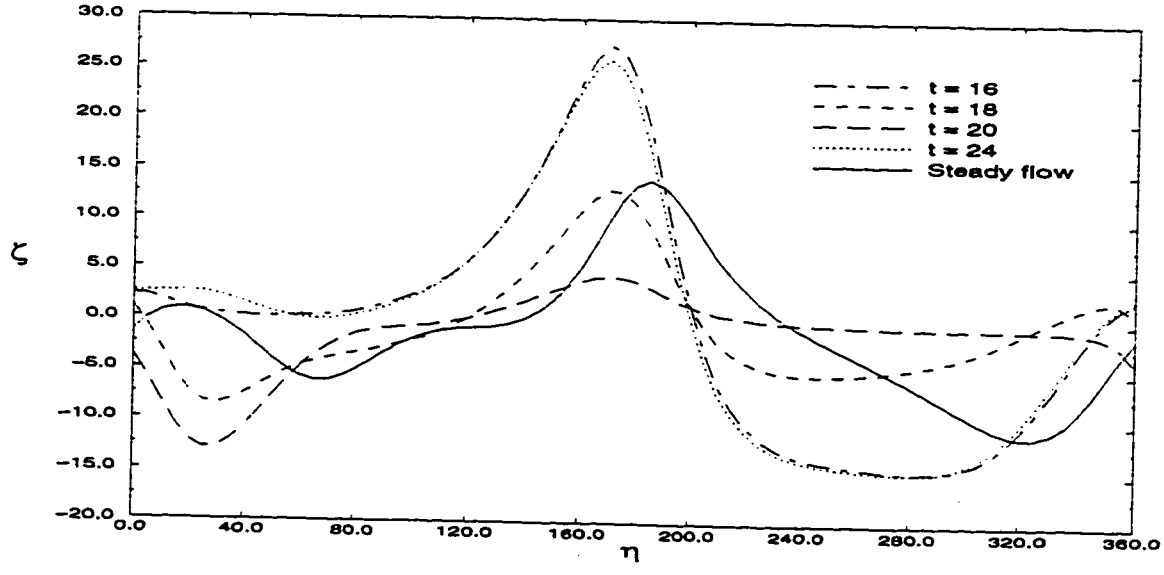

Figure 5.122: The surface vorticity distribution at various times during one complete cycle in case E-2 and comparison with the case of steady free stream.

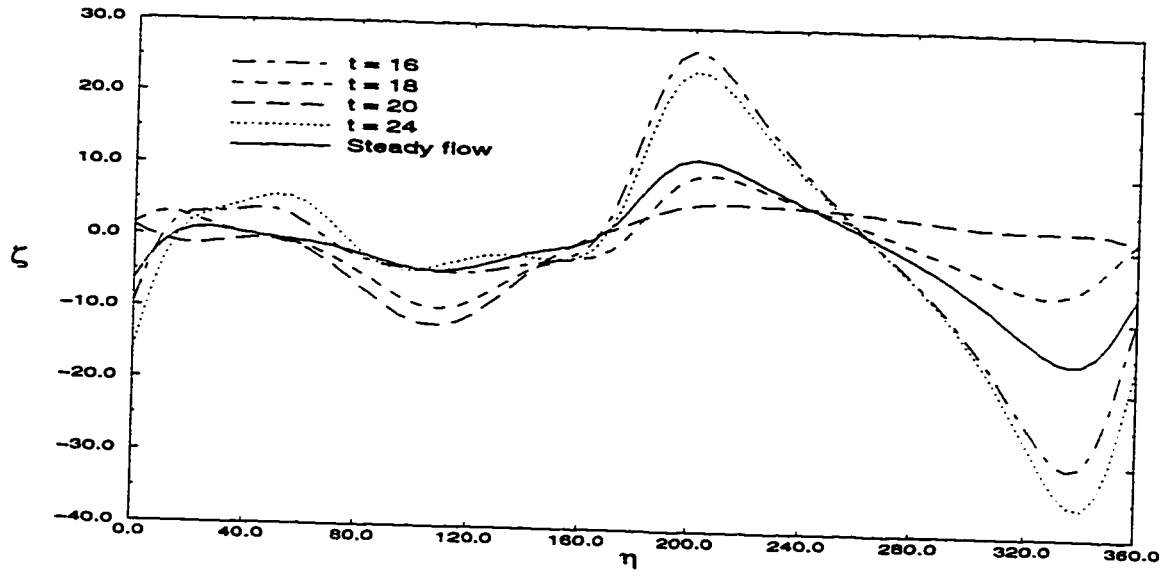

Figure 5.123: The surface vorticity distribution at various times during one complete cycle in case E-3 and comparison with the case of steady free stream.

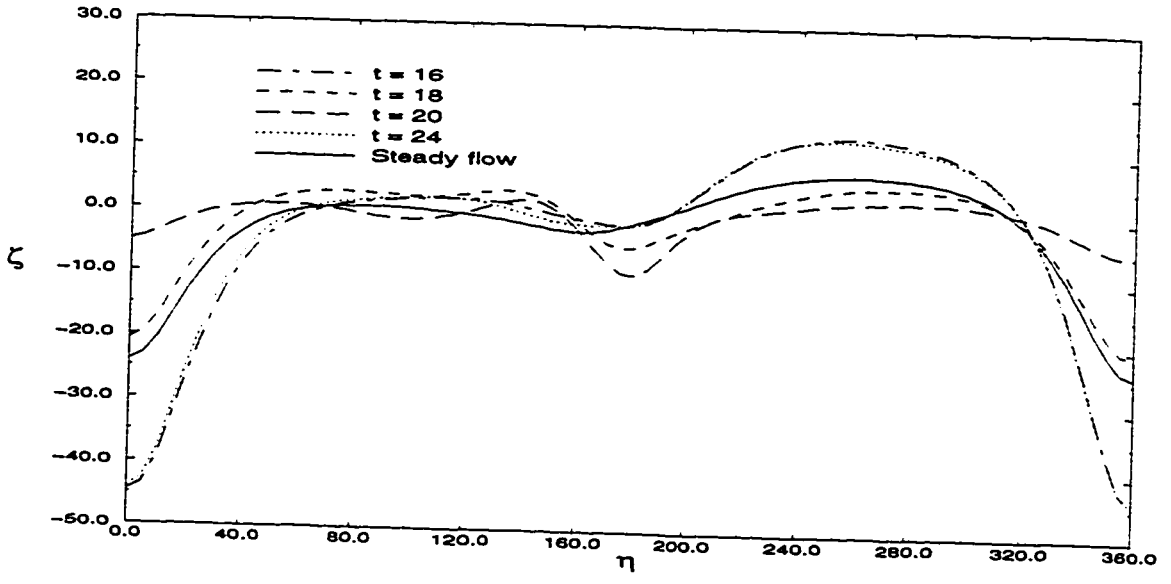

Figure 5.124: The surface vorticity distribution at various times during one complete cycle in case E-5 and comparison with the case of steady free stream.

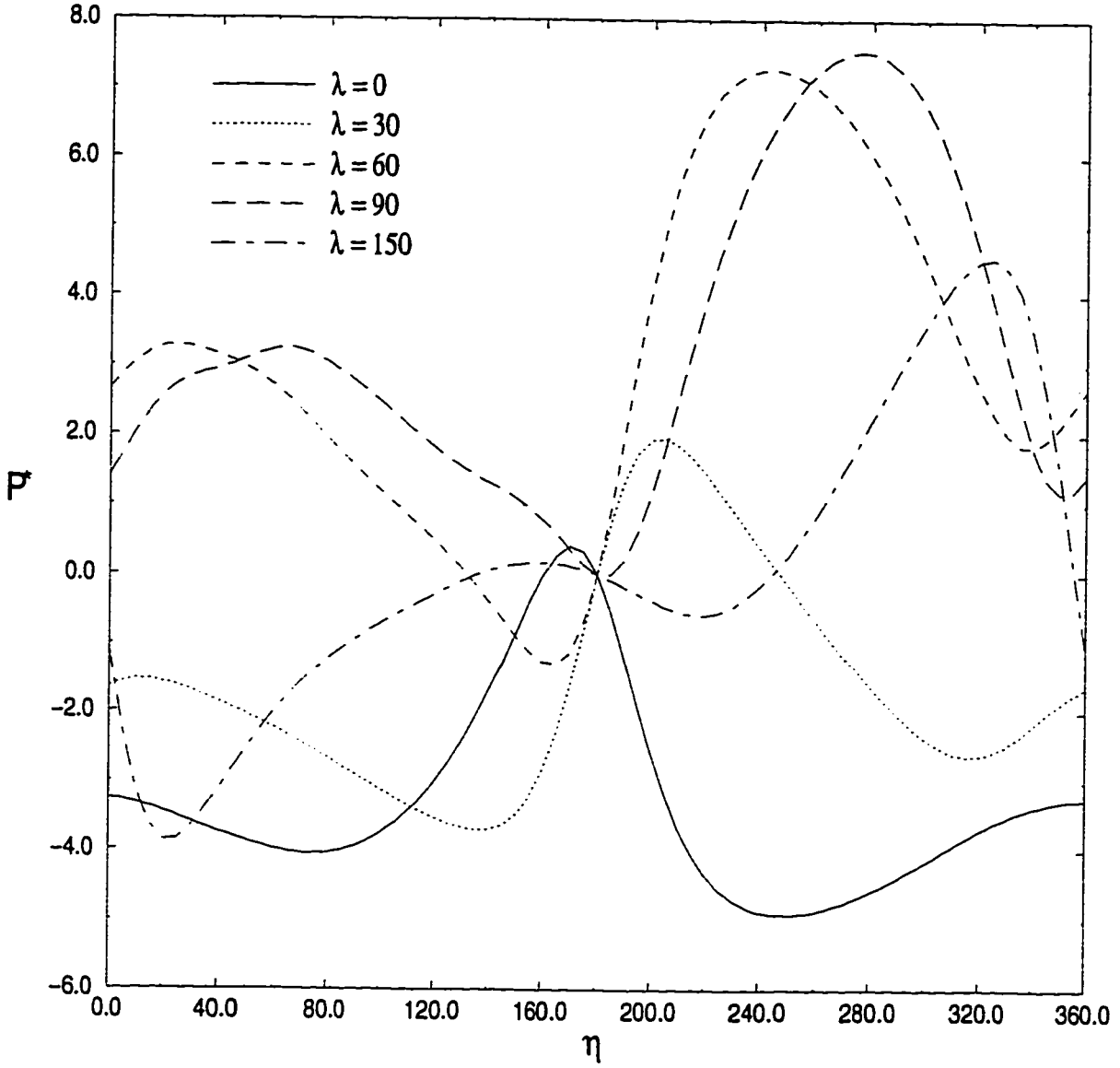

Figure 5.125: The effect of the angle of inclination on the pressure distribution at maximum free stream velocity for the case of Re=100 , Gr=20000, Ar=0.5, $\beta = 0.5$ and $S = \pi/4$.

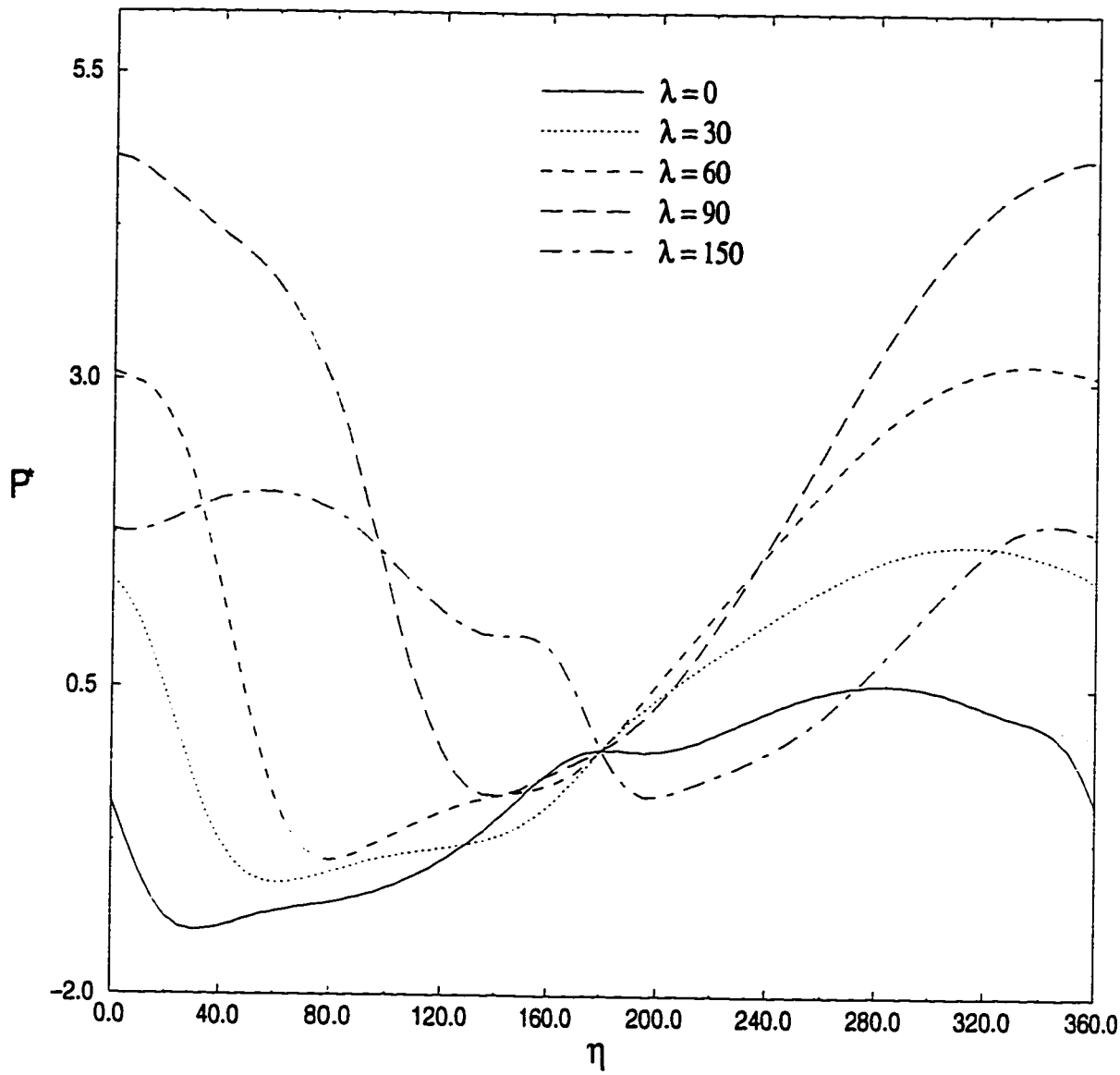

Figure 5.126: The effect of the angle of inclination on the pressure distribution at minimum free stream velocity for the case of Re=100 , Gr=20000, Ar=0.5, $\beta = 0.5$ and $S = \pi/4$.

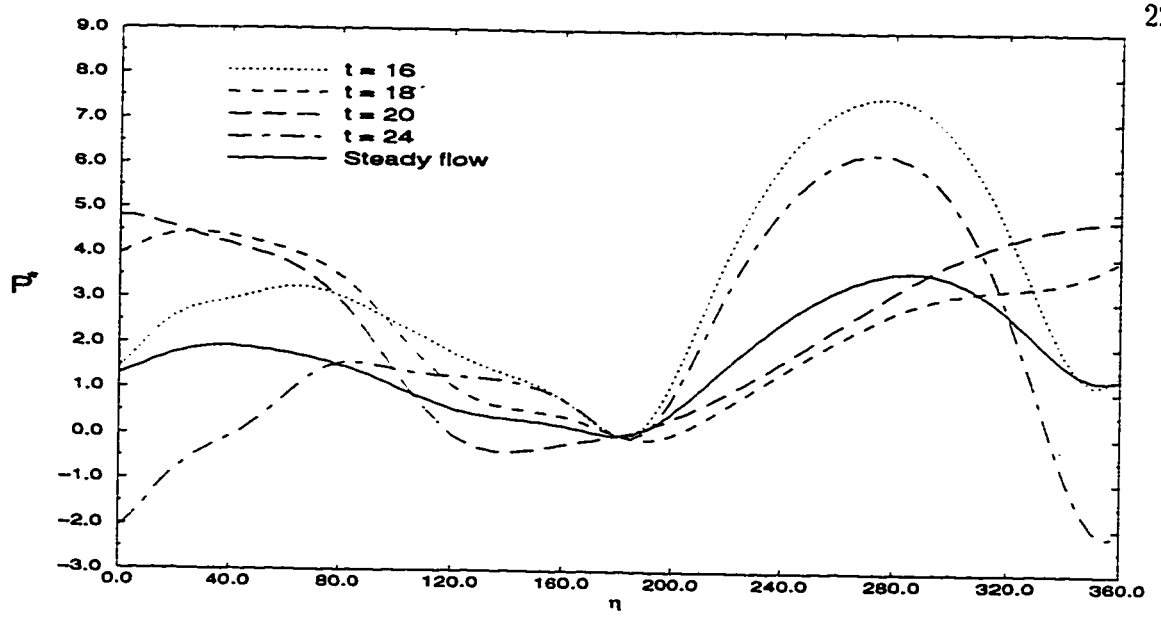

Figure 5.127: The pressure distribution at various times during one complete cycle in case E-3 and comparison with the case of steady free stream.

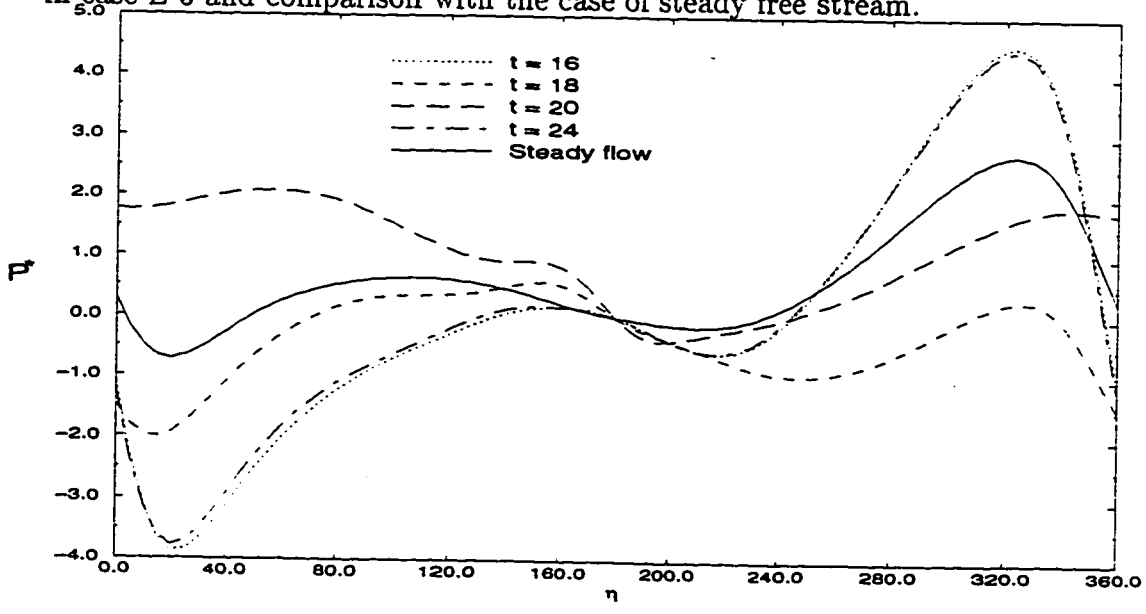

Figure 5.128: The pressure distribution at various times during one complete cycle in case E-5 and comparison with the case of steady free stream.

5.7.3 The Effect of Angle of Inclination on the Streamlines and Isotherms

The effect of the angle of inclination λ on the shape of the streamlines and isotherms is considerable. In this section, the effect of λ is demonstrated by covering the streamlines and isotherms for the only two cases of $\lambda = 0$ and $\lambda = 30^o$ for the forced convection regime. Figures 5.129a-d show the streamlines for one complete cycle of fluctuations for $\lambda = 0$. The figures show the formation of two pairs of vortices, the first is near the tube surface and the other is decaying down stream. the growth of the first pair and the movement and decay of the other pair can be seen in Figure 5.129d. The isotherms for the same case are shown in Figures 5.130a-d where $\lambda = 0^o$ creates a symmetrical thermal field.

Figures 5.131a-d and 5.132a-d show the streamlines and isotherms for the same forced convection case but for $\lambda = 30^o$. The asymmetry in the streamlines appearing in the figures is a result of the angle of inclination. A comparison between Figures 5.129b and 5.131b shows a higher velocity gradient and stronger vortices prevailing in the wake region for the case of $\lambda = 30^o$. Figure 5.131c shows two different size vortices on the tube wake instead of two similar ones when $\lambda = 0$.

The isotherms for this case are shown in Figures 5.132a-d. The angle of inclination in these figures creates asymmetry in the isotherms and higher temperature gradients in the back of the tube when compared to the symmetrical case of $\lambda = 0$.

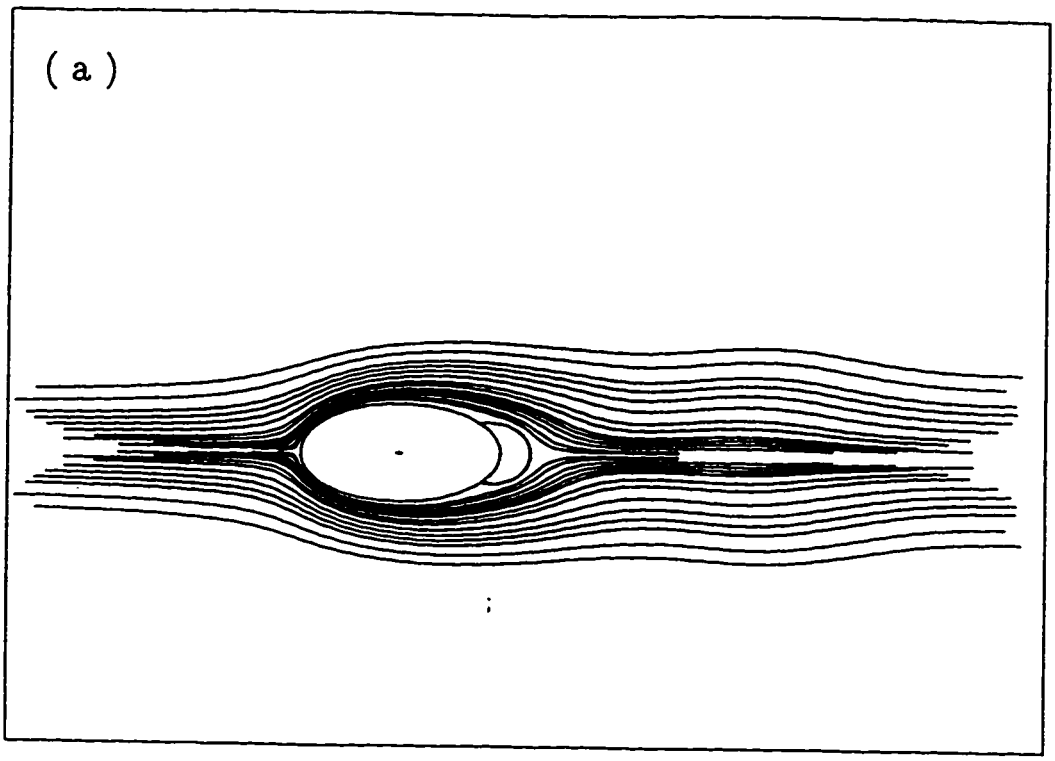
(a)

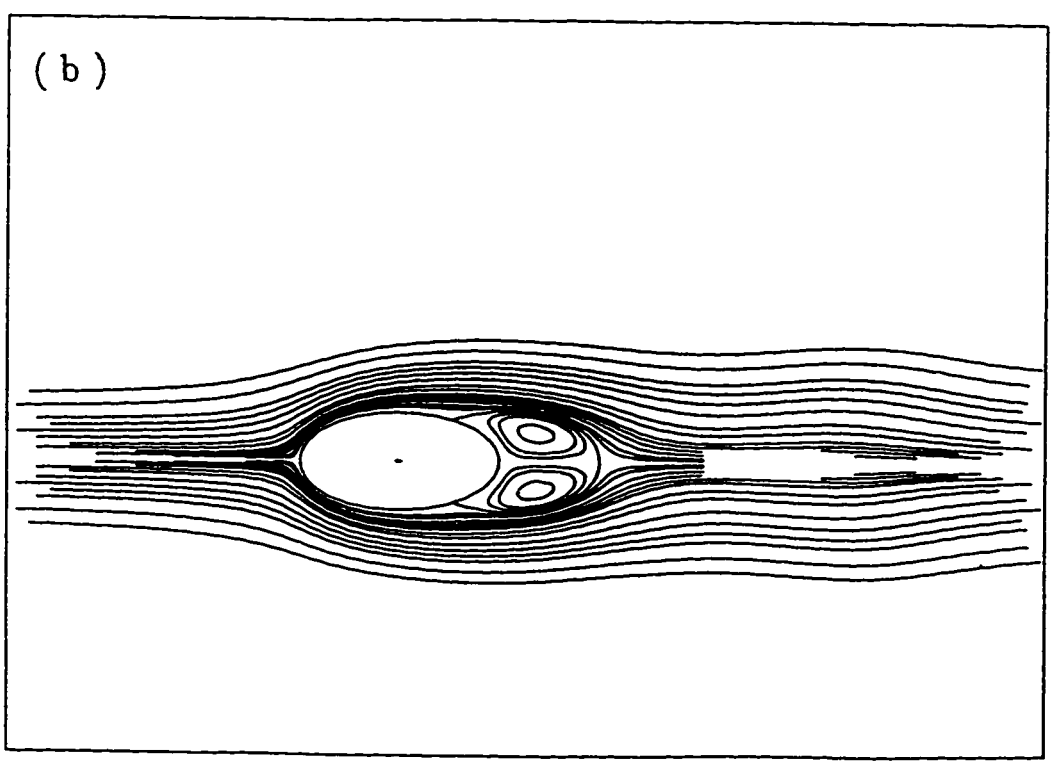
(b)

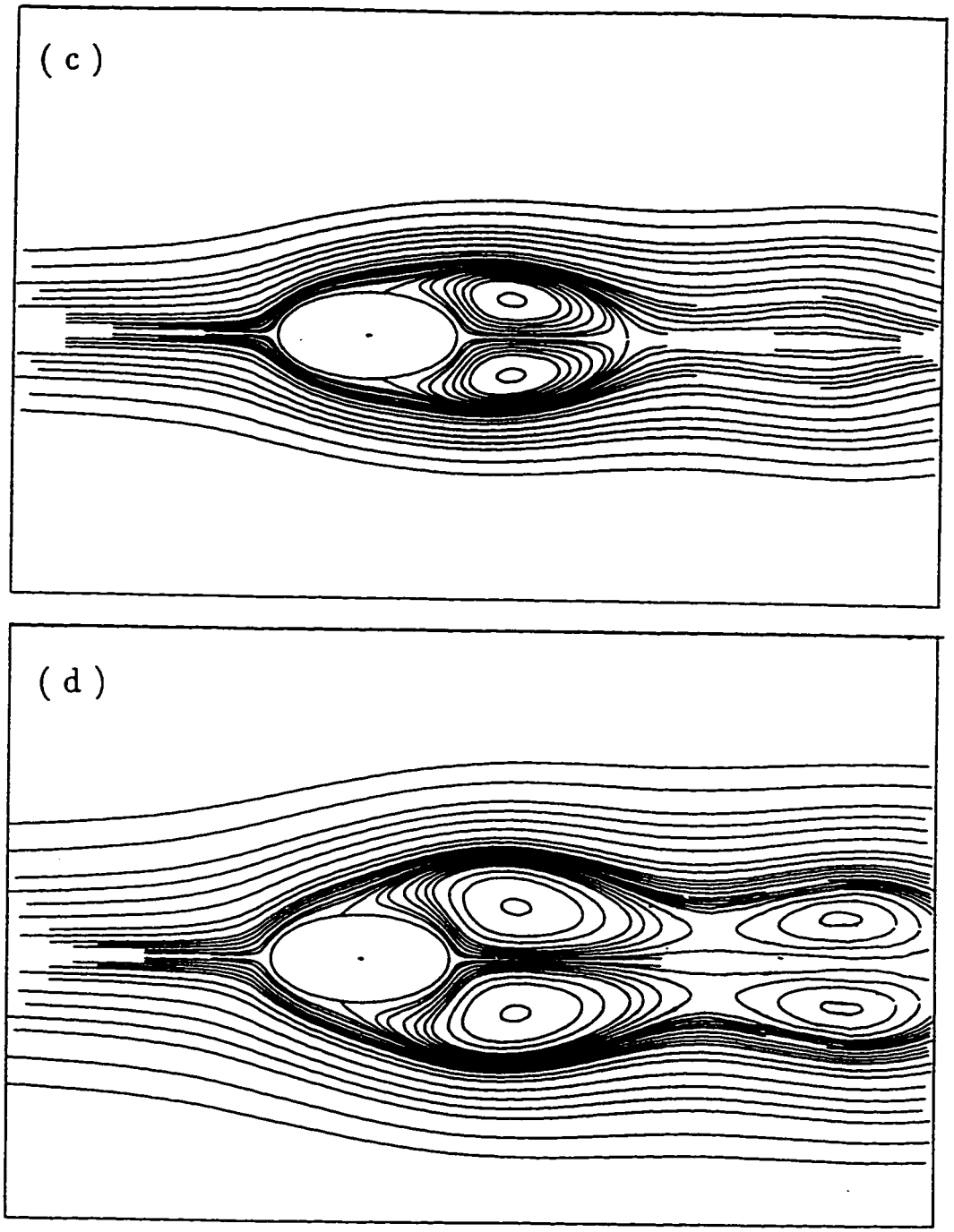

Figure 5.129: The development of the streamline patterns for the case of Re=100, Gr=0, $Ar = 0.5$, $\lambda = 0°$, $\beta = 0.5$ and $S = \pi/4$, during one complete cycle : (a) t = 32; (b) t = 34; (c) t = 36; (d) t = 40.

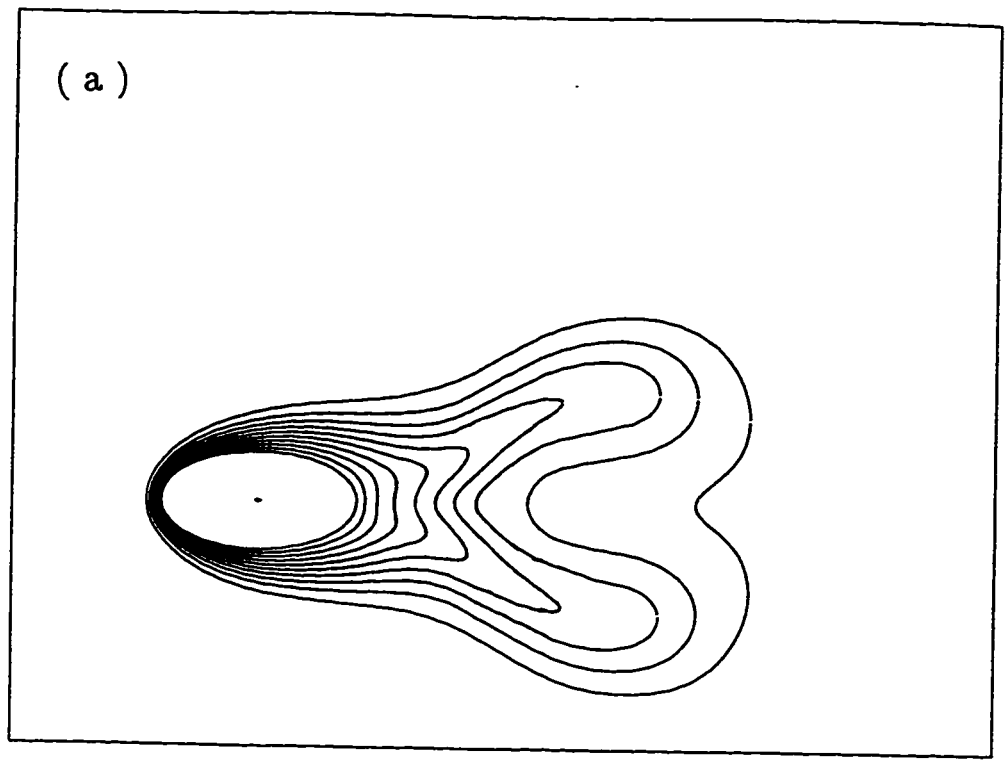
(a)

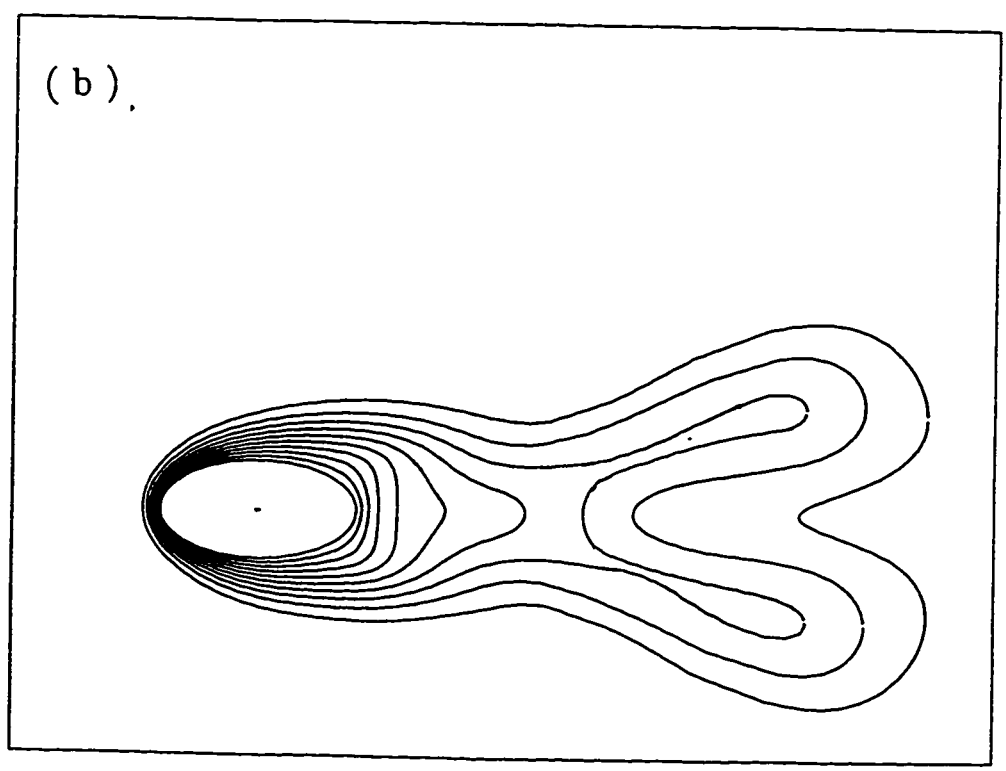
(b)

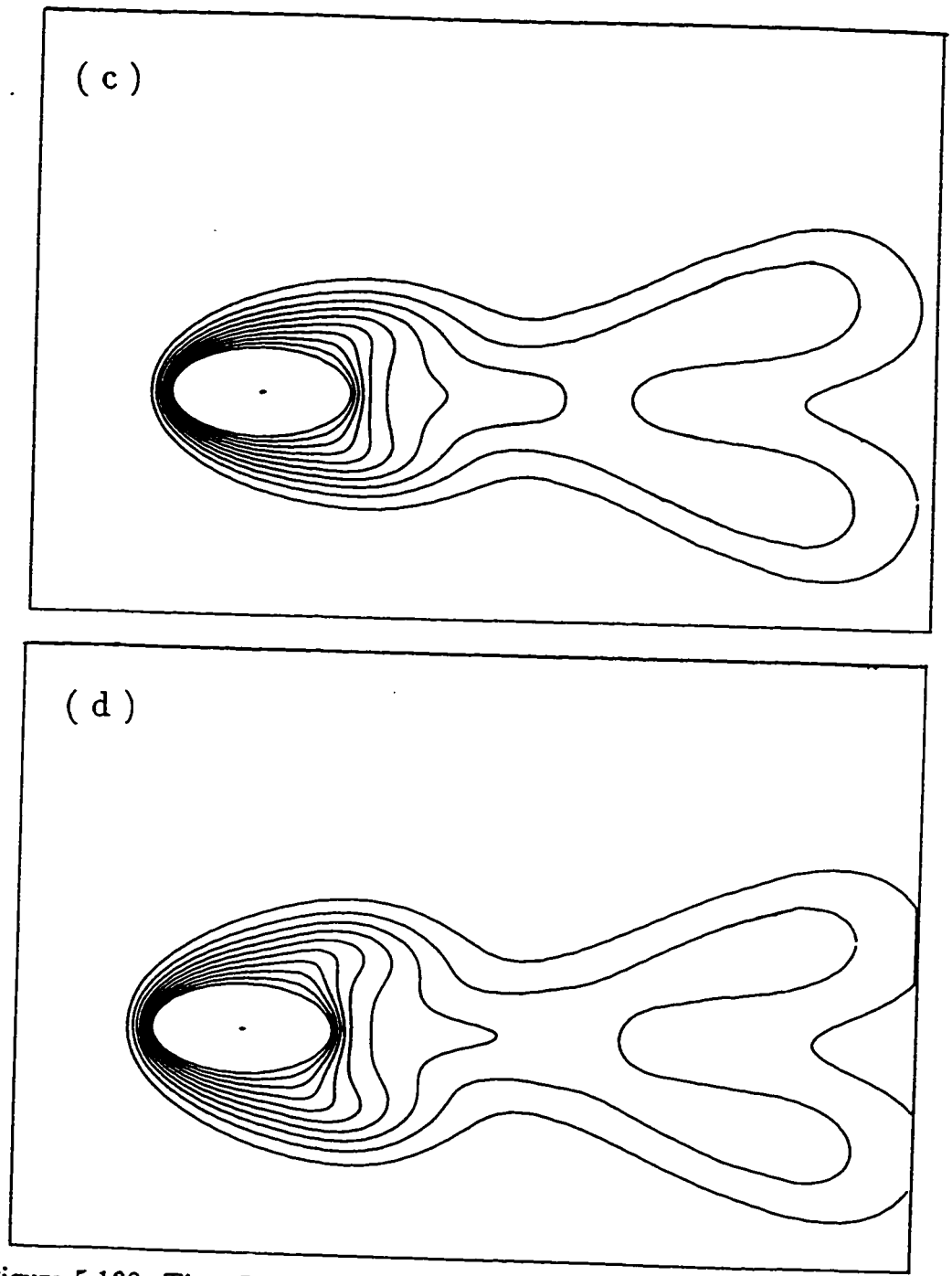

Figure 5.130: Time Development of the isotherm contours for the case of Re=100, Gr=0, Ar=0.5, $\lambda = 0^o$, $\beta = 0.5$ and $S = \pi/4$ during one complete cycle : (a) t = 32; (b) t = 34; (c) t = 36; (d) t = 40.

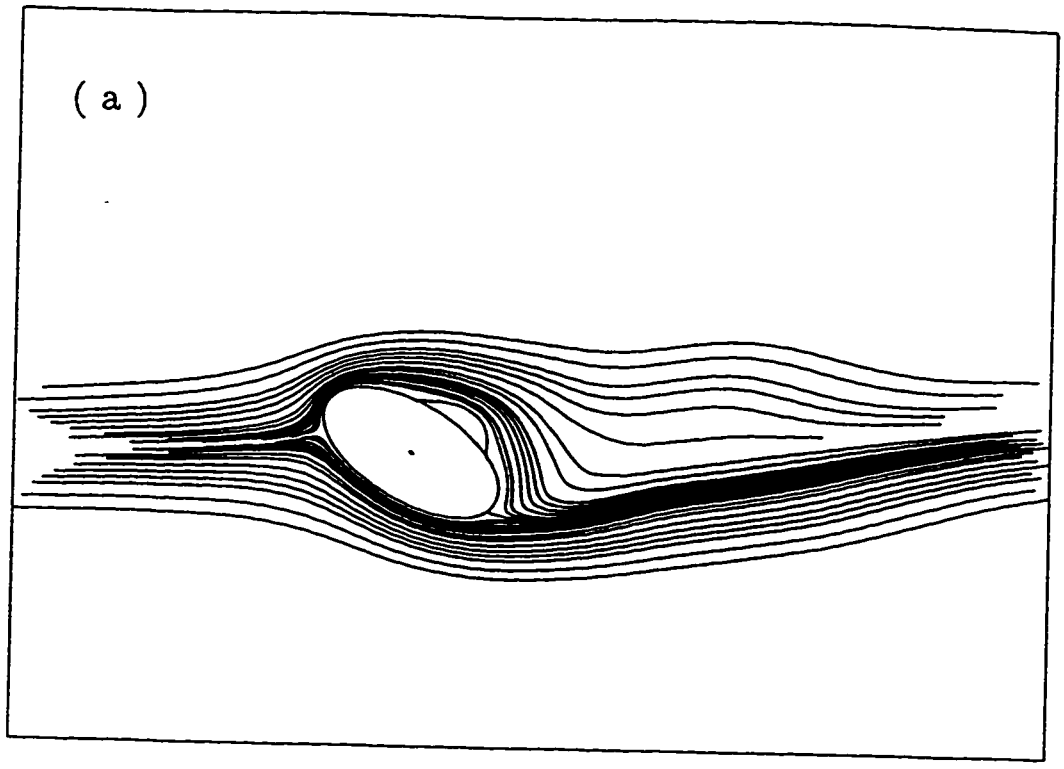
(a)

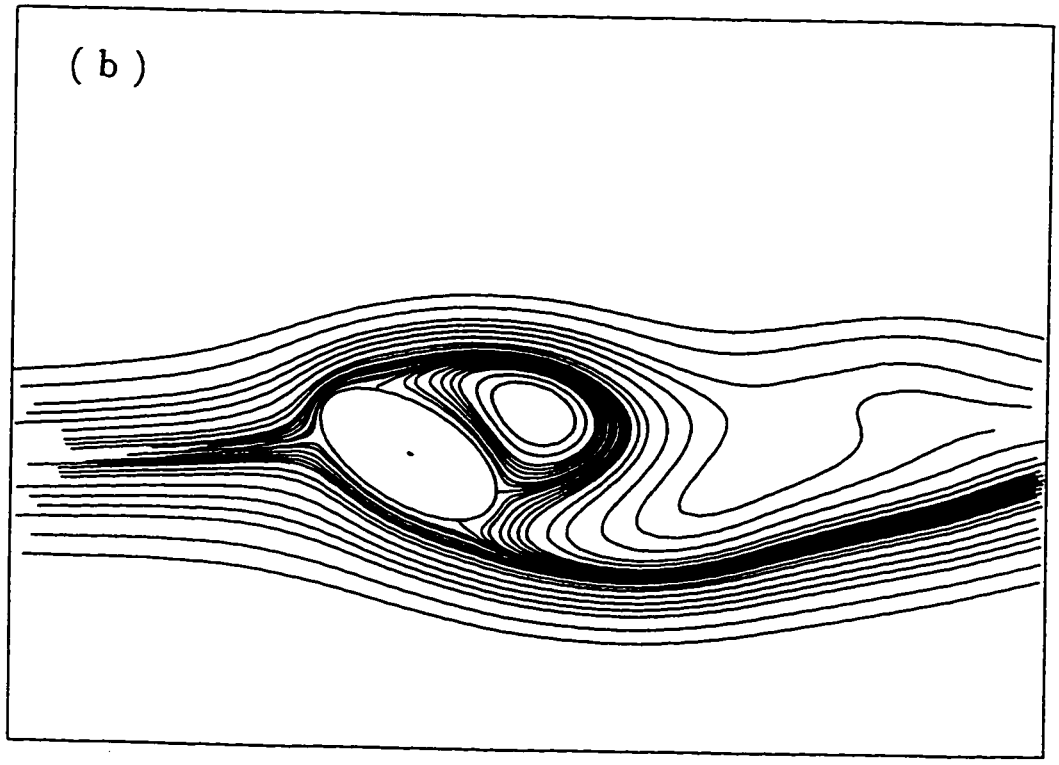
(b)

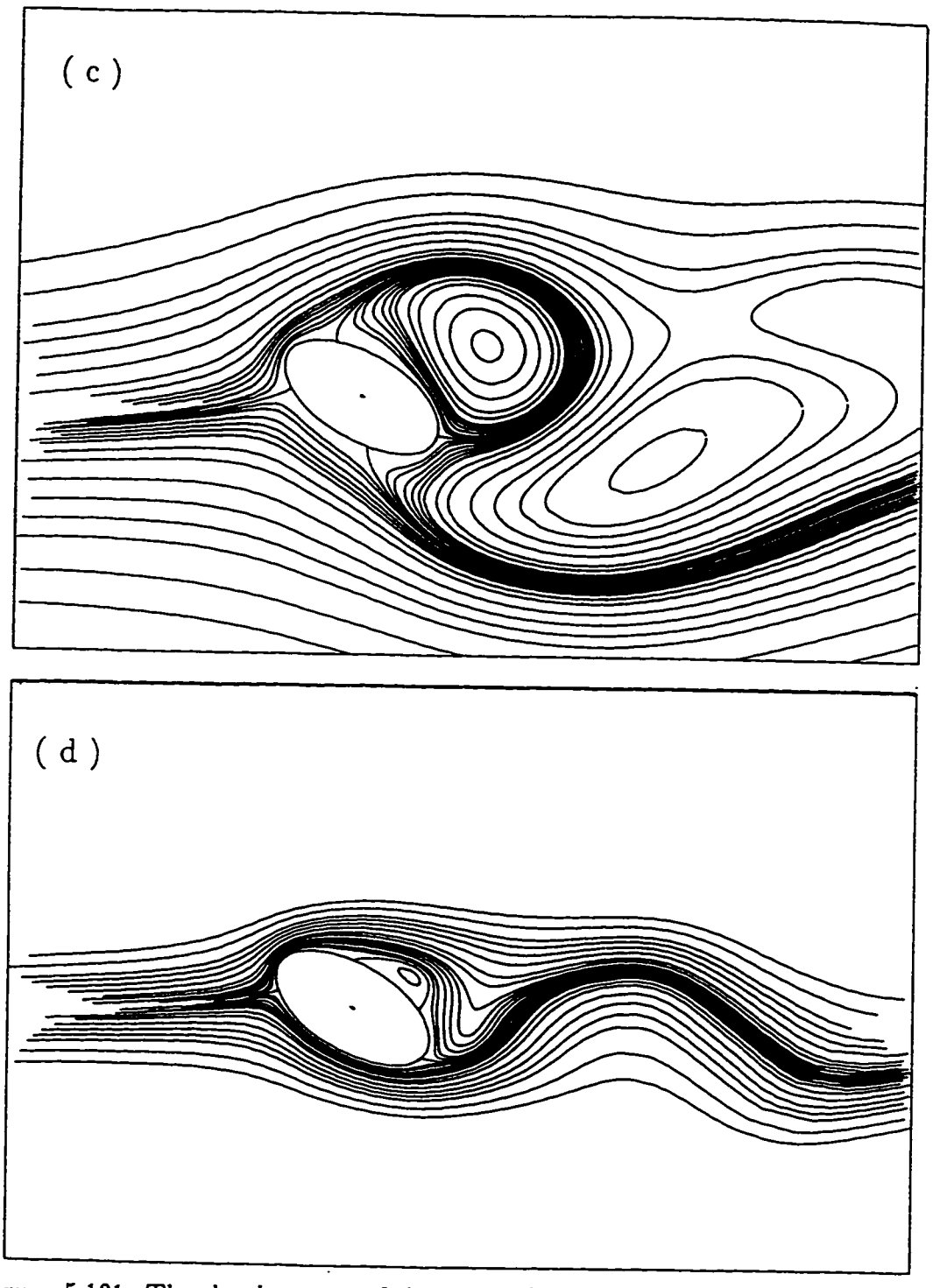

Figure 5.131: The development of the streamline patterns for the case of Re=100, Gr=0, $Ar = 0.5$, $\lambda = 30°$, $\beta = 0.5$ and $S = \pi/4$, during one complete cycle : (a) t = 32; (b) t = 34; (c) t = 36; (d) t = 40.

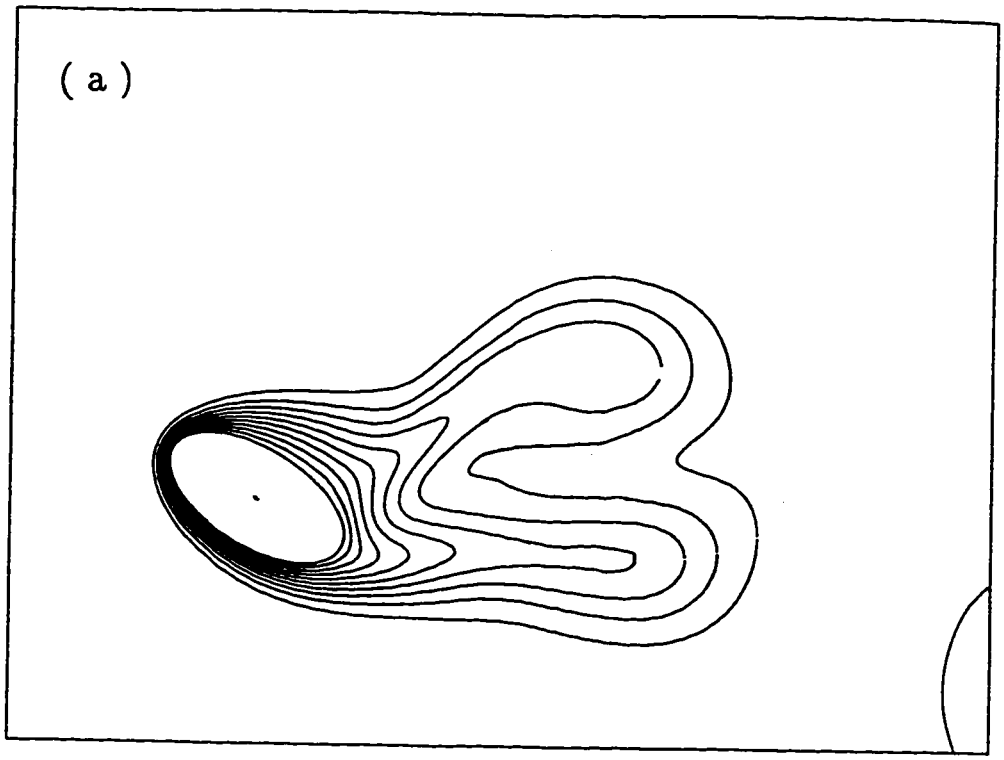
(a)

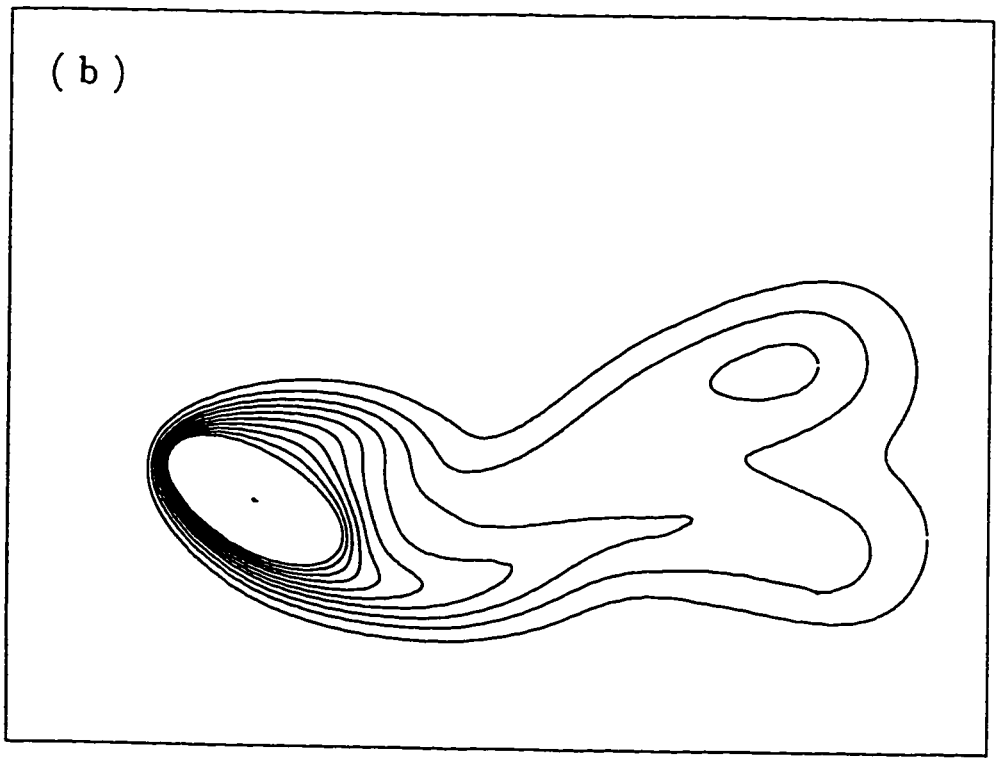
(b)

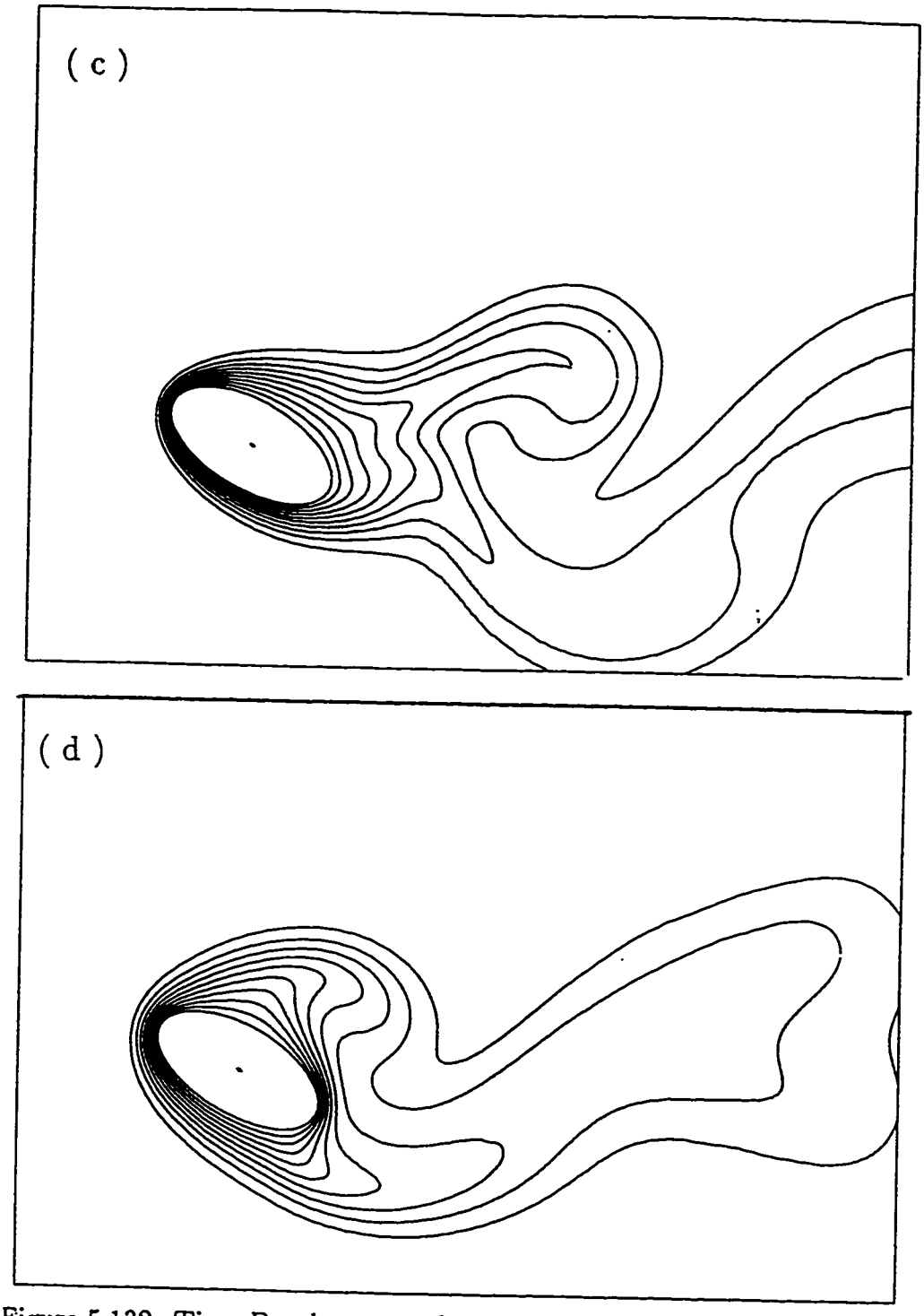

Figure 5.132: Time Development of the isotherm contours for the case of Re=100, Gr=0, Ar=0.5, $\lambda = 30°$, $\beta = 0.5$ and $S = \pi/4$ during one complete cycle : (a) t = 32; (b) t = 34; (c) t = 36; (d) t = 40.

5.8 The Effect of Axis Ratio

5.8.1 The Effect of Axis Ratio on the Average Nusselt Number

Table 5.8 shows the percentage enhancement in the heat transfer rate for different axis ratios and a comparison with the steady stream case. The table shows that the axis ratio has an influence in the enhancement of heat transfer due to the effect of fluctuation. One can see that for Ar=0.2 the enhancement is 8.5% while for Ar=0.8 the enmhancement is 5.1 % . This shows that the heat transfer enhancement is also a function of the axis ratio, as expected.

Figure 5.133 shows the time variation of the average Nusselt number for different axis ratios due to the effect of fluctuations in the mean free stream. One can deduce from the figure that as the axis ratio decreases, the amplitude of $\overline{Nu}$ gets larger. With Ar=0.965 the case approaches that of a circular cylinder and this case was used for validating the accuracy of the mathematical model by comparing the results with those from previous work (see section (5.2)).

Table 5.8: The percentage increase in $\overline{\overline{Nu}}$ for different axis ratios compared to the steady stream case.

Code#	Re	Gr	λ	b/a	S	β	$\overline{\overline{Nu}}$	$\overline{Nu}$ $\beta = 0$	% increase
F-1	100	20000	30°	0.2	$\frac{\pi}{4}$	0.50	6.77	6.24	8.5 %
F-2	100	20000	30°	0.5	$\frac{\pi}{4}$	0.50	6.57	6.23	5.58 %
F-3	100	20000	30°	0.8	$\frac{\pi}{4}$	0.50	6.20	5.94	5.1 %

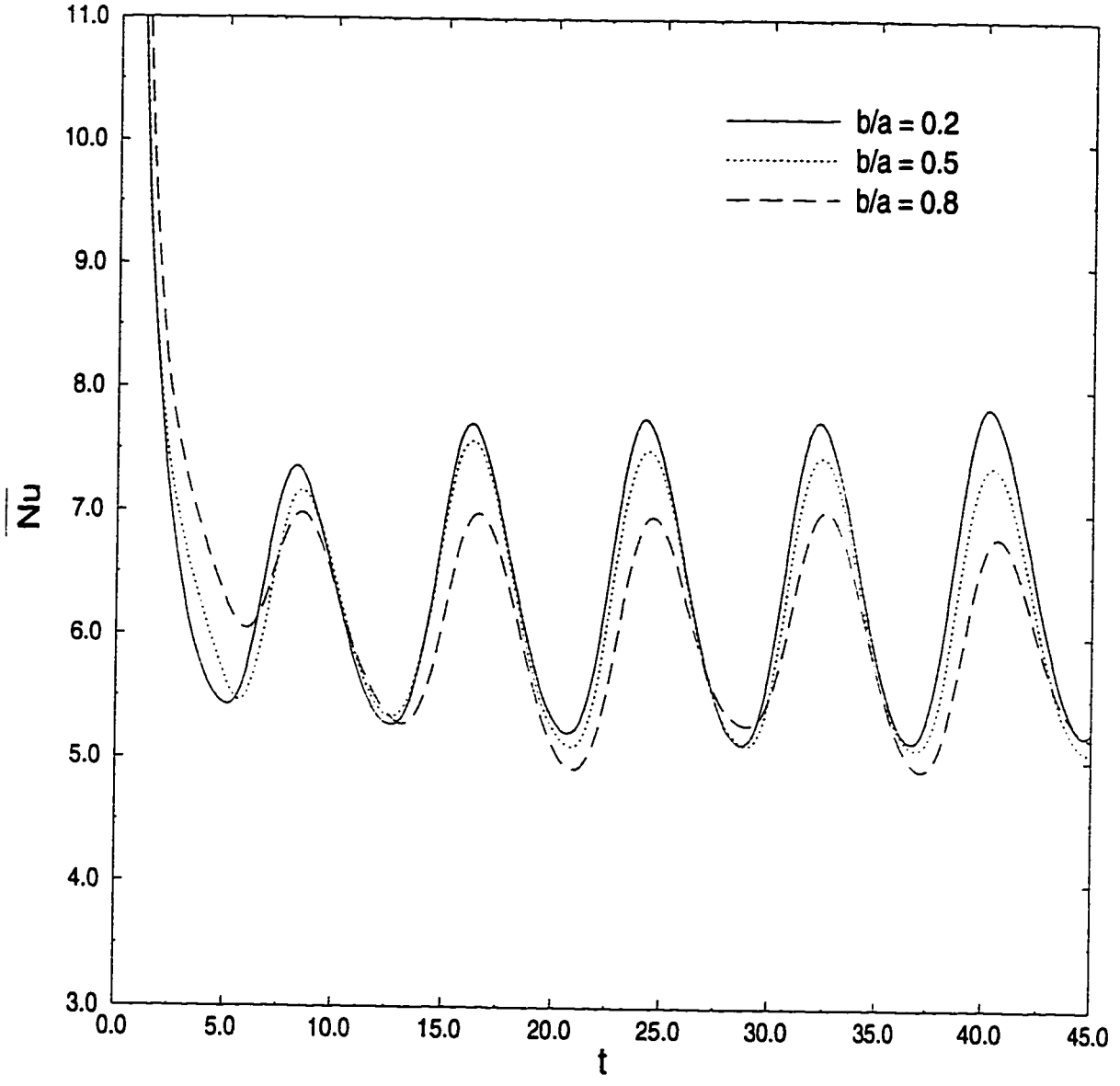

Figure 5.133: The time variation of $\overline{Nu}$ following the sudden temperature rise for various axis ratios for the case of Re=100, Gr=20000, $\lambda = 30°$, $\beta = 0.5$ and $S = \pi/4$.

5.8.2 The Effect of Axis Ratio on the Local Nusselt Number and Vorticity Distributions

Figures 5.134 and 5.135 show the local Nusselt number distributions for axis ratios Ar=0.2 and 0.8. The Nu values are given at different times to show the variation at maximum and minimum free stream velocity. The figures show that the maximum Nu value for axis ratio of 0.2 is three times higher than that for the case of Ar=0.8 while the minimum value is almost the same.

These results conclude how the axis ratio is affecting the local Nusselt number distribution. The very high Nu values for the case of small Ar can be explained by examining the vorticity distributions for axis ratios 0.2 and 0.8 shown in Figures 5.136 and 5.137, respectively. Figure 5.136 shows a very sharp increase in the vorticity values reaching 85 at $\eta = 178^o$. This gives a very high velocity gradient in the region $150^o \leq \eta \leq 200^o$ and this causes a very high heat transfer rate in that region.

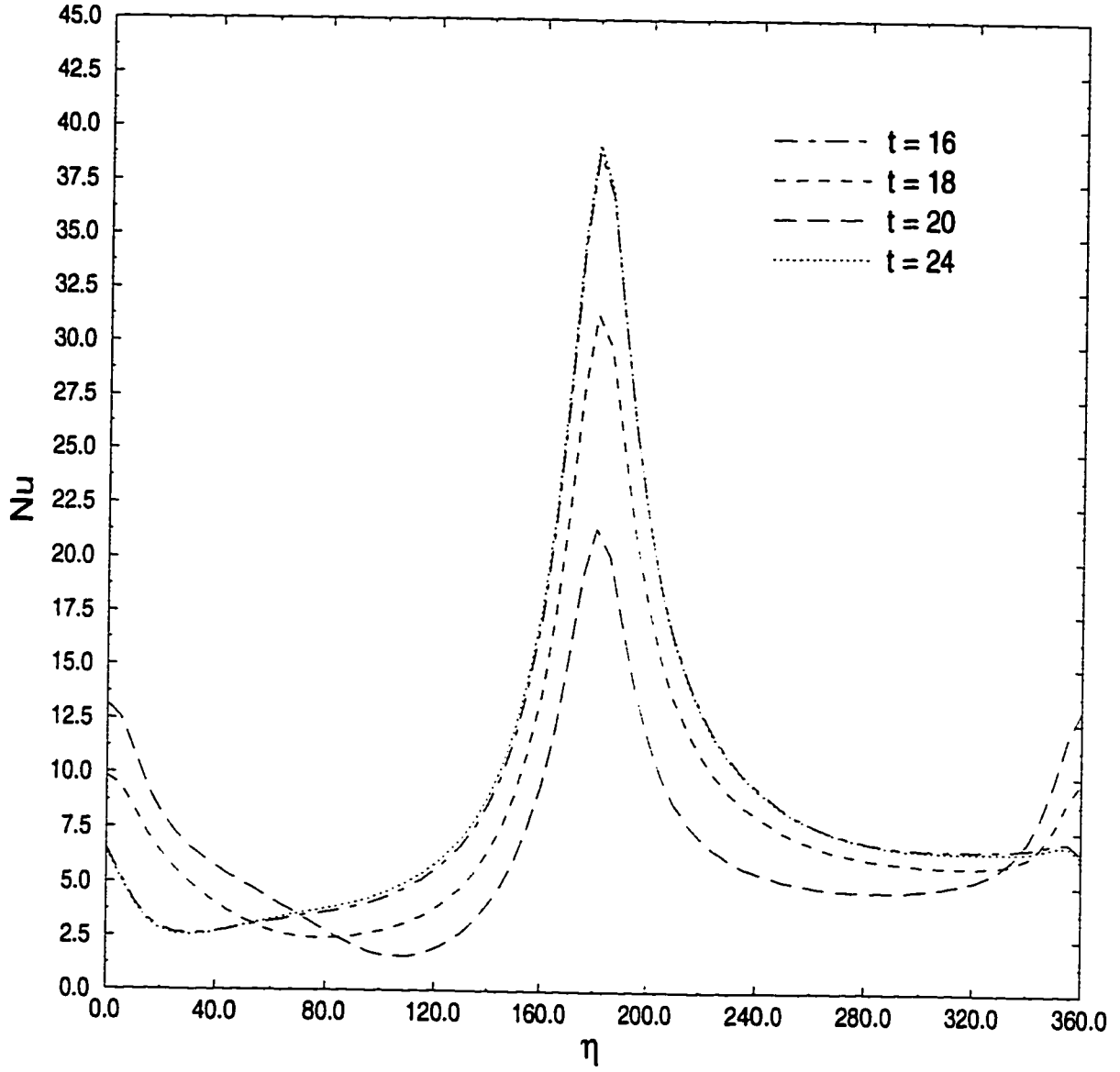

Figure 5.134: The local Nusselt number distribution at various times during one complete cycle for the case of Re=100, Gr=20000, Ar=0.2, $\lambda = 30°$, $\beta = 0.5$ and $S = \pi/4$.

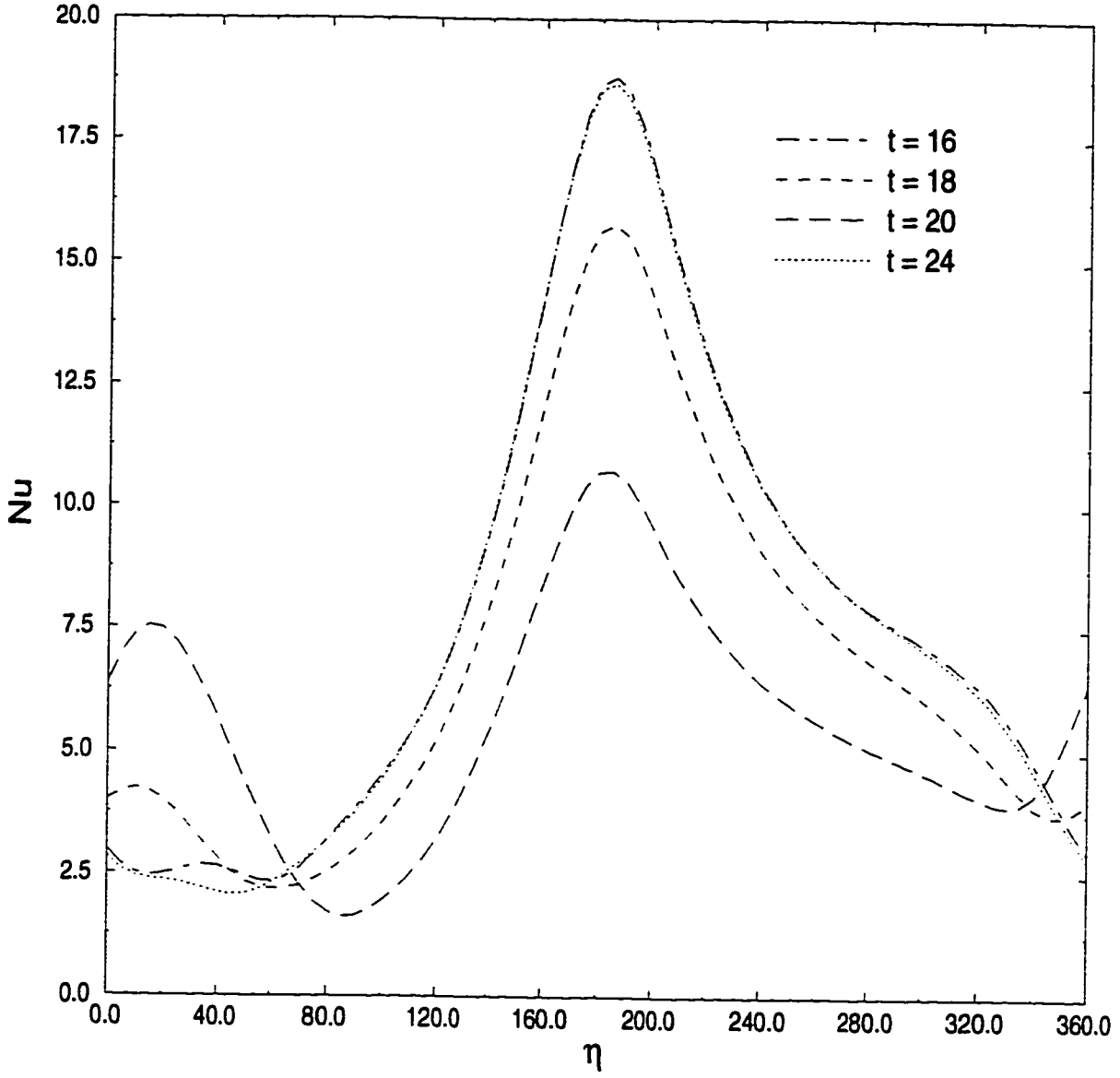

Figure 5.135: The local Nusselt number distribution at various times during one complete cycle for the case of Re=100, Gr=20000, Ar=0.8, $\lambda = 30°$, $\beta = 0.5$ and $S = \pi/4$.

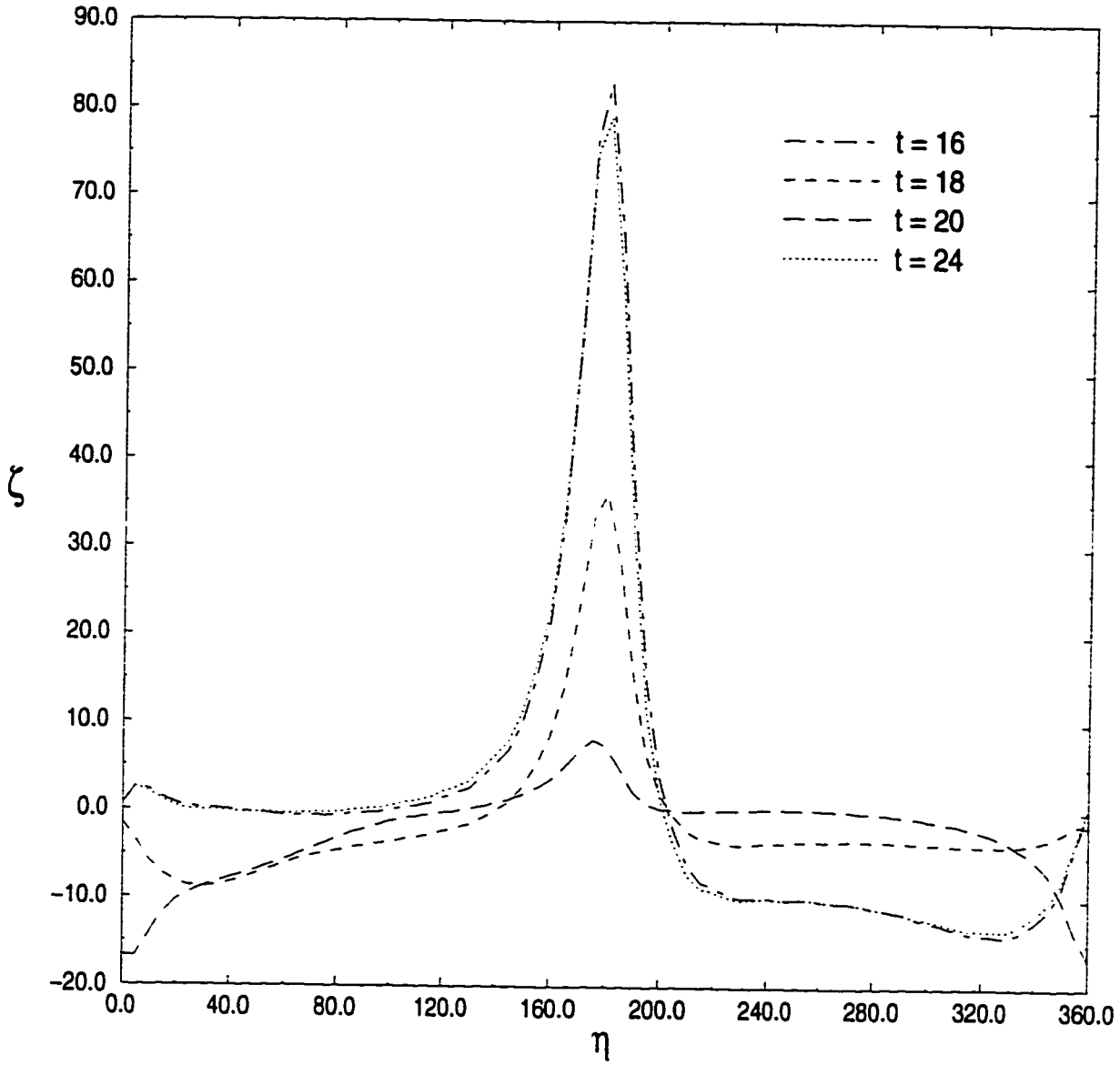

Figure 5.136: The surface vorticity distribution at various times during one complete cycle for the case of Re=100, Gr=20000, Ar=0.2, $\lambda = 30°$, $\beta = 0.5$ and $S = \pi/4$.

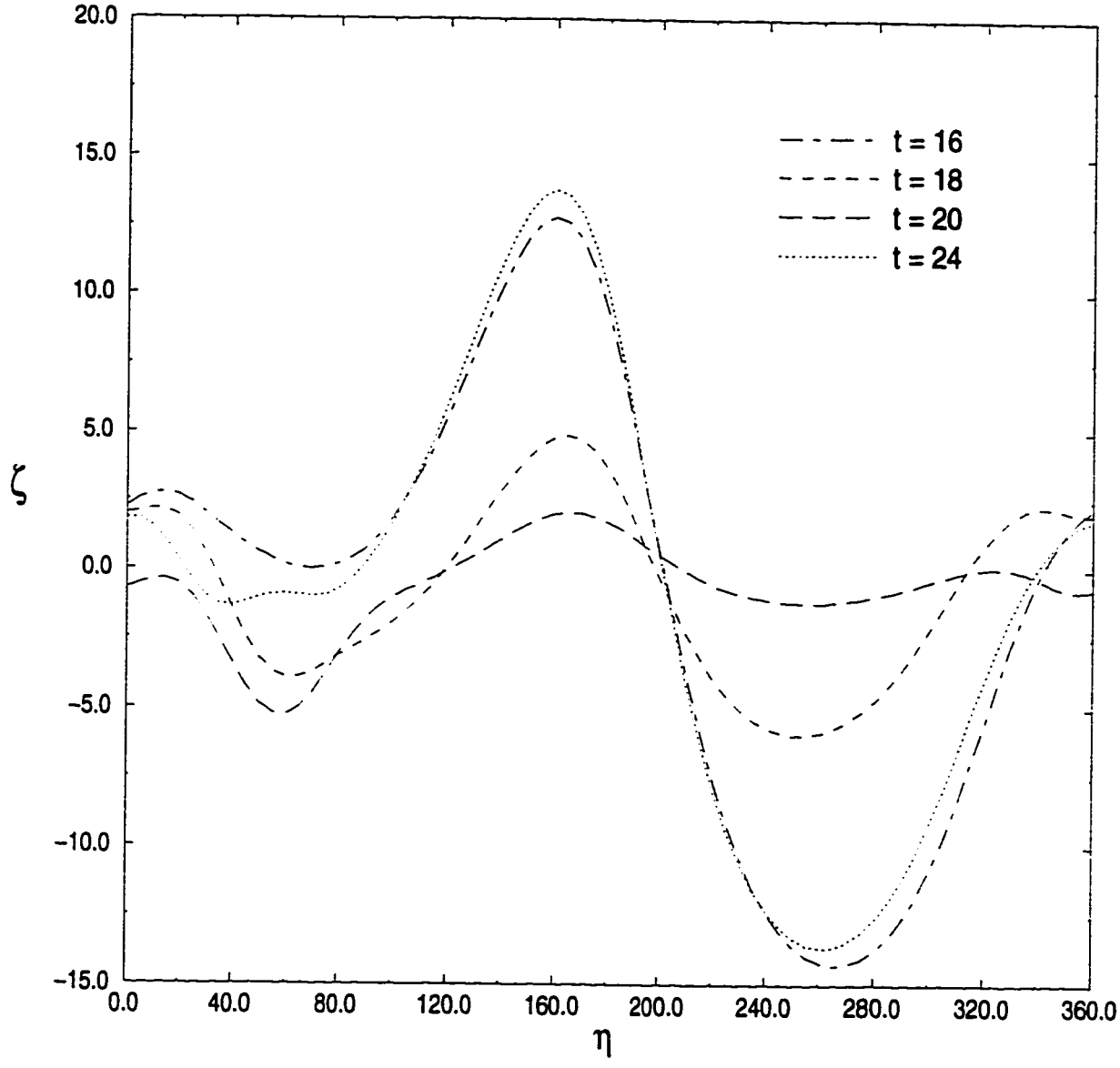

Figure 5.137: The surface vorticity distribution at various times during one complete cycle for the case of Re=100, Gr=20000, Ar=0.8, $\lambda = 30°$, $\beta = 0.5$ and $S = \pi/4$.

5.8.3 The Effect of Axis Ratio on the Streamlines and Isotherms

To show the effect of axis ratio on the streamlines and isotherms, the two extreme cases of Ar=0.2 and 0.8 are plotted for cases (F-1) and (F-3). Figures 5.138a-d show the streamlines for one complete cycle of fluctuation for Ar=0.2. Figure 5.138a shows the streamlines at U = U_{max} with no vortices present in the flow field. As the free stream decelerates, vortices start to form near the tube surface. Figure 5.138c shows the situation when U = U_{min} , where the formed vortices reach their maximum size and the flow near the surface is dominated by vortical motion. One major characteristic of this case is the presence of one major vortex at a time instead of two as was found in case of Ar=0.5 (see Figures 5.43a-f). Figure 5.138d shows the situation at the end of the cycle which is very much the same as in Figure 5.138a.

The isotherms for this case are shown in Figures 5.139a-d. The figures show that vortex shedding causes warm fluid bulks to separate and move away from the tube surface. The thermal field is characterized with large temperature gradient near the surface and extends for a large distance in the wake.

Figures 5.140a-d show the streamlines for Ar=0.8 for one complete cycle corresponding to case (F-3). Figure 5.140a is for the streamlines at the start of the fifth cycle of fluctuations. Similar to the previous case, as the fluid decelerates vortices start to form near the surface and shed into the wake as shown in Figure 5.140b.

When the free stream velocity reaches its minimum (see Figure 5.140c), a large portion of the tube surface becomes dominated by vortical driven flow created by two stronger vortices rather than one vortex in case of Ar=0.2 (see Figure 5.138c). The figure also shows the presence of three stagnation points in comparison with only two points in Figure 5.138c. When U reaches its maximum, Figure 5.140d shows the birth of new vortex which was not present in Figure 5.138d.

Figures 5.141a-d show the isotherms for axis ratio of 0.8. by comparing the two cases of Ar=0.2 and 0.8, one can deduce that with the decrease in axis ratio, the isotherms come closer to the surface at the top and bottom of the tube reflecting high temperature gradients and their extension and size away from the tube surface is smaller and narrower.

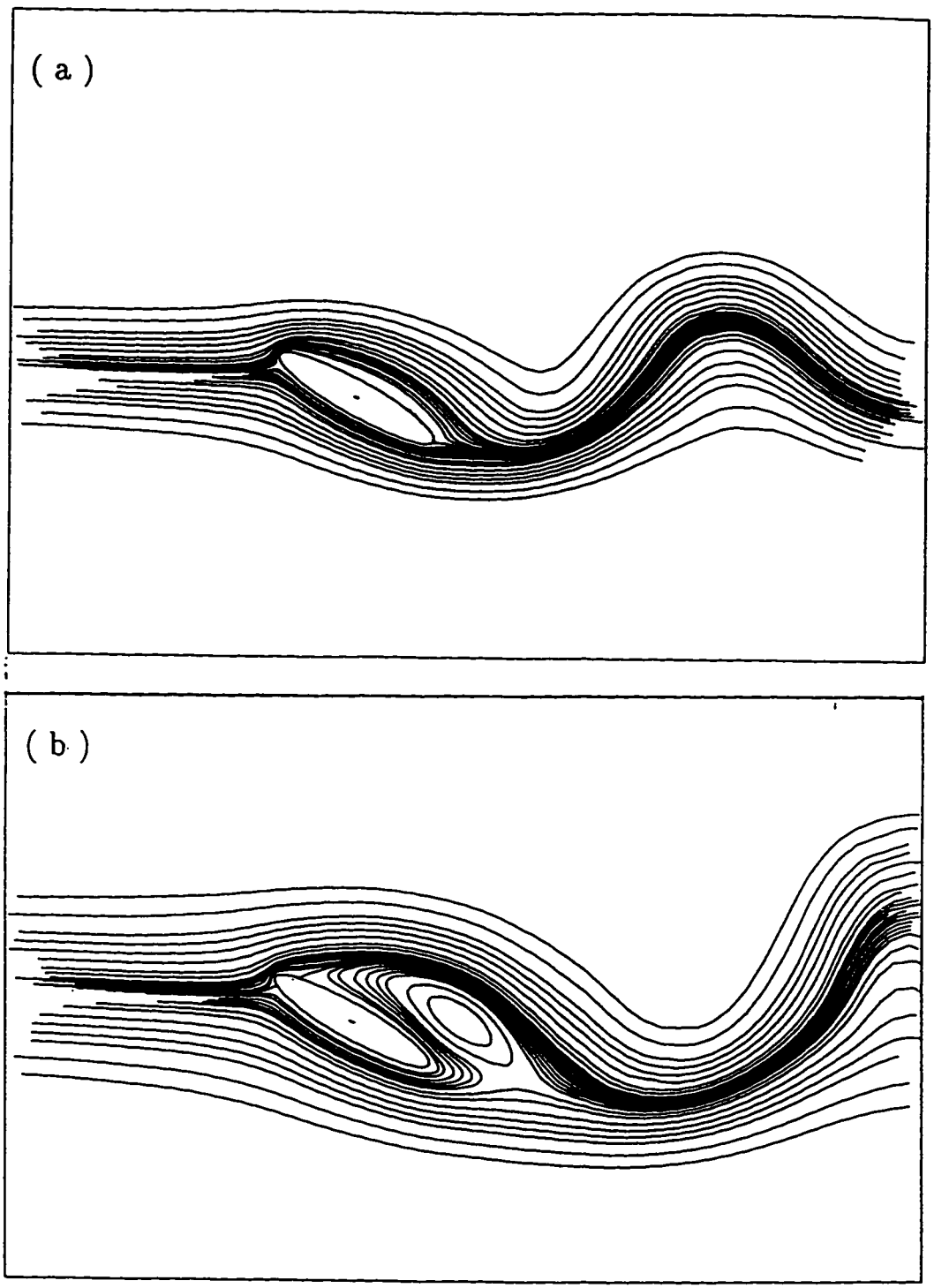
(a)
(b)

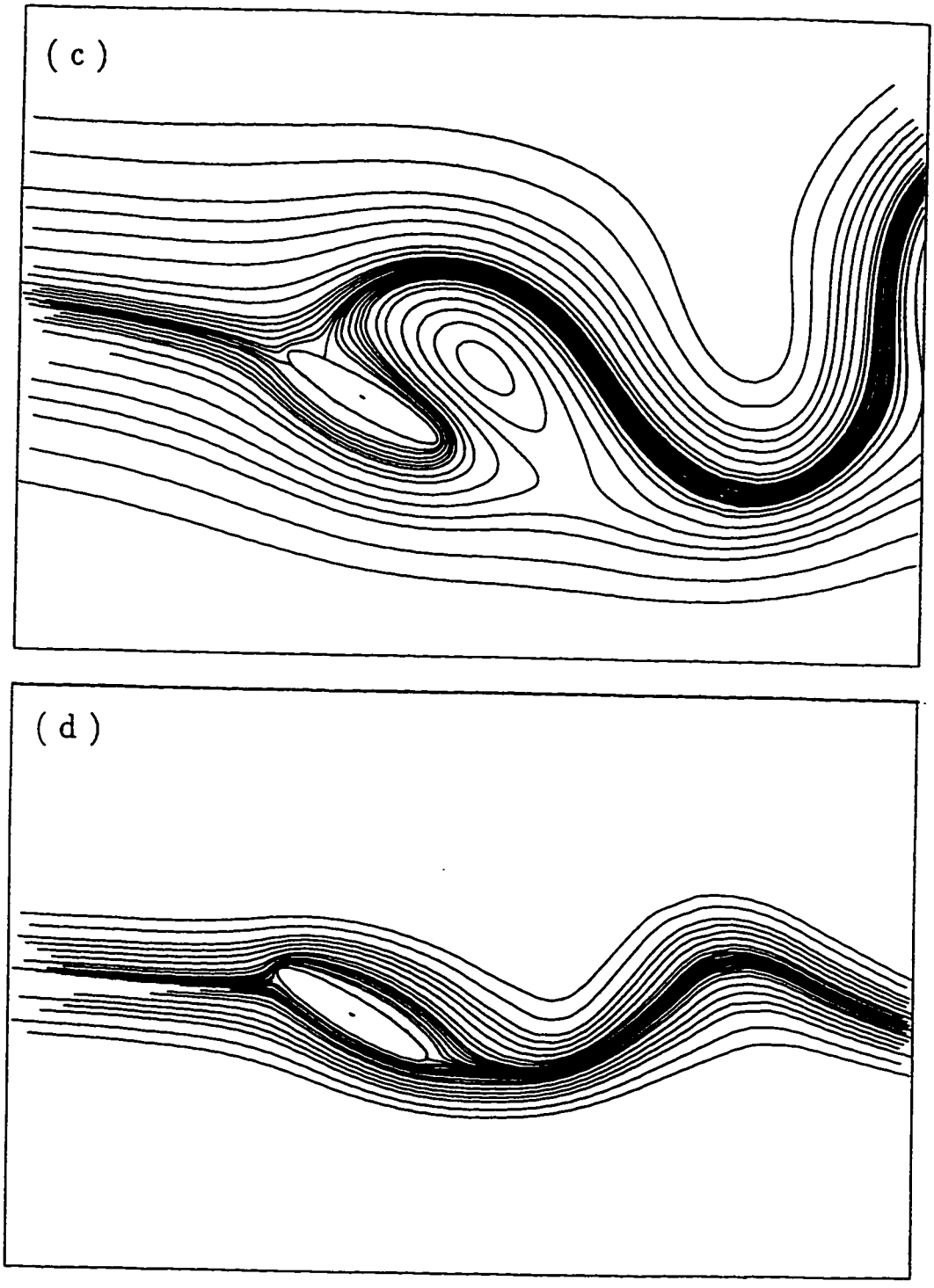

Figure 5.138: The development of the streamline patterns for the case of Re=100, Gr=20000, $Ar = 0.2$, $\lambda = 60°$, $\beta = 0.5$ and $S = \pi/4$, during one complete cycle : (a) t = 32; (b) t = 34; (c) t = 36; (d) t = 40.

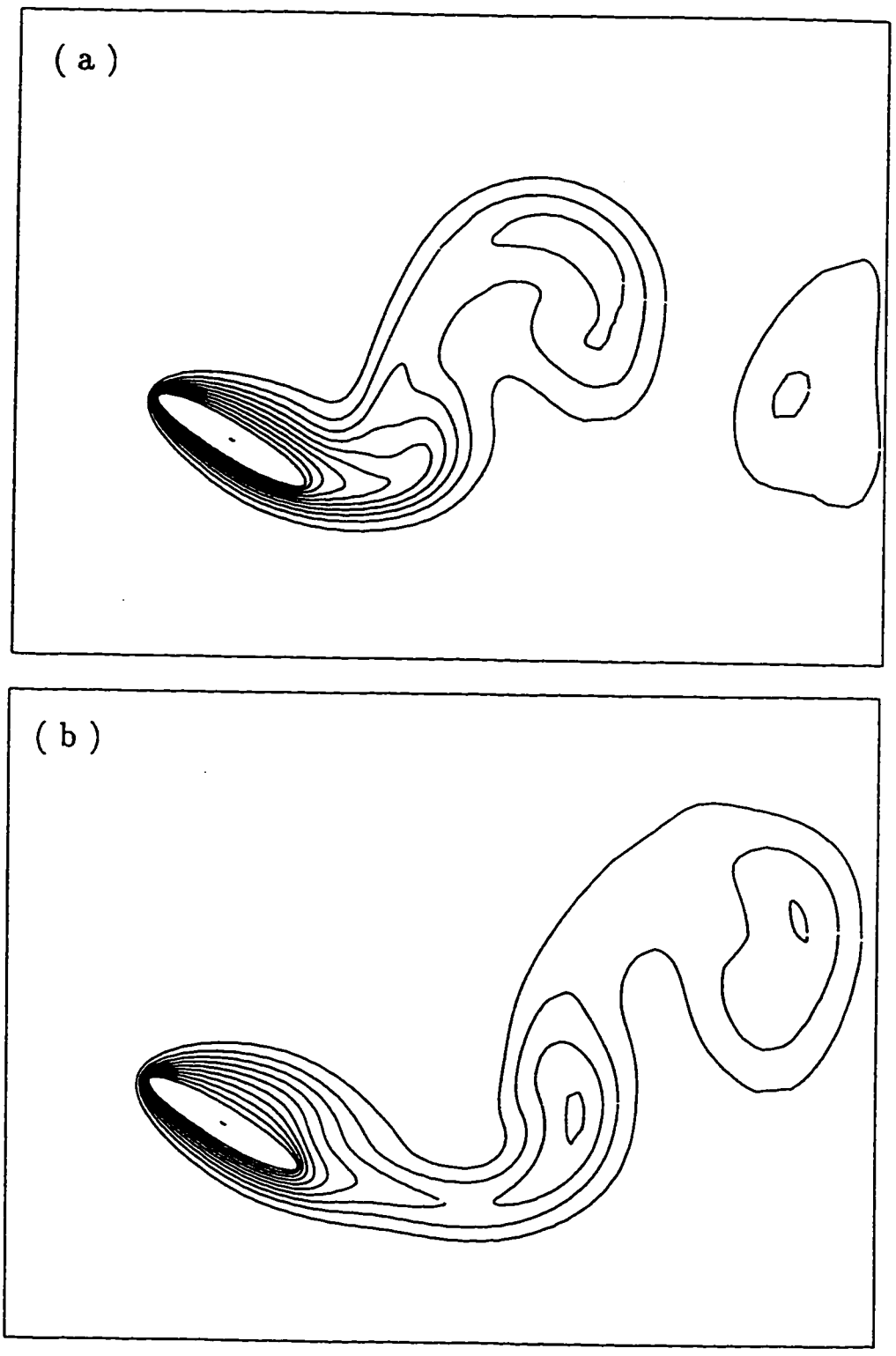
(a)
(b)

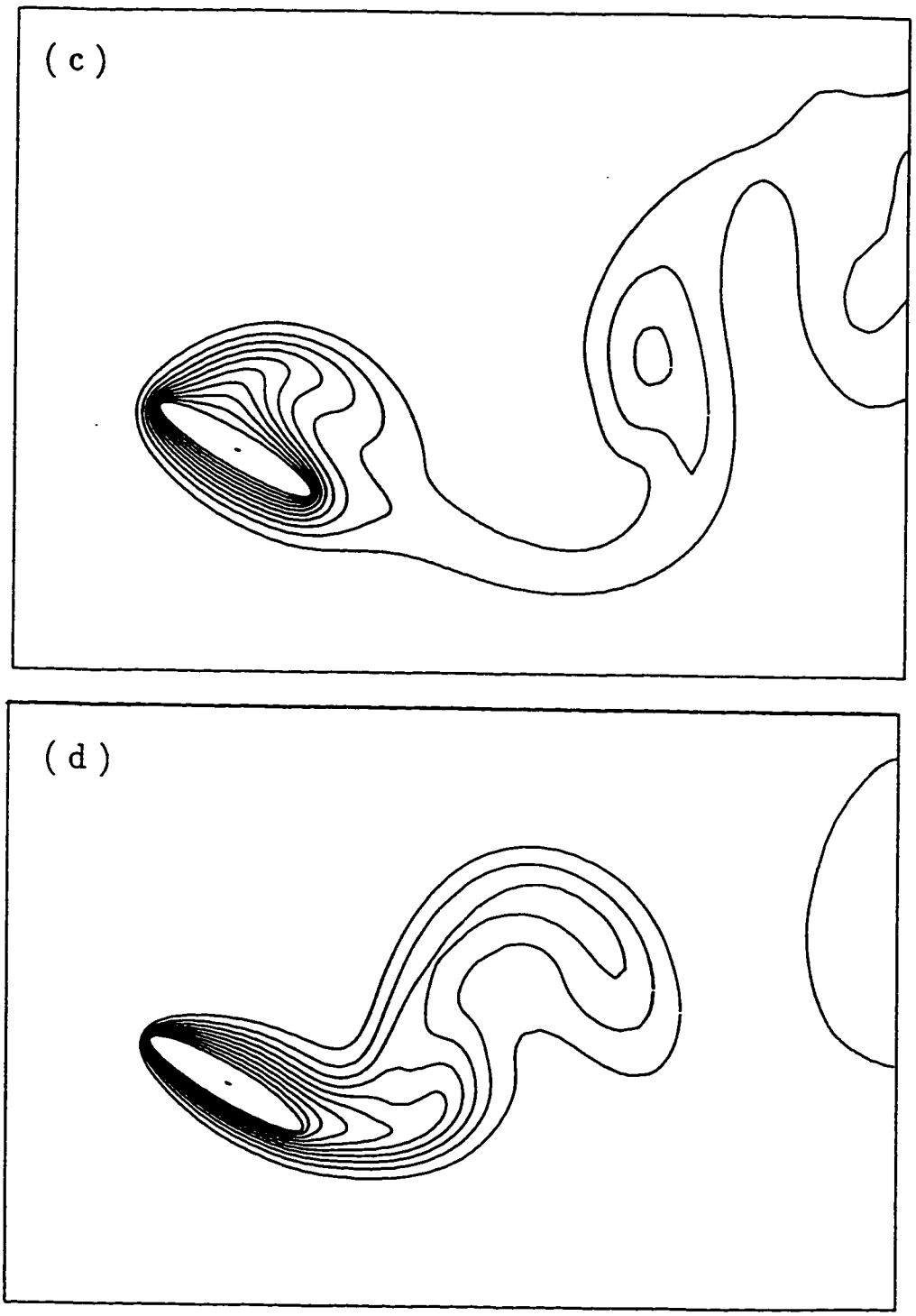

Figure 5.139: The development of the isotherm contours for the case of Re=100, Gr=20000, $Ar = 0.2$, $\lambda = 30^o$, $\beta = 0.5$ and $S = \pi/4$, during one complete cycle : (a) t = 32; (b) t = 34; (c) t = 36; (d) t = 40.

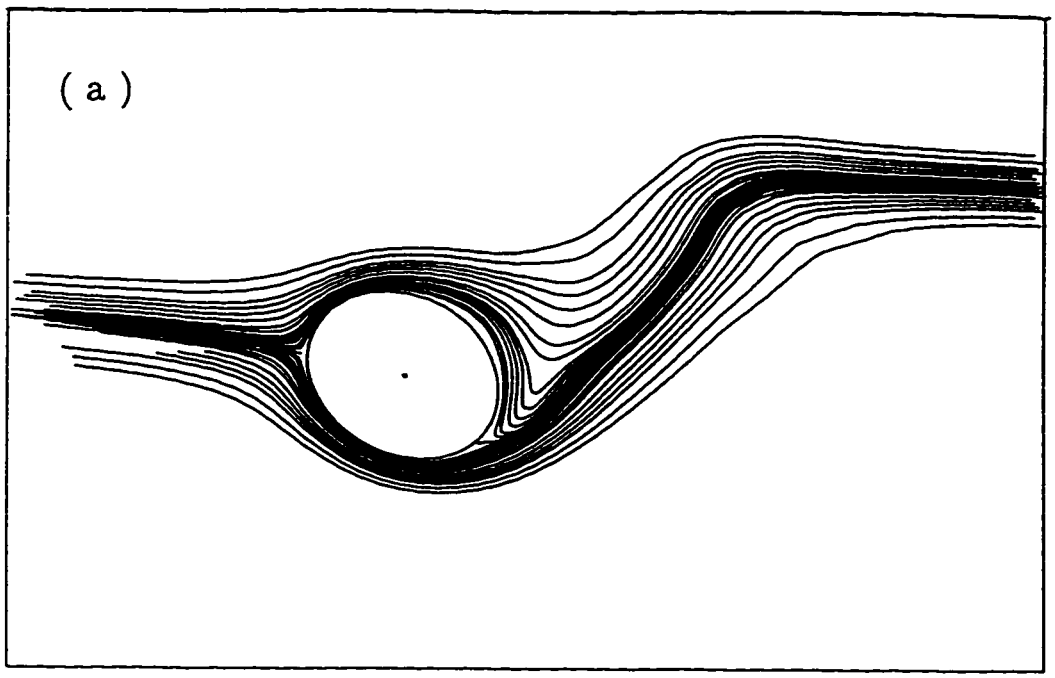
(a)

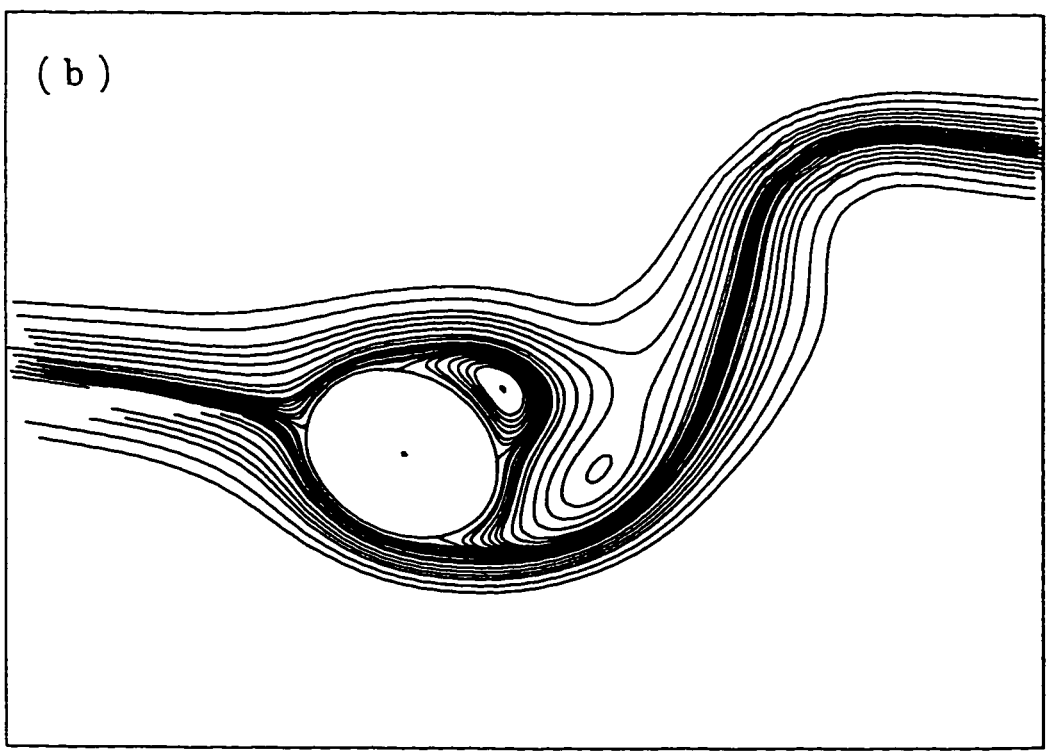
(b)

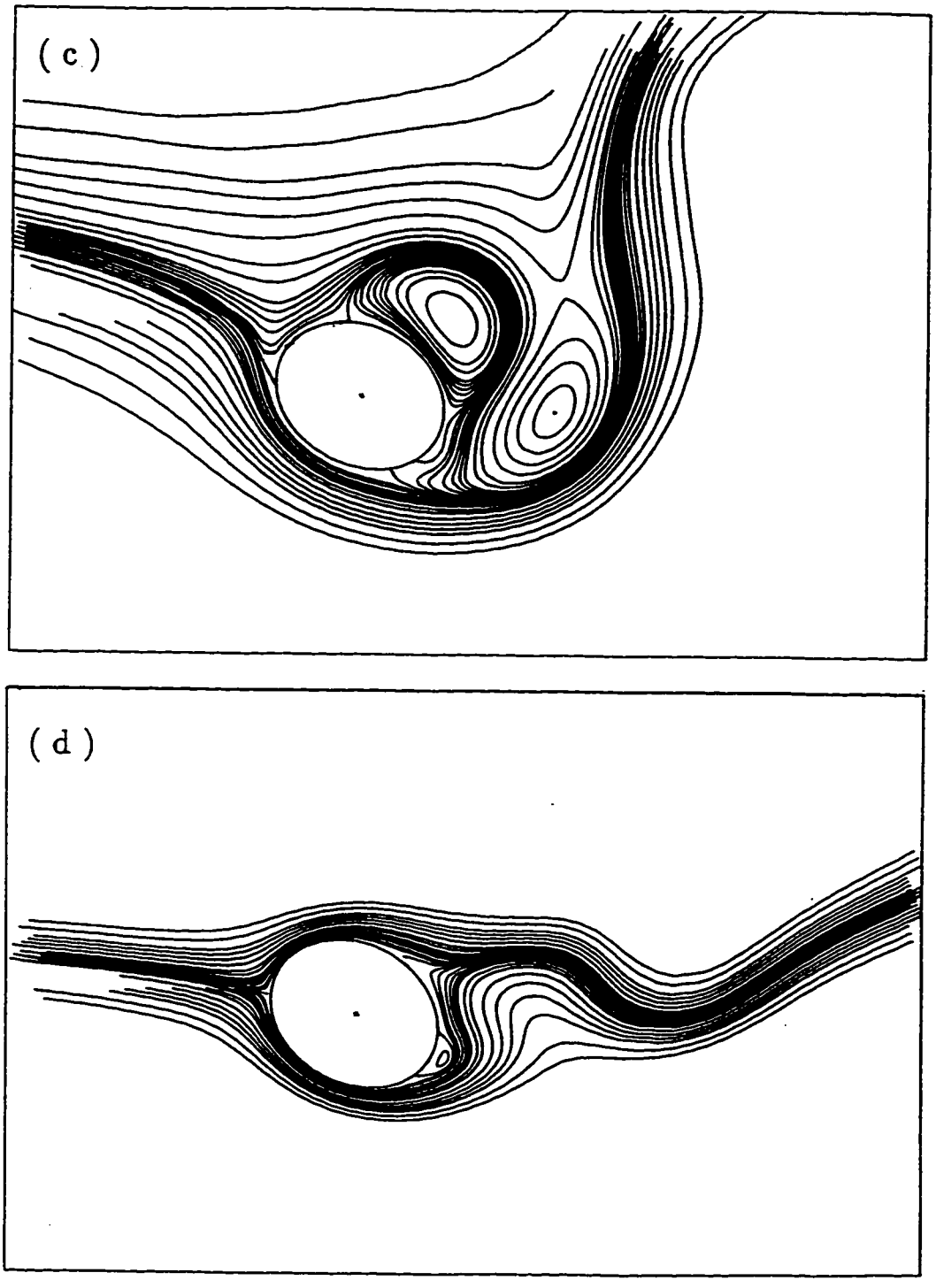

Figure 5.140: The development of the streamline patterns for the case of Re=100, Gr= 20000, $Ar = 0.8$, $\lambda = 30°$, $\beta = 0.5$ and $S = \pi/4$, during one complete cycle : (a) t = 32; (b) t = 33; (c) t = 34; (d) t = 36; (e) t = 38; (f) t = 40 .

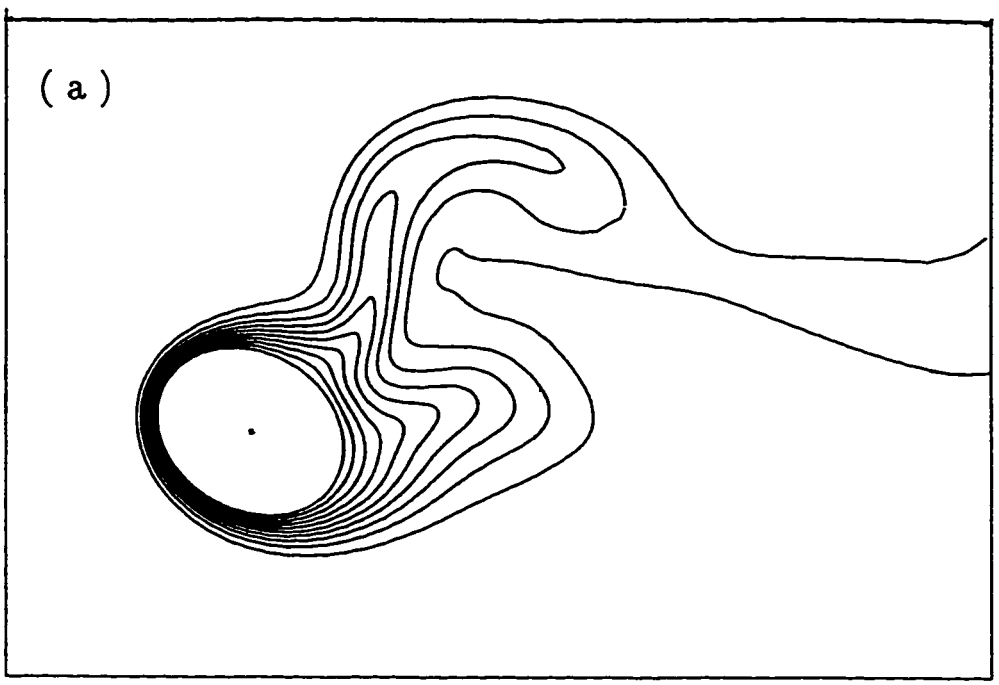
(a)

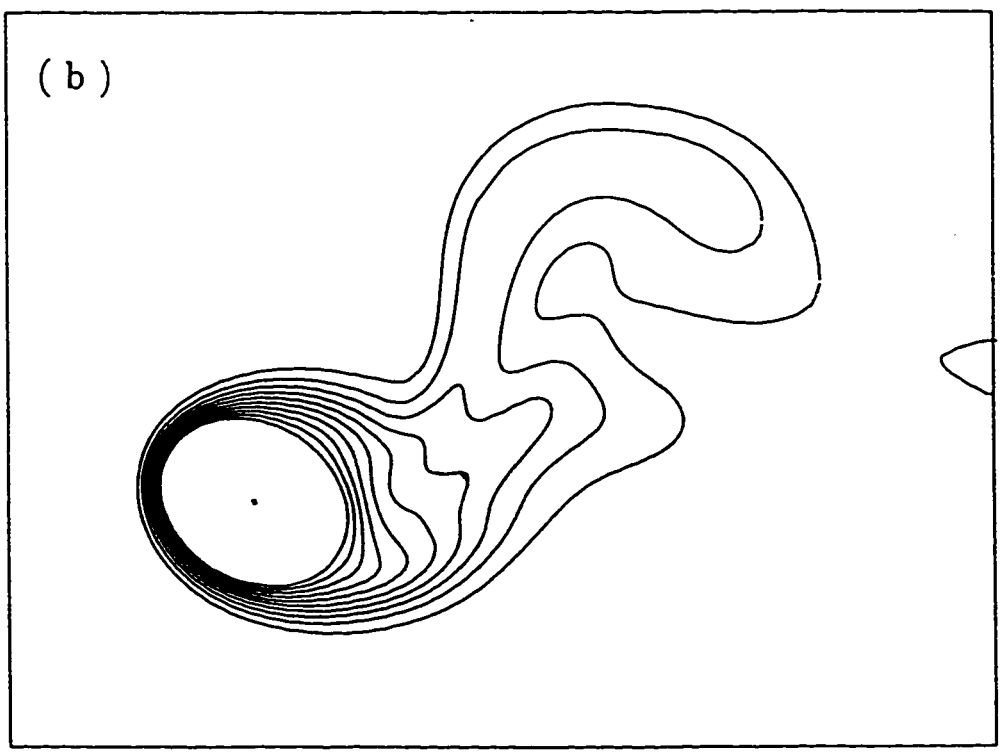
(b)

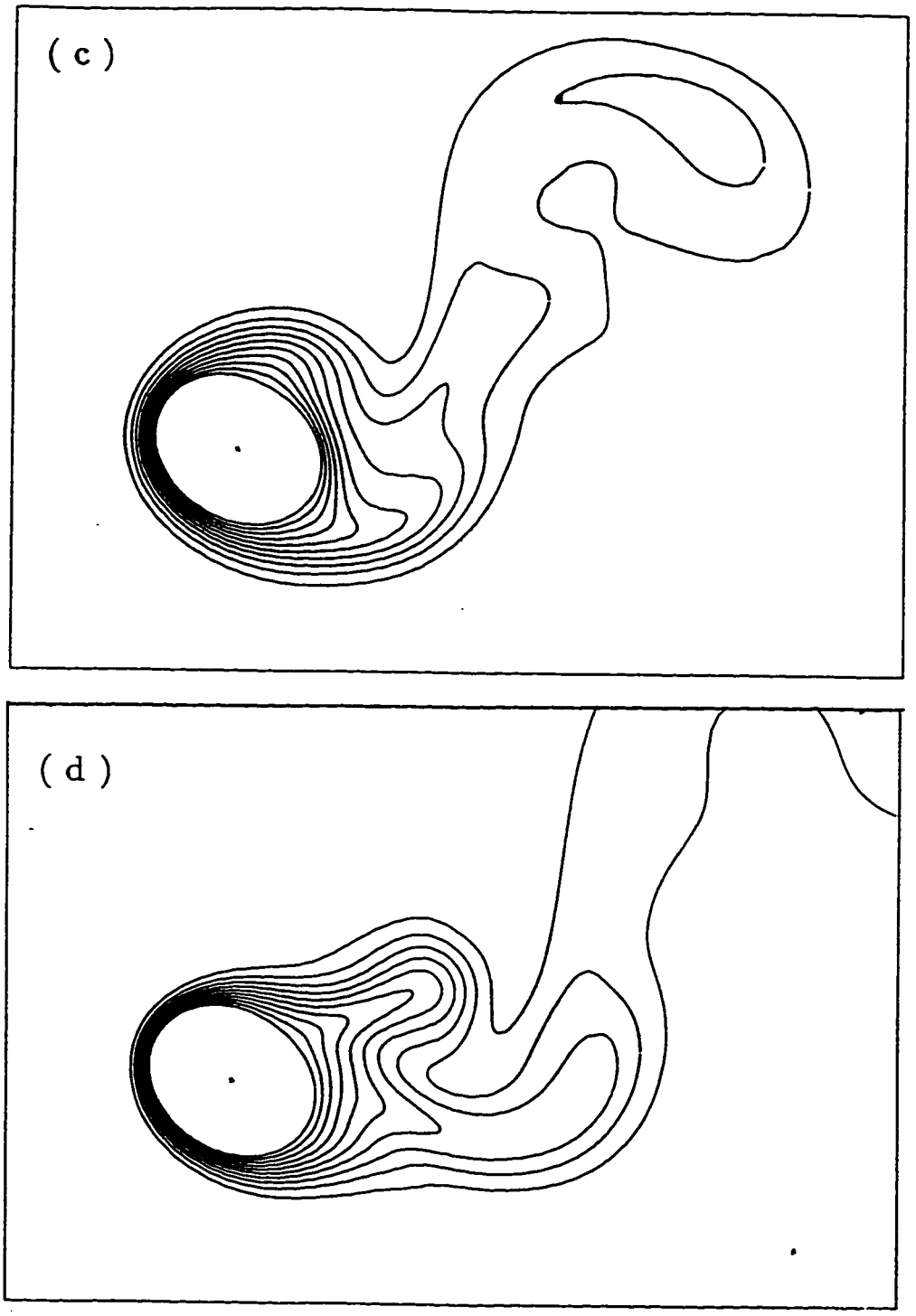

Figure 5.141: The development of the isotherm contours for the case of Re=100, Gr= 20000, $Ar = 0.8$, $\lambda = 30^o$, $\beta = 0.5$ and $S = \pi/4$, during one complete cycle : (a) t = 32; (b) t = 34; (c) t = 36; (d) t = 40.

Chapter 6

Conclusion

The problem of mixed convection from an elliptic tube subjected to fluctuations in the free stream velocity is investigated numerically. The free stream direction is horizontal and normal to the tube axis and the flow field is essentially two-dimensional. The investigation is based on a numerical solution of the conservation equations of mass, momentum and energy. The resulting velocity and thermal fields are found to be quasi-steady because of free stream fluctuations and vortex shedding. The study focuses on the effect of the amplitude and frequency of fluctuations on the heat transfer process in the Reynolds number range from 20 to 500 and Grashof number range from 0 to 5.0×10^4. The method of solution was validated by comparing the average and local Nusselt numbers with available theoretical and experimental data for a circular cylinder and a flat plate as two limiting cases and the agreement is found to be satisfactory. The time-average Nusselt number is found to increase with increasing the amplitude of the fluctuations and with decreasing the frequency. The

heat transfer enhancement due to free stream fluctuations is more pronounced for high Reynolds numbers and moderate Grashof numbers. It was found also that the heat transfer enhancement due to free stream fluctuations increases with the increase of the angle of inclination, λ, until reaching $\lambda = 90°$, after which increasing the angle of inclination has a reversing effect. For small axis ratios, the local Nusselt number and surface vorticity approach very high values near the leading edge. The details of the velocity and thermal fields are presented in the form of isotherms and streamline patterns. It was found that free stream fluctuations tends to enhance vortex shedding and the effect of buoyancy is found to induce an upward flow in the wake region. The local Nusselt number, surface vorticity and pressure distributions are presented for various cases. It is hoped that this work represents a step forward in understanding the effect of free stream fluctuations on forced and mixed convection from elliptic tubes.

Appendix-A

The functions S_{n0} , S_{n1} and S_{n2} used in equations (4.4), (4.5) and (4.6) respectively are as follows:

$$S_{n0}(\xi,t) = \sum n(f_n\frac{\partial g_n}{\partial \xi} - F_n\frac{\partial g_n}{\partial \xi} - g_n\frac{\partial F_n}{\partial \xi} + G_n\frac{\partial f_n}{\partial \xi})$$
$$+\sum \frac{Gr}{2Re^2}[\frac{\partial h_1}{\partial \xi}\, cosh\xi\, \sin\lambda + \frac{\partial H_1}{\partial \xi}\, \sinh\xi\, \cos\lambda +$$
$$H_1\, \cosh\xi\, \cos\lambda + h_1\, \sinh\xi\, \sin\lambda]$$

$$S_{n1} = \sum\{\frac{\partial g_m}{\partial \xi}[kf_k - Jf_j] + \frac{\partial G_m}{\partial \xi}[Kf_k - (m-n)F_j]\}$$
$$+mg_m[\frac{\partial f_k}{\partial \xi} - sgn(m-n)\frac{\partial f_j}{\partial \xi}] + mG_m(\frac{\partial F_k}{\partial \xi} - \frac{\partial F_j}{\partial \xi})\}$$
$$-\frac{Gr}{2Re^2}\{[\delta n1\frac{\partial H_0}{\partial \xi} + \frac{\partial H_{n-1}}{\partial \xi} - \frac{\partial H_{n+1}}{\partial \xi}] * \cosh\xi\, \sin\lambda$$
$$+\sinh\xi\cos\lambda[\frac{\partial h_{n-1}}{\partial \xi} + \frac{\partial hn+1}{\partial \xi}] - \cosh\xi\cos\lambda[(n-1)h_{n-1}$$
$$-(n+1)h_{n+1} - \sinh\xi\, \sin\lambda[(n-1)H_{n-1} + (n+1)H_{n+1}]\}$$

$$S_{n2} = nf_n\frac{\partial G_0}{\partial \xi} + \sum[\frac{\partial g_m}{\partial \xi}[kF_k + (m-n)F_j]$$
$$-\sum\{\frac{\partial G_m}{\partial \xi}(Kf_k + Jf_j) + mg_m(\frac{\partial F_k}{\partial \xi} + \frac{\partial F_j}{\partial \xi}) - mG_m[\frac{\partial f_k}{\partial \xi}$$
$$+sgn(m-1)\frac{\partial f_j}{\partial \xi}] - \frac{Gr}{2Re^2}\{\cosh\xi\, \sin\lambda(\frac{\partial h_{n+1}}{\partial \xi} - \frac{\partial h_{n-1}}{\partial \xi})$$
$$+\sinh\xi\ \cos\lambda\,(\delta n1\,\frac{\partial H_0}{\partial \xi} + \frac{\partial H_{n-1}}{\partial \xi} + \frac{\partial H_{n+1}}{\partial \xi})$$
$$-\cosh\xi\ \cos\lambda((n+1)\,H_{n+1} - (n-1)\,H_{n-1})$$
$$+\sinh\xi\ \sin\lambda\,(\,(n-1)\,h_{n-1} + (n+1)\,h_{n+1}\,)\ \}\ \}$$

The functions Z_0 , Z_{n1} and Z_{n2} used in equations (4.10), (4.11) and (4.12) respec-

tively are as follows:

$$Z_0(\xi,t) = \sum_{n=1}^{N} n(F_n\frac{\partial h_n}{\partial \xi} - f_n\frac{\partial H_n}{\partial \xi} + h_n\frac{\partial F_n}{\partial \xi} - H_n\frac{\partial f_n}{\partial \xi})$$

$$\begin{aligned} Z_{n1}(\xi,t) = \sum_{m=1}^{N}\{&\frac{\partial h_m}{\partial \xi}(Kf_k - Jf_j) + \frac{\partial H_m}{\partial \xi}[KF_k - (m-n)F_j] \\ &+mh_m[\frac{\partial f_k}{\partial \xi} - sgn(m-n)\frac{\partial F_J}{\partial \xi}] + mH_m(\frac{\partial F_k}{\partial \xi} - \frac{\partial F_j}{\partial \xi})\} \end{aligned}$$

$$\begin{aligned} Z_{n2}(\xi,t) = \sum_{m=1}^{N}\{&\frac{\partial h_m}{\partial \xi}(Kf_k + (m-n)F_j) - \frac{\partial H_m}{\partial \xi}(Kf_k + Jf_j) \\ &+mh_m(\frac{\partial F_k}{\partial \xi} + \frac{\partial F_g}{\partial \xi}) - mH_m[\frac{\partial f_k}{\partial \xi} + sgn(m-n)\frac{\partial f_j}{\partial \xi}]\} \end{aligned}$$

where $sgn(m-n)$ means the sign of the term $(m-n)$.

Nomenclature

Ar	Axis ratio, b/a
a,b	semi-major and minor axes
c	focal distance
C_D, C_L	drag and lift coeffcients
F_0, f_n, F_n	functions defined in equations (4.7-4.9)
g	gravitational acceleration
G_0, g_n, G_n	functions defined in equations(4.4-4.6)
Gr	Grashof number defined in equation (3.21)
h	local heat transfer coefficient
H_0, h_n, H_n	functions defined in equations (4.10-4.12)
$\overline{h}$	mean heat transfer coefficient
K	thermal conductivity
L	ellipse section perimeter
Nu	local Nusselt number
$\overline{Nu}$	average Nusselt number
$\overline{\overline{Nu}}$	time-averge Nusselt number
p	fluid pressure
p^*	dimensionless fluid pressure

Pe	Peclet number, Re Pr
Pr	Prandtl number, $\nu\alpha$
$\dot{q}$	local heat flux
Re	Reynolds number, $2\overline{u}c/\nu$
S	Strouhal number, $c\omega/\overline{u}$
t	dimensionless time
T	fluid temperature
U,V or u,v	velocities in the x- and y-directions
u_ξ, u_η	velocities in the $\xi-$ and η-directions
x, y	rectilinear coordinates
z	boundary-layer coordinates

Greek symbols

α	thermal difusivity
β	amplitude of fluctuations in the free stream
δ	kroneker delta
ζ	vorticity
η , ξ	elliptical coordinates
λ	angle of inclination

μ	viscosity
ν	kinematic viscosity
ρ	density
ϕ	dimensionless temperature
ψ	stream function

Subscripts

avg	average
max	maximum/peak
min	minimum
s, 0	at the surface
∞	at infinite distance from the surface

Superscripts

m	iteration number
o	degrees

Pe	Peclet number, Re Pr
Pr	Prandtl number, $\nu\alpha$
$\dot{q}$	local heat flux
Re	Reynolds number, $2\overline{u}c/\nu$
S	Strouhal number, $c\omega/\overline{u}$
t	dimensionless time
T	fluid temperature
U,V or u,v	velocities in the x- and y-directions
u_ξ, u_η	velocities in the $\xi-$ and η-directions
x, y	rectilinear coordinates
z	boundary-layer coordinates

Greek symbols

α	thermal difusivity
β	amplitude of fluctuations in the free stream
δ	kroneker delta
ζ	vorticity
η , ξ	elliptical coordinates
λ	angle of inclination

μ	viscosity
ν	kinematic viscosity
ρ	density
ϕ	dimensionless temperature
ψ	stream function

Subscripts

avg	average
max	maximum/peak
min	minimum
s, 0	at the surface
∞	at infinite distance from the surface

Superscripts

m	iteration number
o	degrees

Bibliography

[1] E. Dec t al. Heat transfer enhancement in the oscillating turbulent flow of a pulse combuster tail pipe. *International Journal of Heat and Mass Transfer*, Vol. 35(9):pp.2311–2325, 1992.

[2] S. Dennis and G. Chang. Numerical solution for steady flow past a circular cylinder at Reynolds numbers up to 100. *Journal of Fluid Mechanics*, Vol.42(3):pp.471–486, 1970.

[3] M. Coutanceau and R. Bouard. Experimental determination of the main features of the viscous flow in the wake of a circular cylinder in uniform translation. *Journal of Fluid Mechanics*, Vol. 79(2):pp.231–256, 1977.

[4] P. Nieuwstadt and H. Keller. Viscous flow past a circular cylinder. *Bull. Univ. Osaka*, Vol. 21(1):pp.205–220, 1973.

[5] Y Lecointe and J. Piquet. On the use of several compact methods for the study of unsteady incompressible viscous flow around a circular cylinder. *Computers*

& Fluids, Vol. 12(4):pp.225–280, 1984.

[6] H Badr and S Dennis. Time-dependent viscous flow past an impulsively started rotating and translating circular cylinder. *Journal of Fluid Mechanics*, Vol. 158:pp.447–448, 1985.

[7] X. Wang and C. Dalton. Numerical solution for impulsively started and decelerated viscous flow past a circular cylinder. *Journal of Fluid Mechanics*, Vol. 211:pp.547–567, 1991.

[8] Y. Zverkhovskiy. Unsteady flow of newtonian or non-newtonian fluids around a rotating vertical cylinder. *Fluid Mechanics Research*, Vol. 21(3):pp.37–42, 1992.

[9] B. Hakizumwami. high Reynolds number flow past an impulsively started circular cylinder. *Computers Fluid*, Vol. 23(7):pp.895–902, 1994.

[10] A. Acrivos. On combined effect of forced and free convection heat transfer in laminar boundary layers flows. *Chem. Engg. Sci*, Vol. 110:pp 343–352, 1966.

[11] C. Vest and M. Lawson. Onset of convection near a suddenly heated horizontal wire. *International Journal of Heat and Mass Transfer*, Vol. 15:pp.1281–1283, 1972.

[12] E. Sparrow and L. Lee. Analysis of mixed convection about a horizontal cylinder. *International Journal of Heat and Mass Transfer*, Vol. 26(5):pp. 639–653, 1975.

[13] H. Badr. A theoretical study of laminar mixed convection from a horizontal cylinder in cross stream. *International Journal of Heat and Mass Transfer*, Vol. 26(5):pp.639–653, 1983.

[14] W. Harrison. Motion of spheres, circular and elliptic cylinders through viscous liquids. *Trans. Comb. Phil. Soc.*, Vol. 23, 1924.

[15] H. Lugt and H. Hausling. laminar flow past an abruptly accelerating elliptic cylinder at 45 degrees incidence. *Journal of Fluid Mechanics*, Vol. 66(4):pp.711–734, 1974.

[16] V. Patel. Flow around the impulsively started elliptic cylinder at various angles of attack. *Computers & Fluids*, Vol. 9(4):pp.435–462, 1981.

[17] P. Loc et al. A comparison of numerical simulation and experimental visualization of the early stages of the flow generated by an impulsively started elliptic cylinder. *Numerical Methods in Laminar and Turbulant Flow*, pages 269–279, Third International Conference held in Seatle, Pineridge Press, U.K.,1983.

[18] S. Lee and L. Leal. Low Reynold number flow past cylindrical bodies of arbitrary cross-sectional shape. *Journal of Fluid Mechanics*, Vol. 164(1):pp.401–427, 1985.

[19] S. Dalessio and C. Dennis. A vorticity model for viscous flow past a cylinder. *Computers & Fluids*, Vol. 23(2):pp.279–293, 1994.

[20] F. Lin and B. Chao. Laminar free convection over two-dimensional and axisymmetric bodies of arbitrary contour. *ASME Journal of Heat Transfer*, Vol. 96(1):pp.435–442, 1974.

[21] G. Raithby and K. Hollands. Laminar and turbulent free convection from elliptic cylinders with a vertical plate and a horizontal circular cylinder as special cases. *ASME Journal of Heat Transfer*, Vol. 98(1):pp.72–82, 1976.

[22] H. Badr and K. Shamsher. Free convection from an elliptic cylinder with major axis vertical. *International Journal of Heat and Mass Transfer*, Vol. 36(14):pp.3593–3602, 1993.

[23] H. Badr. Mixed convection from a straight isothermal tube of elliptic cross section. *International Journal of Heat and Mass Transfer*, Vol 37(15):pp.2343–2365, 1994.

[24] D. Kminiski et al. Numerical and experimental analysis of combined convective and radiative heat transfer in laminar flow over a circular cylinder. *International Journal of Heat and Mass Transfer*, Vol. 38(17):pp.3161–3169, 1995.

[25] J. Watson. A solution of the Navier-Stokes equations illustrating the response of laminar boundary layer to a given change in the external stream velocity. *Quart. Journal of Mechanical Engineering and Applied Math*, Vol. 5(1):pp.302–324, 1958.

[26] C. Wang. On high frequency oscillating flow. *Journal of Fluid Mechanics*, Vol. 32:pp.55–68, 1968.

[27] M. Takallu and J. Williams. Lift hysteresis of an oscillating slender ellipse. *AIAA Journal*, Vol. 22(12):pp.1733–1741, 1984.

[28] U. Kurzweg. Enhanced heat conduction in fluids subjected to sinusoidal oscillations. *Journal of Heat Transfer*, Vol. 107:pp.459–462, 1985.

[29] G. Bearman and O. Downie. Forces on cylinders in viscous oscillatory flow at low Keulegan numbers. *Journal of Fluid Mechanics*, Vol. 154:pp.337–356, 1985.

[30] T. Sarpkaya. Forces on a circular cylinder in viscous oscillating flow at low keulegan-carpenter numbers. *Journal of Fluid Mechanics*, Vol. 165:pp.61–71, 1986.

[31] H. Hojni. Streaked flow around an oscillating circular cylinder. *Journal of Fluid Mechanics*, Vol 107:pp.347–367, 1981.

[32] P. Hall. On the stability of unsteady boundary layer on a cylinder oscillating transversely in a viscous fluid. *Journal of Fluid Mechanics*, Vol. 146:pp.347–367, 1984.

[33] N. Baba and H. Miyata. Higher order accurate difference solutions of vortex generation from a circular cylinder. *Journal of Computational Physics*, Vol. 69:pp.362–396, 1987.

[34] C. Lam. Calculations of laminar boundary layers under small harmonic progressive oscillations of the free stream. *International Journal of Heat and Mass Transfer*, Vol. 9(3):pp.321–325, 1988.

[35] P. Justesen. A numerical study of oscillating flow around a circular cylinder. *Journal of Fluid Mechanics*, Vol. 222:pp.157–196, 1991.

[36] X. Wang and C. Dalton. Oscillating flow past a rigid circular cylinder. *Journal of Fluid Engineering*, Vol. 113:pp.337–383, 1991.

[37] H. Badr. Oscillating inviscid flow over an inclined elliptic cylinders with a flat plates and a circular cylinder as special caes. *Ocean Engineering*, Vol. 21(1):pp.105–113, 1994.

[38] H. Badr. Oscillating viscous flow over an inclined elliptic cylinder. *Ocean Engineering*, Vol. 21(4):pp.401–426, 1994.

[39] S. Nguyen, H. Paik and R. Douglass. Mixed convection about a rotating circular cylinder with small fluctuations in the free-stream velocity. *International Journal of Heat and Mass Transfer*, Vol. 36(1):pp.3311–3325, 1995.

[40] S. Chakrabarti et al. Wave forces on inclined tubes. *Coastal engineering*, Vol. 1:pp.149–165, 1977.

[41] T. Sarpkaya et al. Hydrolic response of cylinders in harmonic and wave flow. pages 383–388, Houston TX., 1981. 13th Annual Offshore Technology Conference, Shell Development Company.

[42] M. Brendel and T. Mueller. Boundary layer measurements on an airfoil at low Reynolds number in an oscillating free stream. *AIAA Journal*, Vol.26(3):pp.257–263, 1988.

[43] A. Staniforth . Studies of symmetrical and asymmetrical viscous flows past impulsively started cylinders. Ph.D. University of Western Ontario, 1972

[44] A Hatton et al. Combined forced and natural convection with low speed air flow over horizontal cylinders. *Journal of Fluid Mechanics*, Vol. 42:pp 17–31, 1970.

[45] D. Collis and G. Williams. Two-dimensional convection from heated wires at low Reynolds numbers. *Journal of Fluid Mechanics*, Vol. 6:pp 357–384, 1959.

[46] S. Dennis et al. steady laminar forced convection from a circular cylinder at low reynolds number. *Physics of Fluids*, Vol. 11:pp 933–940, 1967.

[47] M. Ha and S. Yavuzkurt. A theoretical investigation of a acoustic enhancement of heat and mass transfer in pure oscillating flow. *International Journal of Heat and Mass Transfer*, Vol. 36(8):pp.3128–2192, 1993.

[48] B. Gebhart et al. Bouyancy induced flow and transport. pages pp. 490–491, New York, 1988. Hemisphere.

[49] S. Dennis and N. Smith. Forced convection from a heated flat plate. *Journal of Fluid Mechanics*, Vol. 24:pp 509–519, 1966.

[50] W. Soh. A numerical methods for nonlinear water waves. *Computers & Fluids*, Vol. 12(2):pp. 133–143, 1984.

[51] J. Markin. Free convection boundary layer on cylinders of elliptic cross section. *ASME Journal of Heat Transfer*, Vol. 99(1):pp.453–457, 1977.

[52] H. Badr. Laminar combined convection from a horizontal cylinder, parallel and contra flow regimes. *International Journal of Heat and Mass Transfer*, Vol. 27:pp.15–27, 1984.

[53] H. Badr and S. Dennis. Laminar forced convection from a rotating cylinder. *International Journal of Heat and Mass Transfer*, Vol. 28:pp.253–264, 1985.

[54] H. Badr. Heat transfer in transient bouancy driven flow adjacent to a horizontal rod. *International Journal of Heat and Mass Transfer*, Vol. 30(10):pp.1997–2012, 1987.

[55] W. Collins and S. Dennis. Flow past an impulsively started circular cylinder. *Journal of Fluid Mechanics*, Vol. 60:pp.105–127, 1973.

Vita

- Eball Hifthy A. Ahmad
- Received Bachelor's degree in Mechanical Engineering from King Fahd University of Petroleum and Minerals, Dhahran, Saudi Arabia in August, 1989
- Received Master's degree im Mechanical Engineering from King Fahd University of Petroleum and Minerals, Dhahran, Saudi Arabia in March, 1992.
- Finished all the requirments of the Ph.D. degree in Mechanical Engineering from King Fahd University of Petroleum and Minerals, Dhahran, Saudi Arabia in December, 1996.